D5-15615

SATURN V MODEL BASE HEATING TEST ANALYSIS (S-IC STAGE) VOLUME 2

(NASA-CR-147086) SATURN V MODEL BASE HEATING TEST ANALYSIS (S-IC STAGE), VOLUME 2 (Boeing Co., Seattle, Wash.) 206 p

N76-73541

Unclas

00/98 25914

OCTOBER 24, 1966

REPRODUCED BY
NATIONAL TECHNICAL
INFORMATION SERVICE
U. S. DEPARTMENT OF COMMERCE
SPRINGFIELD, VA. 22161

DOCUMENT NO. D5-15615

TITLE SATURN V MODEL BASE HEATING TEST ANALYSIS (S-IC STAGE) VOLUME 2 OF 2

MODEL NO. SATURN V CONTRACT NO. NAS8-5608

THERMAL ANALYSIS GROUP

OCTOBER 24, 1966

D. B. JACOBS
CHIEF ENGINEER

ISSUE NO. ISSUED TO

THE BOEING COMPANY SPACE DIVISION LAUNCH SYSTEMS BRANCH

CONTENTS

VOLUME 2 OF 2

		Page
	CONTENTS	i
	ILLUSTRATIONS	iv
	SECTION 3 - ANALYSIS OF CORNELL AERONAUTICAL LABORATORY (CAL) 8 BY 8 FOOT TRANSONIC TUNNEL TEST	
3.0	INTRODUCTION	1
3.1	BOUNDARY LAYER	1
3.2	RADIATION	7
3.2.1	RADIATION TO BASE	7
3.2.2	RADIATION TO FIN AND ENGINE FAIRING	7
3.2.3	RADIATION TO CENTER ENGINE (EXTERNAL)	7
3.2.4	COMPARISON WITH RADIATION THEORY	13
3.3	CONVECTION	13
3.3.1	CONVECTION TO BASE	13
3.3.2	CONVECTION TO FIN AND THE ENGINE FAIRING	18
3.3.3	CONVECTION TO CENTER ENGINE (EXTERNAL)	18
3.3.4	COMPARISON WITH THEORY	18
3.4	BASE PRESSURE	21
3.4.1	COMPARISON WITH THEORY	25
3.5	DATA ACCURACY	25
3.6	CONCLUSIONS	25
	SECTION 4 - ANALYSIS OF LEWIS RESEARCH CENTER (LRC) 8 BY 6 FOOT SUPERSONIC WIND TUNNEL TEST	
4.0	INTRODUCTION	32
4.1	BOUNDARY LAYER	34
4.2	RADIATION	34
4.2.1	RADIATION TO BASE	34
4.2.2	RADIATION TO FIN AND ENGINE FAIRING	40
4.2.3	RADIATION TO ENGINES (EXTERNAL)	40
4.2.4	RADIATION TO ENGINES (ENGINE OUT)	44
4.2.5	COMPARISON WITH RADIATION THEORY	44
4.3	CONVECTION	44
4.3.1	CONVECTION TO BASE	48
4.3.2	CONVECTION TO FIN AND ENGINE FAIRING	54
4.3.3	CONVECTION TO ENGINE NOZZLES (EXTERNAL)	54
4.3.4	CONVECTION TO ENGINE NOZZLE (ENGINE OUT)	54
4.3.5	HEATED BASE PLATE	60
4.3.6	COMPARISON WITH CONVECTIVE THEORY	61
4.4	BASE PRESSURE	61
4.4.1	CONFIGURATION EFFECTS ON BASE PRESSURE	70

CONTENTS (Continued)

		Page
4.4.2	CORRELATION WITH THEORY AND PREVIOUS DATA	70
4.5	DATA ACCURACY	92
4.5.1	REPEATABILITY	92
4.5.2	SYMMETRY	92
4.6	CONCLUSIONS	105
	SECTION 5 - ANALYSIS OF LEWIS RESEARCH CENTER (LRC) 10 BY 10 FOOT SUPERSONIC TUNNEL TEST	
5.0	INTRODUCTION	107
5.1	BOUNDARY LAYER	107
5.2	RADIATION	111
5.2.1	RADIATION TO BASE	111
5.2.2	RADIATION TO FIN AND ENGINE FAIRING	111
5.2.3	RADIATION TO ENGINES (EXTERNAL)	116
5.2.4	RADIATION TO ENGINE (ENGINE-OUT)	116
5.2.5	COMPARISON WITH THEORY	116
5.3	CONVECTION	116
5.3.1	CONVECTION TO BASE	116
5.3.2	CONVECTION TO FIN AND ENGINE FAIRING	120
5.3.3	CONVECTION TO ENGINE (EXTERNAL)	125
5.3.4	CONVECTION TO ENGINE (ENGINE-OUT)	129
5.3.5	COMPARISON WITH THEORY	129
5.4	BASE PRESSURE	134
5.4.1	CONFIGURATION EFFECTS ON BASE PRESSURE	134
5.4.2	CORRELATION WITH THEORY	138
5.5	DATA ACCURACY	138
5.5.1	REPEATABILITY	138
5.5.2	SYMMETRY	138
5.6	CONCLUSIONS	145
	SECTION 6 - ANALYSIS OF CORNELL AERONAUTICAL LABORATORY (CAL) ALTITUDE CHAMBER TEST	
6.0	INTRODUCTION	150
6.1	RADIATION	150
6.1.1	RADIATION TO BASE	150
6.1.2	RADIATION TO FIN AND ENGINE FAIRING	153
6.1.3	RADIATION TO ENGINE (EXTERNAL)	153
6.1.4	RADIATION TO ENGINE (ENGINE-OUT)	153
6.1.5	COMPARISON WITH THEORY	153
6.2	CONVECTION	158
6.2.1	CONVECTION TO BASE	158
6.2.2	CONVECTION TO FIN AND ENGINE FAIRING	163
6.2.3	CONVECTION HEATING TO ENGINE (EXTERNAL)	163
6.2.4	CONVECTION TO ENGINE (ENGINE-OUT)	175

CONTENTS (Continued)

		Page
6.2.5	COMPARISON WITH THEORY	175
6.3	BASE PRESSURE	178
6.3.1	CONFIGURATION EFFECT ON BASE PRESSURE	178
6.3.2	COMPARISON WITH THEORY	182
6.4	DATA ACCURACY	182
6.4.1	REPEATABILITY	182
6.4.2	SYMMETRY	189
6.5	HEATED BASE PLATE	189
6.6	CONCLUSIONS	194
	NOMENCLATURE	195

ILLUSTRATIONS

VOLUME II

		Page
FIGURE 1	Model Installation - Cornell 8 by 8 Transonic Wind Tunnel	2
FIGURE 2	Test Conditions - CAL 8 by 8 Tunnel	3
FIGURE 3	Photographs During Test - CAL 8 by 8 Tunnel - M=0.6, $B_1FS_1D_1SC_1N_{1-5}$	4
FIGURE 4	Boundary Layer Rake Data - CAL 8 by 8 Tunnel	5
FIGURE 5	Model Boundary Layer Thickness Versus Theory	6
FIGURE 6	Base Heating - Radiation	8
FIGURE 7	Base Heating - Radiation	9
FIGURE 8	Base Heating - Radiation	10
FIGURE 9	Fin and Engine Fairing Heating - Radiation	11
FIGURE 10	Engine Heating - Radiation (External)	12
FIGURE 11	Base Heating - Radiation Versus Theory	14
FIGURE 12	Base Heating - Convection	15
FIGURE 13	Base Heating - Convection	16
FIGURE 14	Base Heating - Convection	17
FIGURE 15	Fin and Engine Fairing Heating - Convection	19
FIGURE 16	Engine Heating - Convection (External)	20
FIGURE 17	Base Pressure	22
FIGURE 18	Base Pressure	23
FIGURE 19	Base Pressure	24
FIGURE 20	Engines Off Base Pressure Comparison - CAL 8 by 8 Tunnel	26
FIGURE 21	Base Pressure Comparison with Theory - Cornell 8 by 8 Tunnel	27
FIGURE 22	Base Heating - Radiation (Symmetry)	28
FIGURE 23	Base Heating - Convection (Symmetry)	29
FIGURE 24	Base Pressure - Symmetry	30
FIGURE 25	Test Conditions - Lewis 8 by 6 Tunnel	33
FIGURE 26	Boundary Layer Rake Data - Lewis 8 by 6 Tunnel	35
FIGURE 27	Model Boundary Layer Thickness Versus Theory	36
FIGURE 28	Base Heating - Radiation	37
FIGURE 29	Base Heating - Radiation	38
FIGURE 30	Base Heating - Radiation	39
FIGURE 31	Base Heating - Radiation	41
FIGURE 32	Fin and Engine Fairing Heating - Radiation	42
FIGURE 33	Engine Heating - Radiation (External)	43
FIGURE 34	Engine Heating - Radiation (Internal)	45
FIGURE 35	Engine Heating - Radiation (Internal)	46
FIGURE 36	Base Heating - Radiation Versus Theory	47
FIGURE 37	Base Heating - Convection	49
FIGURE 38	Base Heating - Convection	50
FIGURE 39	Turbine Exhaust Timing Effect	51
FIGURE 40	Base Heating - Convection	52
FIGURE 41	Base Heating - Convection	53

ILLUSTRATIONS (Continued)

		Page
FIGURE 42	Fin Heating - Convection	55
FIGURE 43	Engine Heating - Convection (External)	56
FIGURE 44	Engine Heating - Convection (Lip)	57
FIGURE 45	Engine Heating - Convection (Lip)	58
FIGURE 46	Engine Heating - Convection (Engine Out - Internal)	59
FIGURE 47	Base Gas Temperature	62
FIGURE 48	Base Gas Temperature	63
FIGURE 49	Base Gas Temperature	64
FIGURE 50	Base Gas Temperature	65
FIGURE 51	Base Gas Temperature	66
FIGURE 52	Base Gas Temperature	67
FIGURE 53	Base Gas Temperature - Comparison with Theory - Lewis 8 by 6 Tunnel	68
FIGURE 54	Base Heating - Convection Heating Comparison	69
FIGURE 55	Base Pressure	71
FIGURE 56	Base Pressure	72
FIGURE 57	Base Pressure	73
FIGURE 58	Base Pressure	74
FIGURE 59	Base Pressure	75
FIGURE 60	Base Pressure Distribution	76
FIGURE 61	Base Pressure Distribution	77
FIGURE 62	Base Pressure Distribution	78
FIGURE 63	Base Pressure Distribution	79
FIGURE 64	Base Pressure Distribution	80
FIGURE 65	Base Pressure Distribution	81
FIGURE 66	Base Pressure Distribution	82
FIGURE 67	Base Pressure Distribution	82
FIGURE 68	Base Pressure Distribution	84
FIGURE 69	Base Pressure Distribution	85
FIGURE 70	Base Pressure Distribution	86
FIGURE 71	Base Pressure Distribution	87
FIGURE 72	Base Pressure Distribution	88
FIGURE 73	Base Pressure Distribution	89
FIGURE 74	Base Pressure Distribution	90
FIGURE 75	Engines Off Base Pressure Comparison - LRC 8 by 6 Tunnel	91
FIGURE 76	Base Pressure Versus Theory	93
FIGURE 77	Comparison of S-IC Hot and Cold Models Base Pressure Data	94
FIGURE 78	Base Pressure Repeatability	95
FIGURE 79	Base Heating - Repeatability	96
FIGURE 80	Base Heating - Repeabability	97
FIGURE 81	Base Heating - Convection (Symmetry)	98
FIGURE 82	Base Heating - Convection (Symmetry)	99
FIGURE 83	Base Heating - Convection (Symmetry)	100
FIGURE 84	Base Heating - Convection (Symmetry)	101

ILLUSTRATIONS (Continued)

		Page
FIGURE 85	Base Heating - Radiation (Symmetry)	102
FIGURE 86	Base Heating - Radiation (Symmetry)	103
FIGURE 87	Base Pressure - Symmetry	104
FIGURE 88	Model Installation - Lewis 10 by 10 Supersonic Wind Tunnel	108
FIGURE 89	Test Conditions - Lewis 10 by 10 Tunnel	109
FIGURE 90	Boundary Layer Rake Data - Lewis 10 by 10 Tunnel	110
FIGURE 91	Model Boundary Layer Thickness Versus Theory - LRC 10 by 10 Tunnel	112
FIGURE 92	Base Heating - Radiation	113
FIGURE 93	Base Heating - Radiation	114
FIGURE 94	Fin Heating - Radiation	115
FIGURE 95	Engine Heating - Radiation (Internal)	117
FIGURE 96	Base Heating - Radiation Versus Theory	118
FIGURE 97	Base Heating - Convection	119
FIGURE 98	Base Heating - Convection	121
FIGURE 99	Base Heating - Convection	122
FIGURE 100	Fin Heating - Convection	123
FIGURE 101	Engine Fairing Heating - Convection	124
FIGURE 102	Engine Heating - Convection (External)	126
FIGURE 103	Engine Heating - Convection (External)	127
FIGURE 104	Engine Heating - Convection (External)	128
FIGURE 105	Engine and Base Heating - Convection	130
FIGURE 106	Engine and Base Heating - Convection	131
FIGURE 107	Engine Heating - Convection (Internal)	132
FIGURE 108	Convective Heating - Comparison with Theory - Lewis 10 by 10 Tunnel	133
FIGURE 109	Base Pressure	135
FIGURE 110	Base Pressure	136
FIGURE 111	Base Pressure	137
FIGURE 112	Base Pressure	139
FIGURE 113	Base Pressure - Turbine Exhaust Effect	140
FIGURE 114	Engines Off Base Pressure Comparison - Lewis 10 by 10 Tunnel	141
FIGURE 115	Base Pressure Comparison with Theory - Lewis 10 by 10 Tunnel	142
FIGURE 116	Base Heating - Convection (Repeatability)	143
FIGURE 117	Base Pressure Repeatability	144
FIGURE 118	Base Heating - Convection (Symmetry)	146
FIGURE 119	Base Heating - Convection (Symmetry)	147
FIGURE 120	Base Pressure - Symmetry	148
FIGURE 121	Model Installation - Cornell High Altitude Chamber	151
FIGURE 122	Base Heating - Radiation	152
FIGURE 123	Base Heating - Radiation	154
FIGURE 124	Base Heating - Radiation	155

ILLUSTRATIONS (Continued)

		Page
FIGURE 125	Fin and Engine Fairing Heating - Radiation	156
FIGURE 126	Engine Heating - Radiation	157
FIGURE 127	Base Heating - Radiation Versus Theory	159
FIGURE 128	Base Heating - Convection	160
FIGURE 129	Base Heating - Convection	161
FIGURE 130	Base Heating - Convection	162
FIGURE 131	Base Heating - Convection	164
FIGURE 132	Base Heating - Convection	165
FIGURE 133	Base Heating - Convection	166
FIGURE 134	Base Heating - Convection	167
FIGURE 135	Base Heating - Convection	168
FIGURE 136	Fin and Engine Heating - Convection	169
FIGURE 137	Engine Heating - Convection (External)	170
FIGURE 138	Engine Heating - Convection (External)	171
FIGURE 139	Engine and Base Heating - Convection (External)	172
FIGURE 140	Engine and Base Heating - Convection (External)	173
FIGURE 141	Engine and Base Heating - Convection (External)	174
FIGURE 142	Engine Heating - Convection	176
FIGURE 143	Base Gas Temperature - Comparison with Theory - CAL High Altitude Chamber	177
FIGURE 144	Convective Heating - Comparison with Theory - CAL High Altitude Chamber	179
FIGURE 145	Base Pressure	180
FIGURE 146	Base Pressure	181
FIGURE 147	Base Pressure	183
FIGURE 148	Base Pressure	184
FIGURE 149	Base Pressure Comparison with Theory - CAL High Altitude Chamber	185
FIGURE 150	Base Heating - Radiation (Repeatability)	186
FIGURE 151	Base Heating - Convection (Repeatability)	187
FIGURE 152	Base Pressure - Repeatability	188
FIGURE 153	Nozzle Exit Pressure Survey	190
FIGURE 154	Base Heating - Convection (Symmetry)	191
FIGURE 155	Base Pressure - Symmetry	192
FIGURE 156	Base Gas Temperature	193

SECTION 3 - ANALYSIS OF CORNELL AERONAUTICAL LABORATORY (CAL) 8-BY 8 FOOT TRANSONIC TUNNEL TEST

3.0 INTRODUCTION

This section contains the data analysis of Phase II - Part I of the Saturn S-IC Model Base Heating Test Program. The test was conducted in the Cornell Aeronautical Laboratory 8 by 8 foot Transonic Wind Tunnel with a 2.22 percent scale of the Saturn V, S-IC stage afterbody. Figure 1 shows the model installed in the tunnel. Model tests were conducted at Mach numbers of 0.6, 0.8, 1.0, and 1.2 and at the simulated altitudes shown in Figure 2 during the period of February 1 - 9, 1963.

Flow conditions and boundary layer characteristics are determined on the body near the base by a total pressure rake. Model geometry changes consisting of engine fairing length, scoop size, and turbine exhaust simulation are considered and some comparisons are made with theory. In comparing model test data with theory, the model test environment (external flow environment, combustion characteristics, plume shape, and model dimensions) is used in the theoretical calculations. The model and combustion parameters are discussed under paragraph 1.0, Volume 1.

Pictorial evidence indicates that the engines were not exhausting uniformly. Black areas observed near the exit plane shown in Figure 3 indicate that the combustion was fuel rich with a high unburned carbon content for one of the engines while two show a lighter color. Combustion is controlled by monitoring the pressure in the charge tubes. Previous calibration indicated the pressures to use. No other instrumentation is used to determine the oxidizer to fuel (O/F) ratio.

Injection of hydrogen turbine exhaust is controlled by hand, the turbine exhaust being started first and engine firing a few milliseconds later. An accumulation of hydrogen in the base region prior to engine ignition is possible and may affect the turbine exhaust data.

3.1 BOUNDARY LAYER

Total pressure measurements on the model body near the base, taken using a nine probe rake, (Figure 15 Section 1) are used to determine the boundary layer height. Actual total pressure in the boundary layer is determined by correcting the probe readings for the normal shock which stands in front of the rake. Figure 4 shows the ratio of the actual total pressure to tunnel total pressure, at the various probe heights and Mach numbers. The boundary layer edge is defined as the point at which .998 of the free stream velocity is reached. The measured boundary layer thickness coincides with the turbulent flow estimate (Figure 5) described in paragraph 2.1 of Volume 1.

Reproduced from best available copy.

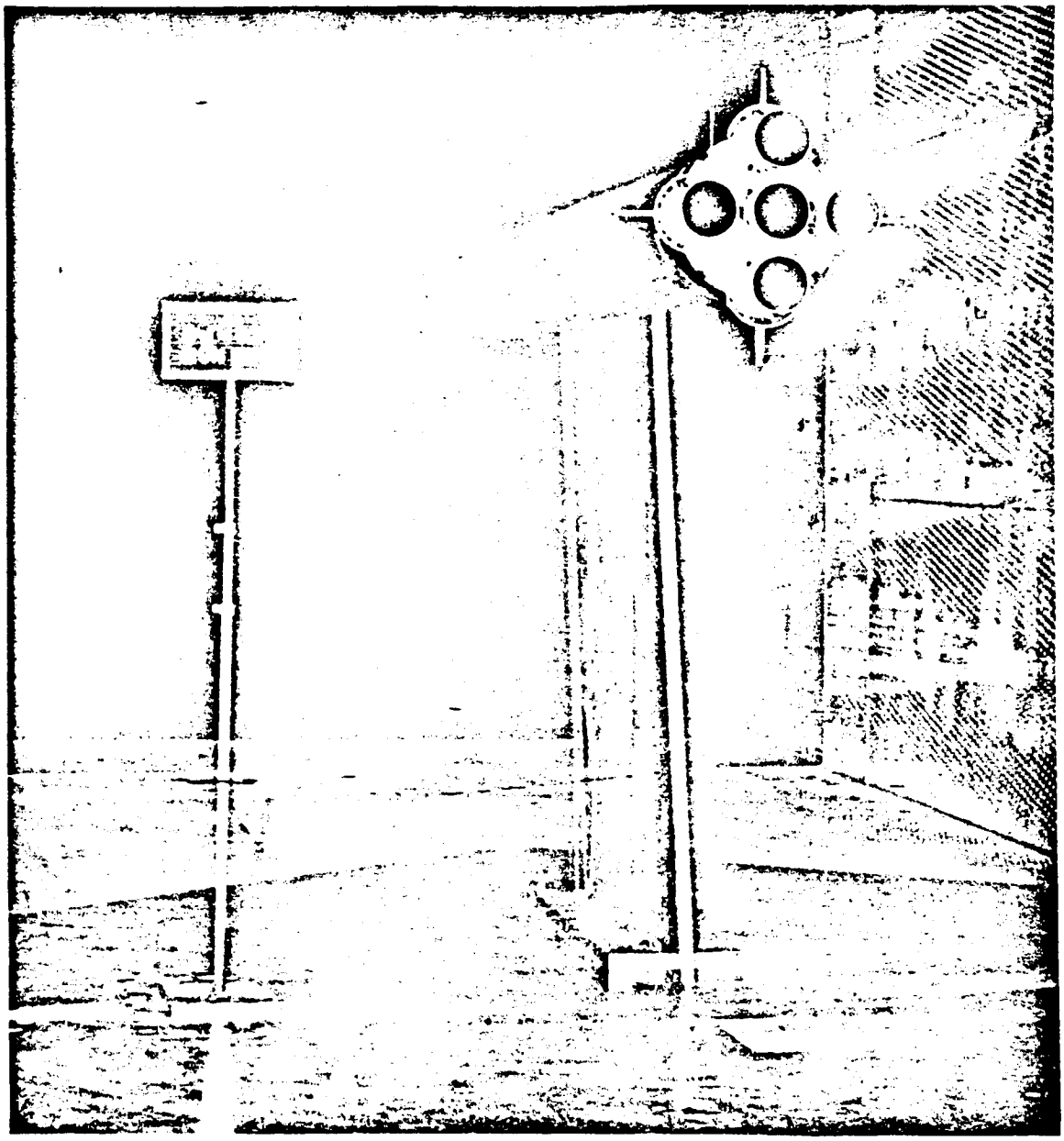

FIGURE 1 Model Installation - Cornell 8 by 8 Transonic Wind Tunnel

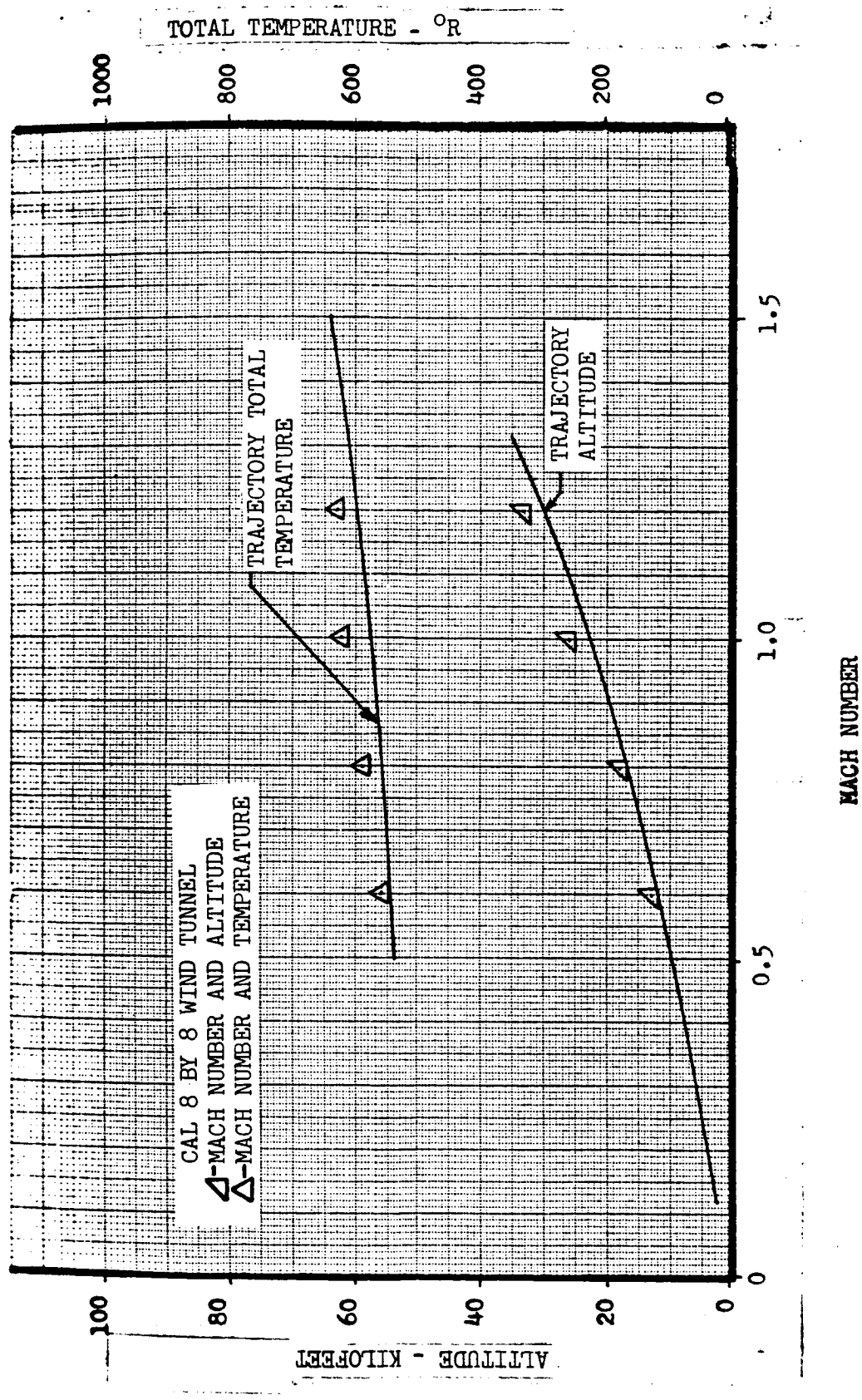

FIGURE 2 Test Conditions - CAL 8 BY 8 Tunnel

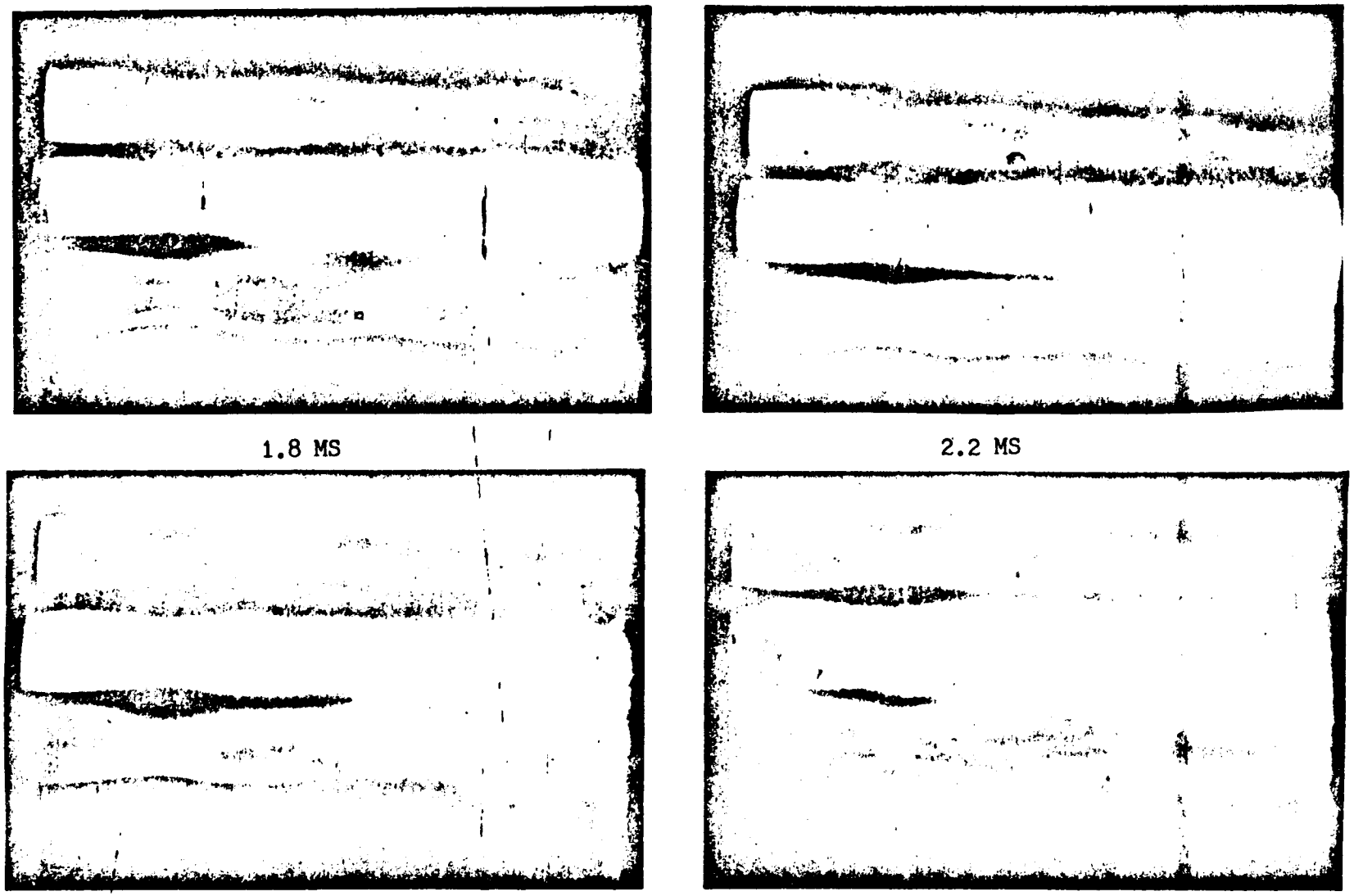

FIGURE 3 Photographs During Test - CAL 8 by 8 Tunnel - M = 0.6, $B_1FS_1D_1SC_1N_{1-5}$

Reproduced from best available copy.

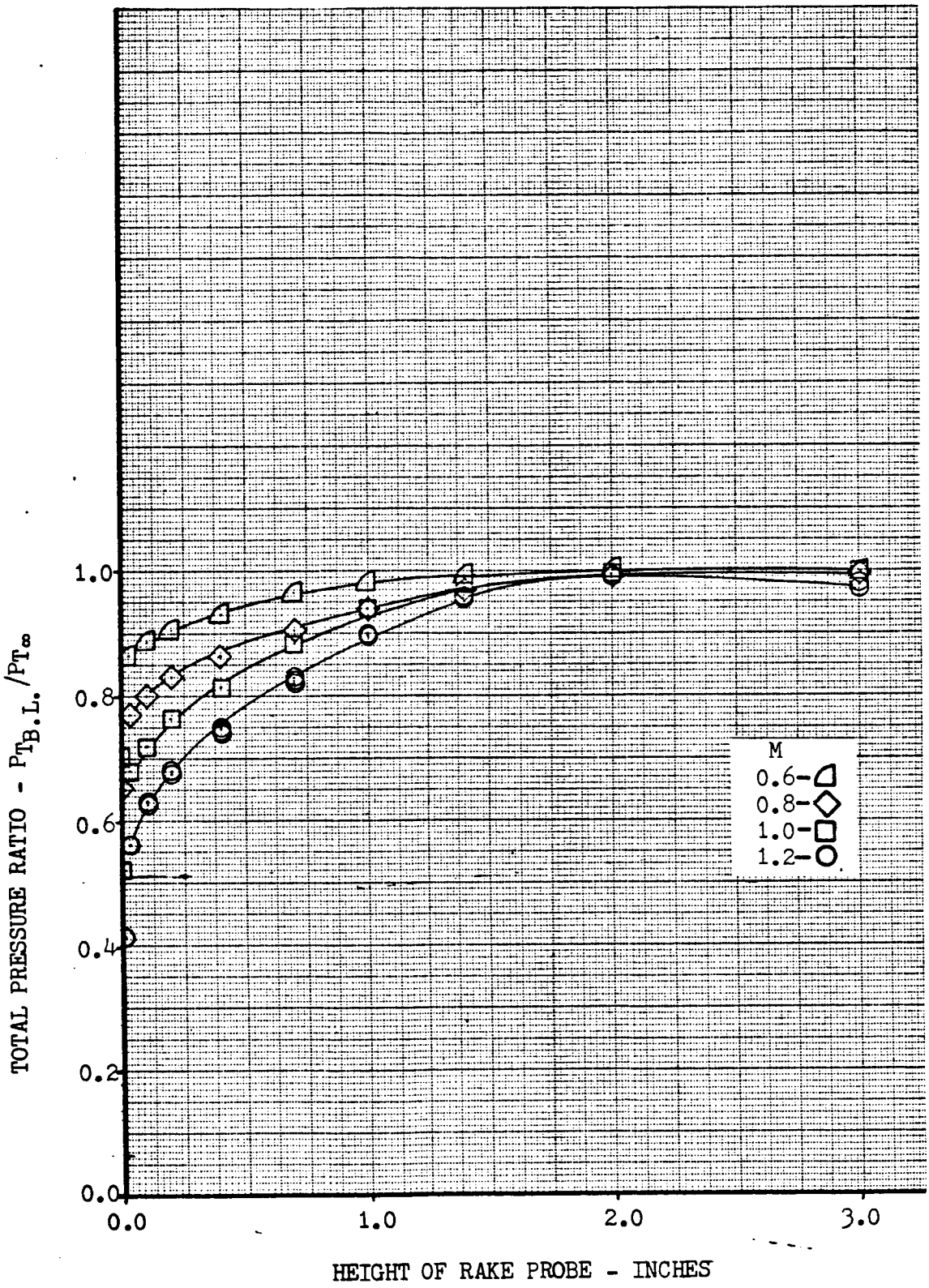

FIGURE 4 Boundary Layer Rake Data - CAL 8 by 8 Tunnel

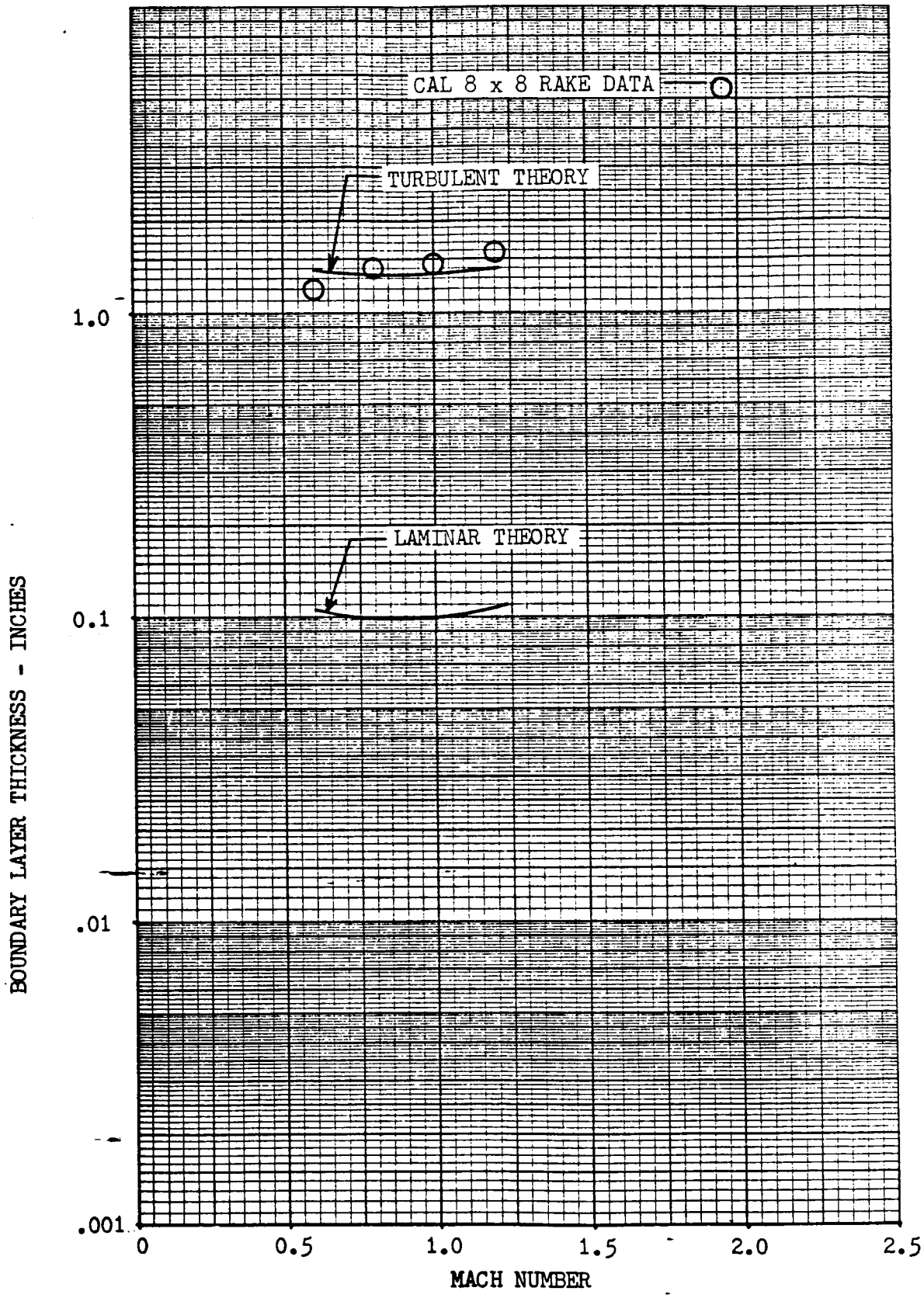

FIGURE 5 Model Boundary Layer Thickness Versus Theory

3.2 RADIATION

For any given structural point only slight changes are expected in the radiation level over the altitude range of this test (13,000 to 34,000 feet) because the size of the plume will not change significantly. Theoretical full expansion in the nozzle will occur at approximately 24,000 feet.

Radiation from the plumes is due primarily to the carbon particles. If a higher percentage of carbon particles occurs in the flow from a given engine, as indicated by the photograph, unsymmetrical heating patterns may result.

3.2.1 Radiation to Base

Considerable scatter is noted in the radiation data (See paragraph 3.5). For this reason the data from gages 2,4,6,8 and 10 located along a ray midway between engines 3 and 4 (See Figure 19, Volume 1) are averaged for display in Figures 6 and 7. Figure 6 shows effects of radiation on scoop area, fairing length and addition of hydrogen turbine exhaust. A slight reduction in heating is noted with increase in scoop size. A slight reduction also occurs as the engine fairing length is reduced. The data show the expected reduction with Mach number increase.

Injection of hydrogen turbine exhaust has no significant effect on the radiation level as can be seen in Figures 6 and 7.

Figure 8 shows an increase in heating rate when going outboard along a radial line. Data from five gages located at various angles (θ) also shown in Figure 8 indicate that maximum radiation to the base occurs midway between outboard engines. The radial and angular position trends are expected from theoretical considerations.

3.2.2 Radiation to Fin and Engine Fairing

Radiation instruments are located on the aft face of the fin near the engine fairing and on the aft face of the fairing at an angle of 65 degrees from the fin center line. Radiation to these gages appear unchanged with Mach number and turbine exhaust variations and are at a heating level of approximately 1.0 BTU/FT^{2}SEC (see Figure 9).

3.2.3 Radiation to Center Engine (External)

Radiation heating data on the center engine nozzle is shown for two locations in Figure 10. Instrument 22 is attached to the outside of the bell near the exit plane and instrument 30 is attached to the outside between the turbine exhaust manifold and the nozzle throat as shown in Figure 22, Volume 1. Instrument 30 is facing away from the engine plume. Radiation level to instrument 30 is approximately half that registered by instrument 22. Addition of hydrogen turbine exhaust has little effect on radiation. Heating rates to both instruments are less than 2.0 BTU/FT^{2}SEC.

TUNNEL CAL 8 BY 8

SYM.	INST.	CONFIG.
□	$H_{2,4,6,8,10}$	$B_1FS_1N_{1-5}PL_1$
○	$H_{2,4,6,8,10}$	$B_1FS_1D_1SC_1N_{1-5}PL_1$
◇	$H_{2,4,6,8,10}$	$B_1FS_2SC_1N_{1-5}PL_1$
◇	$H_{2,4,6,8,10}$	$B_1FS_4D_1SC_1N_{1-5}PL_1$
△	$H_{2,4,6,8,10}$	$B_1FS_1D_3SC_1N_{1-5}PL_1$

NOTE: 1. Solid symbol denotes turbine exhaust
2. Data averaged

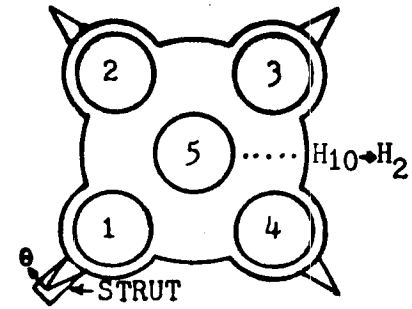

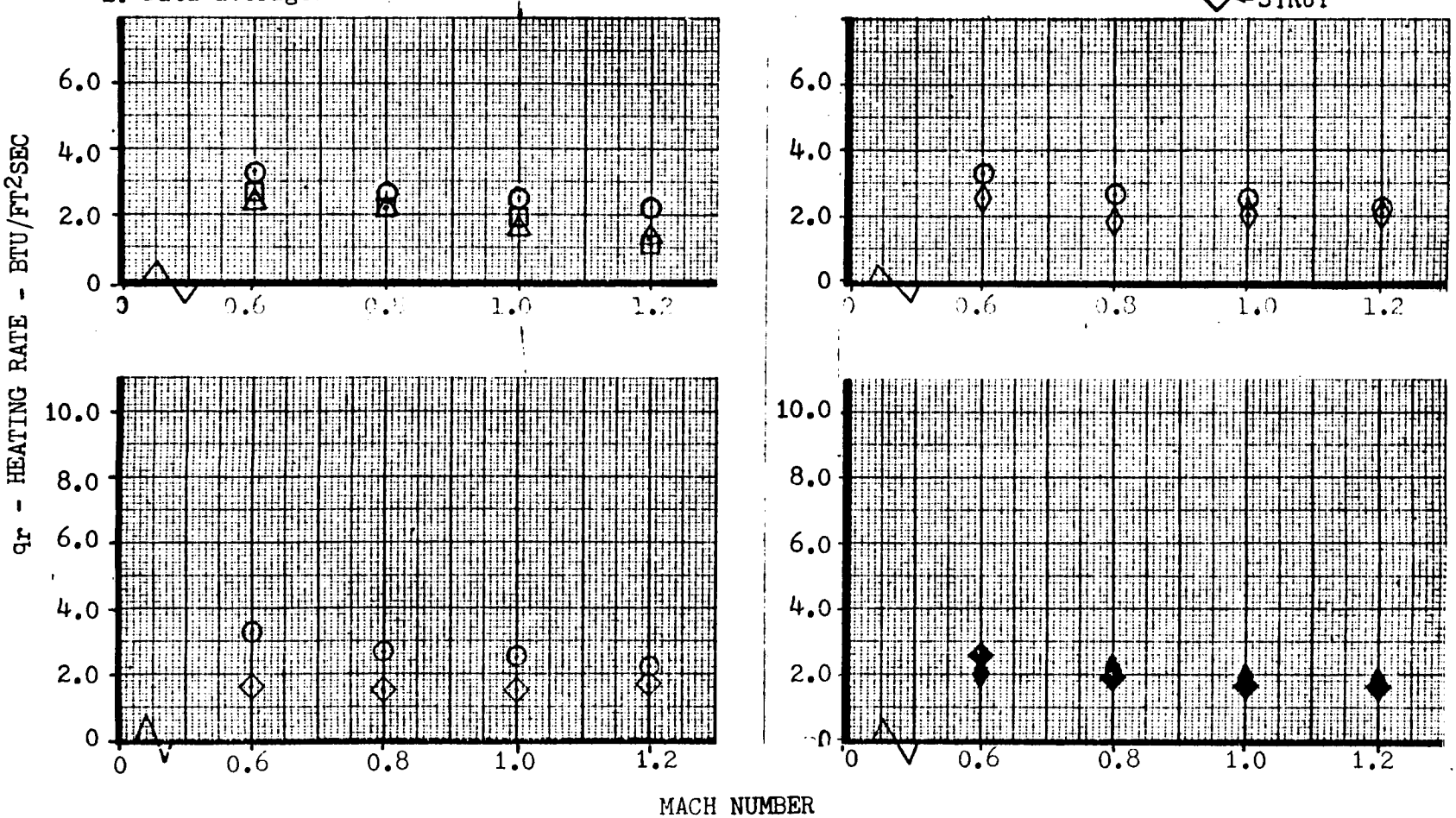

FIGURE 6 Base Heating - Radiation

TUNNEL CAL 8 BY 8

SYM.	INST.	CONFIG.
□	$H_{2,4,6,8,10}$	$B_1FS_1N_{1-5}PL_1$
◇	$H_{2,4,6,8,10}$	$B_1FS_4D_1SC_1N_{1-5}PL_1$

NOTE: 1. Solid symbol denotes turbine exhaust
2. Data averaged

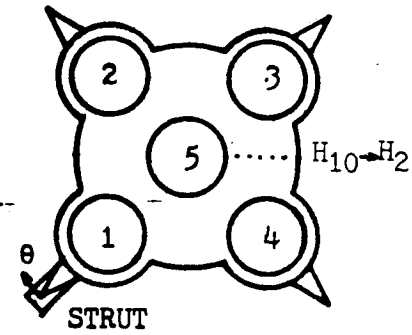

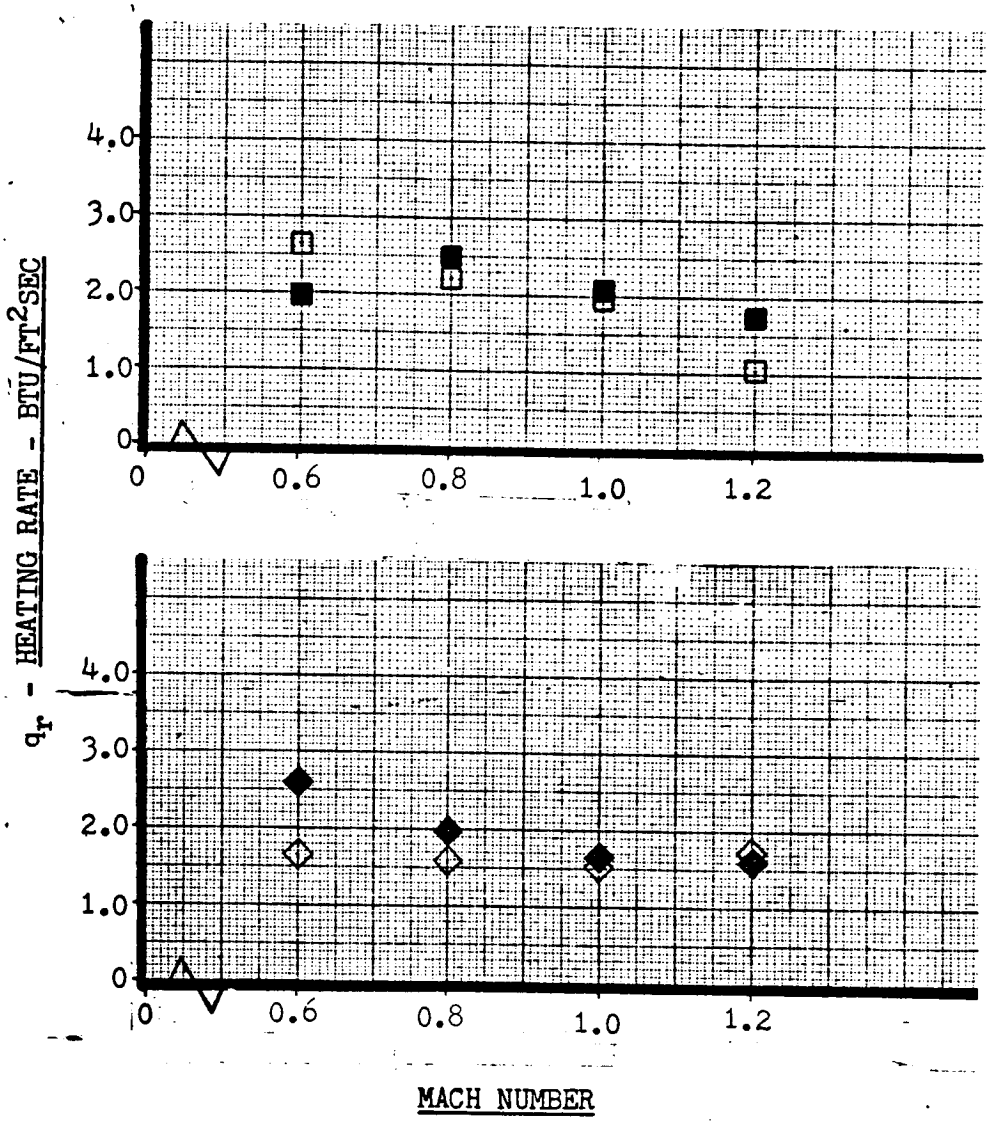

FIGURE 7 Base Heating - Radiation

TUNNEL CAL 8 BY 8

SYM.	INST.	CONFIG.	SYM.	INST.	CONFIG.
□		$B_1FS_1N_{1-5}PL_1$	□		$B_1FS_1N_{1-5}PL_1$
□		$B_1FS_1N_{1-5}PL$	□		$B_1FS_1N_{1-5}PL_1$

NOTE: Solid symbol denotes turbine exhaust

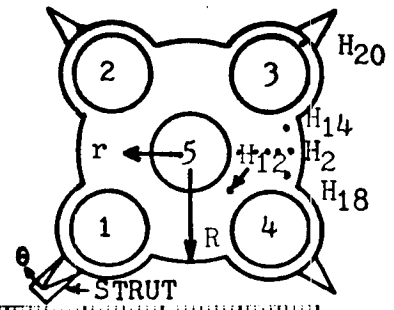

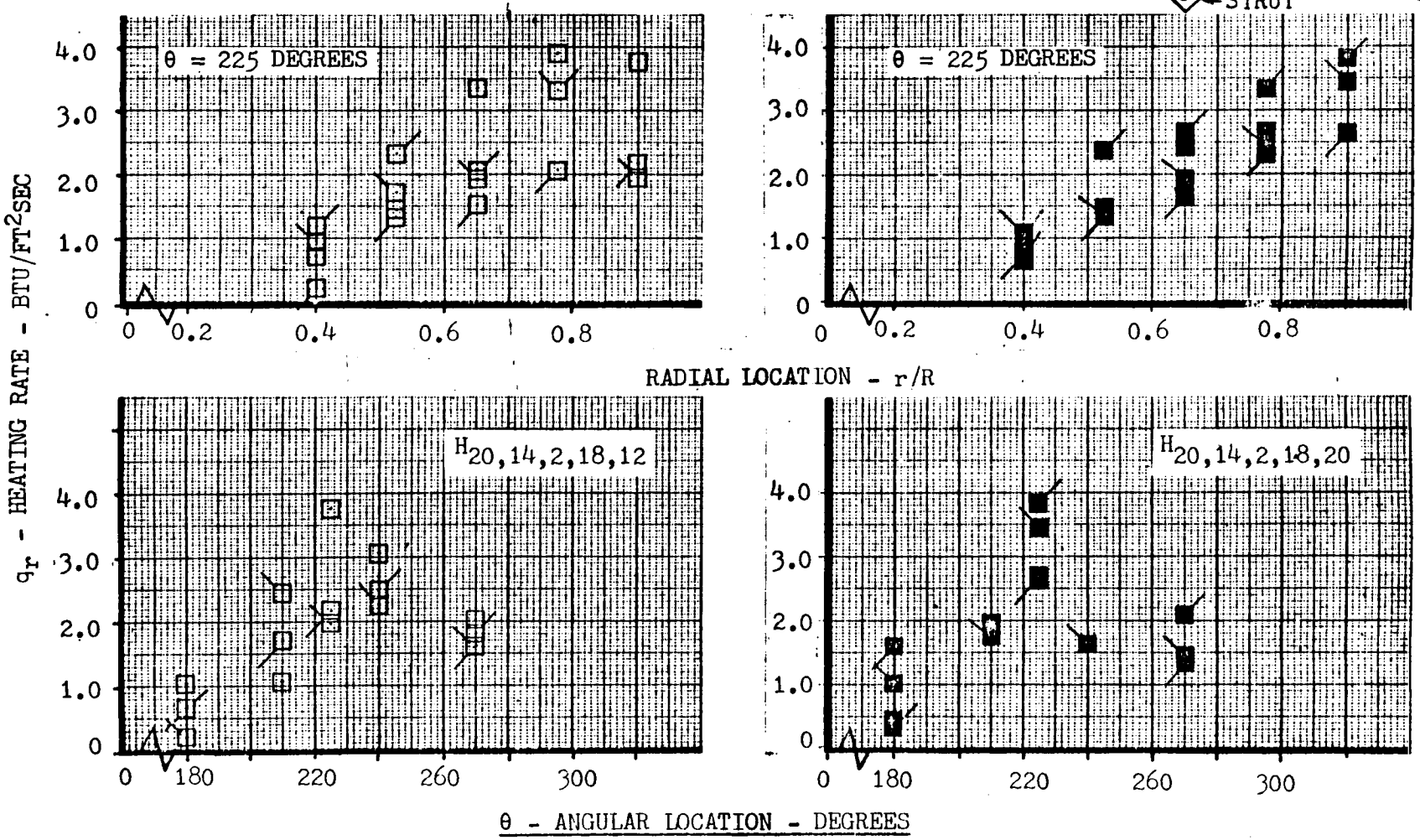

FIGURE 8. Base Heating - Radiation

TUNNEL CAL 8 by 8

SYM.	INST.	CONFIG.
□	H_{64}	$B_1FS_1N_{1-5}PL_1$
◪	H_{58}	$B_1FS_1N_{1-5}PL_1$

NOTE: Solid symbol denotes turbine exhaust

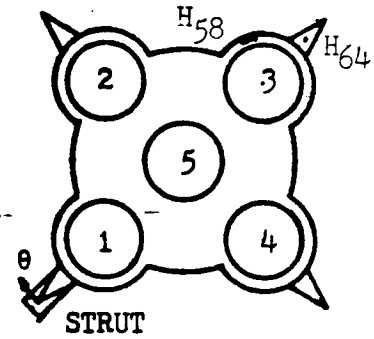

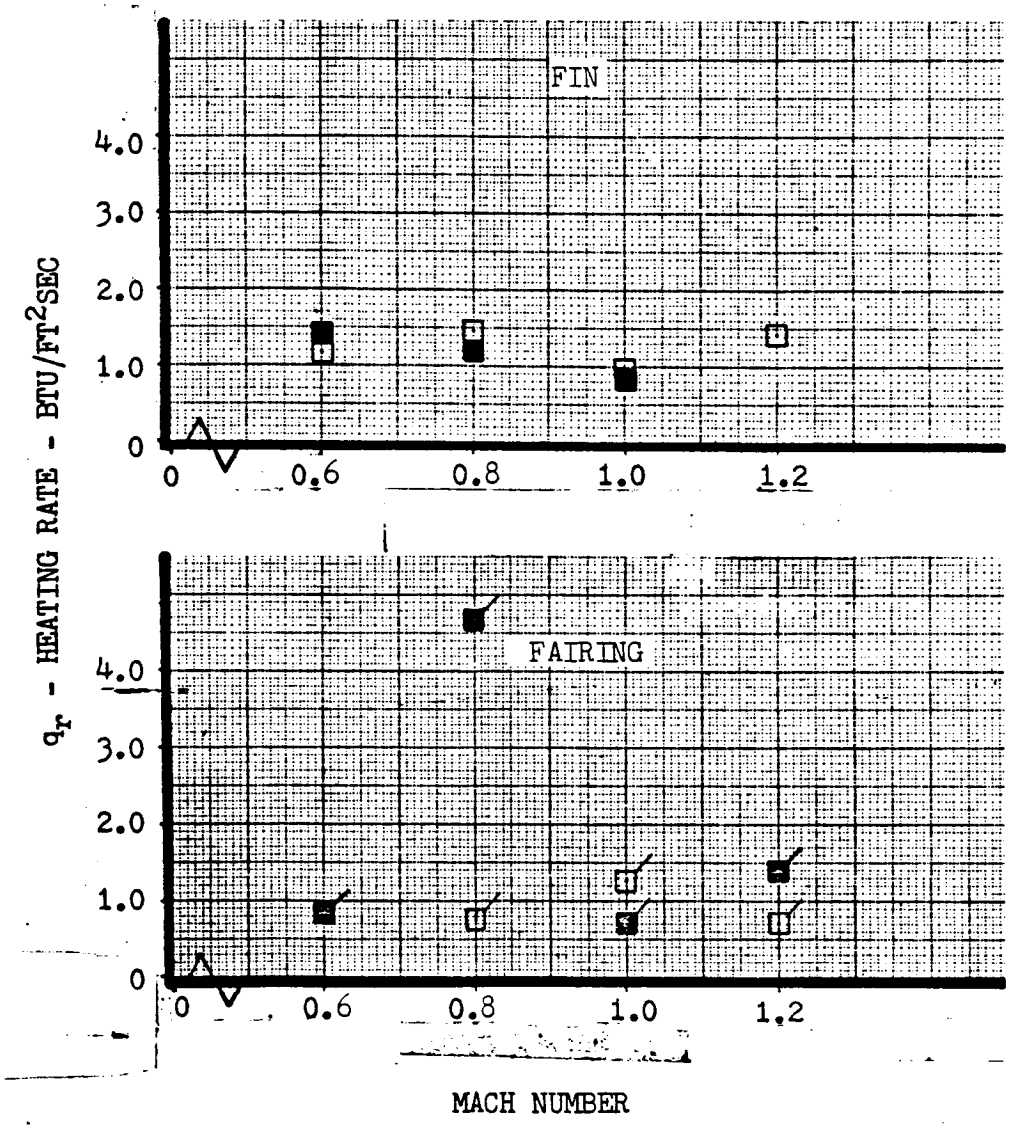

FIGURE 9 Fin and Engine Fairing Heating - Radiation

TUNNEL CAL 8 BY 8

SYM.	INST.	CONFIG.
□	$H_{22,30}$	$B_1FS_1N_{1-5}PL_1$
○	$H_{22,30}$	$B_1FS_1D_1SC_1N_{1-5}PL_1$

NOTE: 1. Solid symbol denotes turbine exhaust
2. Flagged symbol is H_{30}

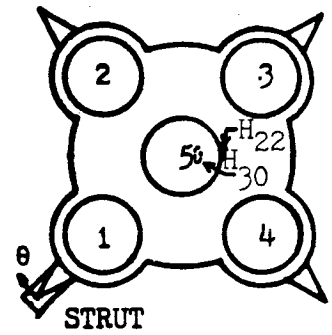

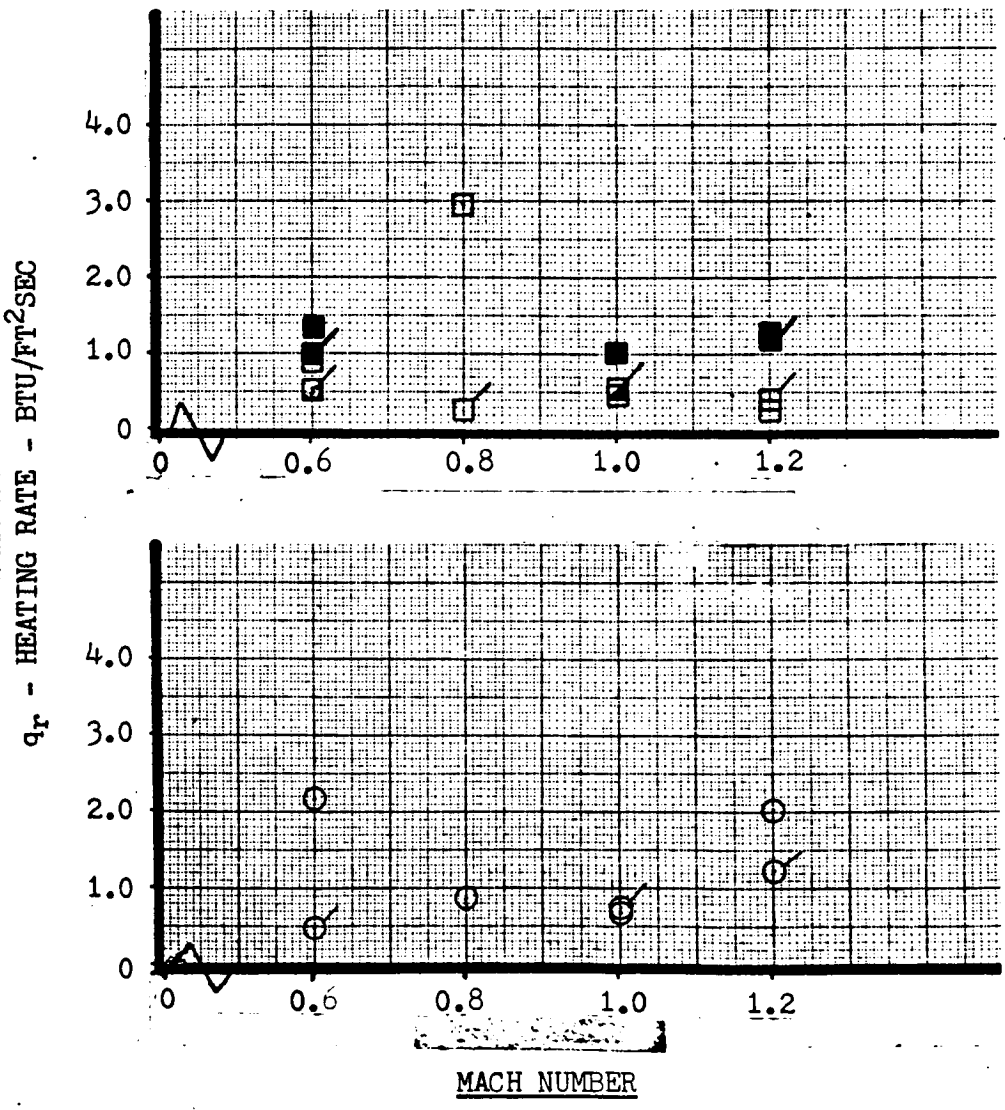

FIGURE 10 Engine Heating - Radiation (External)

3.2.4 Comparison with Radiation Theory

Using the methods discussed in paragraph 2.0 of Volume 1, radiation is estimated assuming both non-luminous hot gases and luminous particle radiation. These estimates are shown in Figure 11 and compared with the test data at an r/R of 0.65.

The experimental data is greater in magnitude than either the luminous particle or non luminous hot gas radiation calculations indicating that most of the radiation is emanating from solid particles in the exhaust flow. Oxygen to fuel ratio (O/F) data from the pre-test calibrations indicate an O/F of 2.25. However, no O/F monitoring equipment was supplied during the test and the actual combustion conditions are not known.

3.3 CONVECTION

In the range of this test it is expected that the base scoops will have a large effect on the convection coefficients, since the surrounding air is relatively dense and the engine plume shape does not have a significant change. Sufficient oxygen is available at these test altitudes to sustain a base burning condition if exhaust products exist in the base region. The convective heating rate is obtained by subtracting the measured radiation rate from the measured total heating rate.

3.3.1 Convection to Base

All data shown are average values for gages H_1, H_3, H_5, H_7 and H_9 which are located along a ray between engines 3 and 4. (See Figure 19, Volume 1). The base convective data is shown in Figures 12, 13 and 14. Data in the upper two charts of Figure 12 show the effects of the various configurations on the convective heating rate without turbine exhaust simulation. Addition of deflectors (lower charts) reduces the base convective heating rate, however the affect of very large deflectors does not materially reduce the rate below that with small deflectors. Shortening the engine fairing length appears to double the convective heating rate at Mach numbers less than 1.0. The addition of fairing scoops (only) tends to keep the heating rate with turbine exhaust elevated over the entire test range.

Injection of hydrogen turbine exhaust significantly increases the convective heating rate on the configurations without scoops or deflectors, especially at Mach 0.6 and 0.8 (see Figure 12 and 13). Addition of scoops and deflectors reduces the heating rate at Mach 0.6 and 0.8, however little effect is noted at the other Mach numbers and it appears that some base burning occurs even with the scoops and deflectors installed. Radial data is shown for configuration B_1 FS_1 N_{1-5} PL_1 on Figure 14.

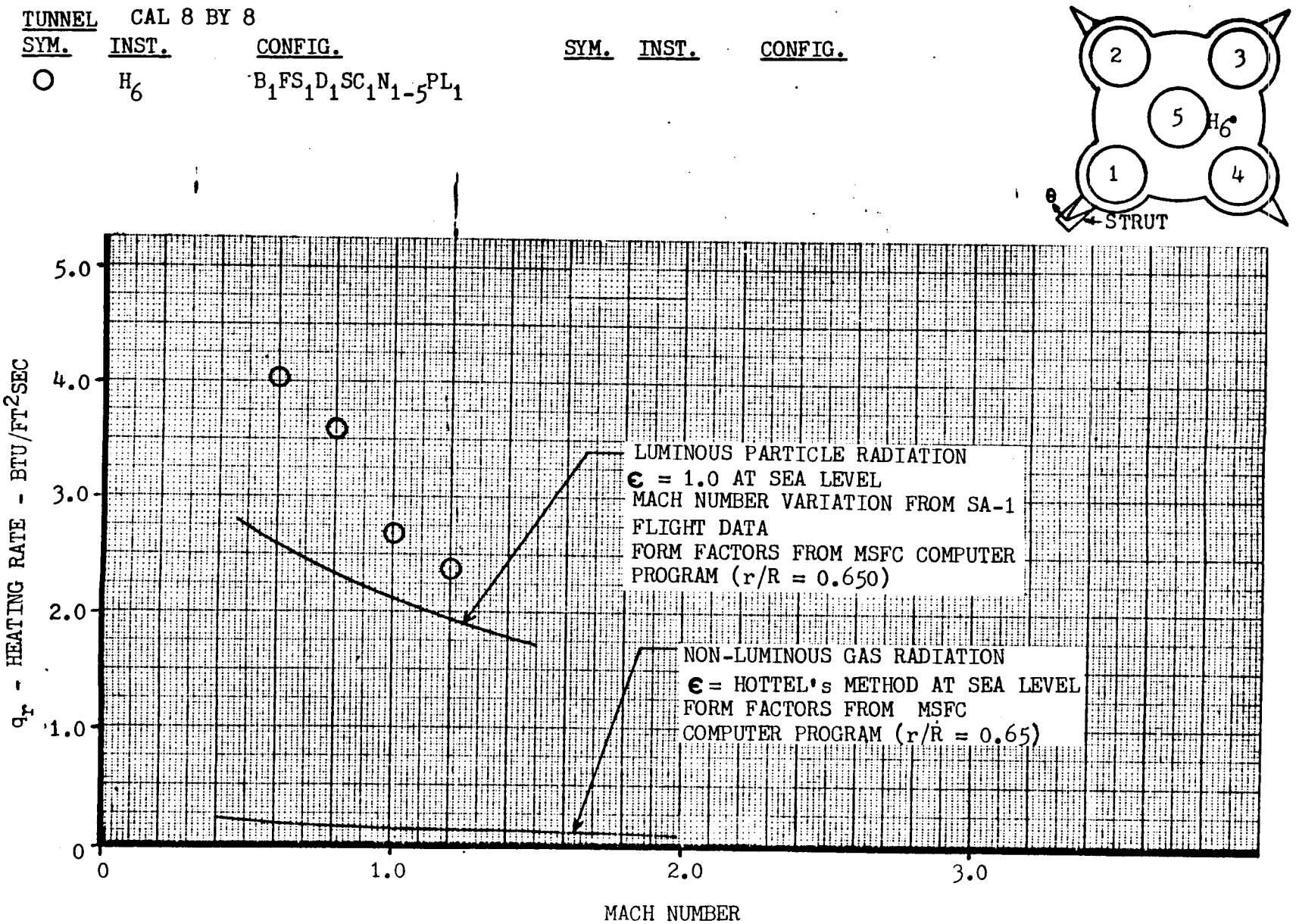

FIGURE 11 Base Heating - Radiation Versus Theory

TUNNEL CAL 8 by 8

SYM.	INST.	CONFIG.
□	$H_{1,3,5,7,9}$	$B_1FS_1N_{1-5}PL_1$
△	$H_{1,3,5,7,9}$	$B_1FS_1D_3SC_1N_{1-5}PL_1$
○	$H_{1,3,5,7,9}$	$B_1FS_1D_1SC_1N_{1-5}PL_1$
◇	$H_{1,3,5,7,9}$	$B_1FS_2SC_1N_{1-5}PL_1$
◇	$H_{1,3,5,7,9}$	$B_1FS_4D_1SC_1N_{1-5}PL_1$

NOTE: 1. Solid symbol denotes turbine exhaust
2. Data averaged

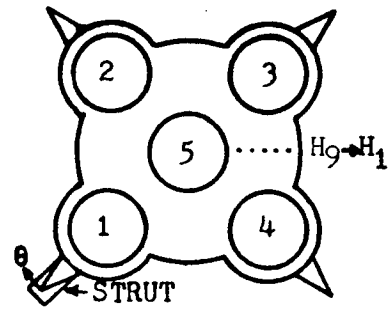

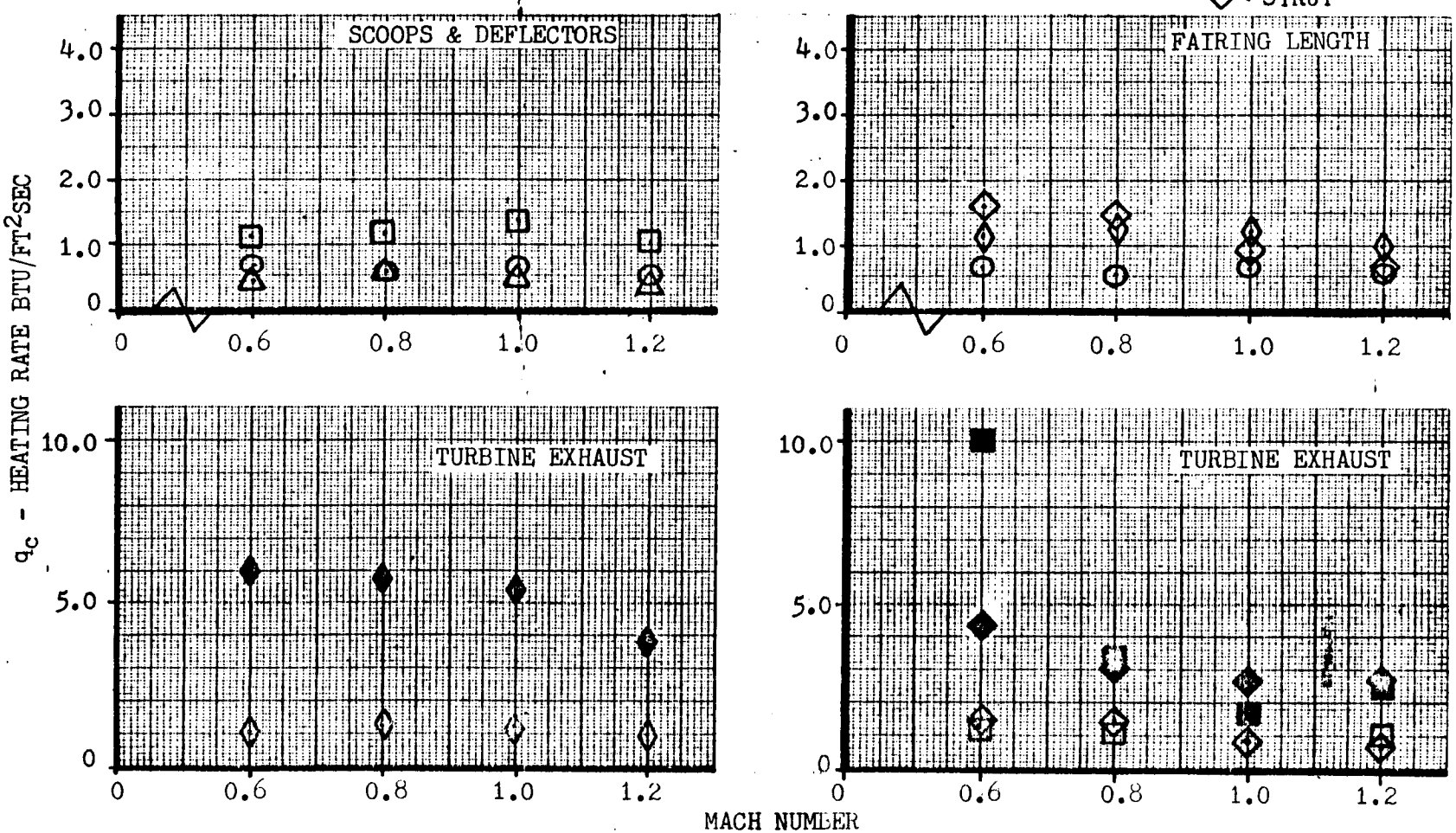

FIGURE 12 Base Heating - Convection

TUNNEL CAL 8 BY 8

SYM.	INST.	CONFIG.
□	$H_{1,3,5,7,9}$	$B_1FS_1N_{1-5}PL_1$
◇	$H_{1,3,5,7,9}$	$B_1FS_4D_1SC_1N_{1-5}PL_1$

NOTE: 1. Solid symbol denotes turbine exhaust
2. Data averaged

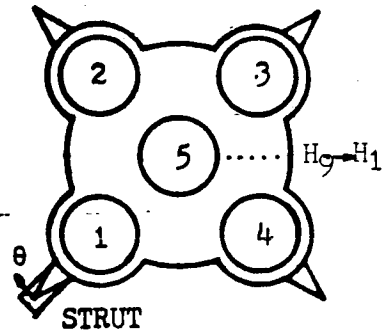

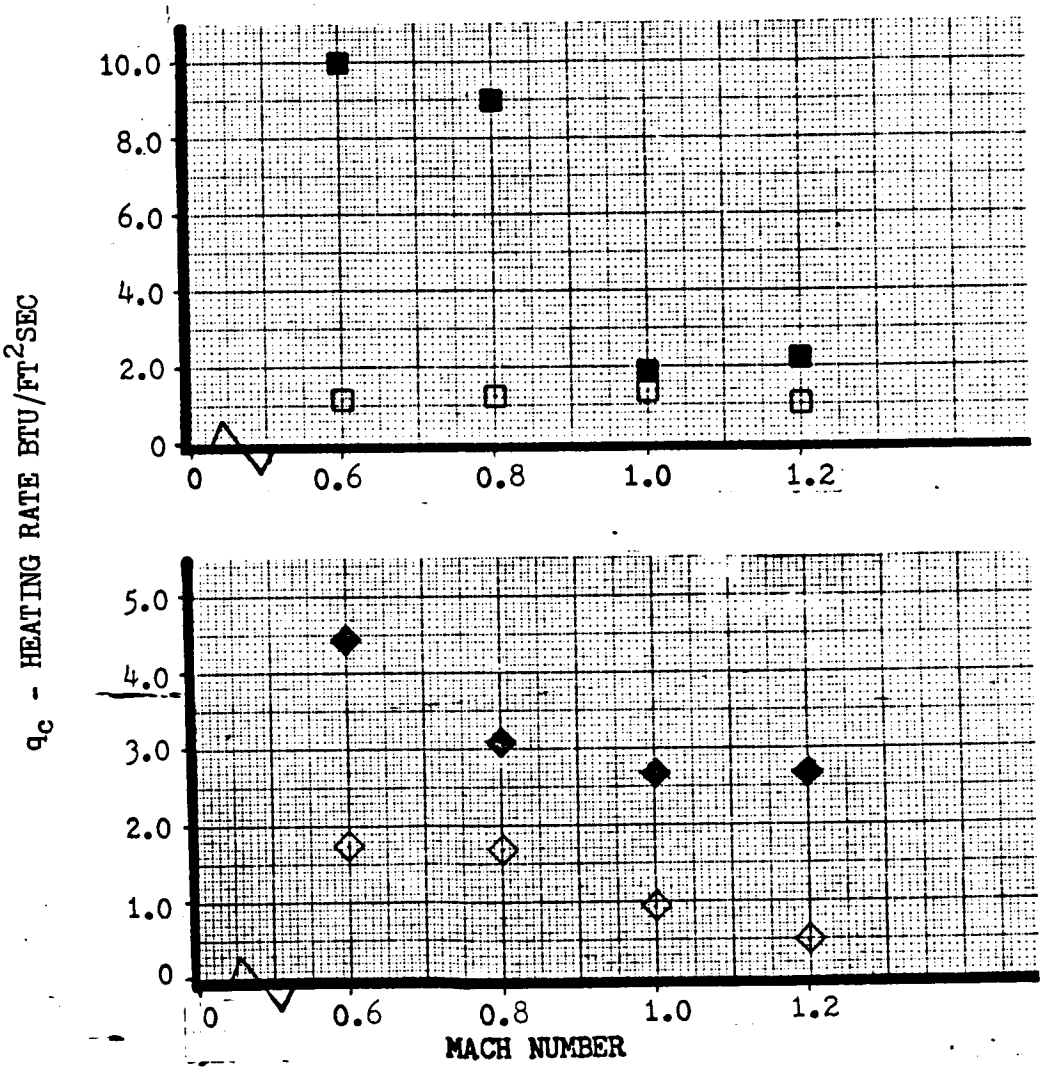

FIGURE 13 Base Heating - Convection

TUNNEL CAL 8 BY 8

SYM.	MACH NO.	CONFIG.	SYM.	MACH NO.	CONFIG.
□	0.6	$B_1FS_1\ N_{1-5}PL_1$	◺□	1.0	$B_1FS_1N_{1-5}PL_1$
◻◿	0.8	$B_1FS_1\ N_{1-5}PL_1$	◻◸	1.2	$B_1FS_1N_{1-5}PL_1$

NOTE: Solid symbol denotes turbine exhaust

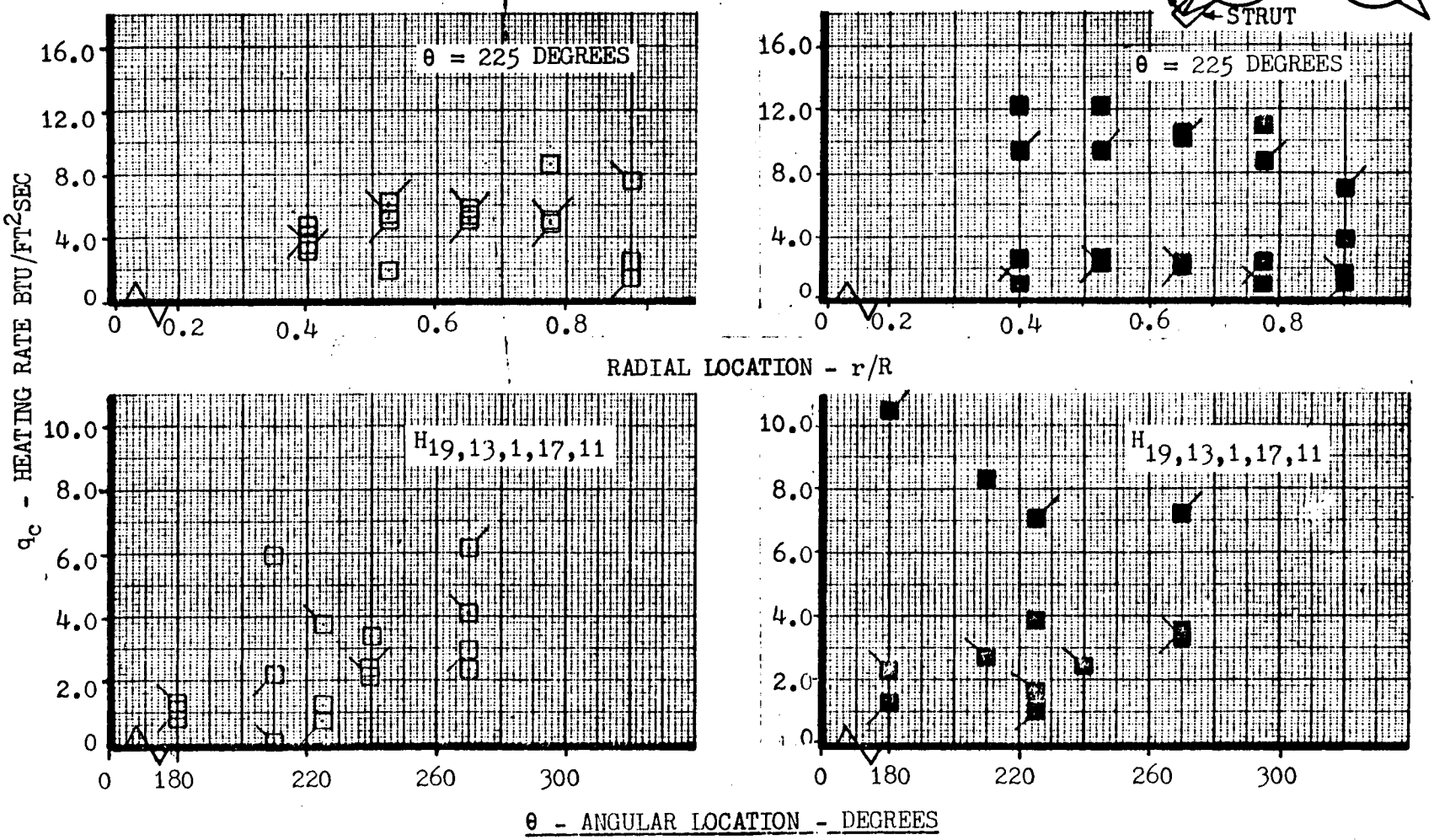

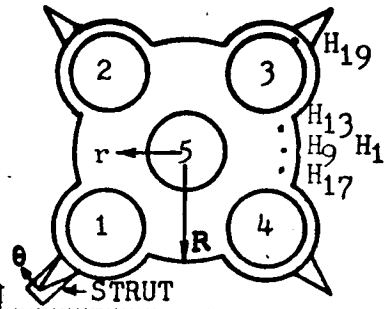

FIGURE 14 Base Heating - Convection

3.3.2 Convection to Fin and the Engine Fairing

Convection to the base of the fin is shown in Figure 15. Instrument number 63 is located on the aft face of the fin near the engine fairing-fin interface (see Figure 26, Volume 1). Without turbine exhaust the heating rate is low and the configuration effect of a short fairing with scoops and deflectors is negligible. With turbine exhaust the heating rate is increased over the entire test range when the short fairing configuration is tested.

The recorded data for the engine fairing shown on Figure 15 are obtained from instrument number 57 located on the inside of the engine fairing at an angle of 65 degrees from the center line of the fin. (See Figure 19 Volume 1). The instrument is facing the nozzle throat and indicates convection on the inside of the fairing. Without turbine exhaust, convection heating is approximately 1.0 BTU/FT^2SEC. With turbine exhaust and without scoops the heating rate is significantly higher and is seen to compare with the magnitude of heating on the center engine under the same test conditions (Figure 16). No other data with turbine exhaust is available.

3.3.3 Convection to Center Engine (External)

Convection heating data on the center engine nozzle is shown for two locations in Figure 16. Instrument 21 is attached to the outside surface of the nozzle near the exit plane and instrument 29 is attached to the outside surface of the nozzle near the throat (see Figures 22 and 23, Volume 1). Without turbine exhaust simulation the heating rates for both gages are relatively low with heating near the lip increasing with increasing Mach number. With addition of hydrogen turbine exhaust there is a significant increase in heating of both locations over the entire test range. The heating rate remains relatively high with scoops and deflectors, again indicating presence of base burning.

3.3.4 Comparison with Theory

Presently used theoretical methods do not predict recirculation of hot gases below 40,000 ft for the non-scoop configuration and 55,000 ft for the scoop configuration. The theory does not consider free stream flow impingement on the exhaust plumes however, which would cause some recirculation earlier than 40,000 or 55,000 ft. Since the Cornell 8 by 8 transonic tunnel maximum altitude is 34,000 ft, theoretical calculation can not be made and no comparison is available. The experimental data indicates convective heating at the very low altitudes (13,000 ft). This measured heating rate could be due to free stream air impinging on the exhaust jets as mentioned above.

TUNNEL CAL 8 BY 8

SYM.	INST.	CONFIG.
□	H_{63}	$B_1FS_1N_{1-5}PL_1$
□	H_{57}	$B_1FS_1N_{1-5}PL_1$
◊	H_{57}	$B_1FS_4D_1SC_1N_{1-5}PL_1$
◊	H_{63}	$B_1FS_4D_1SC_1N_{1-5}PL_1$

NOTE: Closed symbol denotes turbine exhaust

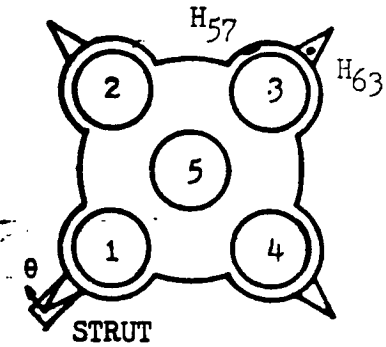

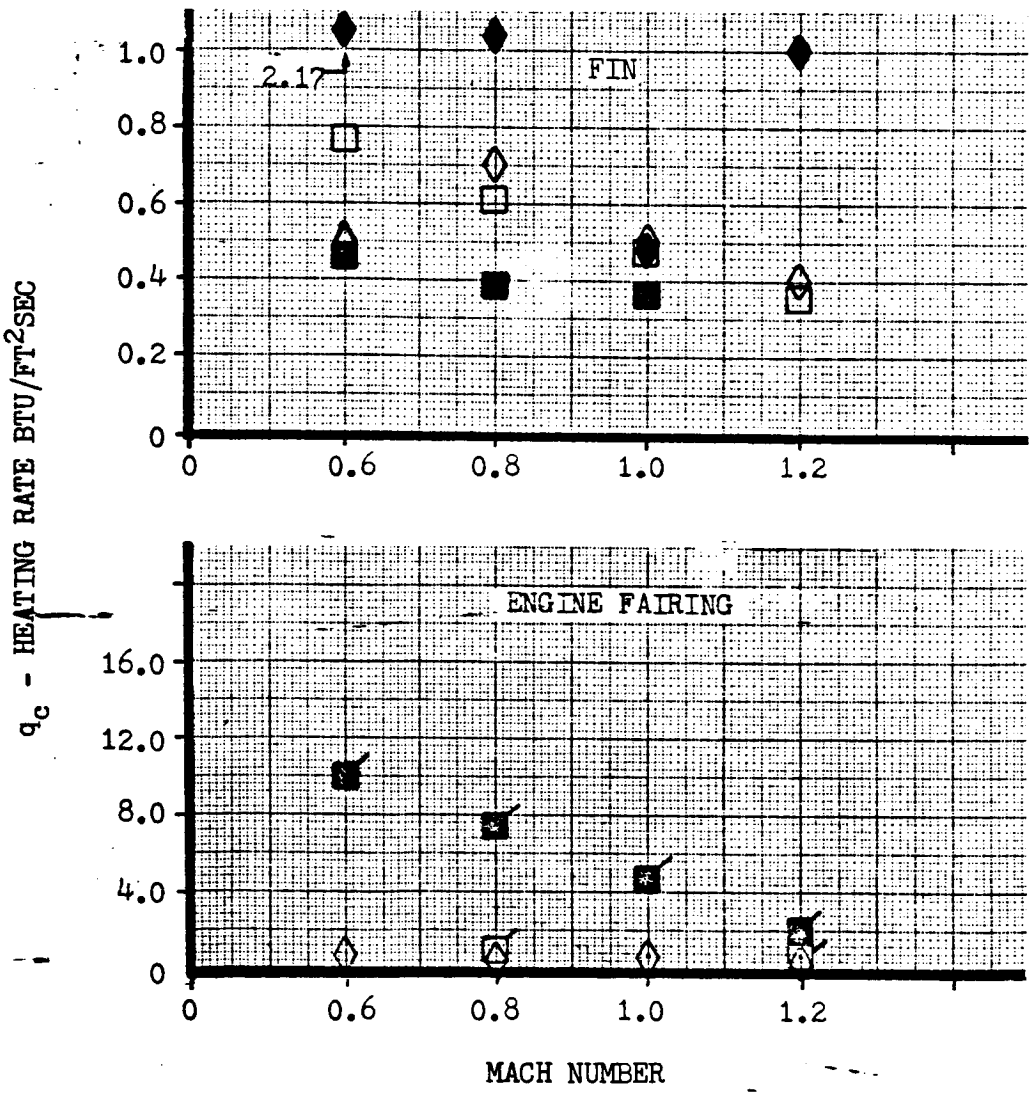

FIGURE 15 Fin and Engine Fairing Heating - Convection

TUNNEL CAL 8 by 8

SYM.	INST.	CONFIG.	SYM.	INST.	CONFIG.
□	$H_{21,29}$	$B_1FS_1N_{1-5}PL_1$	△	$H_{21,29}$	$B_1FS_2SC_1N_{1-5}PL_1$
○	$H_{21,29}$	$B_1FS_1D_1SC_1N_{1-5}PL_1$	◇	$H_{21,29}$	$B_1FS_4D_1SC_1N_{1-5}PL_1$

NOTE: 1. Solid symbol denotes turbine exhaust
2. Flag denotes gauge H_{29}

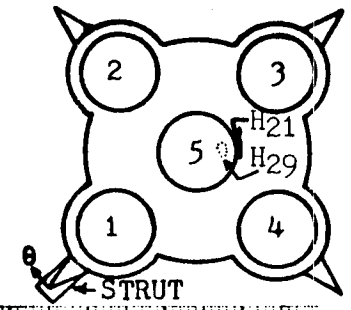

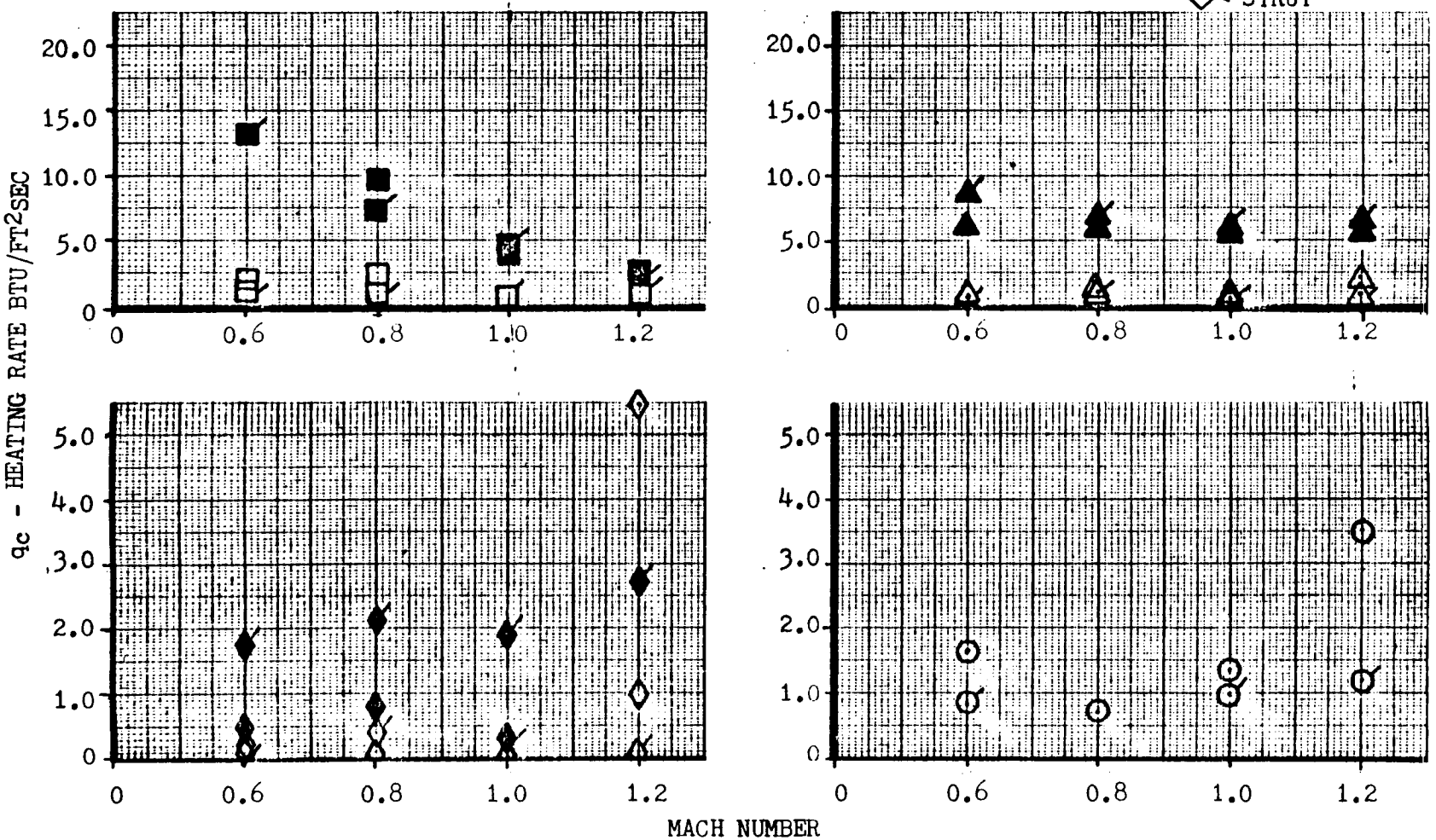

FIGURE 16 Engine Heating - Convection (External)

3.4 BASE PRESSURE

Base pressure data are shown in Figures 17, 18 and 19. The radial distribution data was obtained from pressure taps P_1, P_2 and P_3 which are located along a radial line between engines 2 and 3. In a few instances where data are not available from P_3, data from P_5, similarly located but between engines 1 and 2, are substituted. The base pressure appears essentially constant across the base plate (Figure 17) and an average pressure can be readily used to represent the base pressure at any given Mach number. Although not shown, the base pressures with turbine exhaust are also essentially constant. Figures 18 and 19 indicate that the average base pressures with and without turbine exhaust are generally identical regardless of configuration.

Base pressures obtained before the engines were fired show the effects of two of the mechanisms which contribute to the prototype "in flight" base pressure. The affect of free stream flow expanding around a bluff base is shown by configuration B_1 FS_1 N_{1-5} (S_1) in the lower chart of Figure 19. A very rapid drop in the Pb/P_∞ ratio is noted between Mach 0.7 and 1.1. Addition of flow deflectors and scoops allows mass addition to the base, which reduces the magnitude of the pressure reduction caused by the expanding free stream flow.

Two additional mechanisms affecting the overall base pressure are possible when the engines are firing. They are:

a. the interaction of the plume with the expanding free stream flow and
b. the interaction of the plumes impinging with each other.

Comparison of the "engines on" and "engines off" pressure ratios indicate that the effect of the latter two mechanisms is minor below Mach 1.0. Above Mach 1.0 they become predominant and add significantly to the base pressure. Theory proposed by Korst has only been applied to plume/plume impingement~~s and~~ is not applicable in these low altitude regimes. The theory has not been developed to account for the effects on base pressure of free stream to plume impingement.

Since all configurations in this Mach range show a base pressure increase when the engines are firing, it is concluded that engine exhaust will not create a reduction in base pressure above Mach 0.6 due to aspiration.

Data are insufficient to make an "engines on" configuration comparison. However, the increasing pressure due to the deflectors and scoops is readily apparent for the engines off data shown in Figure 19. It is also apparent that shortening the engine fairing will cause an increase in base pressure.

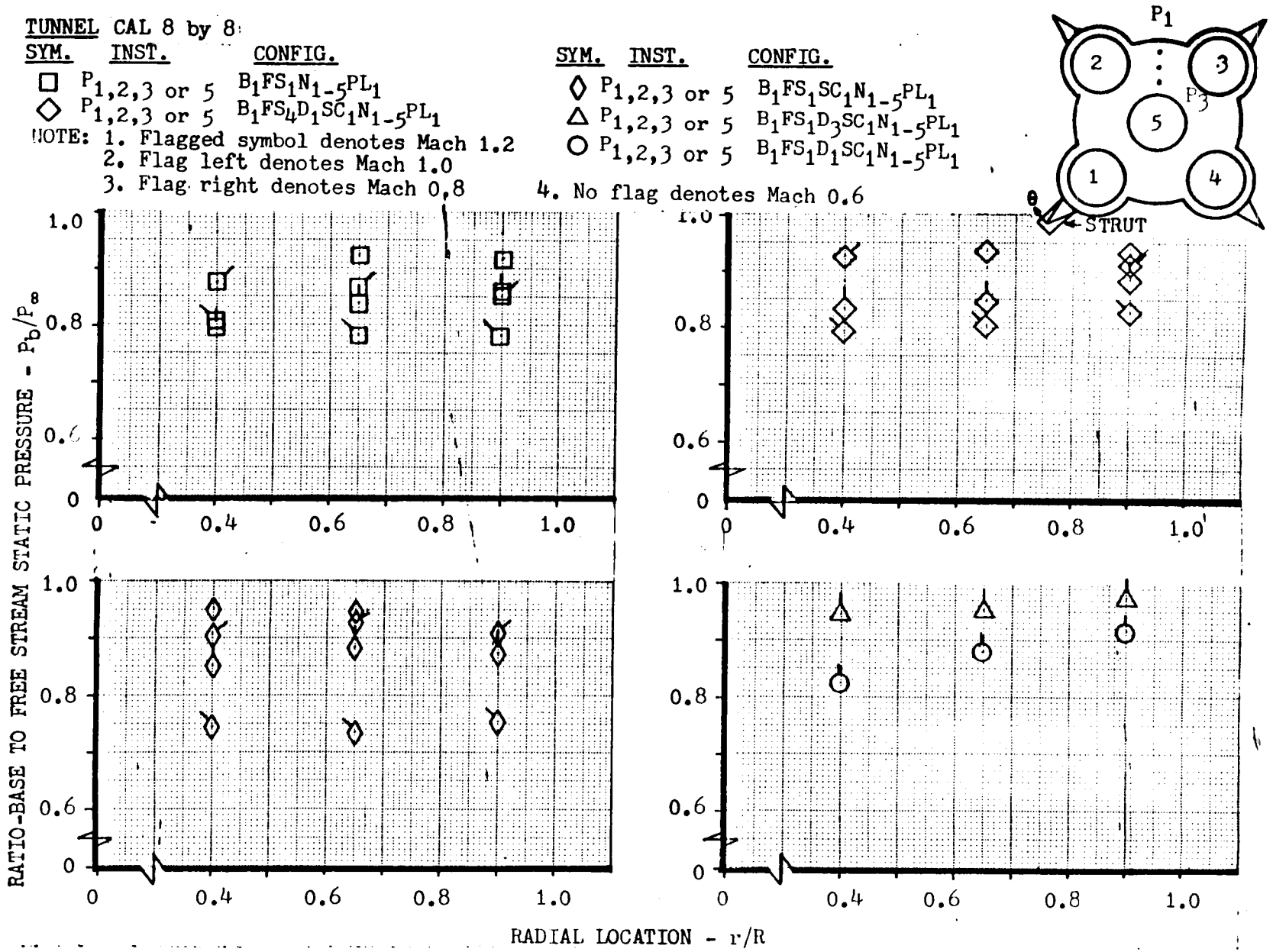

FIGURE 17 Base Pressure

TUNNEL CAL 8 by 8

SYM.	INST.	CONFIG.
□	$P_{1,2,3,4,5}$	$B_1FS_1N_{1-5}PL_1$
◇	$P_{1,2,3,4,5}$	$B_1FS_4D_1SC_1N_{1-5}PL_1$

NOTE: 1. Solid symbol denotes turbine exhaust
2. Data averaged

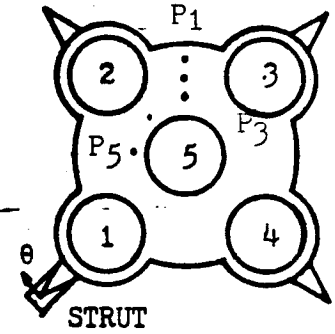

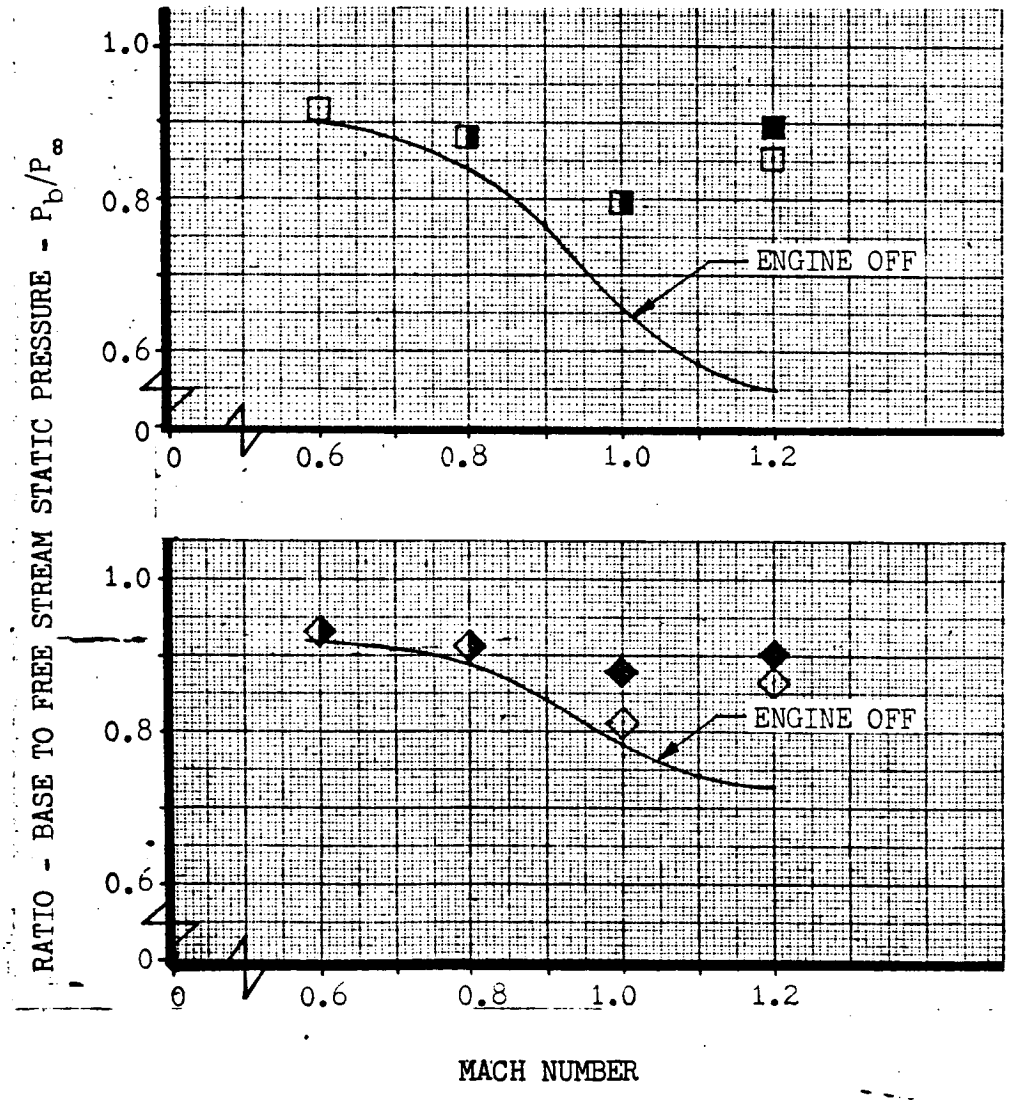

FIGURE 18 Base Pressure

TUNNEL CAL 8 BY 8

SYM.	**INST.**	**CONFIG.**
◊	$P_{1,2,3,4,5}$	$B_1FS_2SC_1N_{1-5}PL_1$

NOTE: 1. Solid symbol denotes turbine exhaust
2. Data averaged

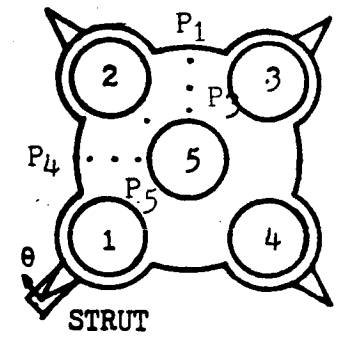

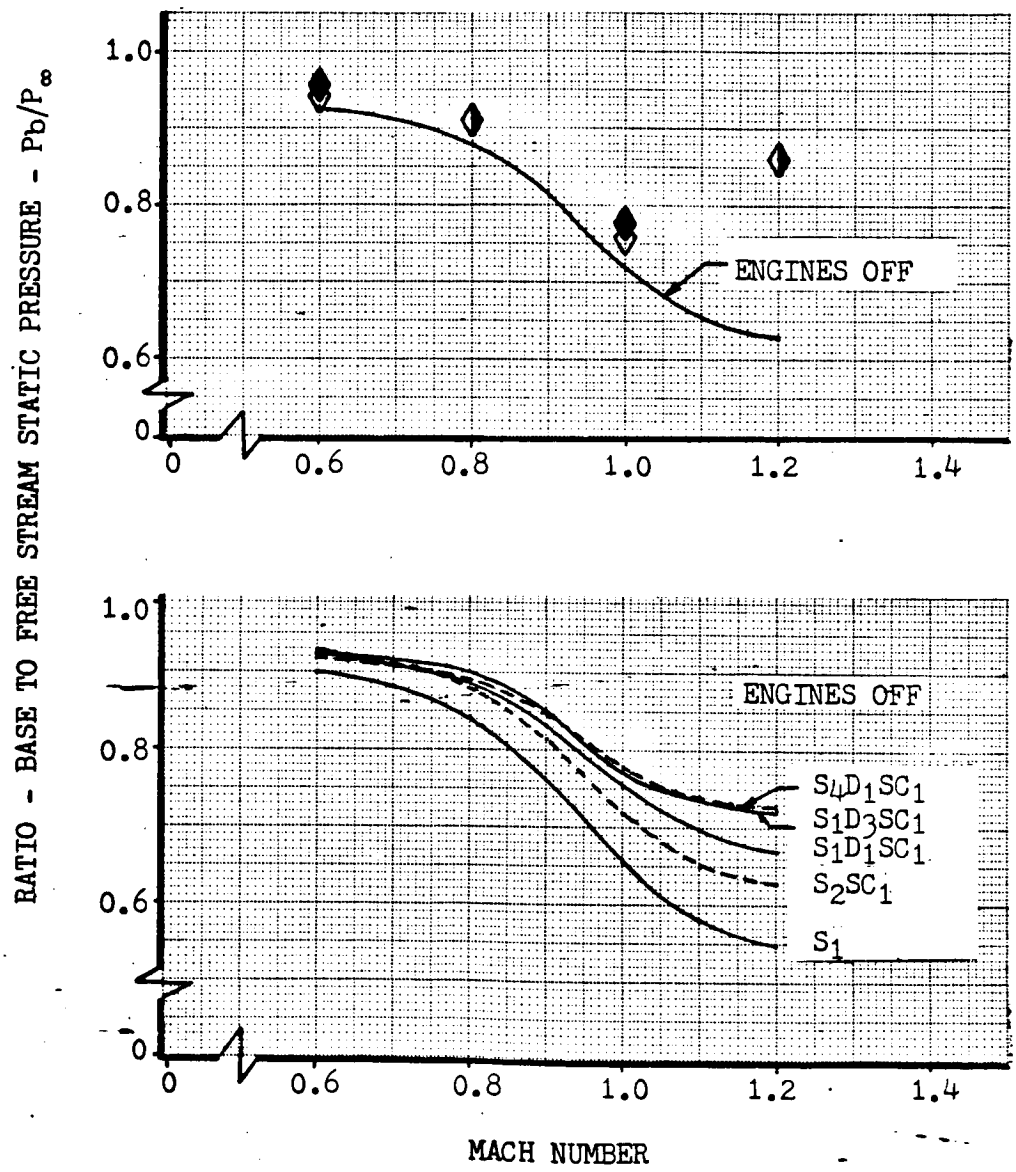

FIGURE 19 Base Pressure

3.4.1 Comparison with Theory

Engines-off base pressure is theoretically calculated in Appendix C using an empirical base pressure coefficient curve (data from blunt base cylinder tests). Figure 20 shows the theoretical calculated base pressure compared with the engines off base pressure data with and without scoops. It is evident that the theory and the "with scoops" data compare closely. The "no scoops" data is below the theoretical curve.

Base pressure during engine firing is compared with the theoretically calculated scoop exit static pressure (Appendix C) in Figure 21. The experimental base pressures are below the theoretical scoop exit static pressure at all Mach numbers. Both the theory and data are below the ambient pressure.

3.5 DATA ACCURACY

Inaccuracies in the test data come from the accuracy level of the gages as well as the ability to accurately read the oscilloscope traces. Unsymmetrical nozzle flow conditions cause additional data variations.

Sufficient data do not exist to conclude anything about recording system repeatability. Unsymmetrical flow conditions are evident in Figures 22, 23 and 24. Figure 22 compares two radiation gages at the same position in opposite halves of the same quadrant. These data show an average spread of 35 percent within a quadrant. No data was obtained to compare different quadrants.

Figure 23 compares two convection heating values symmetrically located in opposite halves of the same quadrant, giving an average spread of 61 percent. Again no data was obtained to compare different quadrants.

Pressure levels in different quadrants are shown to compare favorably in Figure 24. The average spread is between two and six percent.

3.6 CONCLUSIONS

Test data obtained from the CAL 8 by 8 foot transonic tunnel indicate that:

a. The boundary layer ahead of this model base is turbulent and is 1.2 to 1.5 inches thick.

b. Configuration changes and injection of hydrogen turbine exhaust have no appreciable effect on radiation.

c. Radiation increases with increasing radial distance from the center of the base plate and decreases with increasing Mach number.

d. The model engine exhaust has a heavy concentration of carbon particles.

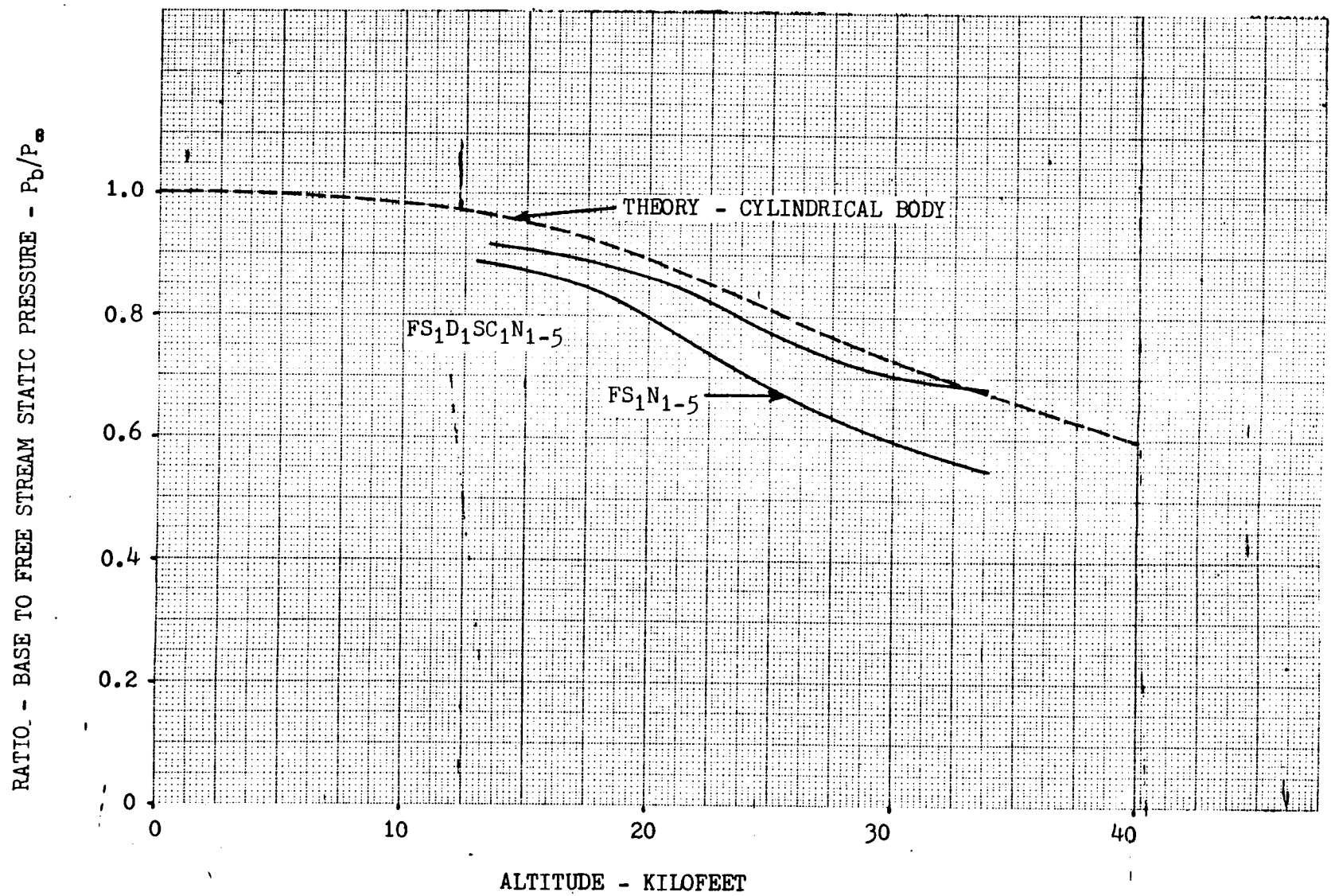

FIGURE 20 Engines Off Base Pressure Comparison - CAL 8 by 8 Tunnel

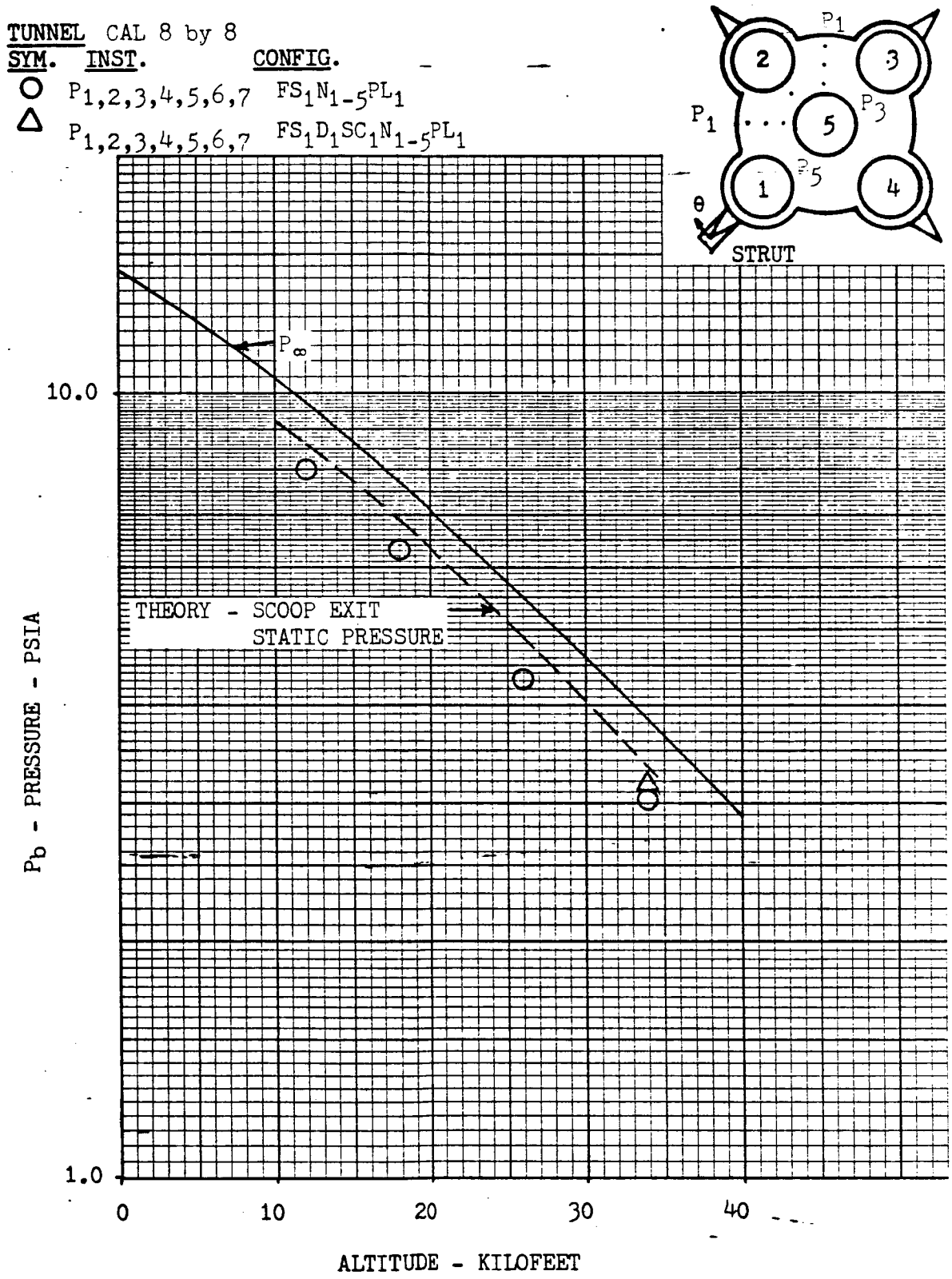

FIGURE 21 Base Pressure Comparison with Theory - Cornell 8 by 8 Tunnel

TUNNEL CAL 8 BY 8

SYM.	INST.	CONFIG.
◇	$H_{14,18}$	$B_1FS_4D_1SC_1N_{1-5}PL_1$
◇	$H_{14,18}$	$B_1FS_2D_1SC_1N_{1-5}PL_1$

NOTE: Flagged symbol is H_{18}

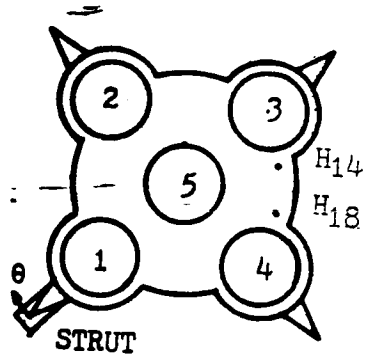

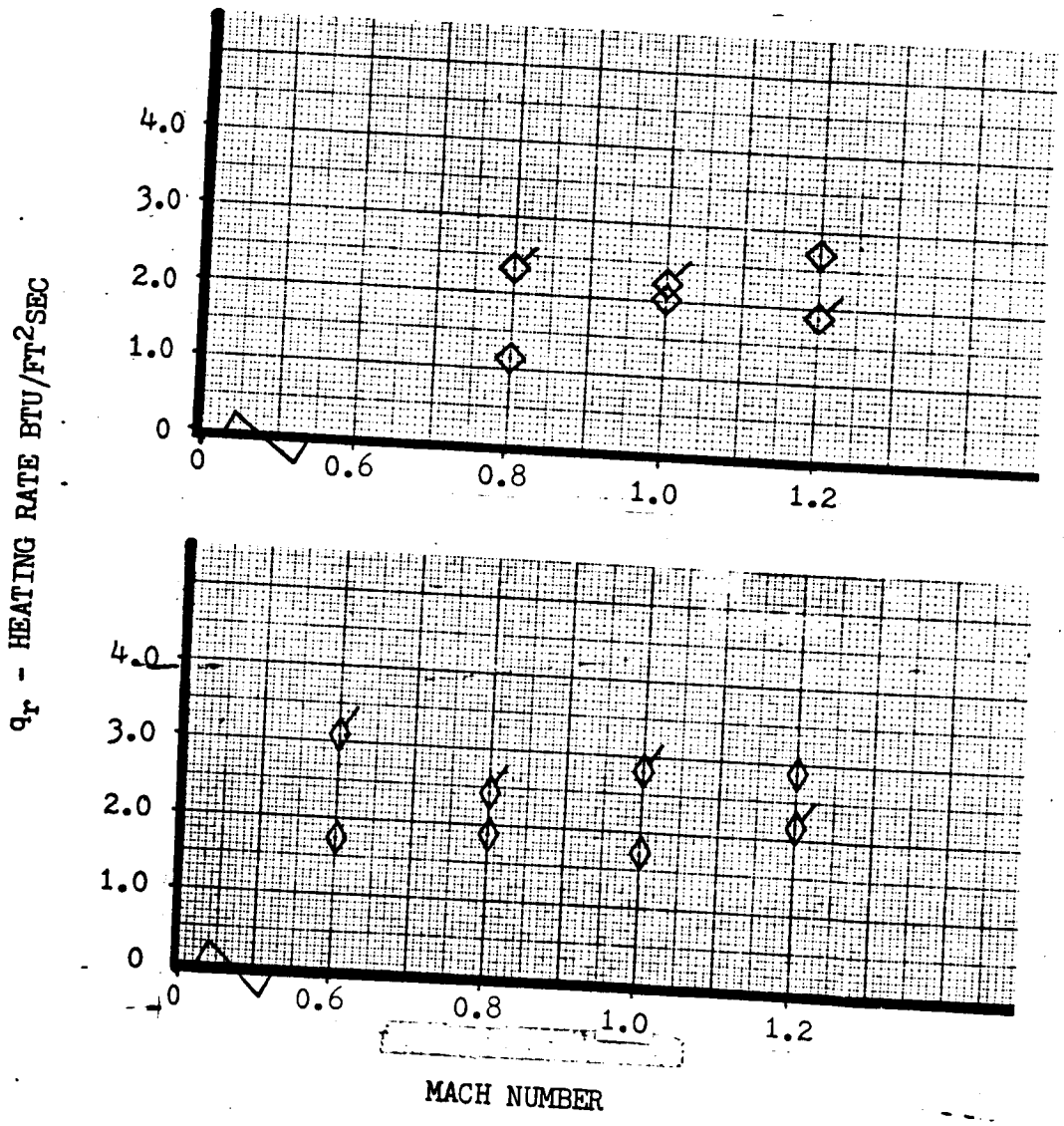

FIGURE 22 Base Heating - Radiation (Symmetry)

TUNNEL CAL 8 by 8

SYM.	INST.	CONFIG.
◇	$H_{13,17}$	$B_1FS_4D_1SC_1N_{1-5}PL_1$
◇	$H_{13,17}$	$B_1FS_2D_1SC_1N_{1-5}PL_1$

NOTE: Flagged symbol is H_{17}

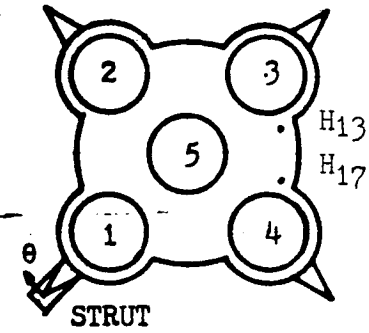

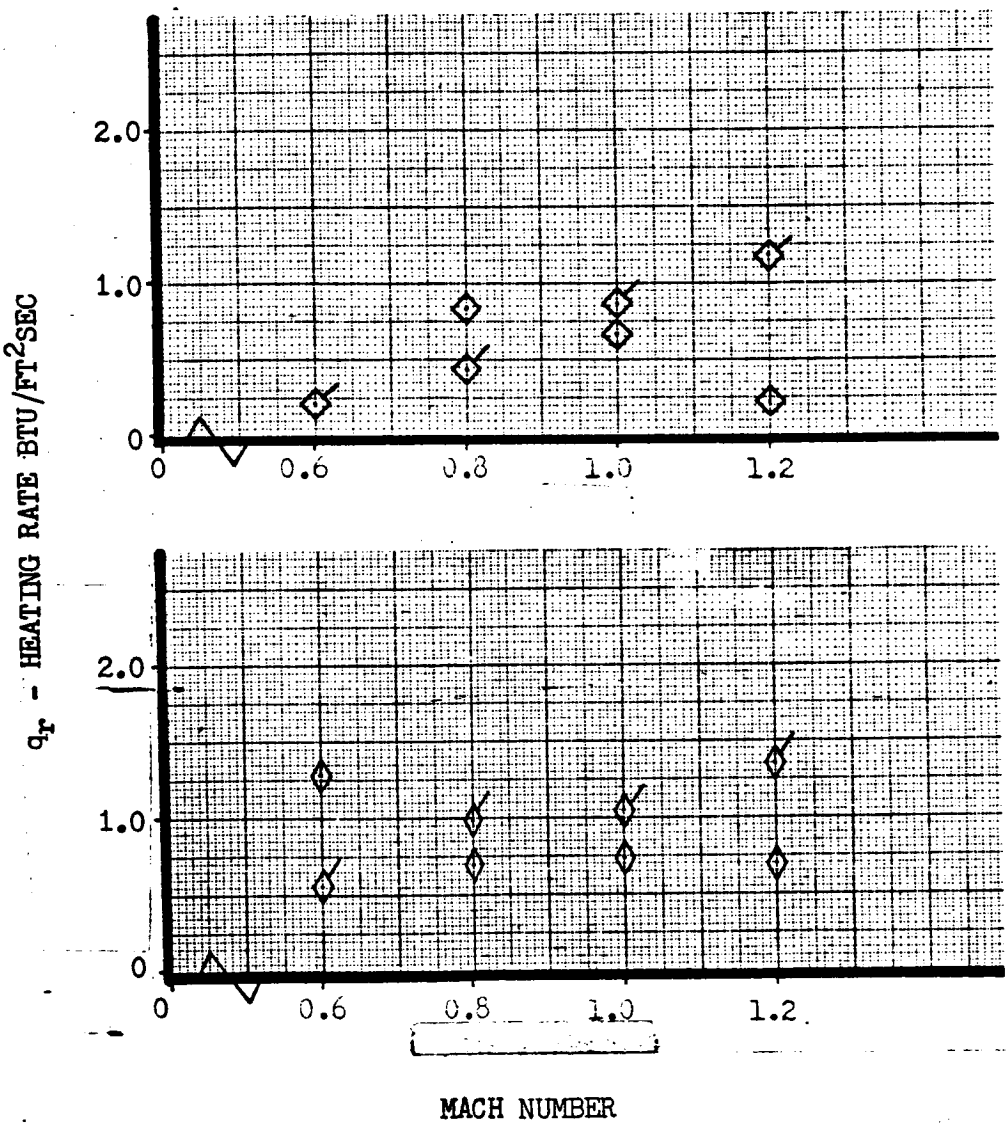

FIGURE 23 Base Heating - Convection (Symmetry)

TUNNEL CAL 8 BY 8

SYM.	INST.	CONFIG.
□	$P_{3,5}$	$B_1FS_1N_{1-5}PL_1$
◇	$P_{3,5}$	$B_1FS_4D_1SC_1N_{1-5}PL_1$
◇	$P_{3,5}$	$B_1FS_2SC_1N_{1-5}PL_1$

NOTE: 1. Flagged symbol denotes P_5
2. Solid symbol denotes turbine exhaust

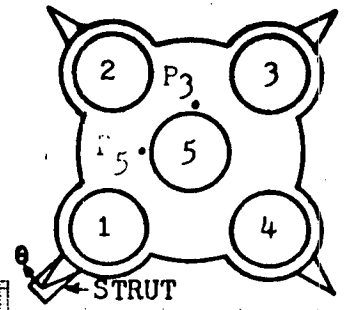

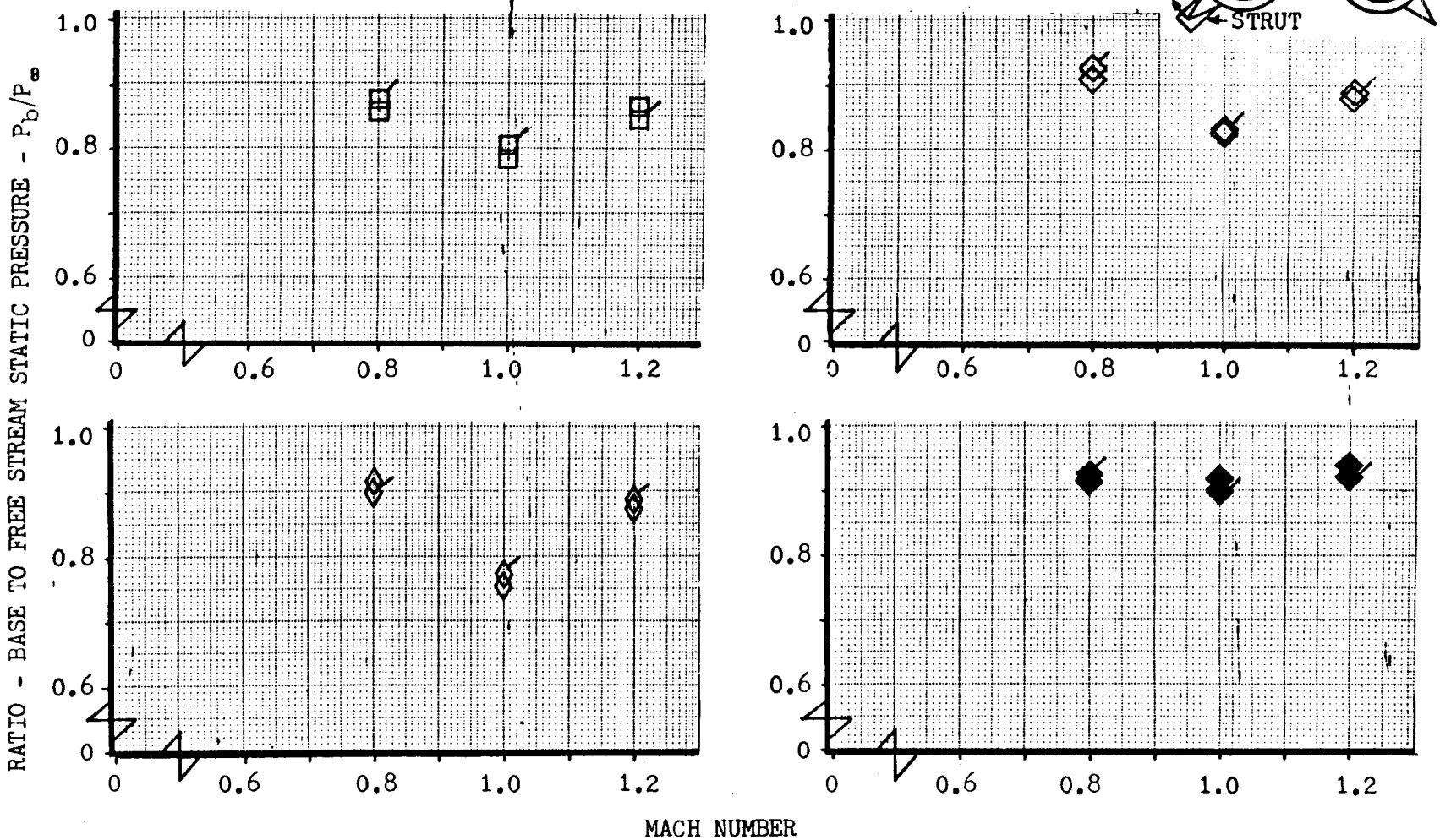

FIGURE 24 Base Pressure - Symmetry

3.6 (Continued)

e. Scooping reduces the base convective heating, and shortening the engine fairing length slightly increases the convective heating.

f. Base burning occurs at Mach 0.6 and 0.8

g. Convection heating level is essentially constant over the base.

h. Base pressure is increased with addition of flow deflectors.

i. Below Mach 1.0 the base pressure is primarily influenced by free stream flow over the aft end of the vehicle and the flow deflectors.

j. The theoretical scoop static exit pressure compares well with the measured base pressure during engine firing.

SECTION 4 - ANALYSIS OF LEWIS RESEARCH CENTER (LRC) 8 BY 6 FOOT SUPERSONIC WIND TUNNEL TEST

4.0 INTRODUCTION

This section contains the data analysis of Phase II, Part III of the Saturn S-IC Model Base Heating Test Program. The test was conducted in the NASA - Lewis Research Center 8 by 6 Foot Supersonic Wind Tunnel with a 2.22 percent scale model of the S-IC stage afterbody. Model tests were conducted at Mach numbers of 0.55, 0.80, 1.00, 1.35, 1.66 and 1.95 at the simulated altitudes shown in Figure 25 during the period of May 1 - August 1, 1965.

Flow conditions and boundary layer characteristics are determined on the body near the base by a total pressure rake. Model geometry changes consisting of engine fairing length, scoop size, deflector size, engine gimbal patterns, engine out and turbine exhaust simulation are considered. The model and combustion parameters are discussed under paragraph 1.0 in Volume 1.

Considerable rework of the combustion system and the addition of combustion system instrumentation was accomplished after the supersonic test series at the Lewis Research Center (10 by 10 foot tunnel) and prior to the 8 by 6 test. Combustion was controlled at the prototype O/F ratio. The exhaust from all engines appeared, from pictures taken during test set-up, to be well mixed and flowing evenly. No pictures were taken during the actual test runs because of a structural failure of the strut which destroyed the camera window.

During the early runs turbine exhaust was simulated by using both ethylene and hydrogen. Ethylene produced the highest radiation rates, however hydrogen produced the highest convection rates above Mach 1.0

The ethylene produced soot which severely coated the instrumentation and which had to be cleaned after each run. Because of this it was decided for future runs to use only hydrogen to simulate turbine exhaust injection.

The S-IC trajectory is not well simulated in the Lewis 8 by 6 foot tunnel, as seen in Figure 25. For instance, at Mach number 1.95 the simulated altitude is 15,000 feet lower than the trajectory altitude. This discrepancy has a major effect on exhaust expansion and may affect both convection and radiation heating rates.

Analysis of the data is related to geometry changes and a comparison with theory. In comparing model test data with theory, model test environment (external flow environment, combustion characteristics, plume shape and model dimensions) is used in the theoretical calculations.

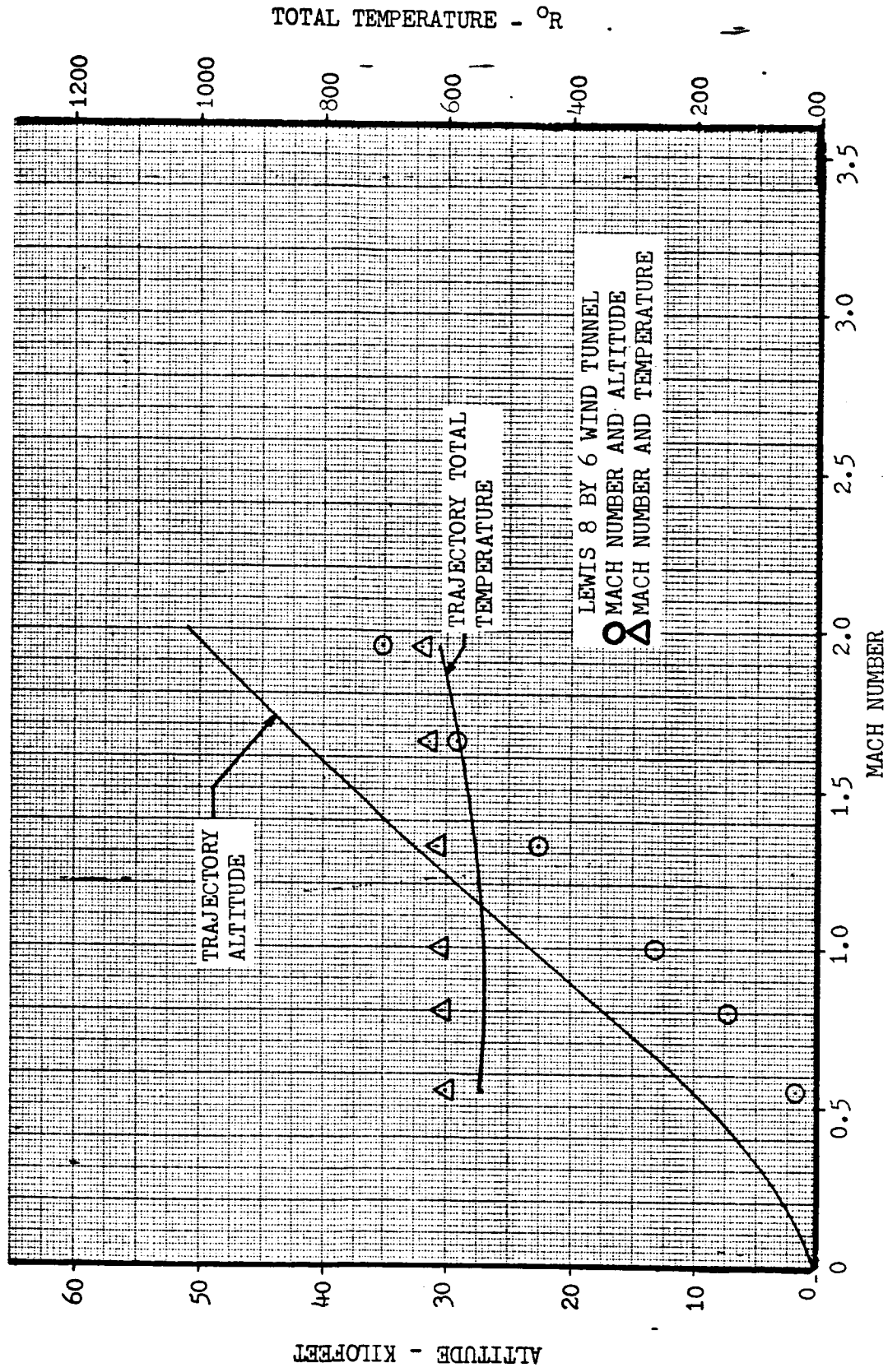

FIGURE 25 Test Conditions - Lewis 8 by 6 Tunnel

4.1 BOUNDARY LAYER

Total pressure boundary layer measurements near the model base, obtained using the ten probe rake illustrated in Figure 16, section 1, are used to determine boundary layer height. Actual total pressure in the boundary layer is determined by correcting the probe readings for the normal shock which stands in front of the rake. Figure 26 shows the ratio of the actual total pressure to tunnel total pressure at the various probe heights and Mach numbers. The boundary layer edge is defined as the point at which 0.998 of the free stream velocity is reached. Measured boundary layer thickness (Figure 27) coincides with the turbulent flow theory described in paragraph 2.1 of Volume 1.

4.2 RADIATION

Although the Mach number range is greater than the range covered in the CAL Transonic Tunnel the upper altitudes are approximately equal (compare Figure 1 and 25), due to the Lewis 8 by 6 foot tunnel operating characteristics. Therefore, at identical combustion conditions and neglecting effect of free stream velocity on exhaust expansion, the radiation at Mach number 1.85 in the Lewis tunnel should theoretically be the same as the radiation in the CAL 8 by 8 foot tunnel at Mach number 1.2. However, combustion conditions between the two tests are considerably different and the velocity effect on exhaust expansion must be considered.

For any given point only slight changes are expected in the radiation level over the altitude range of this test (3,000 to 35,000 feet). Theoretical full expansion in the nozzle will occur at approximately 24,000 feet and relatively little additional plume expansion will occur over the remaining test range.

4.2.1 Radiation to Base

Data from gages 2, 4, 6, 8 and 10 located on a ray mid-way between engines 3 and 4 (see Figure 19, Volume 1) are averaged for display in Figures 28, 29 and 30. Effects of variations in scoop area, engine fairing length, center engine out and gimballing on radiation are shown in Figure 28. The data are very erratic and trends are difficult to establish. However, in general it appears that radiation is highest with neither scoops nor deflectors. Loss of the center engine will reduce radiation as will shortening the engine fairing. Gimballing the engines toward each other appears to reduce radiation. This trend was not anticipated. No significant reduction is noted with increasing Mach number.

Affects of turbine exhaust simulation are shown in Figure 29 for the configuration without scoops or deflectors. Injection of ethylene created higher radiation rates at all Mach numbers which indicates that the fuel is burning with an increase in temperature or emmissivity or both. Injection of hydrogen has no apparent heating effect since radiation from hydrogen is negligible. Figure 30 shows comparison of scooped configurations with and without hydrogen turbine exhaust simulation.

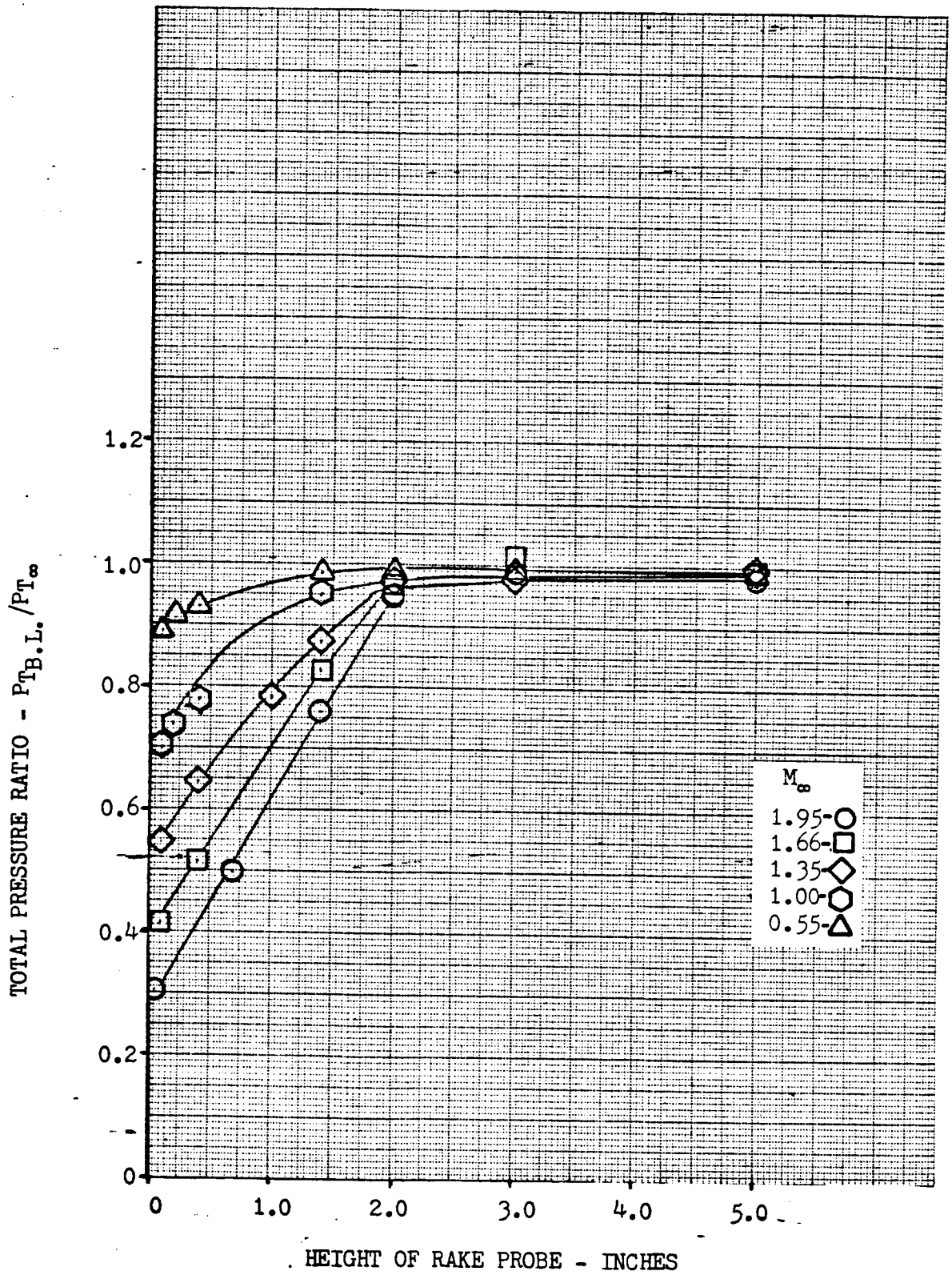

FIGURE 26 Boundary Layer Rake Data - Lewis 8 by 6 Tunnel

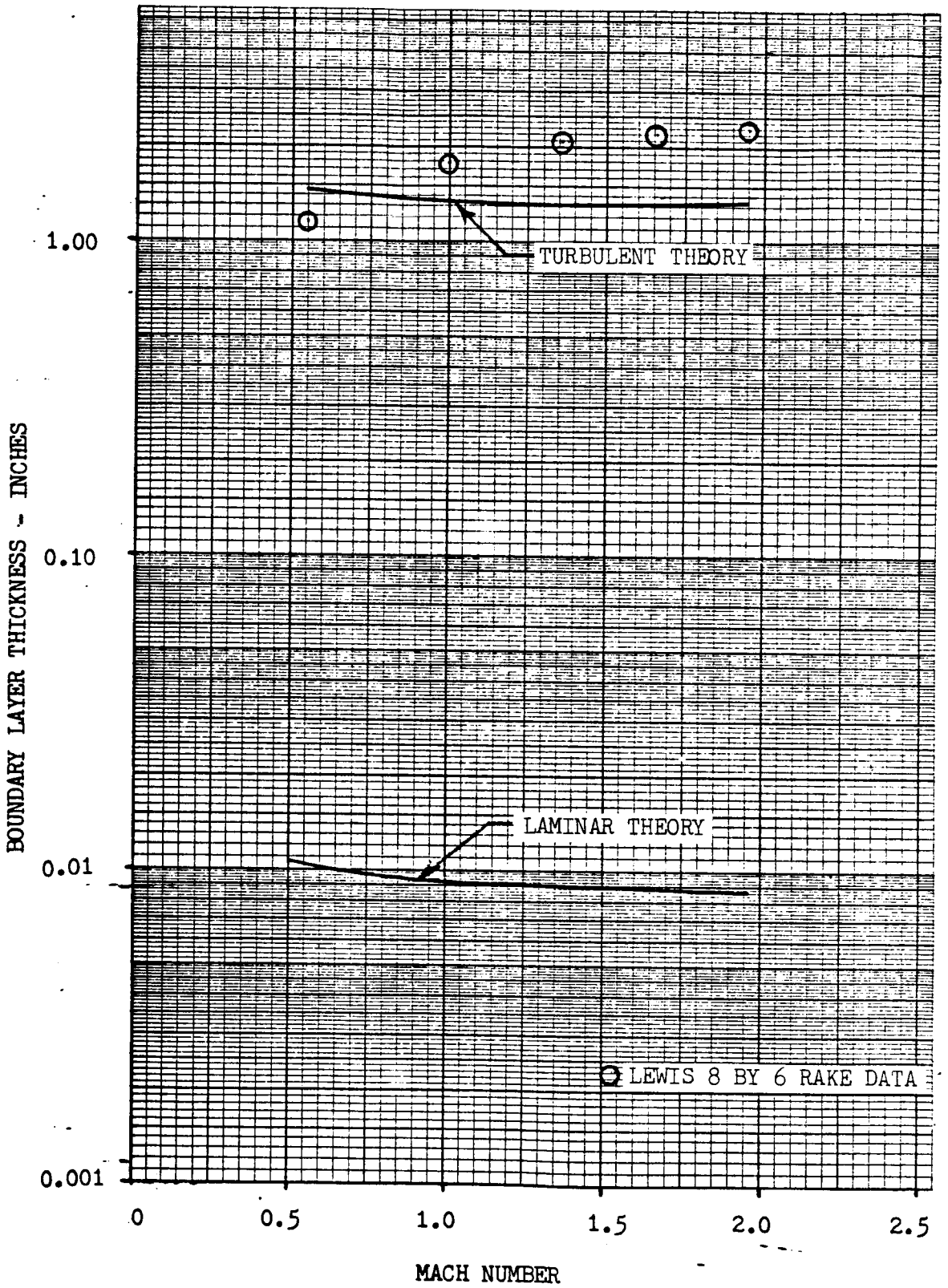

FIGURE 27 Model Boundary Layer Thickness Versus Theory

TUNNEL LEWIS 8 BY 6

SYM.	INST.	CONFIG.
○	$H_{2,4,6,8,10}$	$B_4FS_1N_{1-5}PL_1$
□	$H_{2,4,6,8,10}$	$B_4FS_1D_1SC_2N_{1-5}PL_1$
◇	$H_{2,4,6,8,10}$	$B_4FS_1D_2N_7PL_1$
△	$H_{2,4,6,8,10}$	$B_4FS_1D_2N_{1-5}PL_1$
◿	$H_{2,4,6,8,10}$	$B_4FS_1D_2N_{G_7}N_{G_8}PL_1$
◊	$H_{2,4,6,8,10}$	$B_4FS_4N_{1-5}PL_1$

NOTE: Data averaged

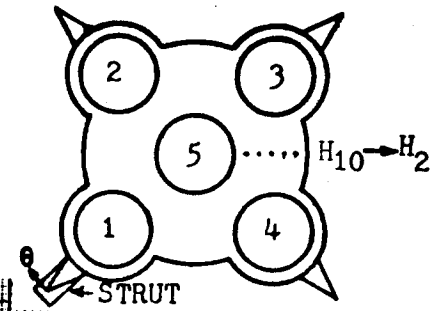

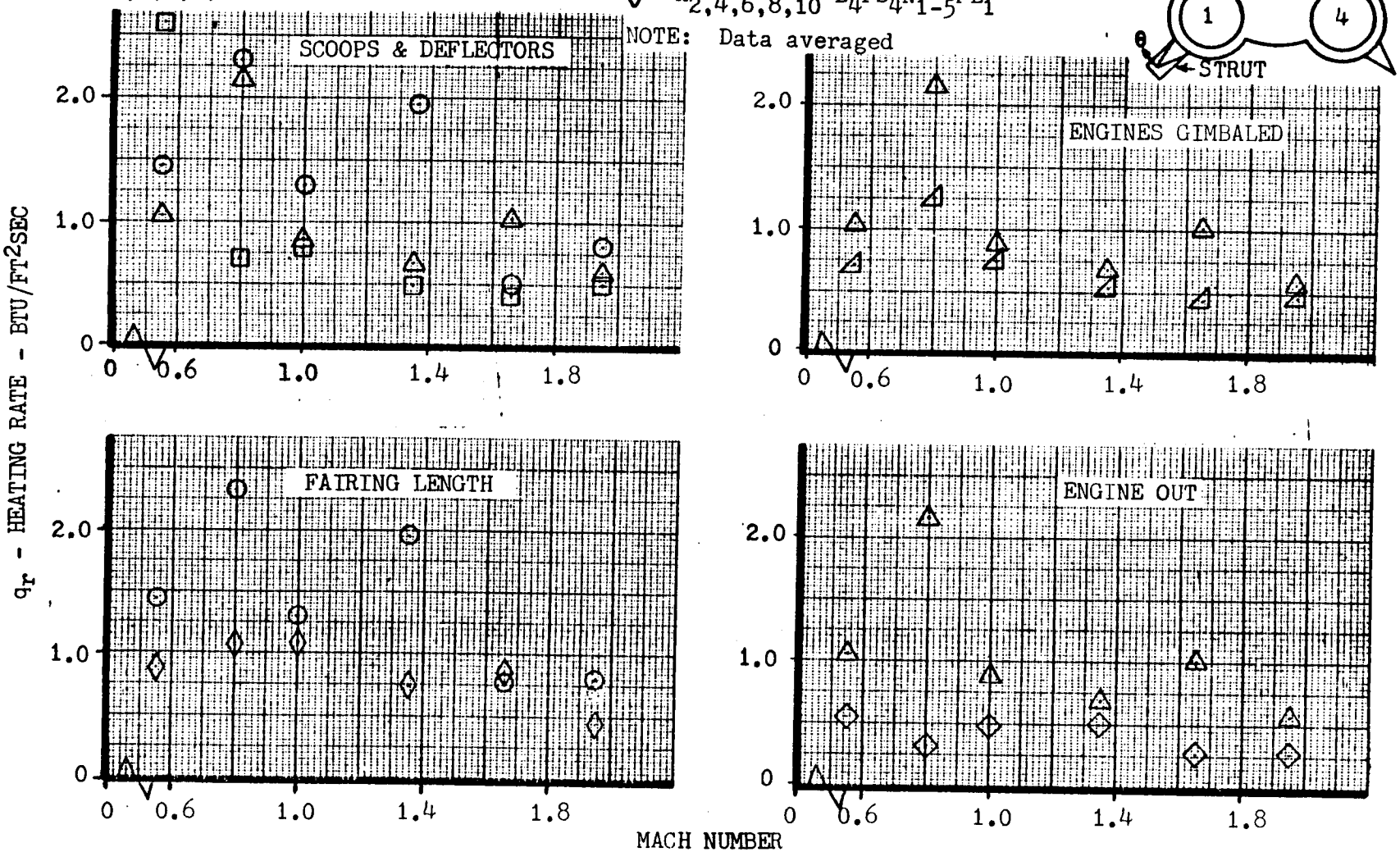

FIGURE 28 Base Heating - Radiation

TUNNEL Lewis 8 by 6

SYM.	INST.	CONFIG.	SYM.	INST.	CONFIG.
○	$H_{10,8,6,4,2}$	$B_4FS_1N_{1-5}PL_1$			

NOTE: 1. Solid symbol denotes H_2 turbine exhaust
2. Half solid symbol denotes C_2H_4 turbine exhaust

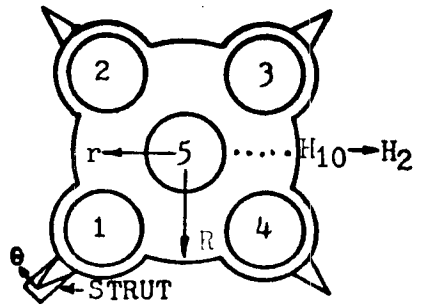

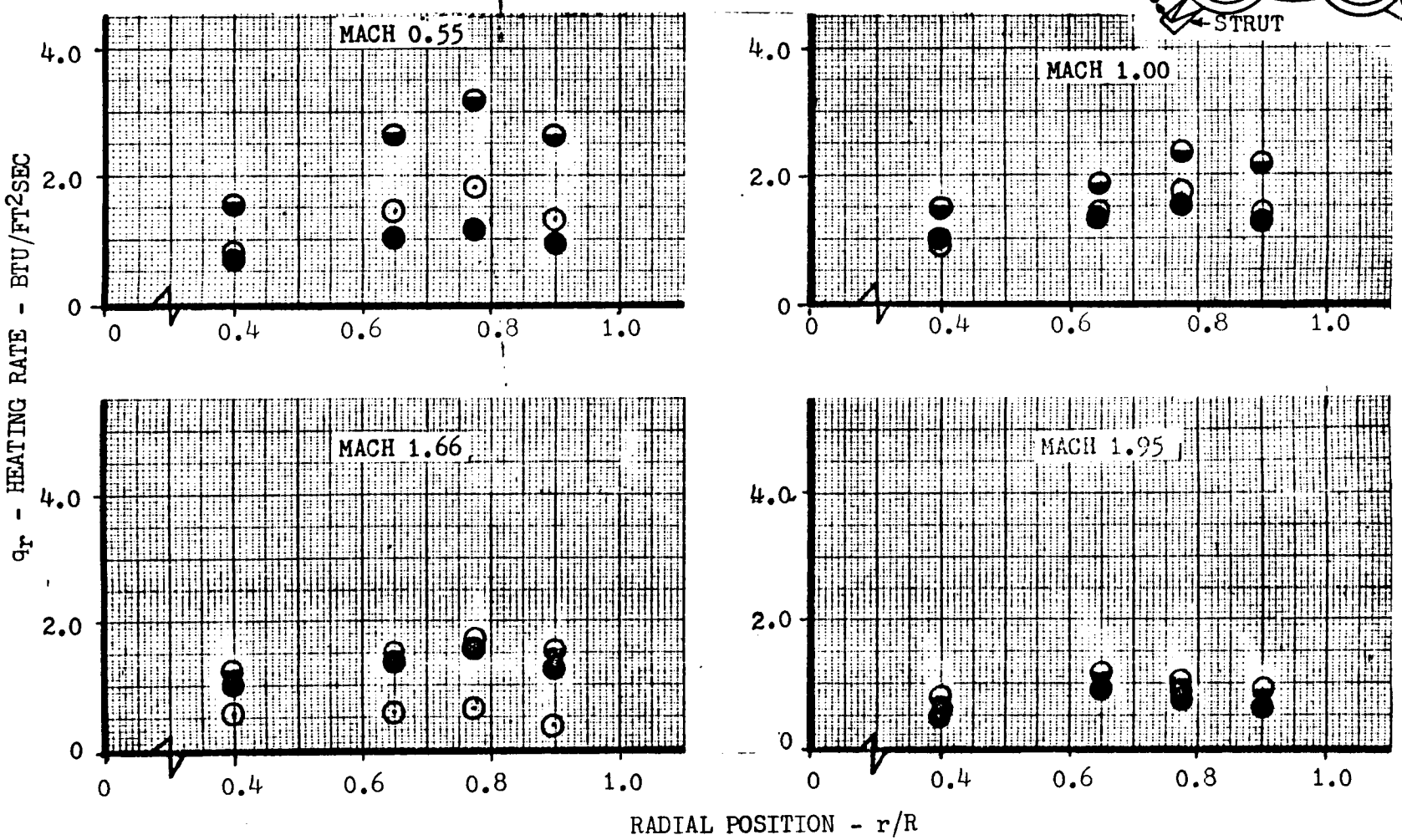

FIGURE 29 Base Heating - Radiation

TUNNEL LEWIS 8 BY 6

SYM.	INST.	CONFIG.
△	$H_{2,4,6,8,10}$	$B_4FS_1D_2N_{1-5}PL_1$
□	$H_{2,4,6,8,10}$	$B_4FS_1D_1SC_2N_{1-5}PL_1$

NOTE: 1. Solid symbol denotes turbine exhaust
2. Data averaged

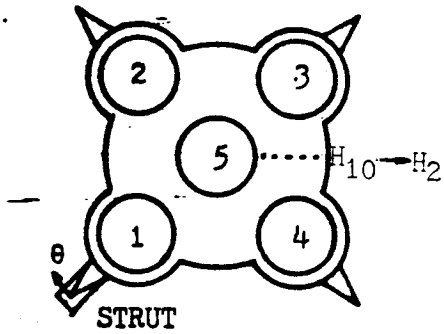

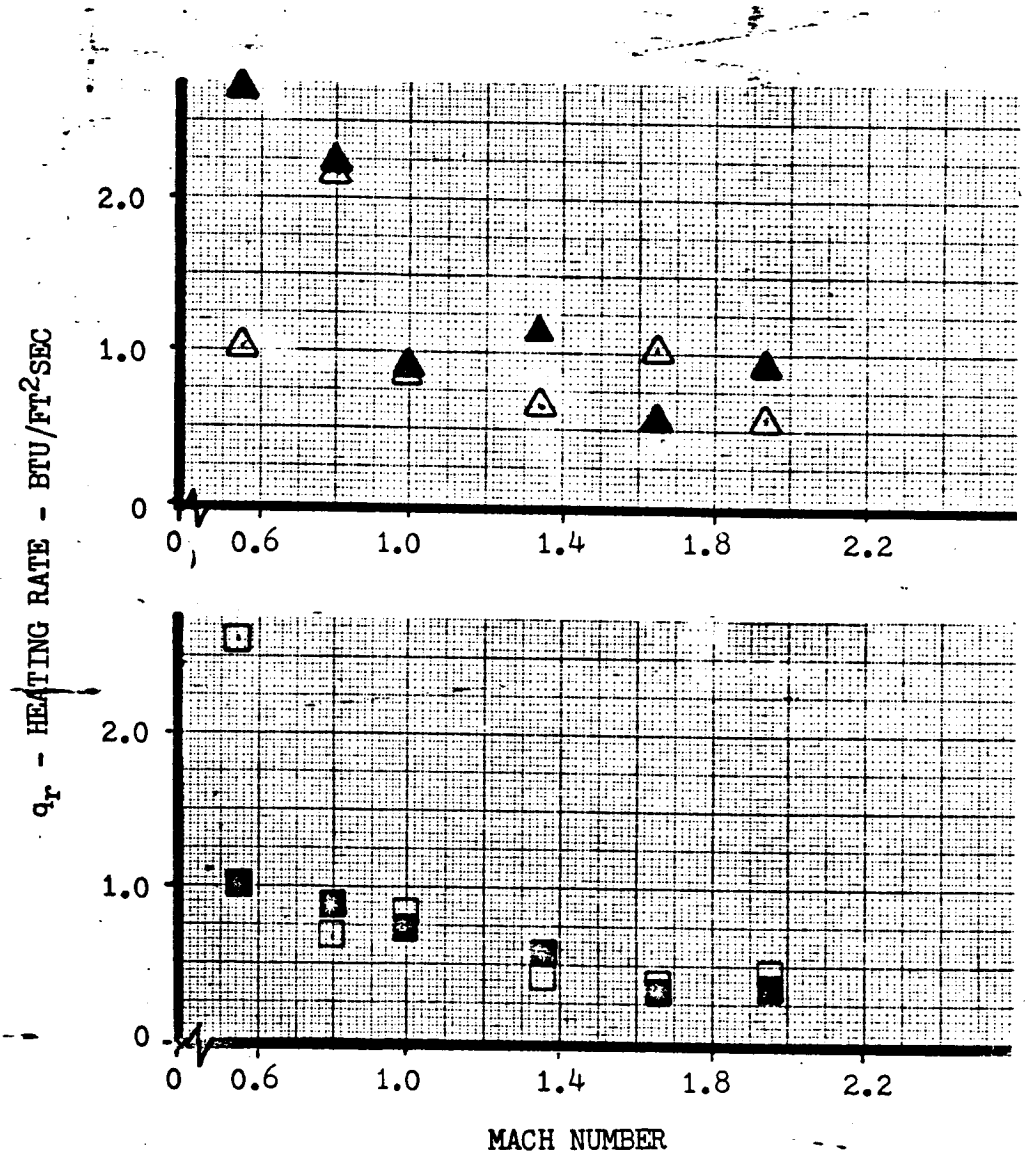

FIGURE 30 Base Heating - Radiation

4.2.1 (Continued)

No consistent increase in heating is noted. Data are not available with ethylene as the simulation fuel.

Inspection of Figures 29 and 31 indicates that radiation increases from inboard to outboard as predicted by theory. Data from four gages located at an r/R of 0.9 and at various angles (θ) are also shown on Figure 31. Radiation to these outboard points is essentially constant at given Mach numbers. Radiation at θ equal to 225° should theoretically be the highest.

4.2.2 Radiation to Fin and Engine Fairing

Radiation instruments 64 and 66 are located on the aft face of the fin near the fin-engine fairing interface and about half-way out on the face of the fin respectively. These gauges face directly aft. Radiation to the fin increases slightly with distance outboard (Figure 32).

Radiation to the inside of the engine fairing near the aft face is obtained from instrument 60. The gauge is located 32.5 degrees from the fin centerline (Figure 27, Volume 1) and faces the throat of the nozzle approximately. As expected, radiation to this gauge is low since the gauge does not receive radiation from the "near engine" exhaust.

4.2.3 Radiation to Engines (External)

Data on the engines is spotty and relatively inconsistent due to instrumentation failure. Data from three instruments located on the center engine are shown in Figure 33. Detailed locations are shown in Figures 22 and 23 (Volume 1). Instrument 22 is attached to the exterior surface of the nozzle near the exit plane facing outboard between engines 3 and 4. Instrument 24 is similarly mounted except that it faces engine 3. Instrument 28 is located on the surface in line with 24 and just aft of the turbine exhaust manifold. Data for instrument 28 was obtained from the same configuration as data from the other instruments, but on different test runs. The data show radiation to be highest near the lip and between outboard engines. The trend is as expected, but magnitude is low.

Data for a short engine fairing configuration is also shown in Figure 33. Instrument 40 is located similar to 22 and 24 except that it is on engine number 4 and faces the engine fairing. Magnitude of the data for all instruments is essentially identical and is slightly lower for this configuration.

TUNNEL LEWIS 8 BY 6

SYM.	INST.	CONFIG.
△	$H_{2,4,6,8,10}$	$B_4FS_1D_2N_{1-5}PL_1$

NOTE: 1. △ Mach 0.55
2. △ Mach 1.00
3. △ Mach 1.66

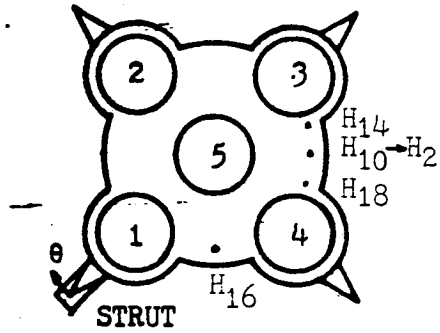

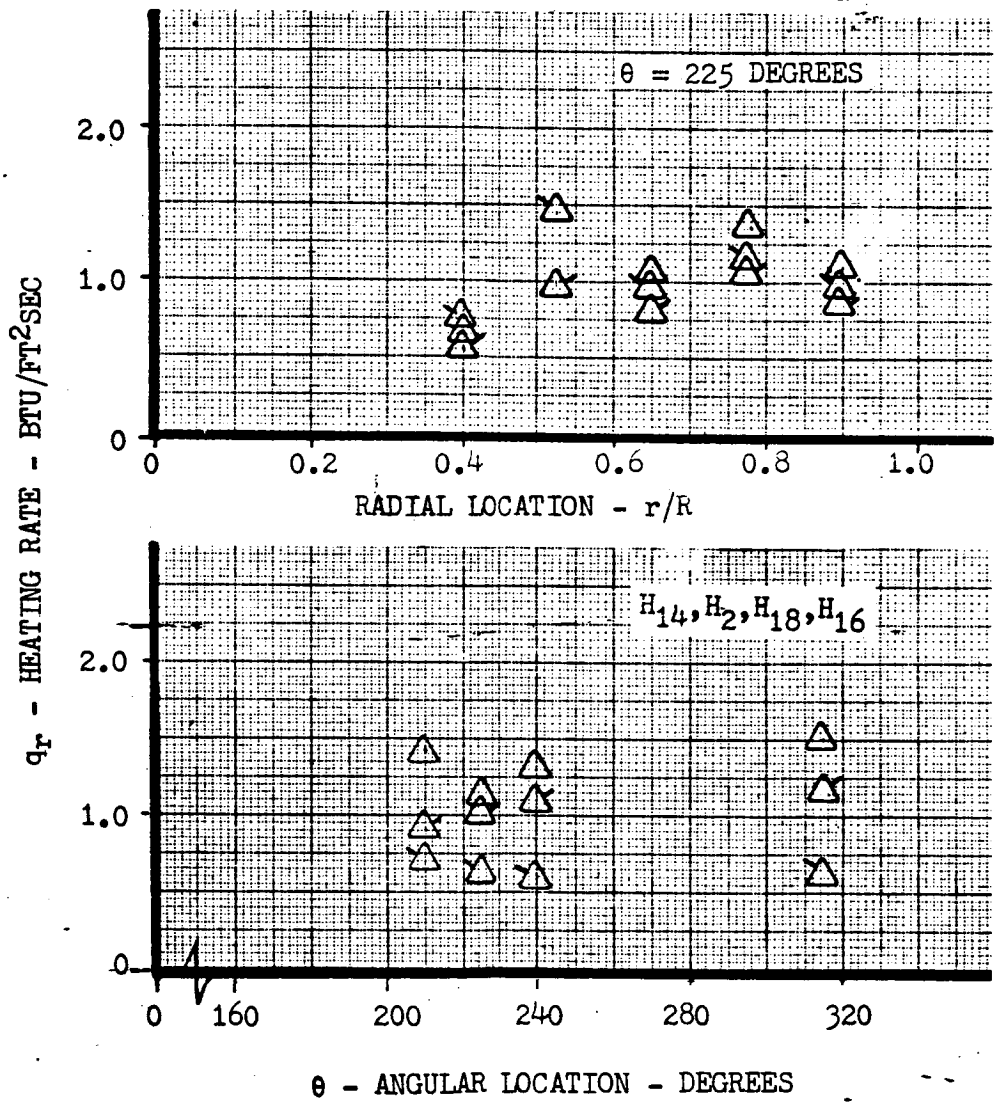

FIGURE 31 Base Heating - Radiation

TUNNEL LEWIS 8 BY 6

SYM.	INST.	CONFIG.
△	H_{60}	$B_4FS_1D_2N_{1-5}PL_1$
△	H_{64}	$B_4FS_1D_2N_{1-5}PL_1$
△	H_{66}	$B_4FS_1D_2N_{1-5}PL_1$

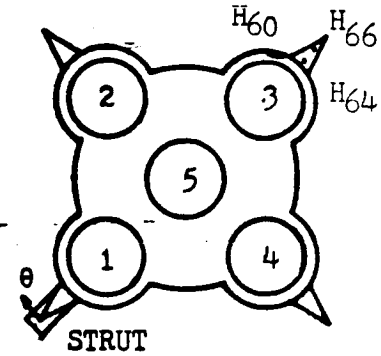

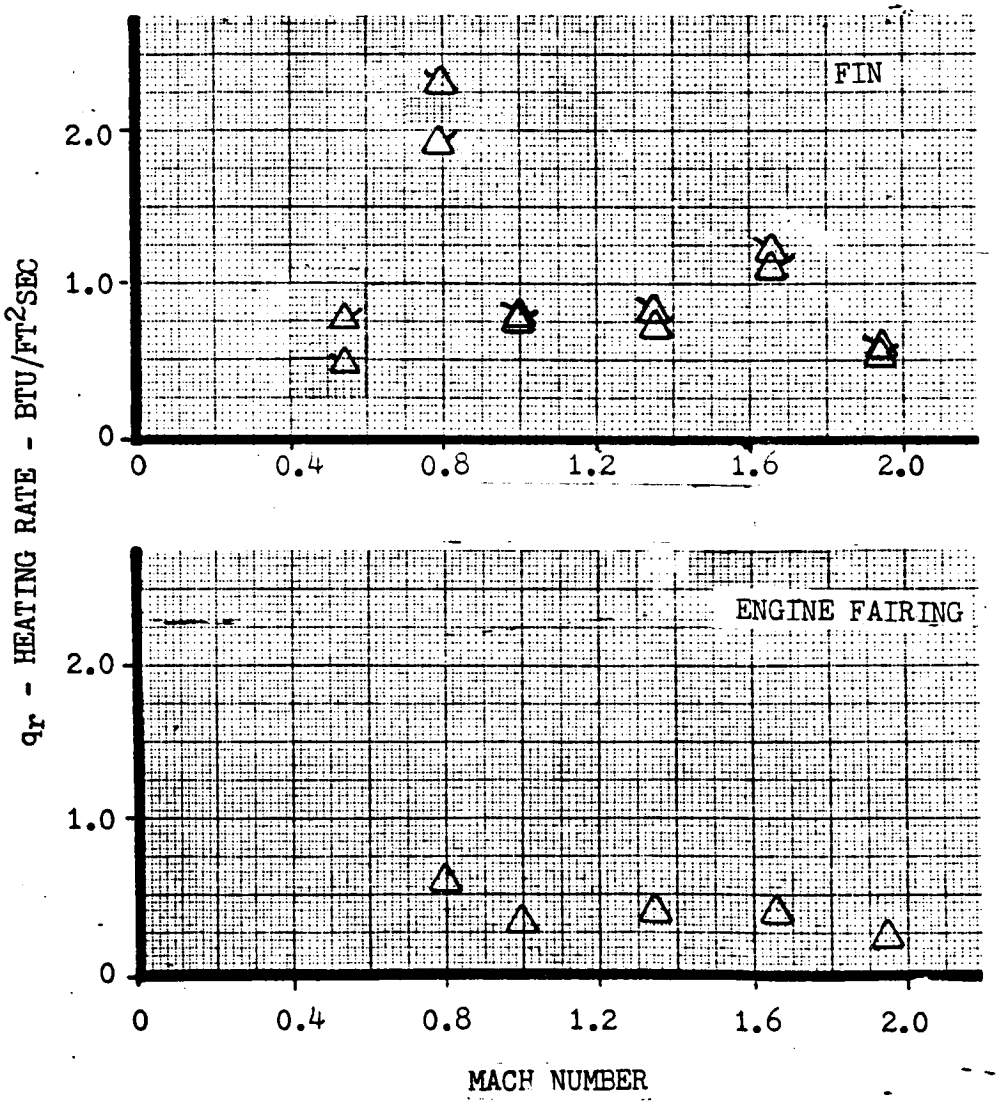

FIGURE 32 Fin and Engine Fairing Heating - Radiation

TUNNEL LEWIS 8 BY 6

SYM.	INST.	CONFIG.
□	H_{22}	$B_4FS_1D_1SC_2N_{1-5}PL_1$
□	H_{24}	$B_4FS_1D_1SC_2N_{1-5}PL_1$
□	H_{28}	$B_4FS_1D_1SC_2N_{1-5}PL_1$
◇	H_{22}	$B_4FS_4D_2N_{1-5}PL_1$
◇	H_{24}	$B_4FS_4D_2N_{1-5}PL_1$
◇	H_{40}	$B_4FS_4D_2N_{1-5}PL_1$

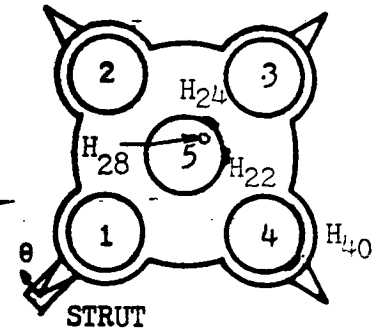

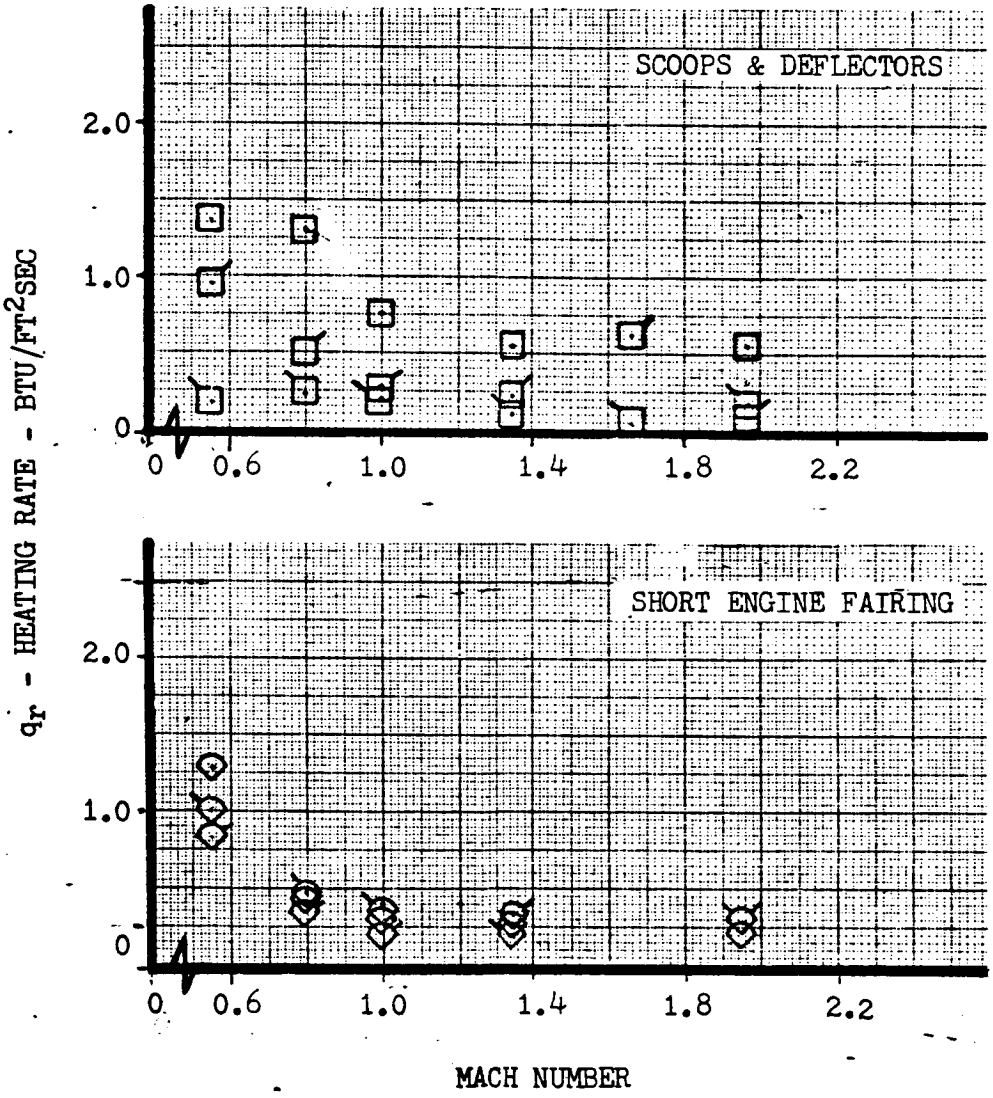

FIGURE 33 Engine Heating - Radiation (External)

4.2.4 Radiation to Engines (Engine Out)

Data was obtained on the inside and outside surfaces of an instrumented and plugged nozzle to determine heating effects on an inoperative engine. Radiation and total heating gages are located on the inoperative engine nozzle as shown on Figure 24, Volume 1. The inoperative engine was used in the center engine position (#5) and the outboard engine position (#2). Figure 34 shows the radiation heating rates to the inside and outside gages.

Radiation to the center engine is nearly uniform along the inside surface with the gauge near the throat showing the highest rate. The radiation to the outside gages is small due to the view factor involved.

Radiation to the inoperative outboard engine is higher than radiation to the center engine. Turbine exhaust does not have any significant effect on the data whether on an outboard engine or on the center engines.

Radiation is also recorded on the lip of the nozzle using gages H_{54} and H_{56}. These gages are located as shown in Figures 24 and 25 (Volume 1) and are facing aft. The data are shown in Figure 35. Turbine exhaust has no significant effect on heating. No reason for the discrepancy between gages H_{54} and H_{56} for the center engine out can be advanced. In general, the trend of the reduction in heating rate with altitude increase is as expected.

4.2.5 Comparison with Radiation Theory

Using the methods discussed in Appendix A of Volume 1, radiation on the base is estimated assuming both non-luminous hot gases and luminous particle radiation with an emissivity of 1.0. These estimates are shown on Figure 36 and compared with test data from a configuration which closely resembles the prototype. These base plate data fall between the theoretical estimates and indicate an emissivity of approximately 0.5 if the theoretical temperatures are correct. Emissivity from the engine exhaust is considerably less for this test series than it was in the CAL 8 by 8 tunnel test (Compare Figure 11 with Figure 36). Oxygen to fuel ratio was closely controlled at the prototype value of 2.25.

4.3 CONVECTION

In the range of this test it is expected that the base scoops will have a large effect on the convection coefficients, since the surrounding air is relatively dense and the engine plumes only slightly expanded. The convective heating rate is obtained by subtracting the measured radiation rate from the measured total heating rate.

TUNNEL Lewis 8 by 6

SYM.	INST.	CONFIG.
	H_{44}	$B_4FS_1D_2N_7PL_1$
	H_{48}	$B_4FS_1D_2N_7PL_1$
	H_{50}	$B_4FS_1D_2N_7PL_1$
	H_{52}	$B_4FS_1D_2N_7PL_1$

SYM.	INST.	CONFIG.
	H_{44}	$B_4FS_1D_2N_{10}N_{G11}N_{G12}N_{G13}PL_2$
	H_{52}	$B_4FS_1D_2N_{10}N_{G11}N_{G12}N_{G13}PL_2$
	H_{48}	$B_4FS_1D_2N_{10}N_{G11}N_{G12}N_{G13}PL_2$
	H_{50}	$B_4FS_1D_2N_{10}N_{G11}N_{G12}N_{G13}PL_2$

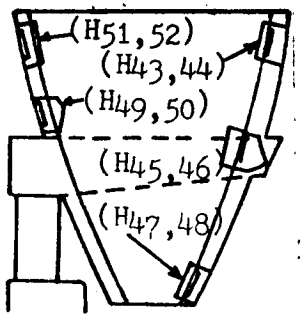

NOTE: Solid symbol denotes turbine exhaust

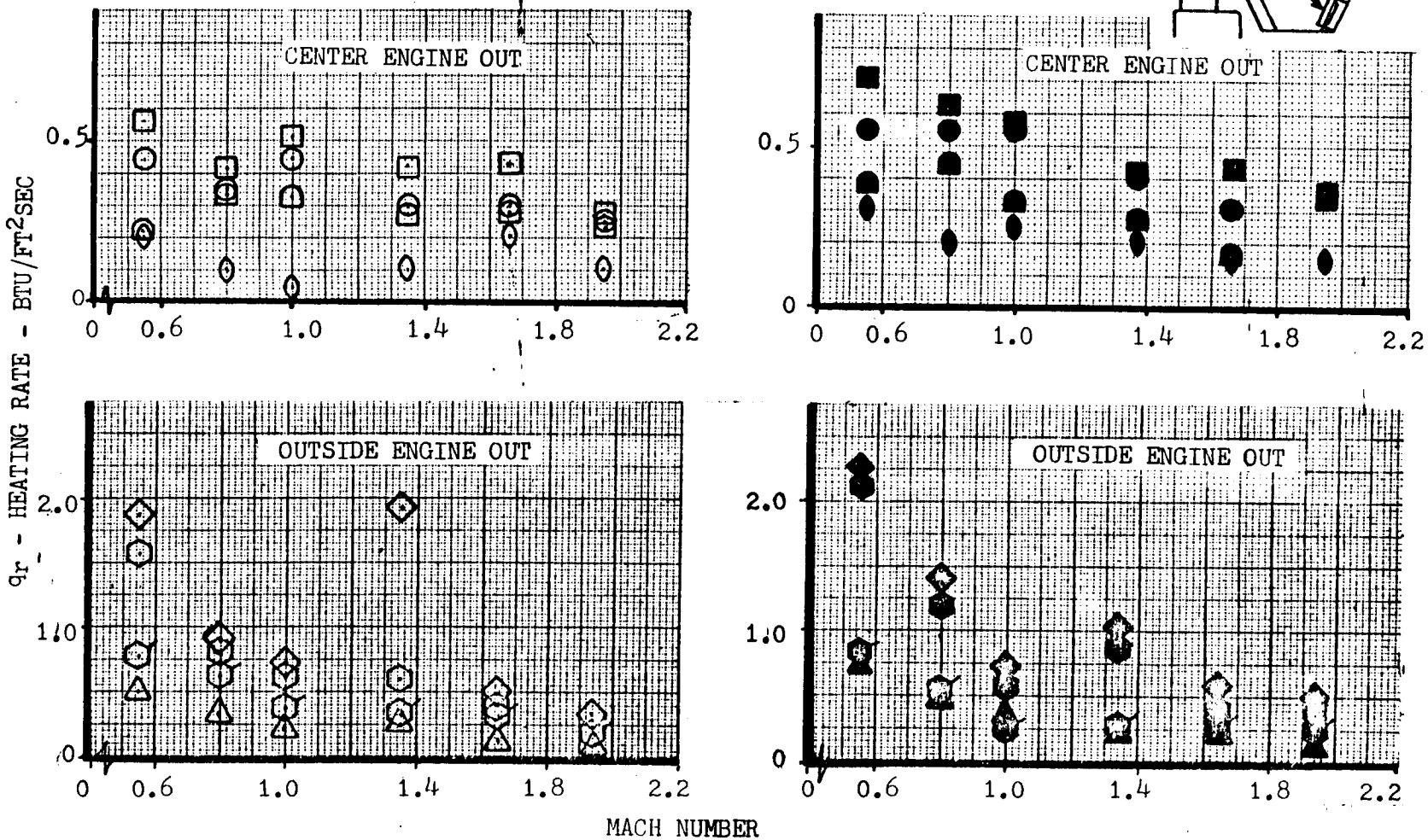

FIGURE 34 Engine Heating - Radiation (Internal)

TUNNEL LEWIS 8 BY 6

SYM.	INST.	CONFIG.
◇	$H_{54,56}$	$B_4FS_1D_2N_7PL_1$

SYM.	INST.	CONFIG.
◇	$H_{54,56}$	$B_4FS_1D_2N_{10}N_{G_{11}}N_{G_{12}}N_{G_{13}}PL_2$

NOTE: 1. Flag denotes gauge H_{56}

2. Solid symbol denotes turbine exhaust

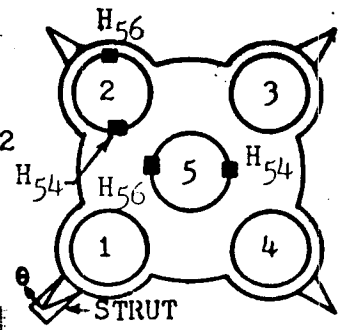

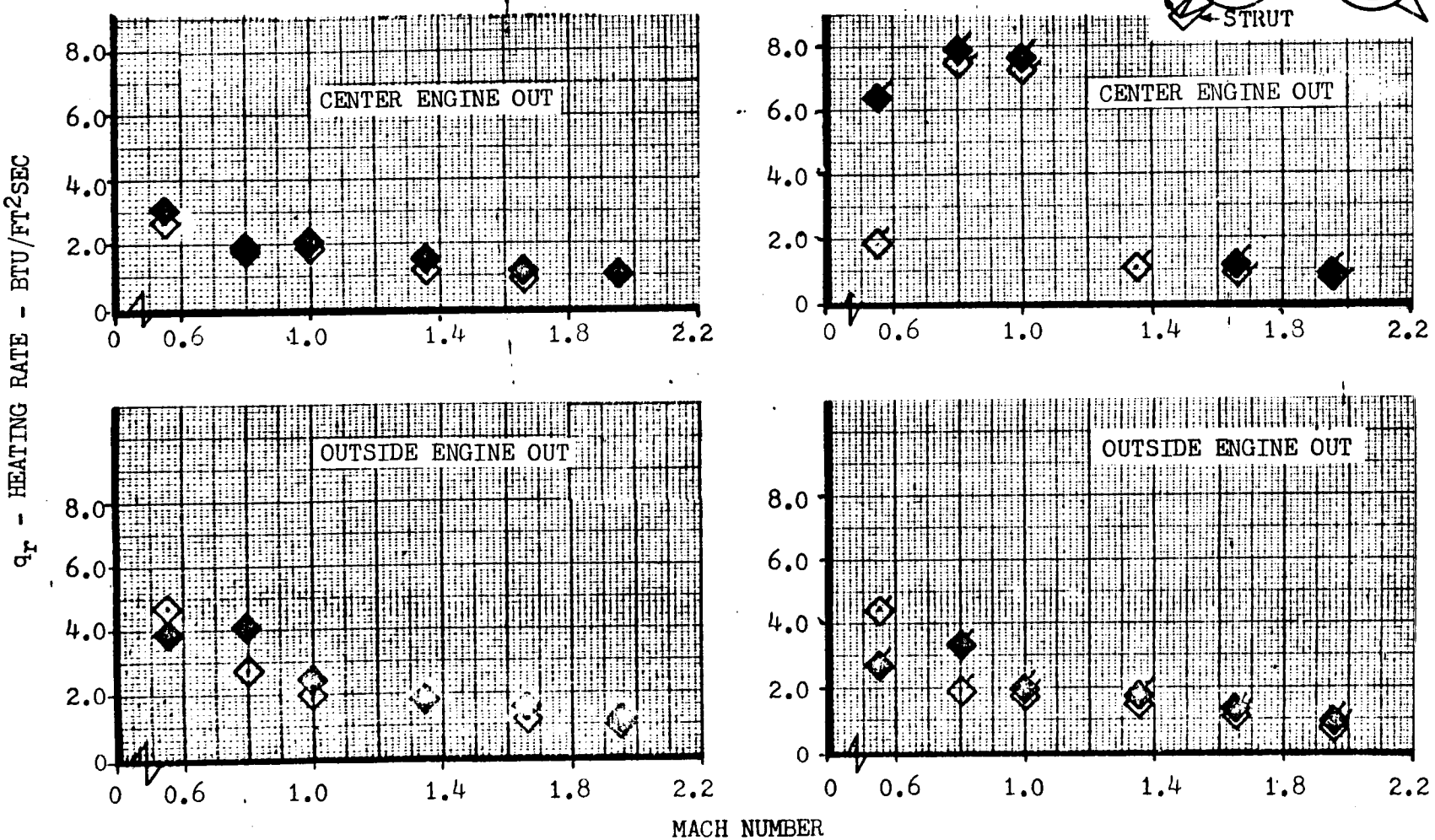

FIGURE 35 Engine Heating - Radiation (Internal)

TUNNEL LEWIS 8 BY 6

SYM.	INST.	CONFIG.
△	H_6	$B_4FS_1D_2N_{1-5}PL_1$

NOTE: Solid symbol denotes turbine exhaust

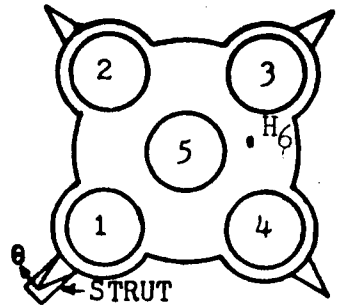

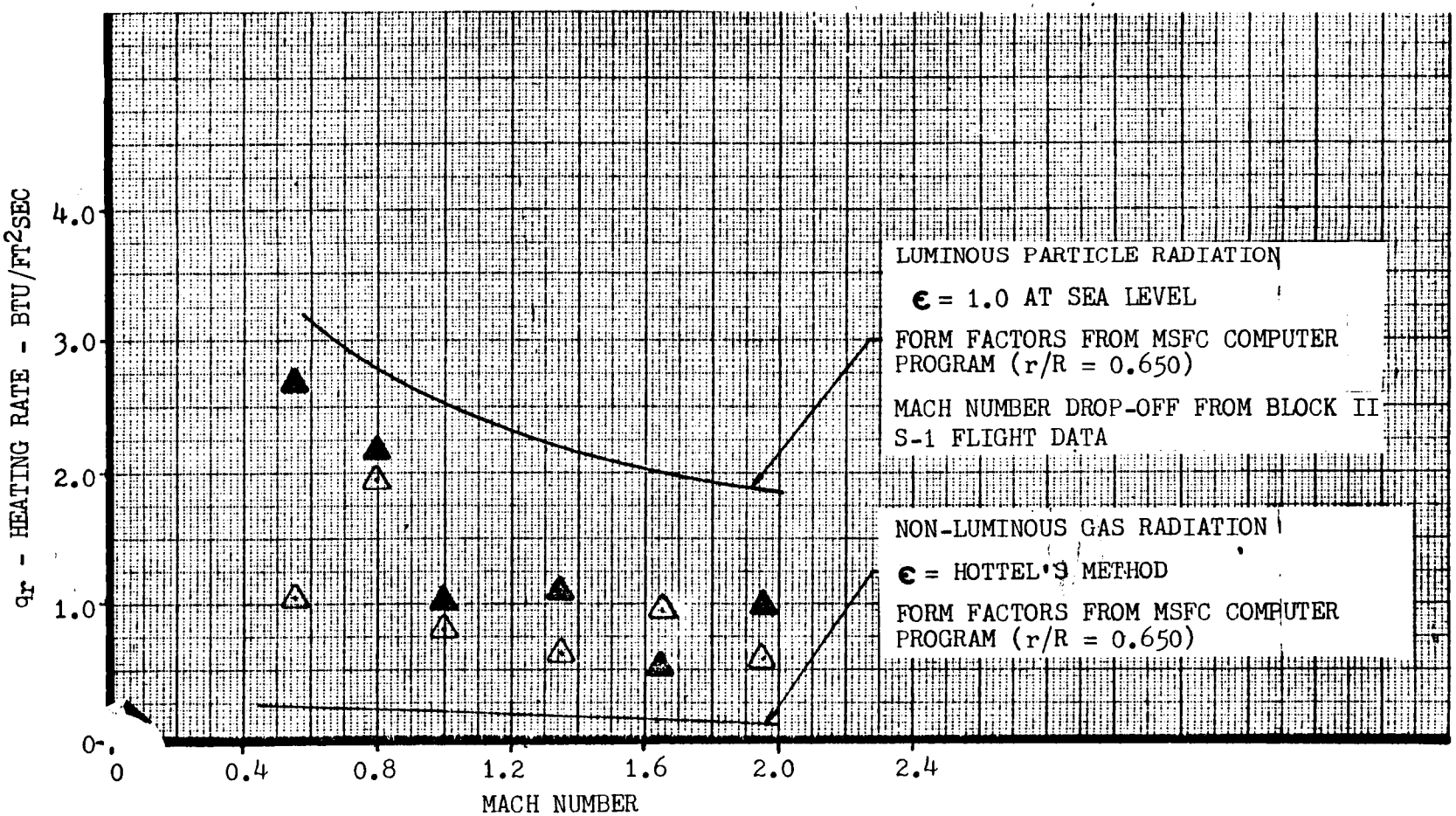

FIGURE 36 Base Heating - Radiation Versus Theory

4.3.1 Convection to Base

Results obtained using both hydrogen and ethylene (gaseous) as turbine exhaust simulation on a configuration without deflectors or scoops are shown in Figure 37. The high heating rates at low Mach numbers indicate that the turbine exhaust is burning in the base. Above Mach 1.0 the effect is minimal. Injection of hydrogen produces the highest heating rates at all Mach numbers greater than 0.55. Above Mach 1.0 it appears that ethylene does not ignite which is consistent with its flamibility limit.

In Figure 38, the data from gages H_1, H_3, H_5, H_7 and H_9 are averaged. At each Mach number, injection of turbine exhaust substantially increases the heating rate for the configuration without scoops or deflectors. However, for the other three configurations with engine fairing scoops and/or deflectors present, the turbine exhaust gas does not affect the base convective heating, indicating that the scoops and deflectors are purging the base of exhaust gases before burning can occur. The five gauges are located along a ray between engines 3 and 4.

The increase in convective heating from turbine exhaust is strongly dependent upon timing the combustion chamber with the turbine exhaust injection. Early arrival of the hydrogen significantly increases the heating level (Figure 39).

Average effects due to the various configurations are compared in Figure 40. The addition of scoops and/or deflectors is shown to substantially reduce the convective heating rates. A slight reduction in heating is obtained with the center engine out, and a slight increase occurs by shortening the engine fairing. However, gimballing the engines does not affect the base convective heating rates.

Average rates on the base are essentially constant at 0.5 BTU/FT^{2}SEC for Mach 1.0 ~~- 1.95~~ and rise only slightly at Mach 0.55 and 0.80 (0.75 - 1.00 BTU/FT^{2}SEC). This applies to all configurations as long as scoops and/or deflectors are present.

Sample radial and angular distributions are shown in Figure 41. The radial distribution data obtained along a ray at θ = 225 degrees shows a drop-off in heating rate toward the center engine. The angular distribution data is obtained from instruments located at an r/R of approximately 0.9 except for the data at $\theta = 180^\circ$ (gauge 19) which is under the engine fairing (See Figure 13, Volume 1). Convection appears slightly higher directly between the outboard engines.

Comparison of data at $\theta = 210^\circ$ and $\theta = 240^\circ$ indicates reasonable symmetry within a quadrant. However, data at $\theta = 225^\circ$ and $\theta = 315^\circ$ is not in agreement, and indicates unsymmetri flow between quadrants.

TUNNEL LEWIS 8 BY 6

SYM.	INST.	CONFIG.
○	$H_{1,3,5,9}$	$B_4FS_1N_{1-5}$

NOTE: 1. Solid symbol denotes H_2 turbine exhaust
2. Half solid symbol denotes C_2H_4 turbine exhaust

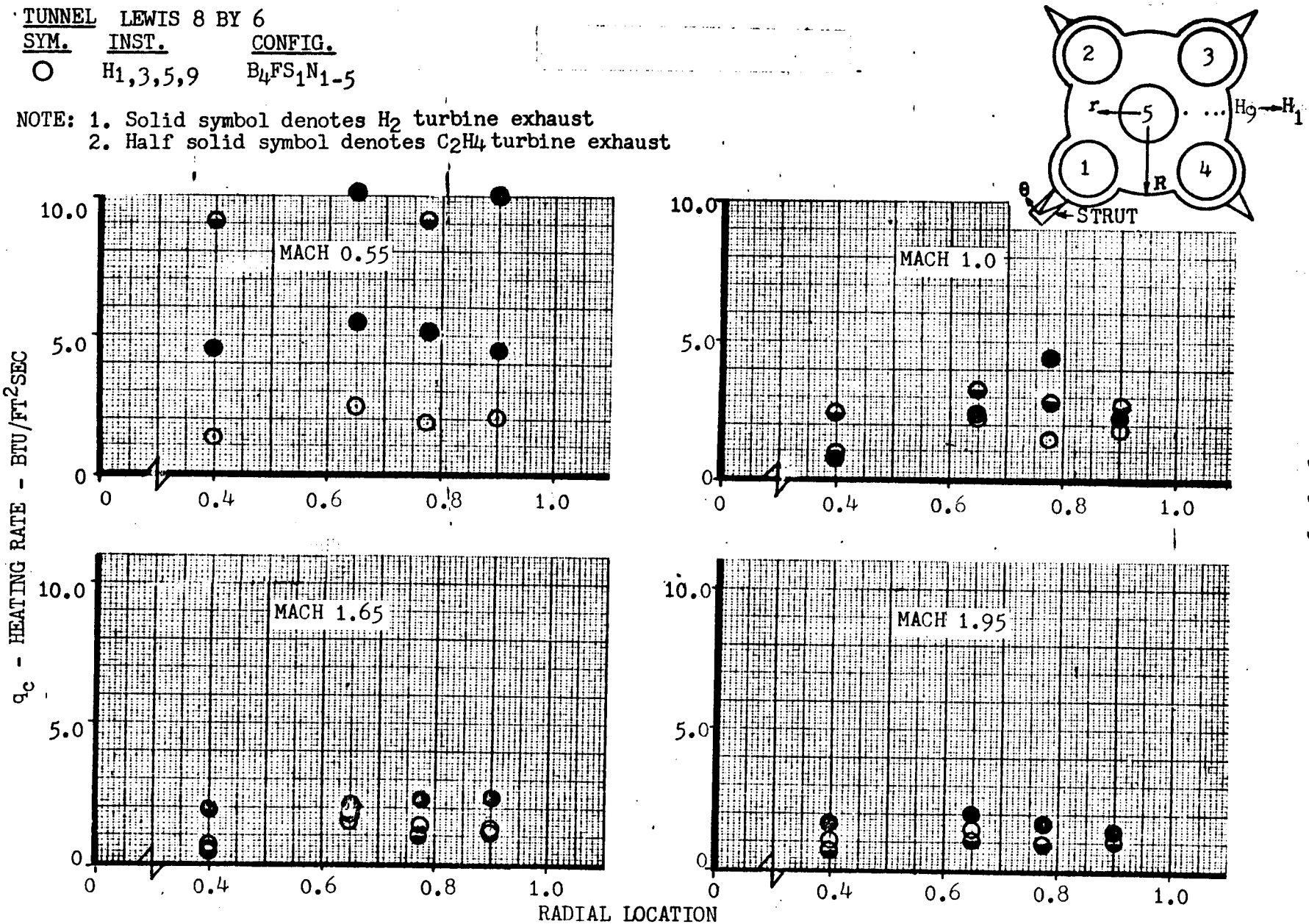

FIGURE 37 Base Heating - Convection

TUNNEL LEWIS 8 BY 6

SYM.	INST.	CONFIG.
○	$H_{1,3,5,7,9}$	$B_4FS_1N_{1-5}PL_1$
□	$H_{1,3,5,7,9}$	$B_4FS_1D_2N_{1-5}PL_1$
◇	$H_{1,3,5,7,9}$	$B_4FS_1D_1SC_2N_{1-5}PL_1$
△	$H_{1,3,5,7,9}$	$B_4FS_1D_2N_{G_7}N_{G_8}PL_1$

NOTE: 1. Solid symbol denotes turbine exhaust 2. Data averaged

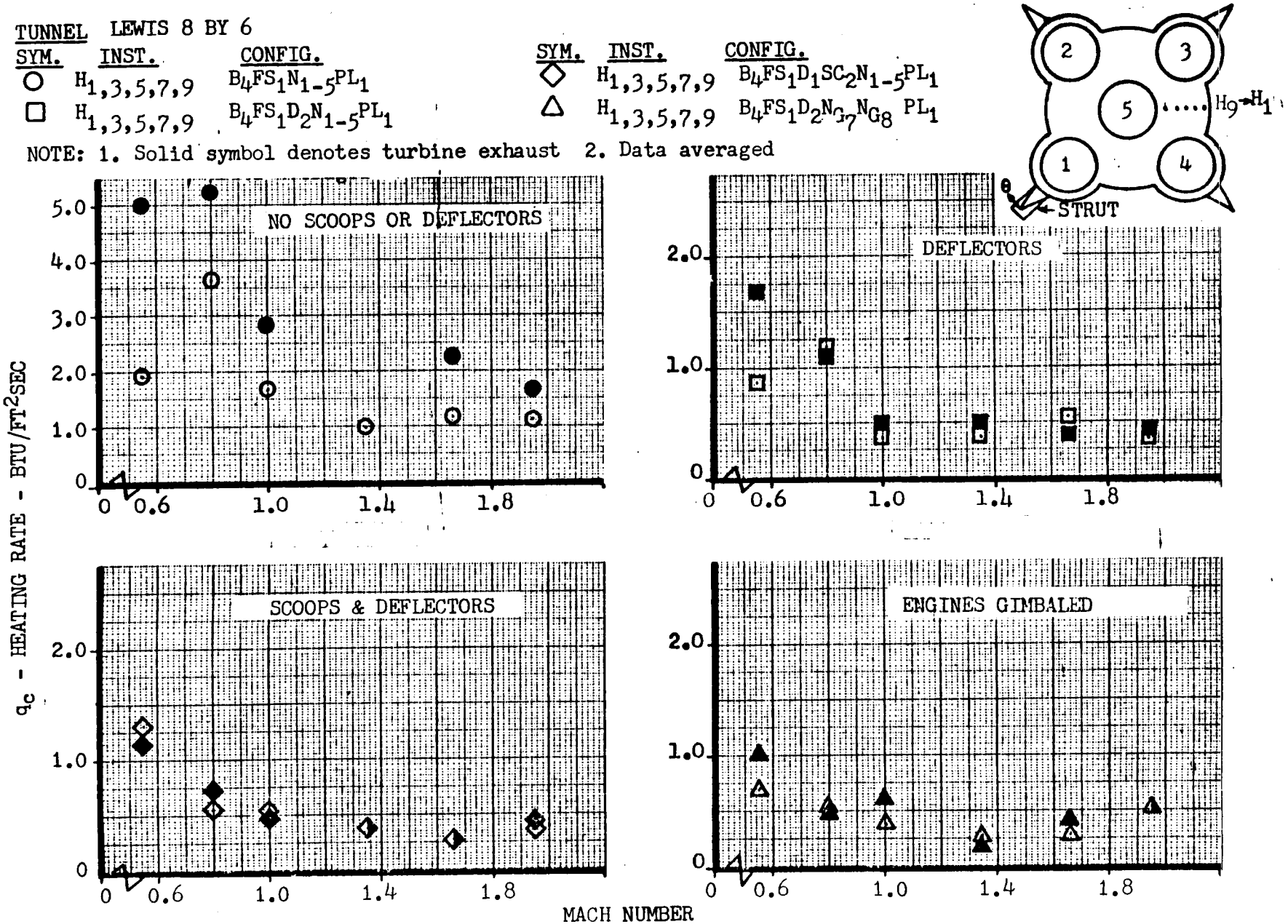

FIGURE 38 Base Heating - Convection

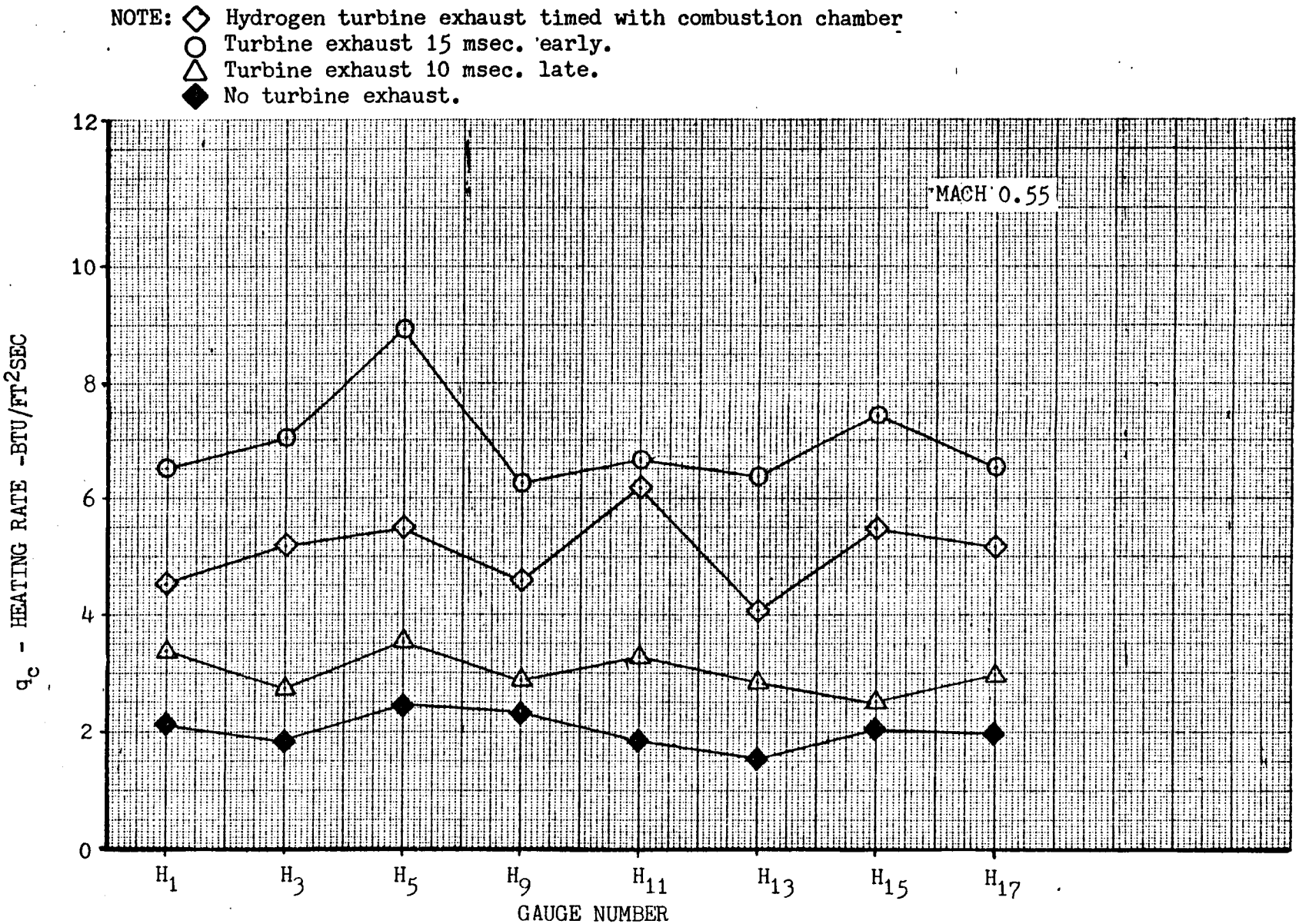

FIGURE 39 Turbine Exhaust Timing Effect

TUNNEL Lewis 8 by 6

SYM.	INST.	CONFIG.
○	$H_{1,3,5,7,9}$	$B_4FS_1N_{1-5}PL_1$
□	$H_{1,3,5,7,9}$	$B_4FS_1D_2N_7PL_1$
◇	$H_{1,3,5,7,9}$	$B_4FS_1D_1SC_2N_{1-5}PL_1$
△	$H_{1,3,5,7,9}$	$B_4FS_1D_2N_{1-5}PL_1$
◿	$H_{1,3,5,7,9}$	$B_4FS_1N_{1-5}PL_1$
◊	$H_{1,3,5,7,9}$	$B_4FS_1D_2N_{G_7}N_{G_8}PL_1$

NOTE: Data Averaged

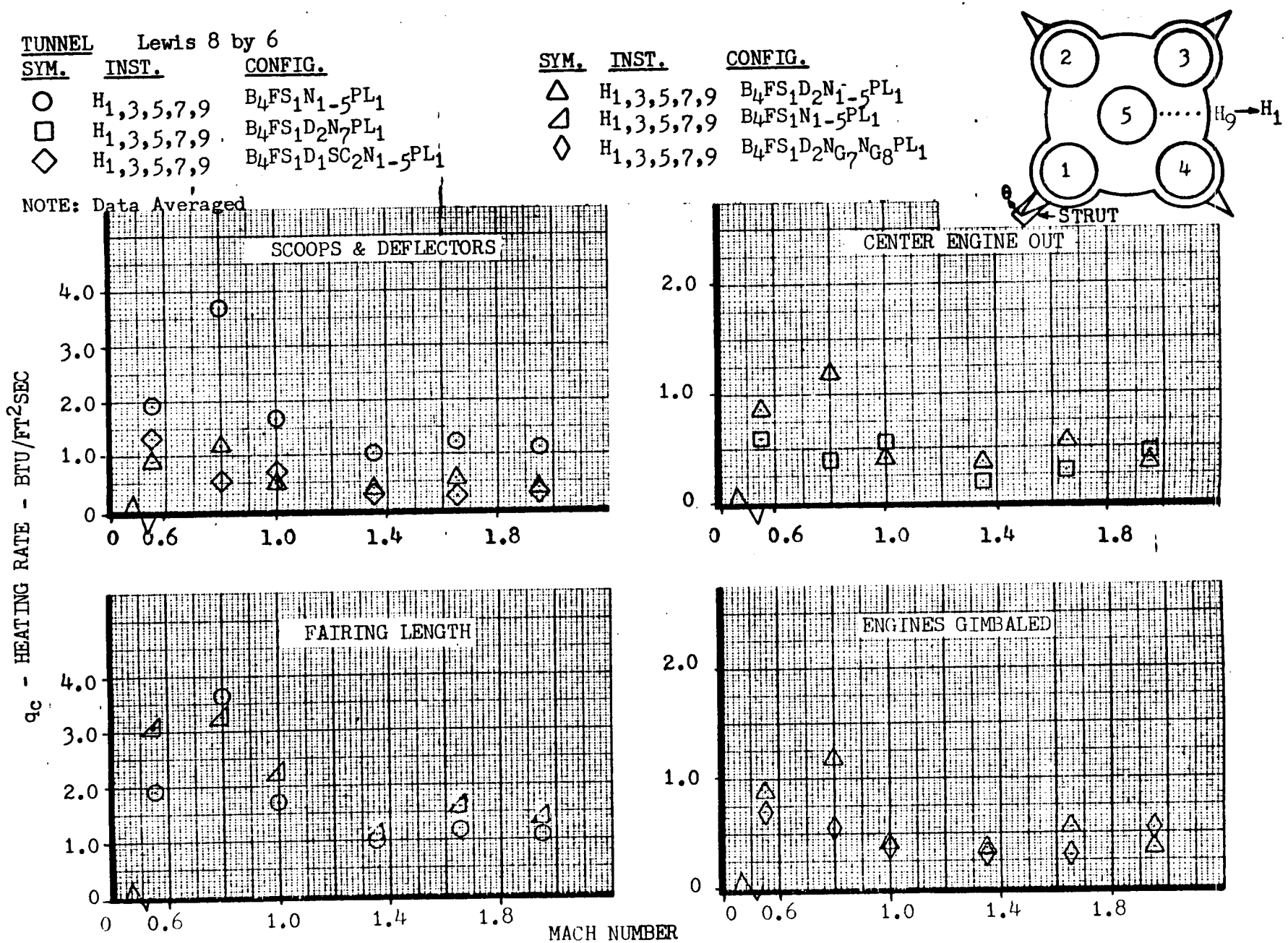

FIGURE 40 Base Heating - Convection

TUNNEL LEWIS 8 BY 6

SYM.	INST.	CONFIG.
□		$B_4FS_1D_2N_{1-5}PL_1$
◇		$B_4FS_1D_1SC_2N_{1-5}PL_1$

NOTE: Unflagged Symbol - M = 0.55
Flagged Right - M = 1.00
Flagged Left - M = 1.66

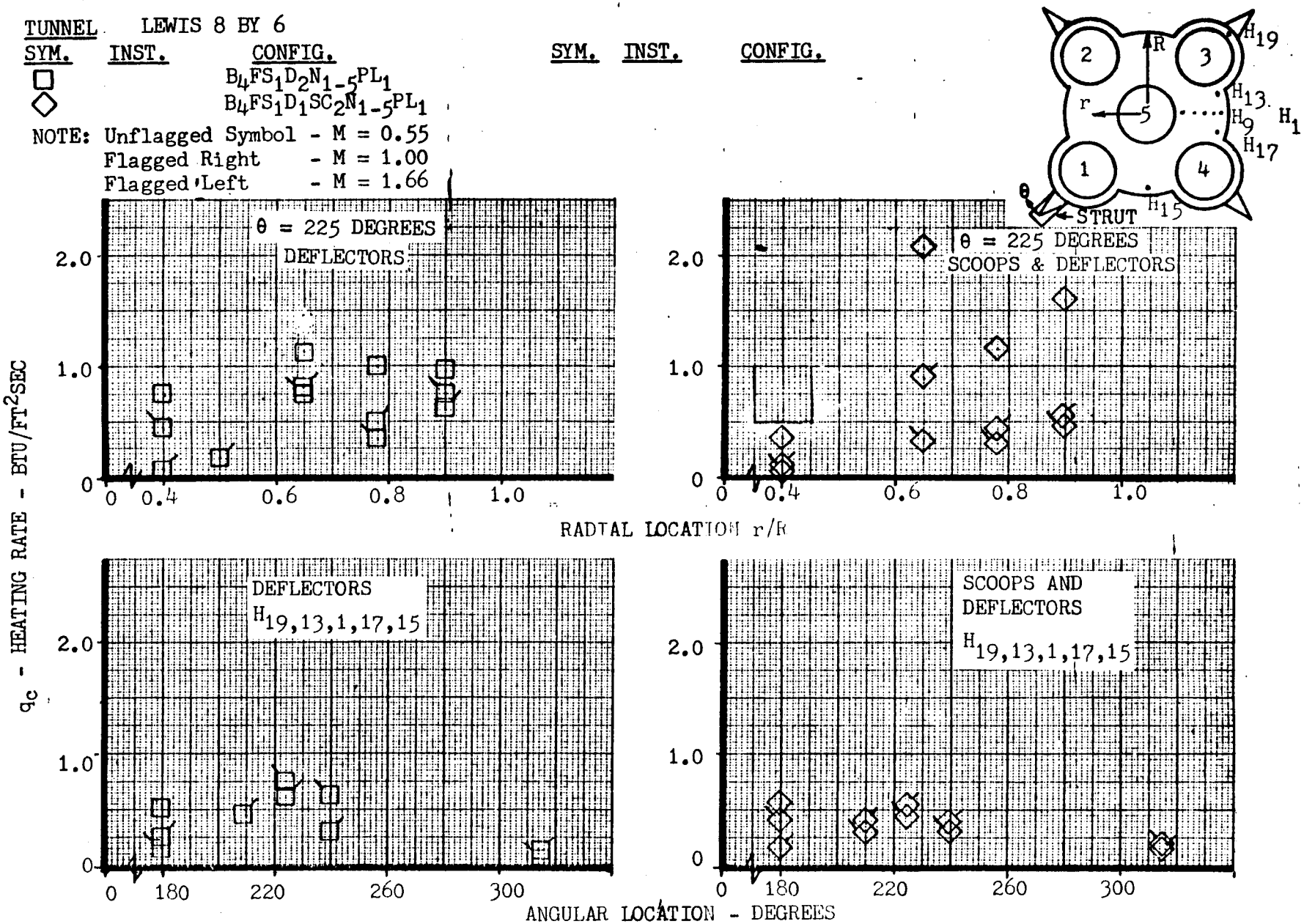

FIGURE 41 Base Heating - Convection

4.3.2 Convection to Fin and Engine Fairing

The locations of the two fin base gages (H_{63} and H_{65}) are shown in Figure 26, Section 1. The fin convective data is presented in Figure 42. These data show that the convective heating rate nearest the engine fairing (H_{63}) is essentially constant at 0.250 BTU/FT^{2}SEC and unaffected by turbine exhaust. The heating rate on the fin further outboard (H_{65}) is higher and shows a decrease with altitude. It is also unaffected by turbine exhaust. No data is available on the engine fairing due to instrumentation failure.

4.3.3 Convection to Engine Nozzles (External)

Convective heating data on the outside of the center engine nozzle are shown in Figure 43. Gages (H_{21} and H_{23}) are located near the lip of the nozzle (see Figure 22, Volume 1); gage H_{21} faces outboard between 3 and 4, gage 23 faces engine 3. Without turbine exhaust, the heating averages 0.3 BTU/FT^{2}SEC through the test Mach range. With turbine exhaust, a considerable heating increase is noted for Mach 0.5 through 1.0

Both center and outboard engine out cases were considered by means of a plugged nozzle. Instruments H_{53} and H_{55} are located on the nozzle lip. facing aft between engines 2 and 3 and engines 1 and 4 respectively (see Figure 17, Volume 1) when the center engine is inoperative. For this case the heating data are shown in Figures 44 and compared to the average convection heating rate on the base. Between Mach numbers 0.55 and 1.0 the nozzle lip heating rate is an order of magnitude greater than the base convection heating rate. Turbine exhaust does not appear to affect the heating rate. The data from both gages are in reasonable agreement except at Mach number 1.0

Gage H_{55} ~~is on~~ the outboard side of the nozzle wall away from other engines. The other outboard engines gimbal away from the inoperative engine (see Figure 5, Volume 1). Data for this configuration shown on Figure 45 indicates lower heating rates than occurred with center engine out at all Mach numbers. Total heating on the lip is essentially the same as convection heating on the base above Mach 1.0. Turbine exhaust increased the total heating rates from Mach 0.55 through 1.0.

4.3.4 Convection to Engine Nozzle (Engine Out)

Data were obtained on the inside surface of an instrumented and plugged nozzle to determine heating effects on an inoperative engine. Gages located per Figure 24, Volume 1 and as described in paragraph 4.2.4 are used to obtain the convection heating rates shown in Figure 46.

TUNNEL LEWIS 8 BY 6

SYM.	**INST.**	**CONFIG.**
○	H_{63}	$B_4FS_1D_1SC_2N_{1-5}PL_2$
△	H_{65}	$B_4FS_1D_1SC_2N_{1-5}PL_2$

NOTE: Solid symbol denotes turbine exhaust

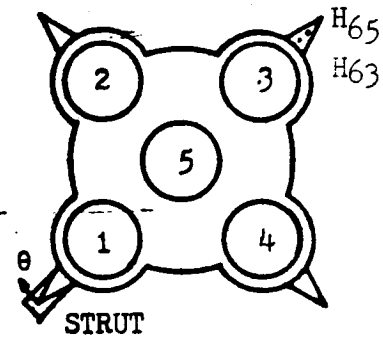

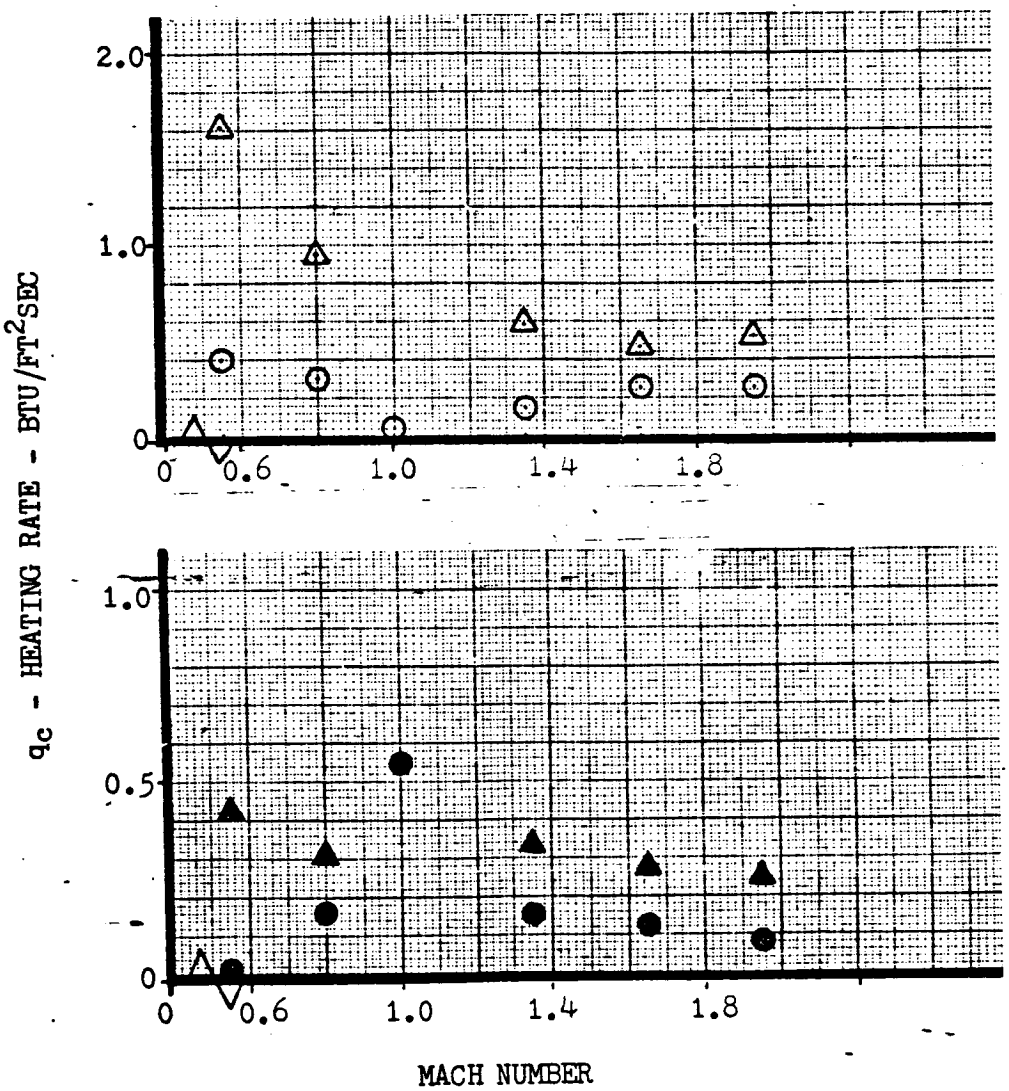

FIGURE 42 Fin Heating - Convection

TUNNEL LEWIS 8 BY 6

SYM.	INST.	CONFIG.
○	H_{23}	$B_4FS_1D_1SC_2N_{1-5}PL_1$
△	H_{21}	$B_4FS_1D_1SC_2N_{1-5}PL_1$

NOTE: Solid symbol denotes turbine exhaust

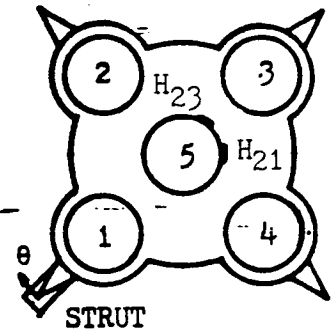

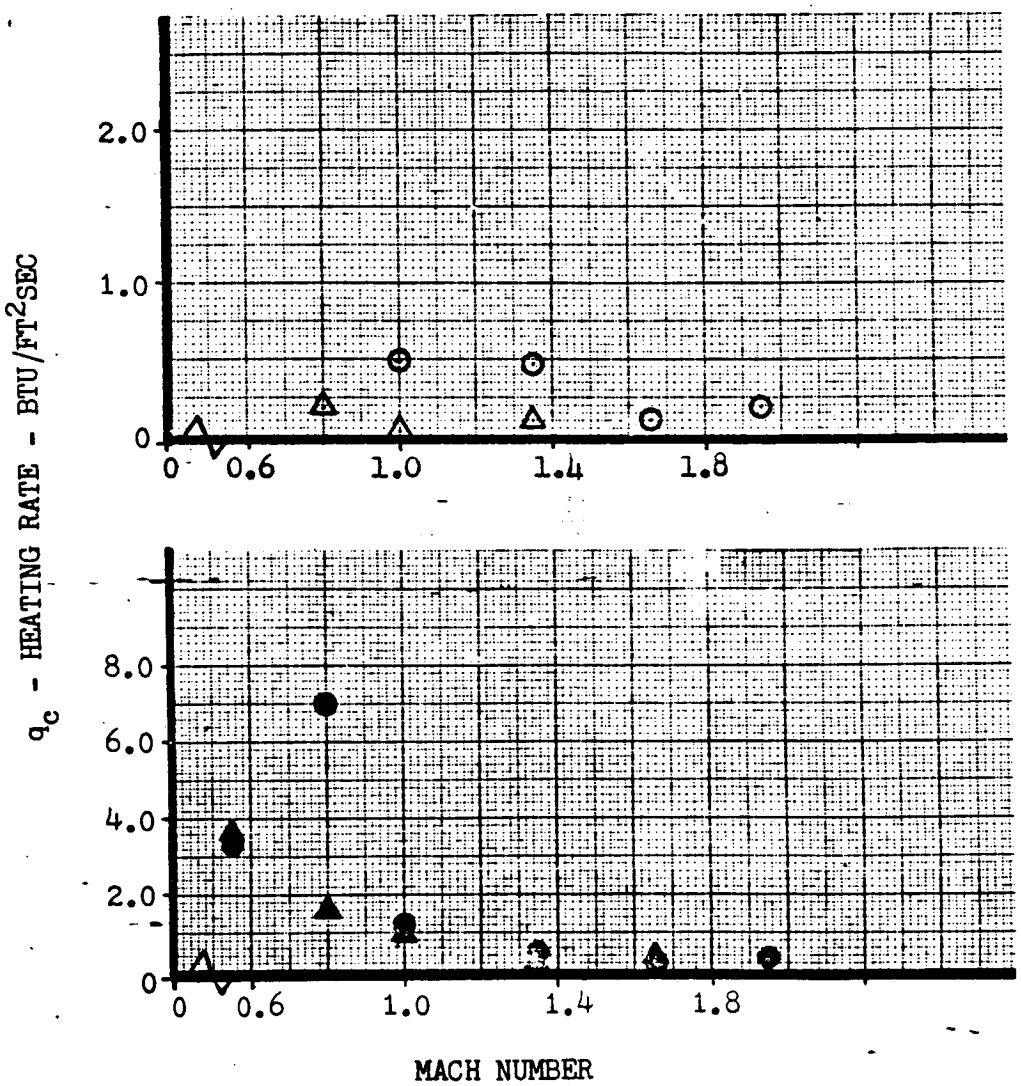

FIGURE 43 Engine Heating-Convection (External)

TUNNEL LEWIS 8 BY 6

SYM.	INST.	CONFIG.
○	H_{53}	$B_4FS_1D_2N_7PL_1$
△	H_{55}	$B_4FS_1D_2N_7PL_1$
◇	Average base plate value	

NOTE: Solid symbol denotes turbine exhaust

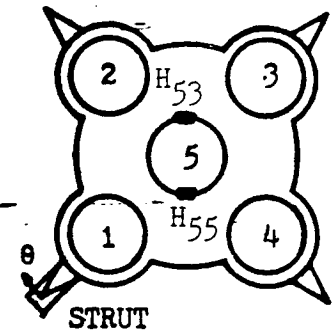

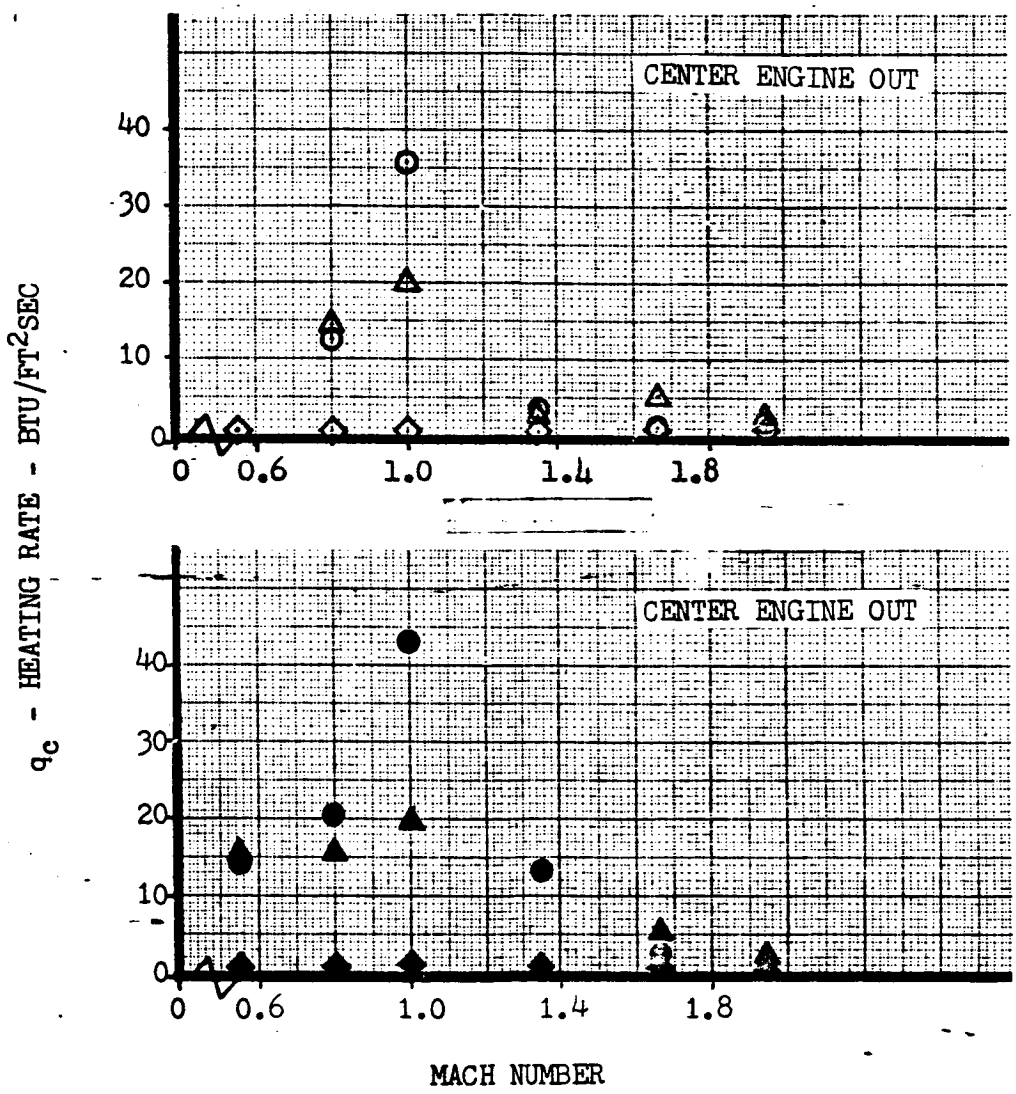

FIGURE 44 Engine Heating - Convection (Lip)

TUNNEL LEWIS 8 BY 6

SYM.	INST.	CONFIG.
○	H_{53}	$B_4FS_1D_2N_{10}N_{G_{11}}N_{G_{12}}N_{G_{13}}PL_2$
△	H_{55}	$B_4FS_1D_2N_{10}N_{G_{11}}N_{G_{12}}N_{G_{13}}PL_2$
◇	Average base plate value	

NOTE: Solid symbol denotes turbine exhaust

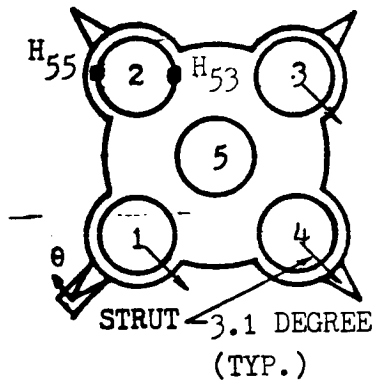

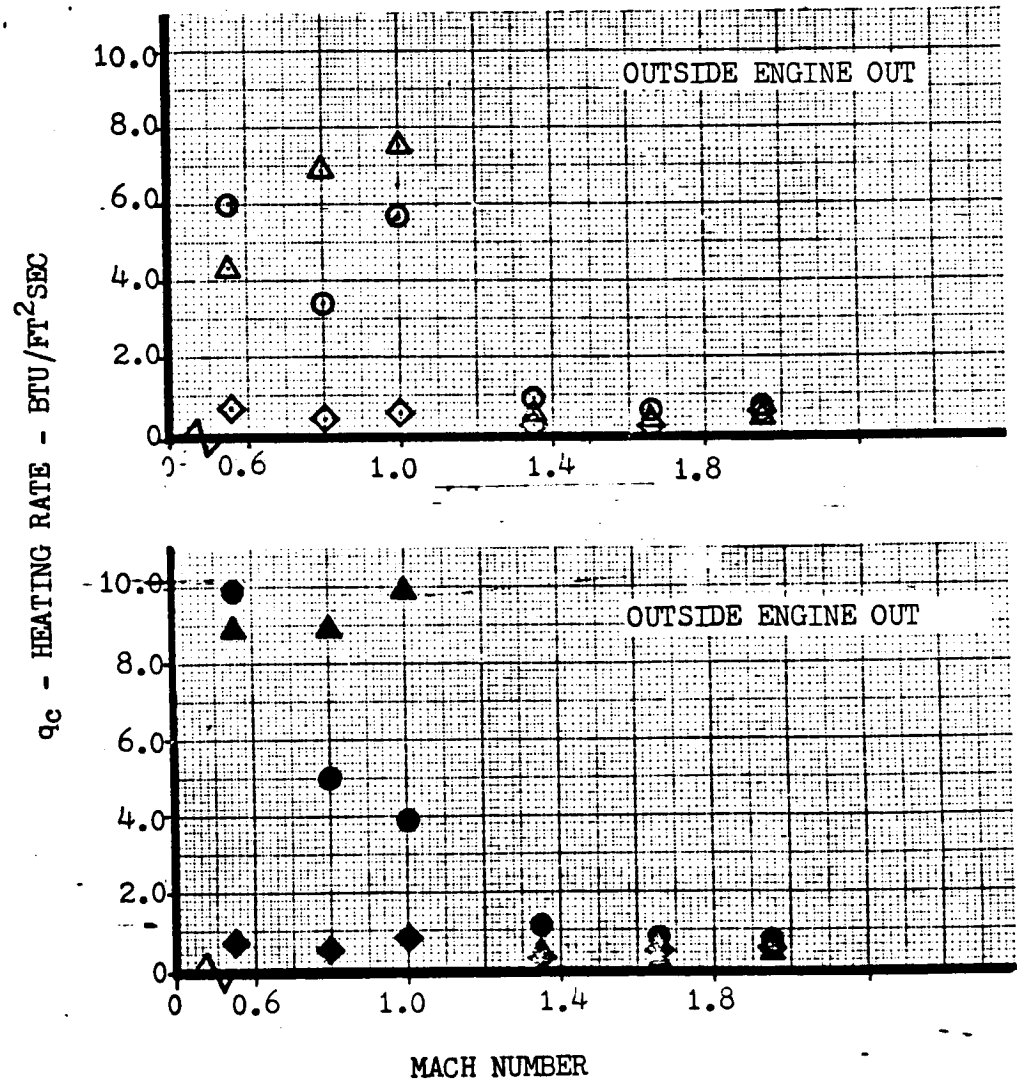

FIGURE 45 Engine Heating - Convection (Lip)

TUNNEL Lewis 8 by 6

SYM.	INST.	CONFIG.
○	H_{43}	$B_4FS_1D_1N_7PL_1$
□	H_{47}	$B_4FS_1D_1N_7PL_1$
◊	H_{49}	$B_4FS_1D_1N_7PL_1$
⌂	H_{51}	$B_4FS_1D_1N_7PL_1$

SYM.	INST.	CONFIG.
⬡	H_{43}	$B_4FS_1D_2N_{10}N_{G_{11}}N_{G_{12}}N_{G_{13}}PL_2$
⬡	H_{51}	$B_4FS_1D_2N_{10}N_{G_{11}}N_{G_{12}}N_{G_{13}}PL_2$
◇	H_{47}	$B_4FS_1D_2N_{10}N_{G_{11}}N_{G_{12}}N_{G_{13}}PL_2$
△	H_{49}	$B_4FS_1D_2N_{10}N_{G_{11}}N_{G_{12}}N_{G_{13}}PL_2$

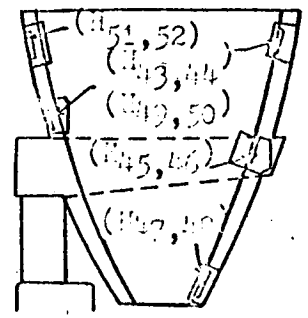

NOTE: Solid Symbol denotes turbine exhaust

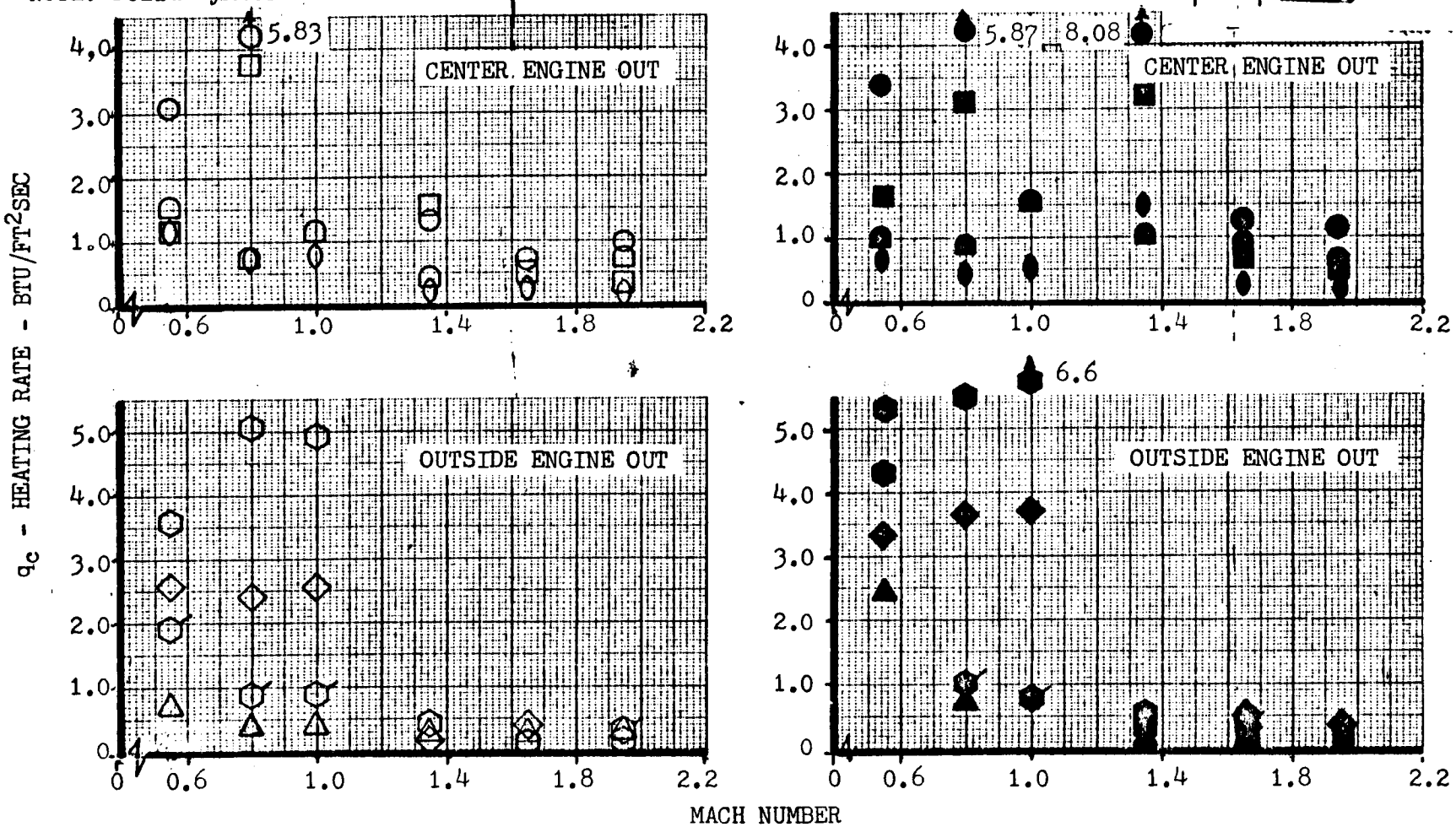

FIGURE 46 Engine Heating - Convection (Engine Out - Internal)

4.3.4 (Continued)

Two configurations are shown: one with center engine out and the outside engines firing straight away; one with engine number 2 out and the other three outside engines firing away from the inoperative engine as shown in Figure 5, Volume 1. The highest convection rates occur between Mach numbers 0.55 and 1.0 on the inside of the inoperative engine for both configurations and fall off drastically for Mach number 1.35 thru 1.95. No explanation for the rapid reduction in convective heating at the higher Mach numbers is evident. The same trends are noted at the nozzle lip in Figures 44 and 45. Comparison between Figures 46 and 43 show that through Mach number 1.0 convection heating to the inside of an inoperative engine nozzle will be significantly greater than heating to the outside of the nozzle with all engines firing.

A point of interest should be noted with the engine-out data. The high measured rates substantiate the expected high model plume gas temperatures. However, the low measured base plate convective rates and the heated base plate data (Section 4.3.1) indicate a low base gas recovery temperature. This suggests that very little of the entrained hot gas is reaching the base plate.

4.3.5 HEATED BASE PLATE

A special base plate was fabricated with internal electrical coils so that convective heating rates could be obtained at various wall temperatures. The equation and sketch below illustrate the procedure used to calculate recovery temperature and heat transfer coefficients:

$$q = h_c (T_r - T_w)$$

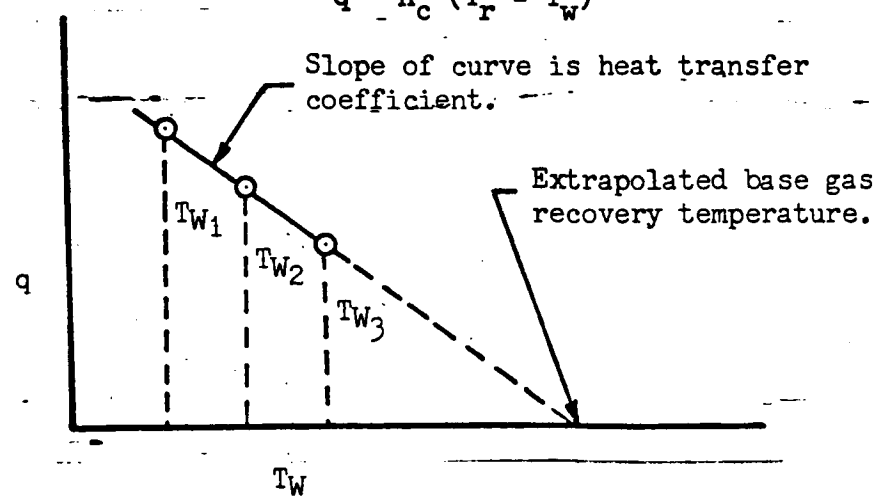

Heating rate data was obtained at three wall temperatures; 350°F, 200°F, and the cold base temperature of 130°F. The heating rates are plotted as a function of wall temperature and the line through the data is then

4.3.5 (Continued)

extrapolated to the zero heating rate point which is the adiabatic wall temperature or assumed base gas recovery temperature. The slope of the curve corresponds to the heat transfer coefficient as is evident from the equation.

Typical test results are shown in Figures 47 through 52. The base recovery temperature ranged from 400°F to 600°F for all configurations tested. The heat transfer coefficients were in the range of 0.008 to 0.016 BTU/FT^{2}SEC°R. Data from this portion of the test are of low quality, containing a large amount of scatter. Some of the data even indicated a physical impossibility, an increase in heating rate with increase in wall temperature. (See Figure 50). However, the results are generally substantiated by the convection heating rate data.

4.3.6 Comparison with Convective Theory

Theoretical calculations in Appendix B have indicated that no hot exhaust gases will recirculate below an altitude of 40,000 ft (maximum Lewis 8 by 6 tunnel altitude is 35,200 ft). The theory however does not consider external air impinging on the nozzle exhaust which would occur at lower altitudes and could cause some recirculation.

A hot base plate, previously described, was used to measure the base gas recovery temperature shown in Figure 53. The theoretical calculations of the base gas temperature (tunnel total temperature) are compared with the data in Figure 53 and found to be significantly below the experimental data. This comparison again indicates recirculation at lower altitude, possibly due to the above mentioned reason. Convective heating rates were also measured on the base at low altitude, confirming this conclusion.

Shown in Figure 54 are the comparisons of the Lewis 8 by 6 convective data with the Cornell 8 by 8 test data. The rising convective heating data trend at the lower Mach numbers was not anticipated and did not occur in the CAL 8 by 8 foot tunnel tests.

4.4 BASE PRESSURE

Pressure data are obtained on two base plates during the test. The PL_1 base plate (Figure 19, Volume 1) contains seven pressure taps and a large number of heating gages. Base plate PL_2 (Figure 20, Volume 1) which has 16 pressure tap locations was used to obtain a detailed pressure distribution over the model base for comparison with the cold flow model data which are to be obtained in the same facility. These data also show the pressure in the quadrant between gimballed engines.

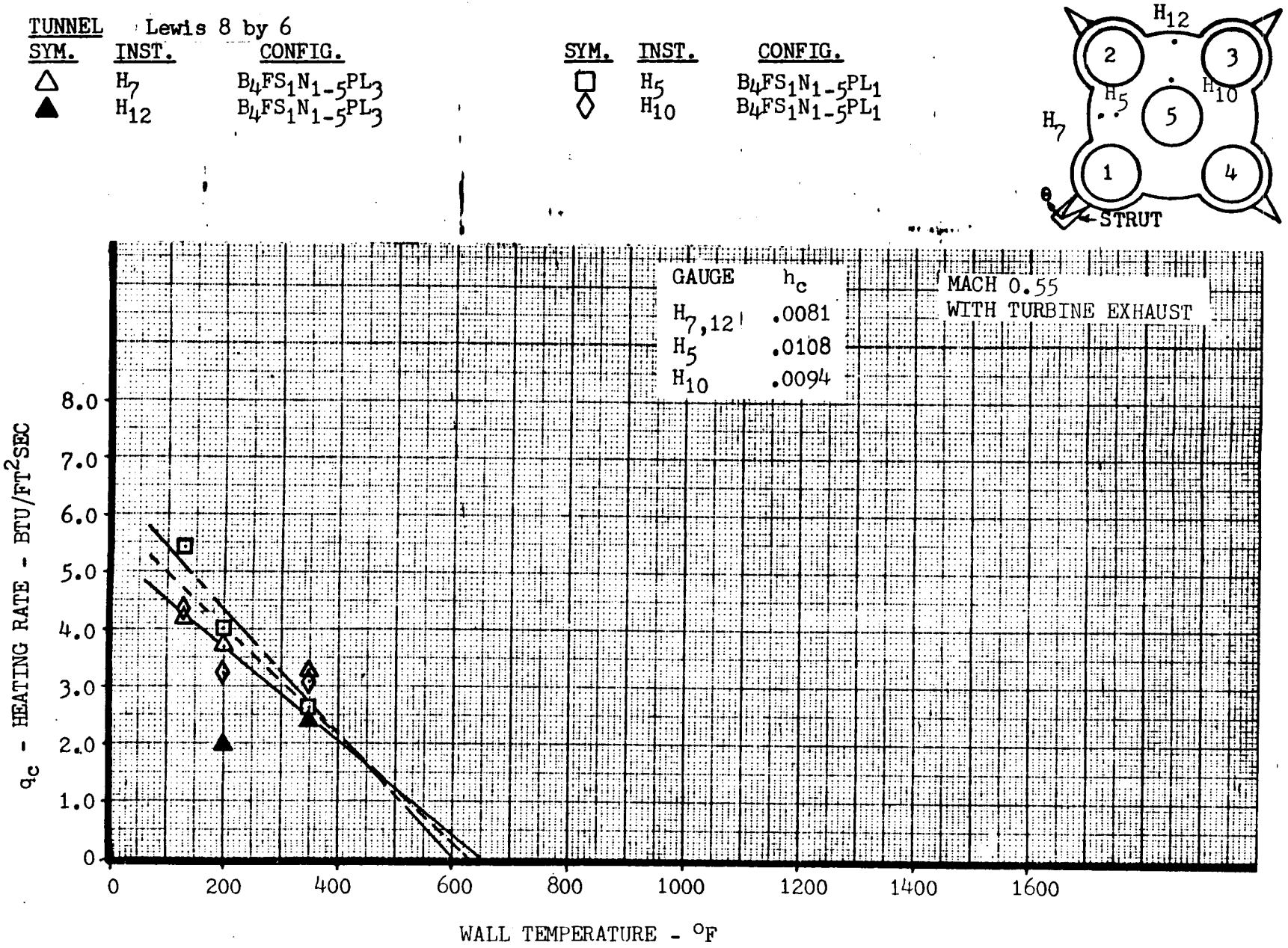

FIGURE 47 Base Gas Temperature

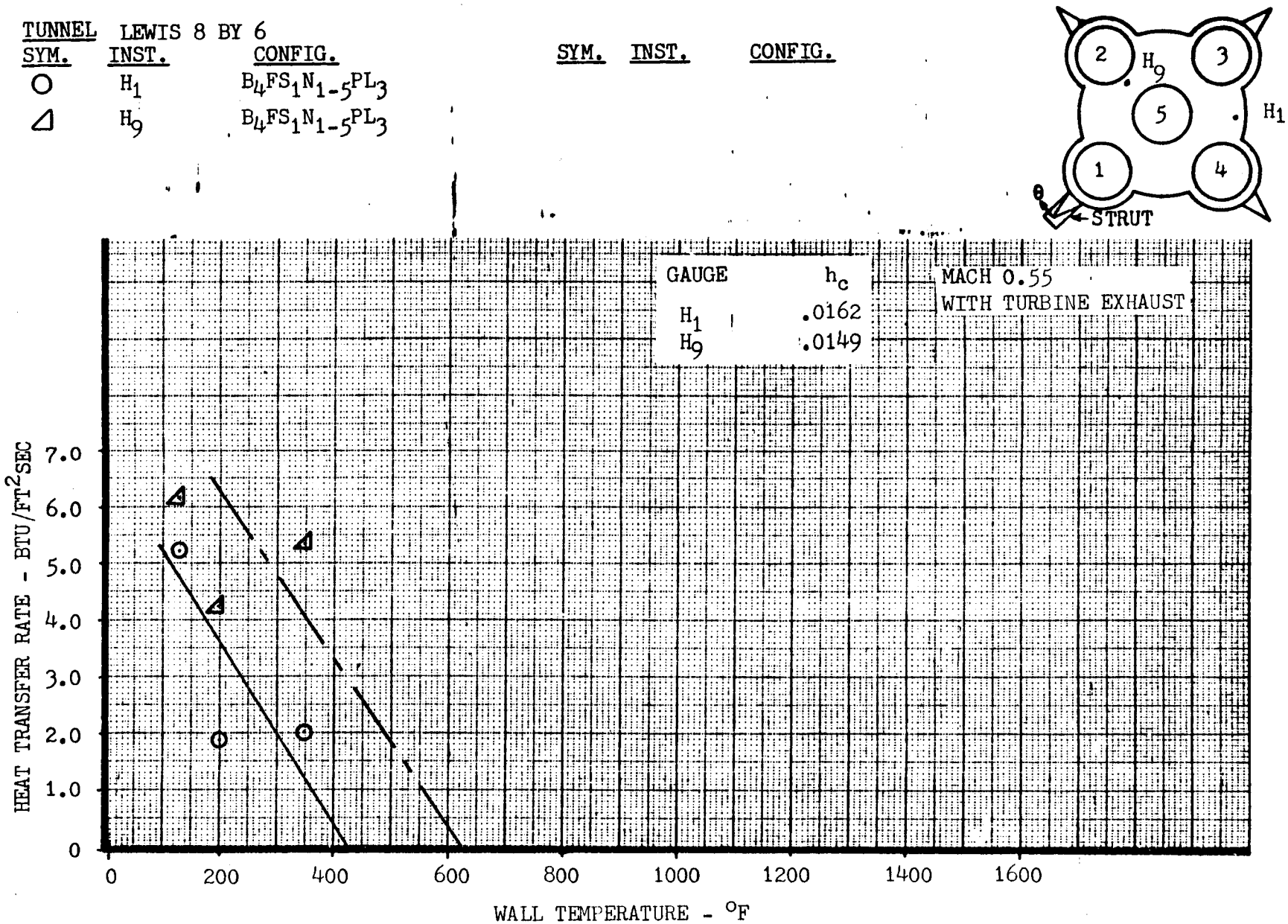

FIGURE 48 Base Gas Temperature

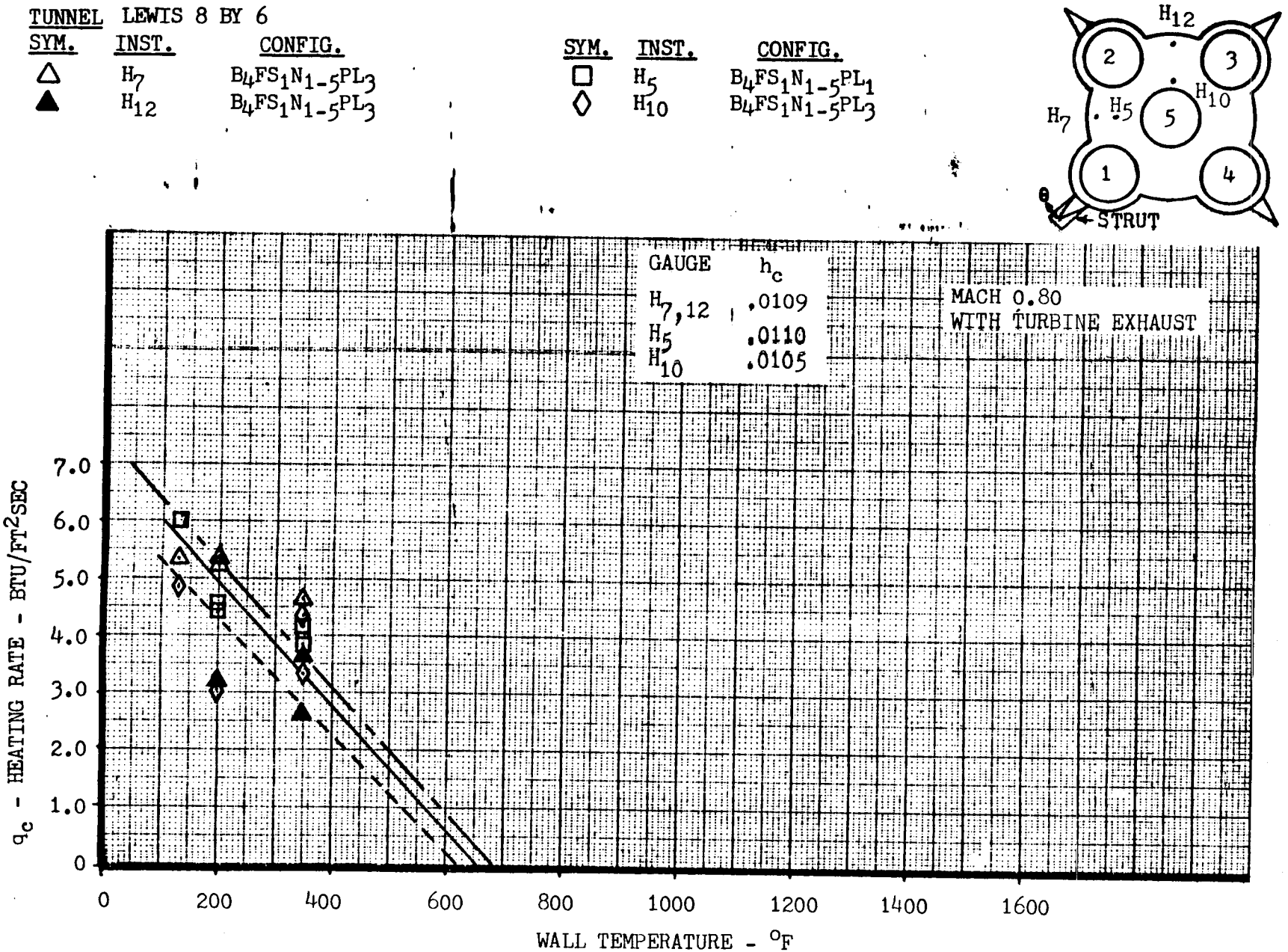

FIGURE 49 Base Gas Temperature

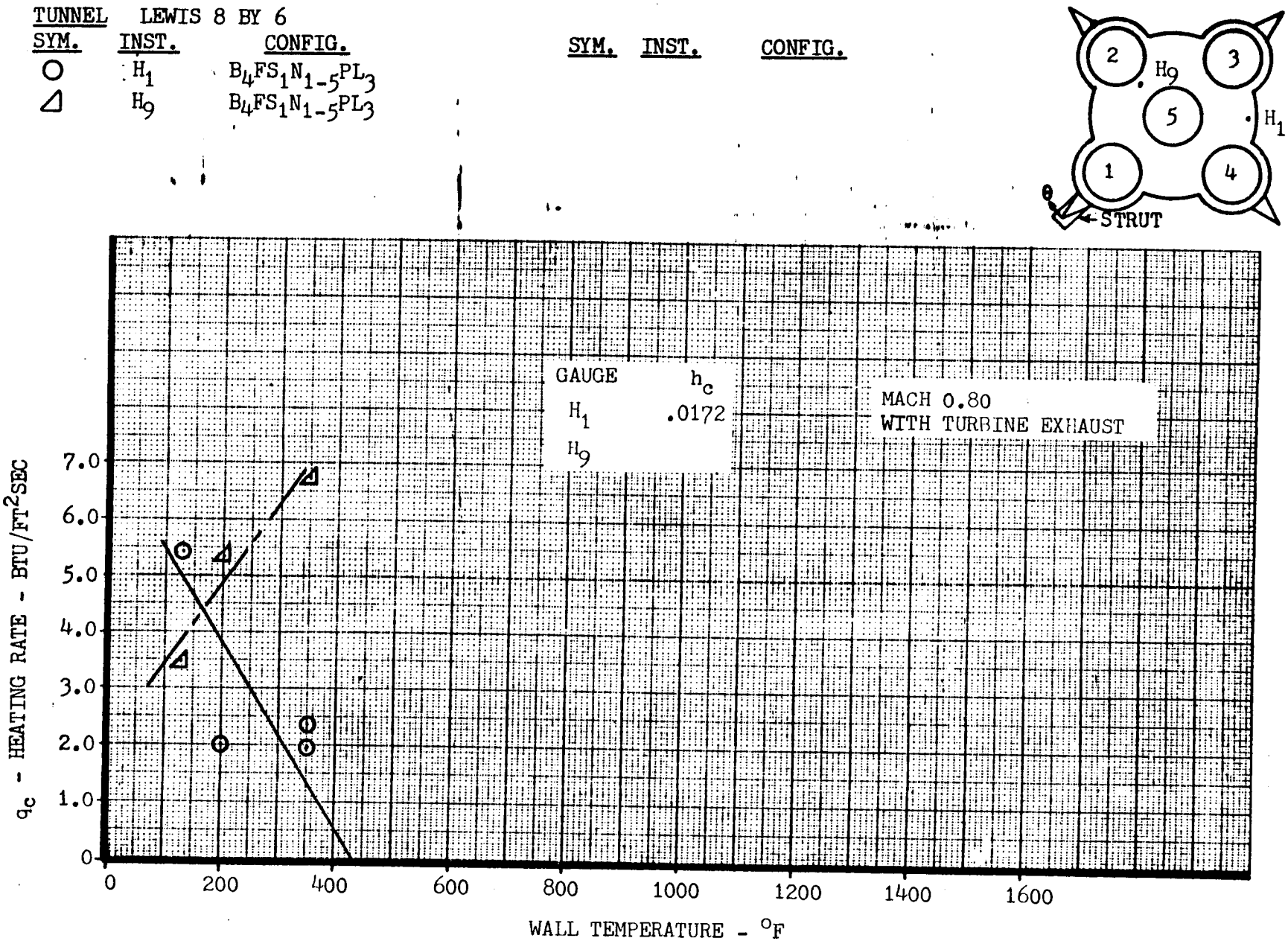

FIGURE 50 Base Gas Temperature

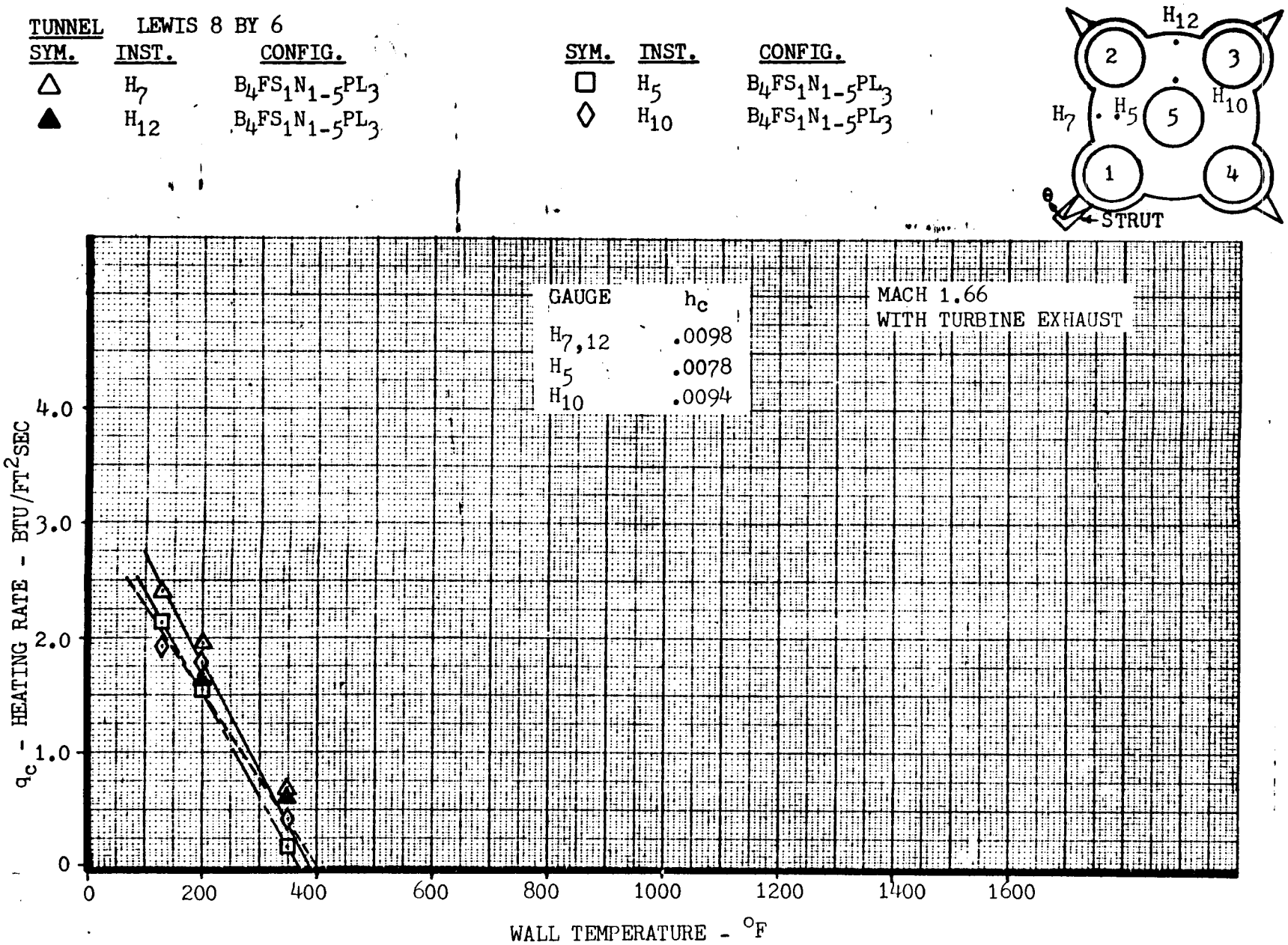

FIGURE 51 Base Gas Temperature

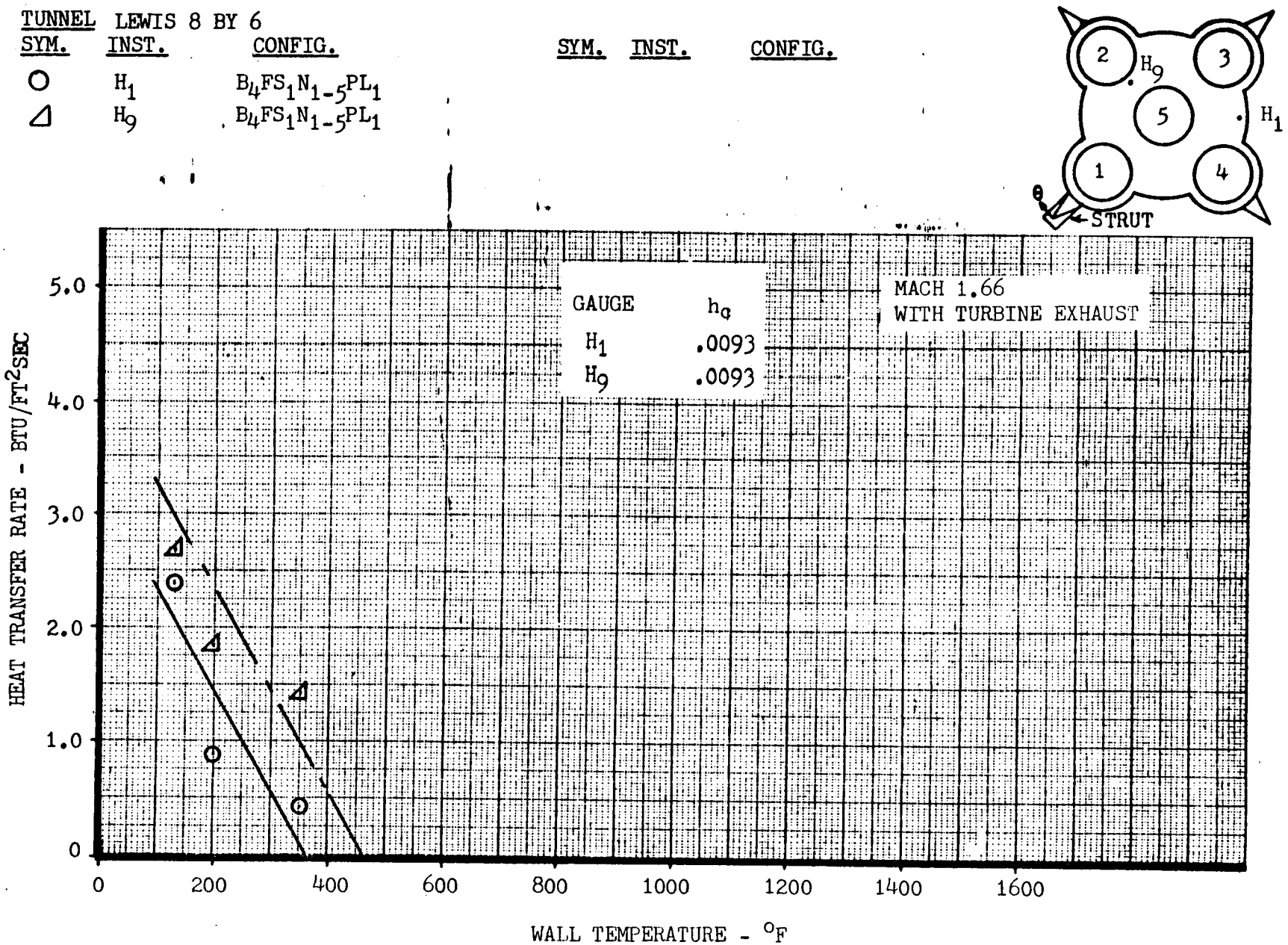

FIGURE 52 Base Gas Temperature

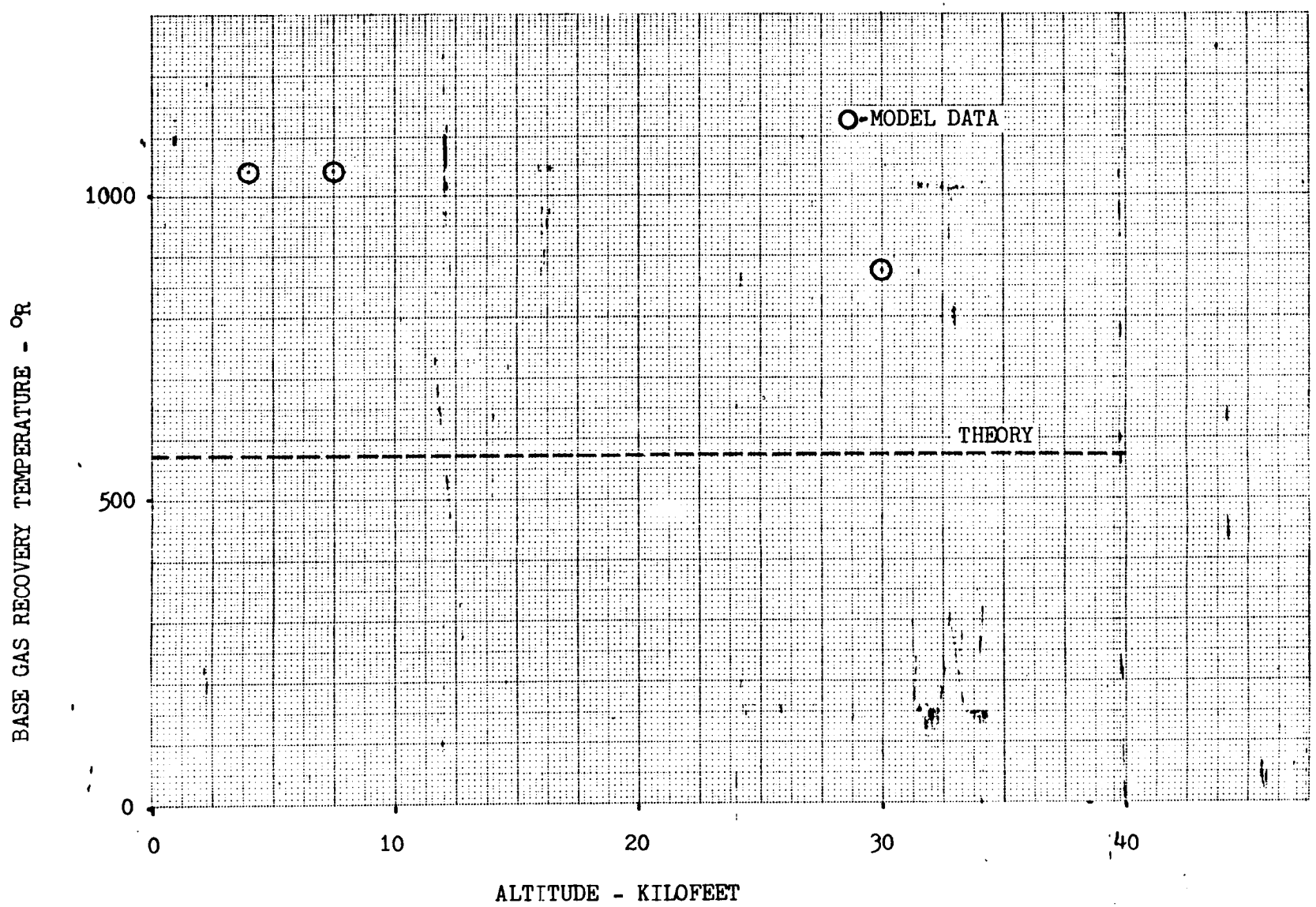

FIGURE 53 Base Gas Temperature - Comparison with Theory - Lewis 8 by 6 Tunnel

TUNNEL LEWIS 8 BY 6

SYM.	INST.	CONFIG.
□	$H_{1,3,5,7,9}$	$B_1FS_1N_{1-5}PL_1$
◇	$H_{1,3,5,7,9}$	$B_1FS_1D_1SC_2N_{1-5}PL_1$

NOTE: 1. Solid symbol denotes turbine exhaust
2. Flagged symbol is data from CAL 8 by 8 tunnel test

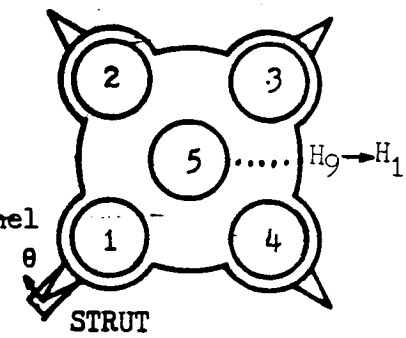

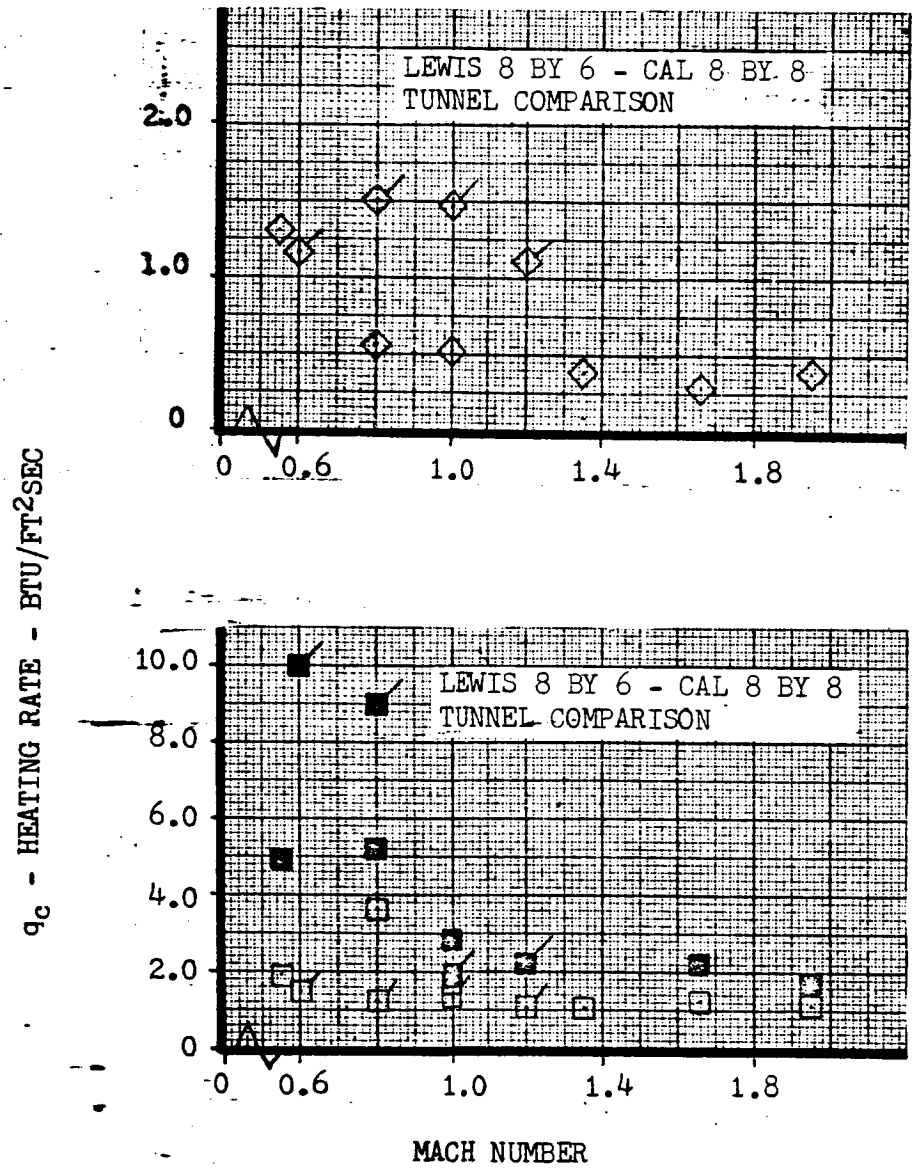

FIGURE 54 Base Heating - Convection Heating Comparison

4.4.1 Configuration Effects on Base Pressure

Typical radial pressure distribution across the base is shown for two configurations in Figure 55. In general the pressure is constant for Mach numbers 1.0 and less, which agrees with the data obtained in the CAL 8 by 8 foot tunnel (see Figure 17). Engine off pressures are compared to engine on pressures in Figures 56 and 57. In general these data agree with the CAL 8 by 8 tunnel data with the exception of the magnitude of the pressure decrease near Mach 1.0. The excessive drop is believed due to the tunnel trajectory density mismatch. The engine off data indicates considerable pressure fluctuation on the base which is probably caused by reflected shocks from the tunnel wall.

The effects of adding hydrogen turbine exhaust is negligible (Figure 58). Configuration comparisons without turbine exhaust are shown in Figure 59. Addition of deflectors and scoops increases the base pressure. Reducing the engine fairing length with deflectors has no apparent effect on base pressure with engines on. There is a pressure increase with the short fairing with engines off. Base pressure is reduced when the center engine is inoperative.

Detailed heat shield pressure distributions obtained from base plate PL_2 are shown in Figures 60 through 74. The base pressure is essentially constant at each Mach number, with a mean distribution from the average pressure of only 0.22 psia. The mean distribution is the same magnitude for all Mach numbers, giving a percentage spread of 1.5 to 6.5 percent.

Two exceptions to the constant pressure are noted. At Mach 0.55 and 0.80, a slightly higher pressure is recorded in close to the center engine (P_{10} and P_{19}), indicating gas flow inboard slowing as it approaches the center engine. (Figures 60, 61, 65, 71 and 74).

A second exception is noted in the engine fairing area for the configuration with scoops on - $B_4FS_1D_1SC_2N_{1-5}$. At Mach 1.66 and 1.95, the pressure in this area is higher than the rest of the base (see Figures 69 and 70).

Figures 71 through 74 show that the two gimbal patterns slightly increase the base pressure in the quadrants towards which the engines were gimballed. However, the effect is negligible and indicates that gas recirculation due to plume-plume impingement is not affecting the base in this test range. This result confirms the similar conclusion from the convection heating data.

4.4.2 Correlation with Theory and Previous Data

The engines off base pressure data are shown in Figure 75 and are compared with theoretical calculations based on a blunt based cylinder. It is evident that early in flight the theory is above the experimental data with or without scoops. At the higher altitudes the scoop configuration base pressure becomes larger than the theoretical calculations and the no scoop configuration data approaches the theory.

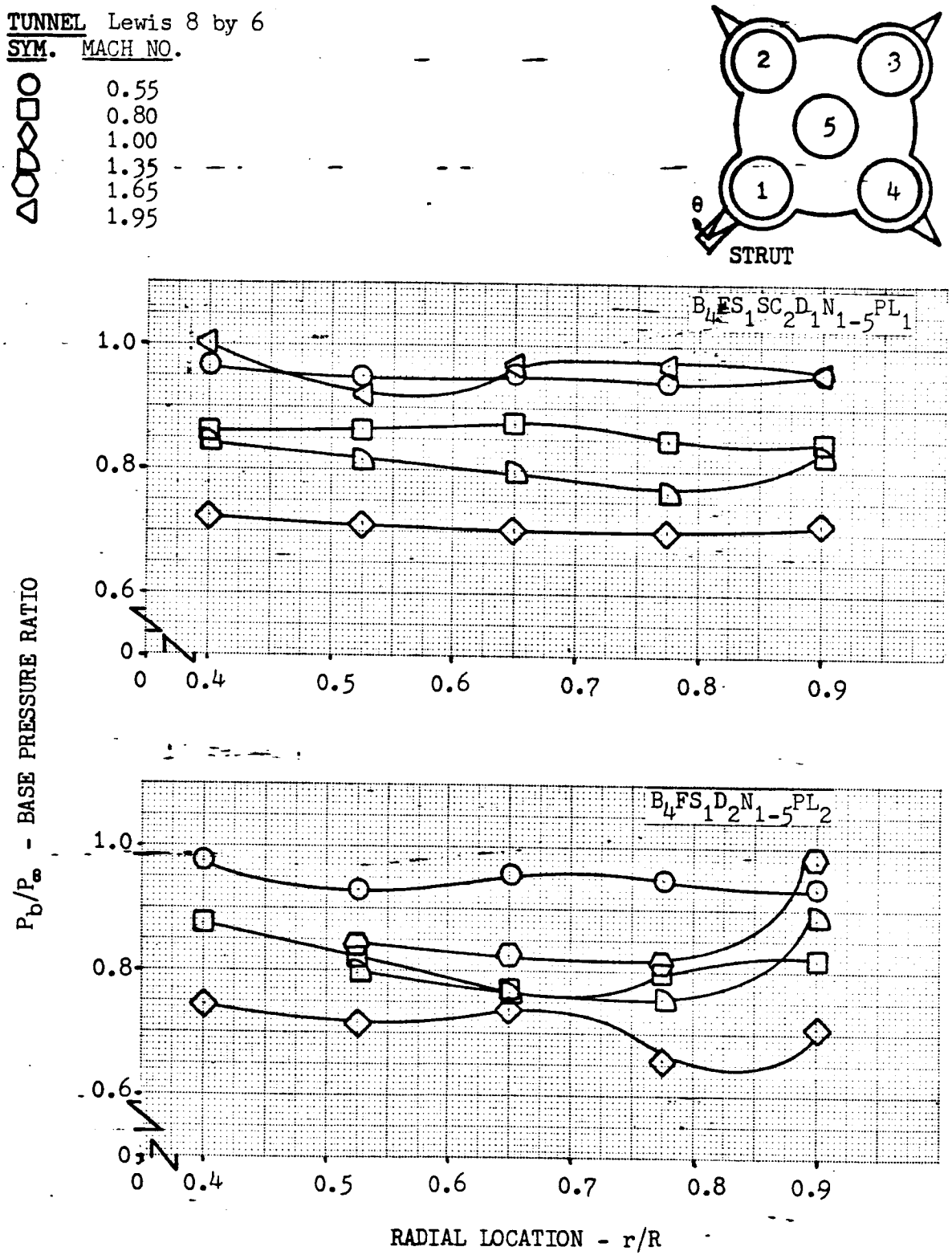

FIGURE 55 Base Pressure

TUNNEL Lewis 8 by 6

SYM.	INST.	CONFIG.
○	$P_{1,3,4,6,7}$	$B_4FS_1N_{1-5}PL_1$
◇	$P_{1,3,4,6,7}$	$B_4FS_4N_{1-5}PL_1$
△	$P_{1,3,4,6,7}$	$B_4FS_1D_2N_{1-5}PL_1$
◊	$P_{1,3,4,6,7}$	$B_4FS_1D_1SC_2N_{1-5}PL_1$
0	$P_{1,3,4,6,7}$	$B_4FS_4D_2N_{1-5}PL_1$

NOTE: 1. Flag up denotes Mach 0.57
2. Flag left denotes Mach 0.80
3. Flag right denotes Mach 1.01
4. Flag down denotes Mach 1.36
5. No flag denotes Mach 1.97

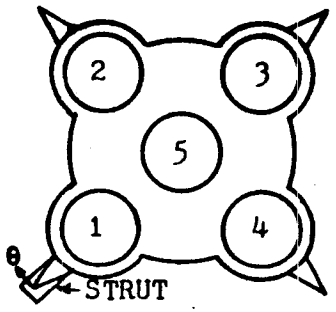

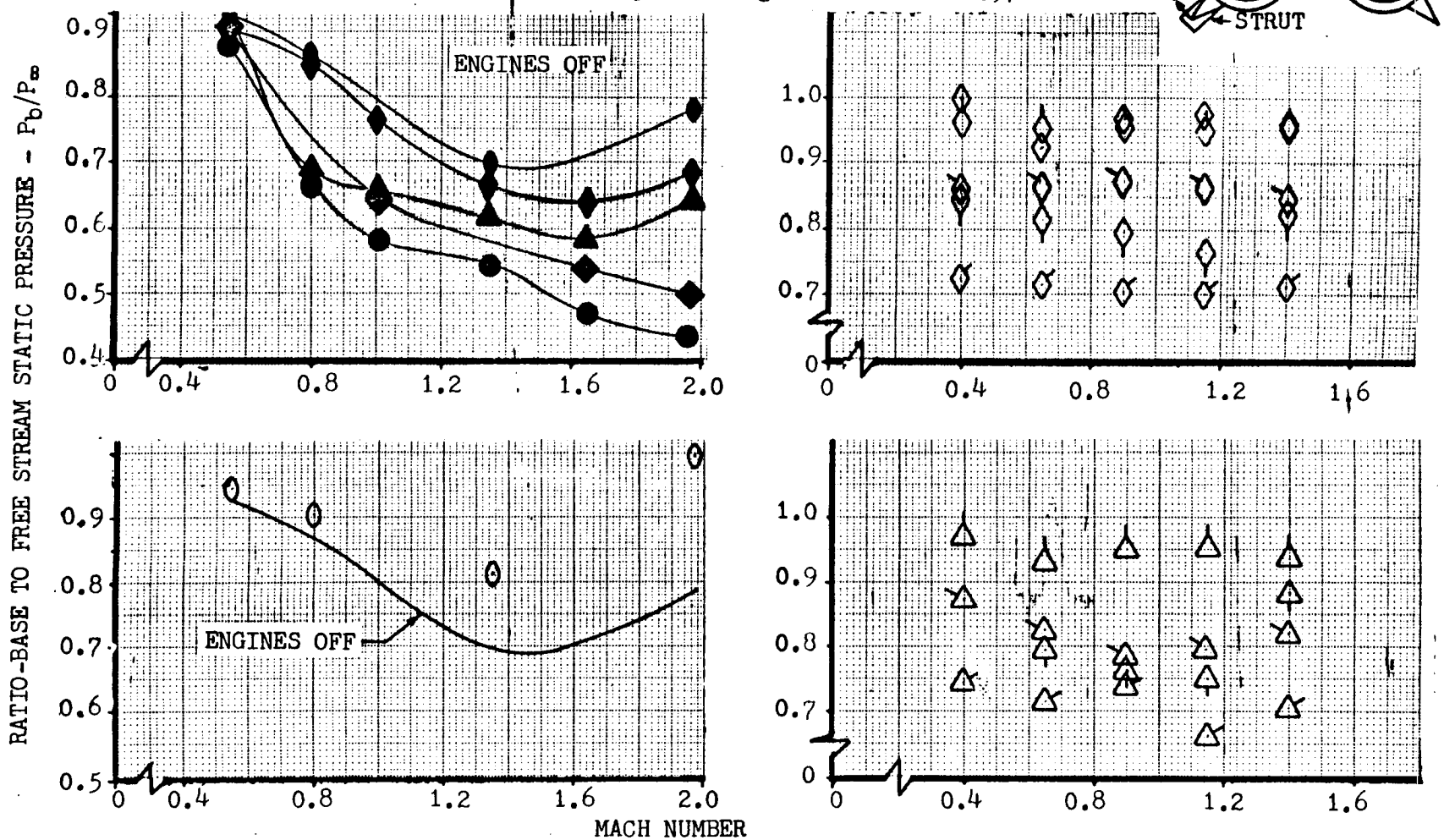

FIGURE 56 Base Pressure

TUNNEL Lewis 8 by 6

SYM.	INST.	CONFIG.
	$P_{1,3,4,6}$	$B_4FS_1N_{1-5}PL_1$
	$P_{1,3,4,6}$	$B_4FS_4N_{1-5}PL_1$

SYM.	INST.	CONFIG.
	$P_{1,3,4,6}$	$B_4FS_1D_2N_{1-5}PL_1$
	$P_{1,3,4,6}$	$B_4FS_1D_1SC_2N_{1-5}PL_1$

NOTE: 1. Data averaged
2. Solid line denotes engine off data

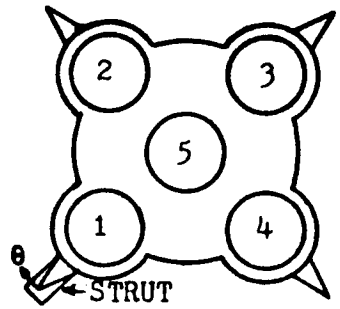

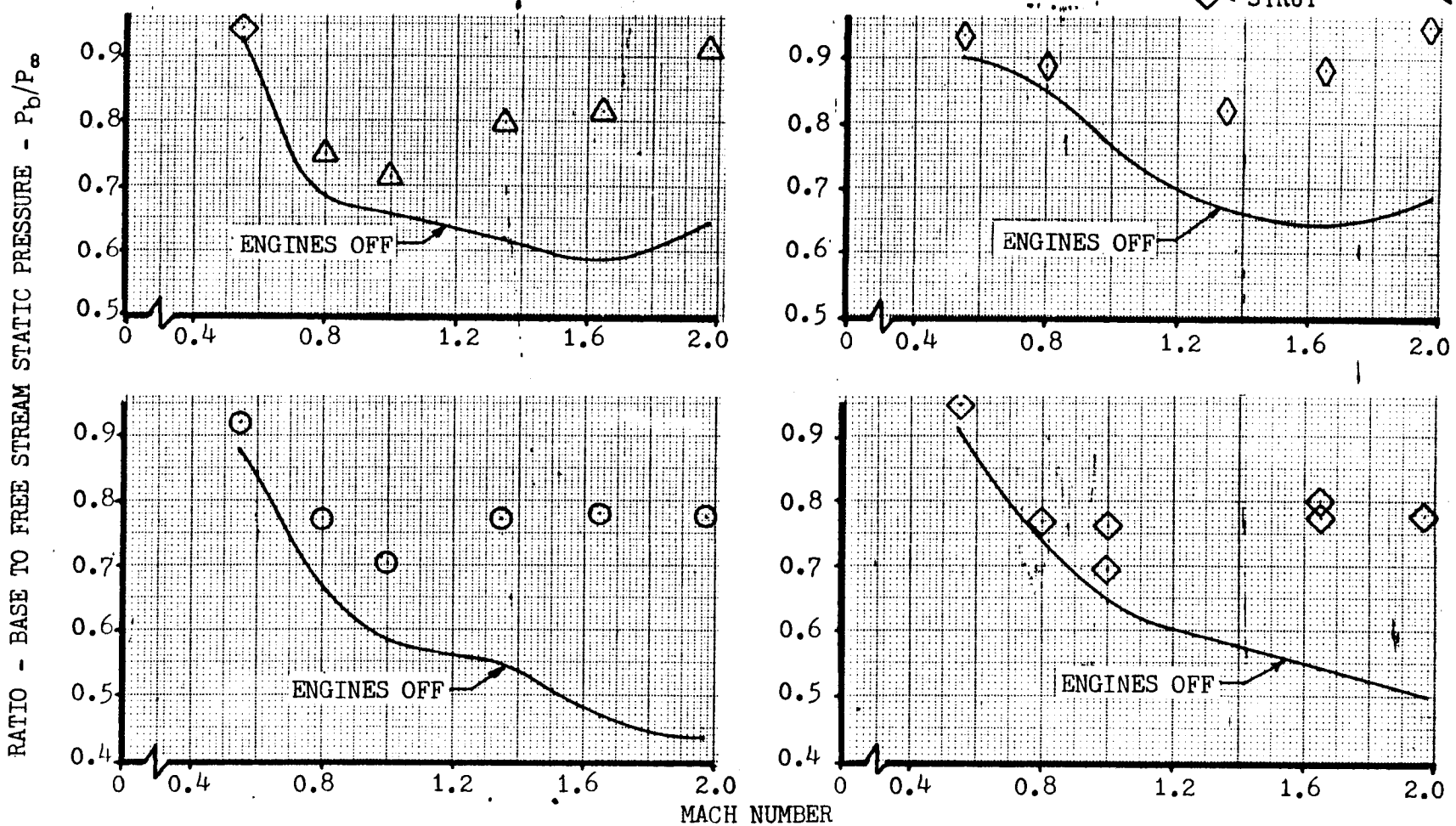

FIGURE 57 Base Pressure

TUNNEL Lewis 8 by 6

SYM.	INST.	CONFIG.
○	$P_{1,3,4,6,7}$	$B_4FS_1N_{1-5}PL_1$
□	$P_{1,3,4,6,7}$	$B_4FS_1D_2N_{1-5}PL_1$
◇	$P_{1,3,4,6,7}$	$B_4FS_1D_1SC_2N_{1-5}PL_1$
△	$P_{1,3,4,6,7}$	$B_4FS_1D_2NG_7NG_8PL_1$

NOTE: 1. Solid symbol denotes turbine exhaust
2. Data averaged

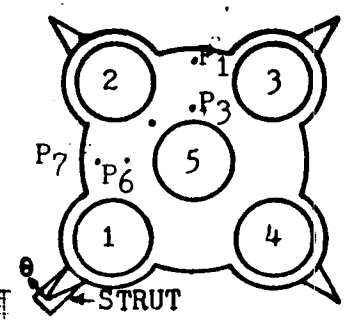

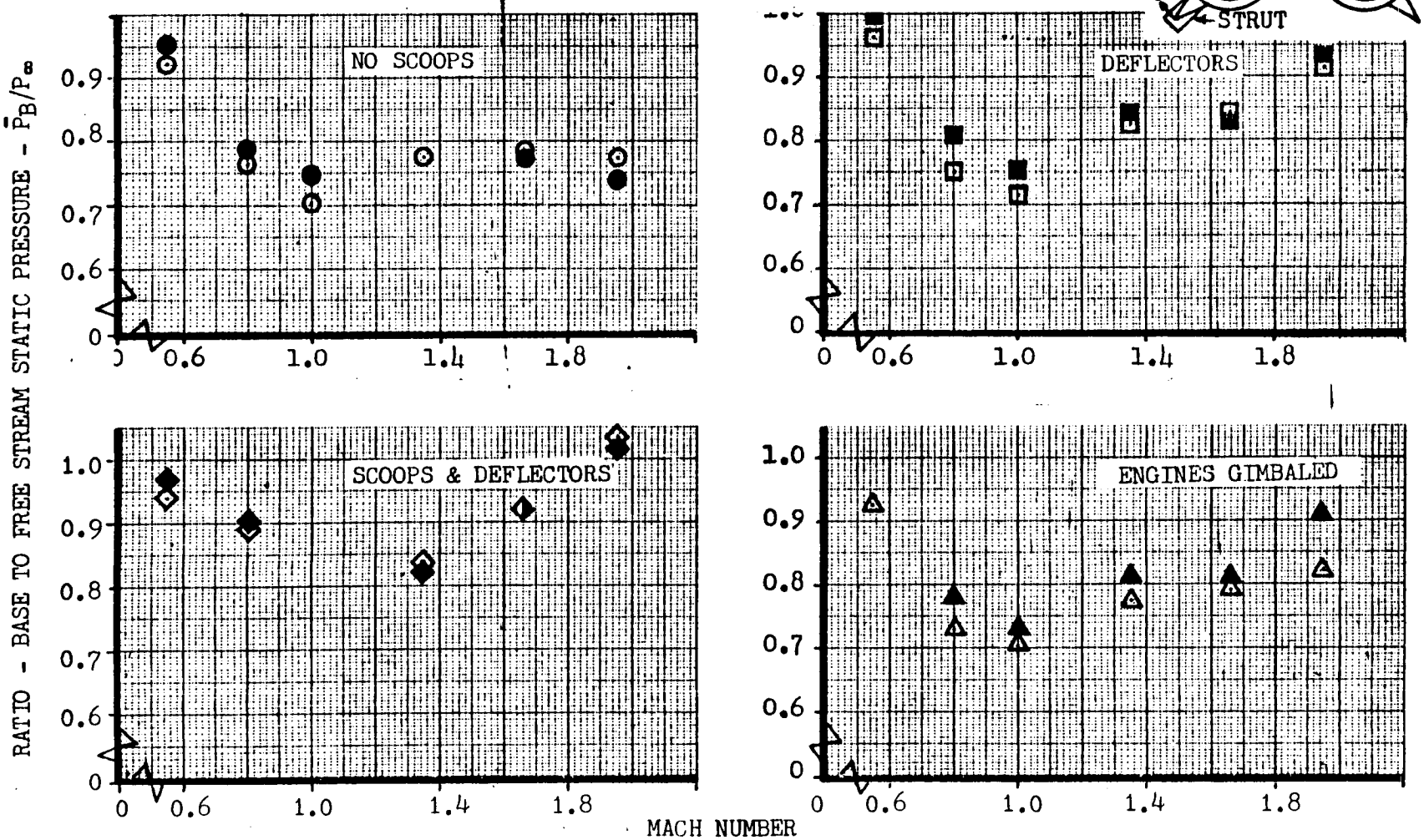

FIGURE 58 Base Pressure

TUNNEL LEWIS 8 BY 6

SYM.	INST.	CONFIG.
○	$P_{1,3,4,6,7}$	$B_4FS_1N_{1-5}PL_1$
□	$P_{1,3,4,6,7}$	$B_4FS_1D_2N_7PL_1$
◇	$P_{1,3,4,6,7}$	$B_4FS_4N_{1-5}PL_1$

SYM.	INST.	CONFIG.
△	$P_{1,3,4,6,7}$	$B_4FS_1D_2N_{1-5}PL_1$
◿	$P_{1,3,4,6,7}$	$B_4FS_1D_2N_{G_7}N_{G_8}PL_1$
◇	$P_{1,3,4,6,7}$	$B_4FS_1D_1SC_2N_{1-5}PL_1$

NOTE: Data averaged

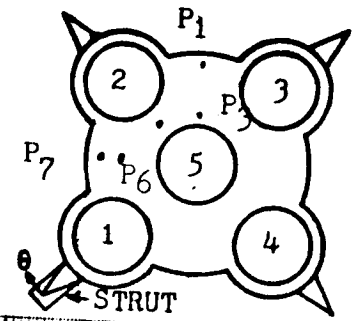

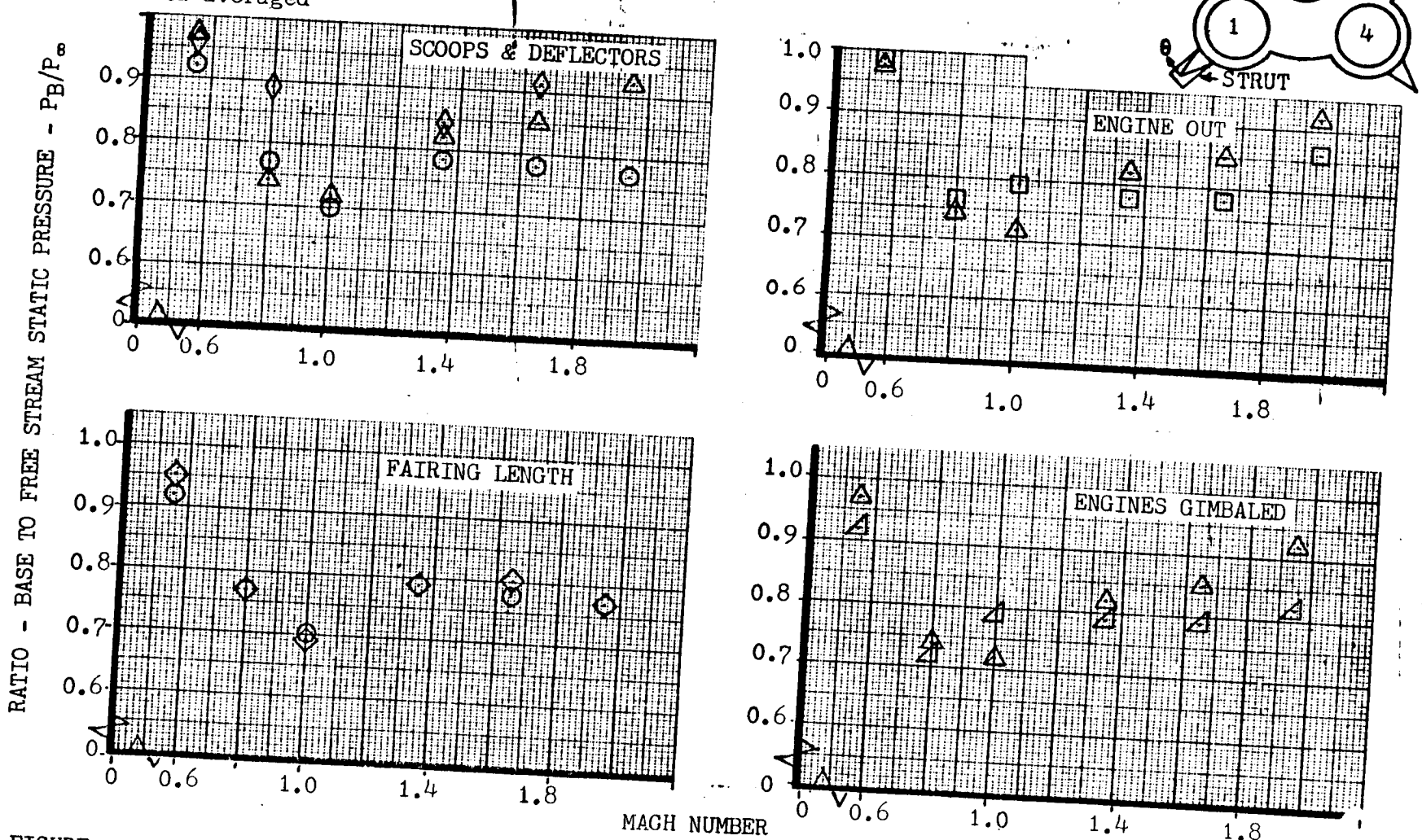

FIGURE 59 Base Pressure

CONFIG: $B_4FS_1D_2N_{1-5}PL_2$
M: 0.55

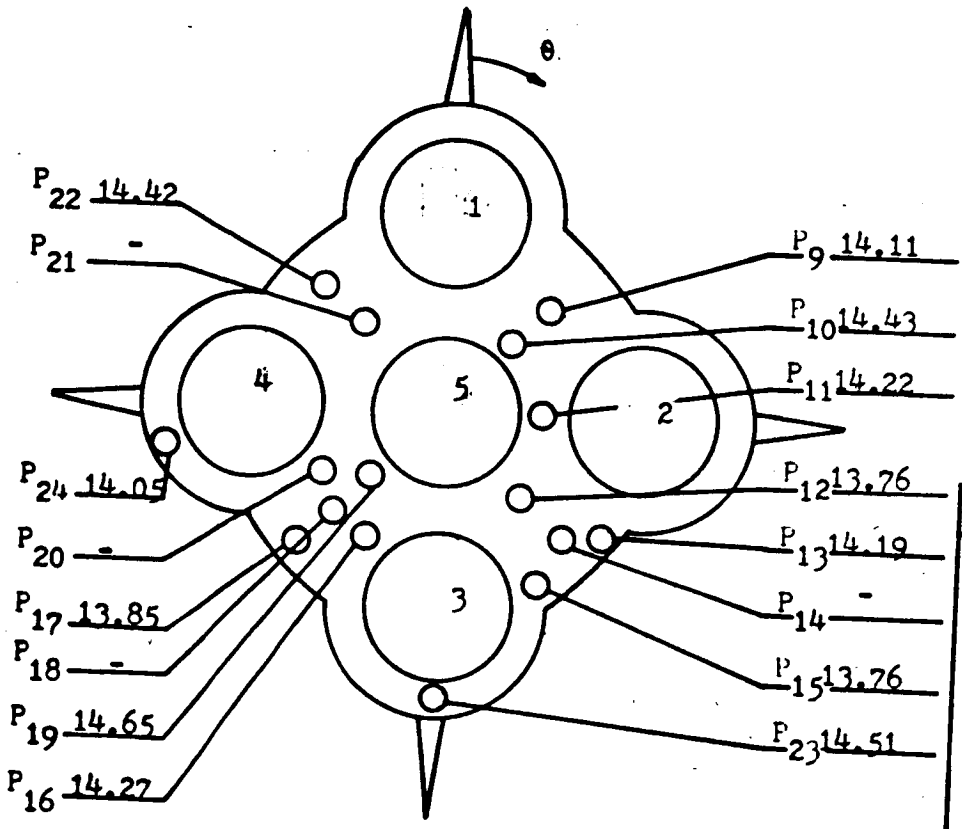

P	r/R	θ
9	.650	45°
10	.400	45
11	.451	90
12	.525	135
13	.900	125
14	.776	135
15	.864	158
16	.659	210
17	.900	225
18	.650	225
19	.400	225
20	.500	244
21	.525	315
22	.776	315
23	1.170	180
24	1.171	262

P_∞ 14.79

$P_{AVG.}$ 14.19

MAX. ΔP .462 AT P_{19}

MEAN ΔP .232

ΔP IS DIFFERENCE FROM $P_{AVG.}$

FIGURE 60 Base Pressure Distribution

CONFIG: $B_4FS_1D_2N_{1-5}PL_2$
M: 0.80

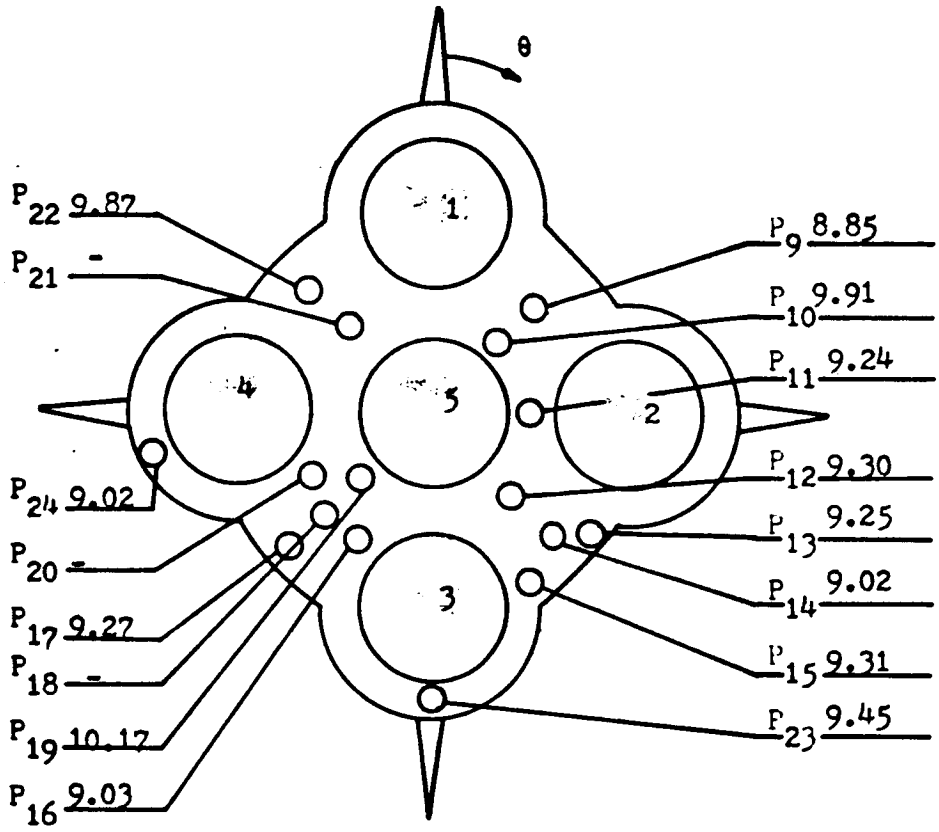

P	r/R	θ
9	.650	45°
10	.400	45
11	.451	90
12	.525	135
13	.900	125
14	.776	135
15	.864	158
16	.659	210
17	.900	225
18	.650	225
19	.400	225
20	.500	244
21	.525	315
22	.776	315
23	1.170	180
24	1.171	262

P_∞ 11.309

$P_{AVG.}$ 9.361

MAX. ΔP .811 AT P_{19}

MEAN ΔP .304

ΔP IS DIFFERENCE FROM $P_{AVG.}$

FIGURE 61 Base Pressure Distribution

CONFIG: $B_4FS_1D_2N_{1-5}PL_2$
M: 1.00

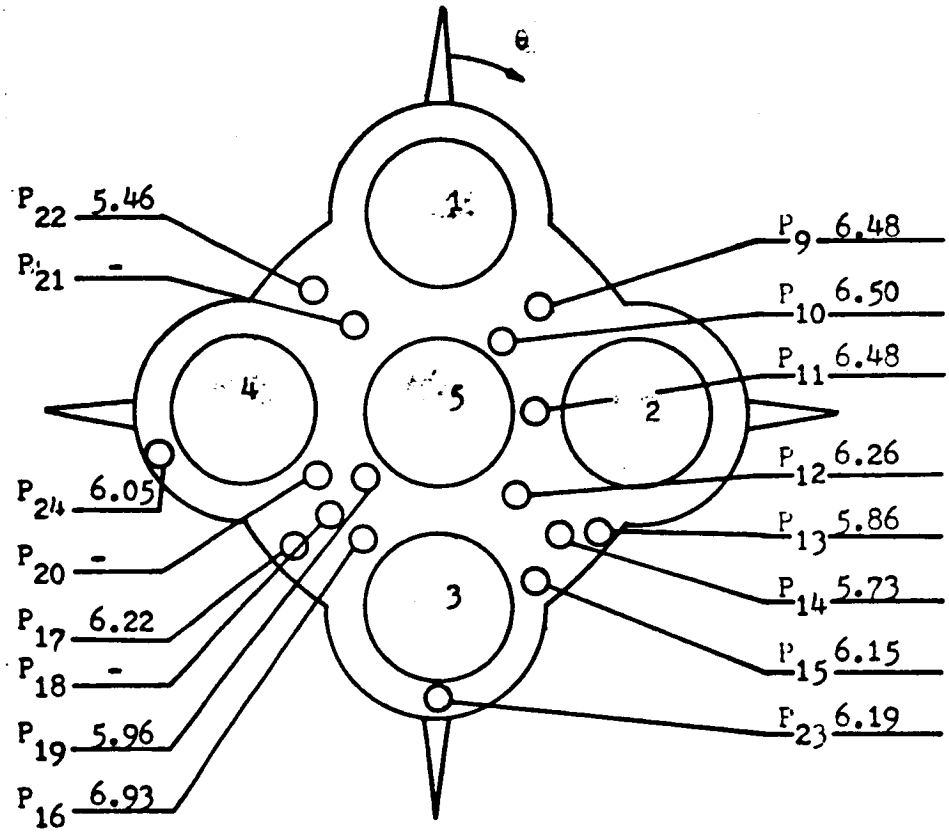

P	r/R	θ
9	.650	45°
10	.400	45
11	.451	90
12	.525	135
13	.900	125
14	.776	135
15	.864	158
16	.659	210
17	.900	225
18	.650	225
19	.400	225
20	.500	244
21	.525	315
22	.776	315
23	1.170	180
24	1.171	262

P_∞ 8.755

$P_{AVG.}$ 6.175

MAX. ΔP .756 AT P_{16}

MEAN ΔP .282

ΔP IS DIFFERENCE FROM $P_{AVG.}$

FIGURE 62 Base Pressure Distribution

CONFIG: $B_4FS_1D_2N_{1-5}PL_2$
M: 1.35

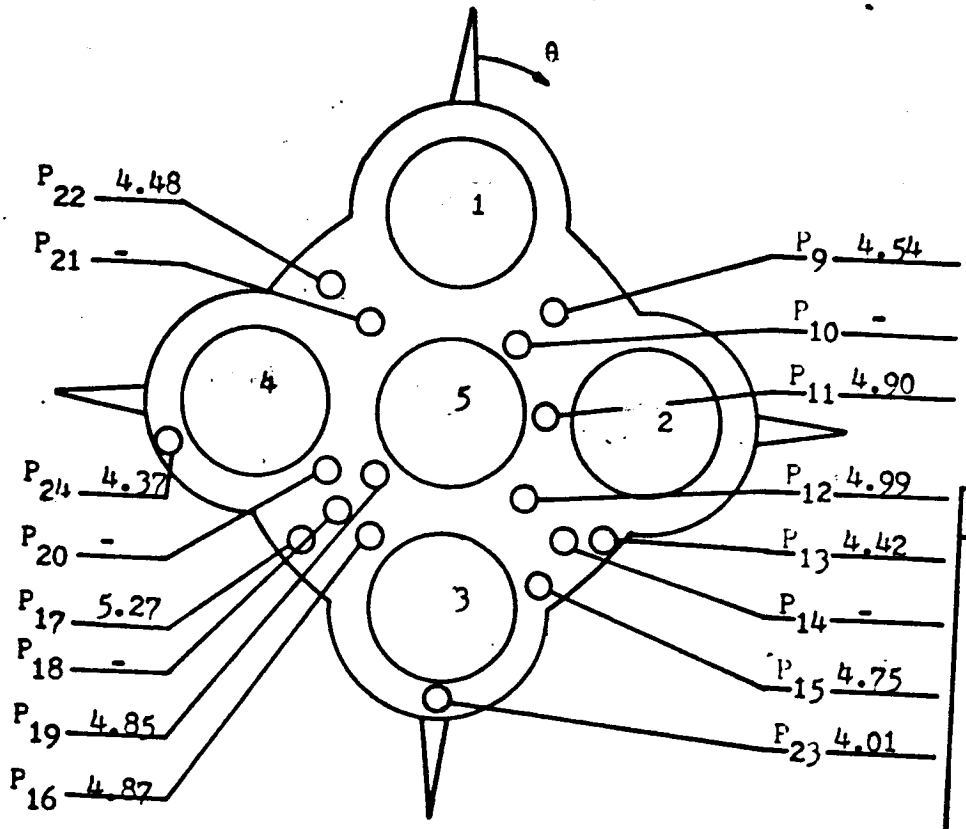

P	r/R	θ
9	.650	45°
10	.400	45
11	.451	90
12	.525	135
13	.900	125
14	.776	135
15	.864	158
16	.659	210
17	.900	225
18	.650	225
19	.400	225
20	.500	244
21	.525	315
22	.776	315
23	1.170	180
24	1.171	262

P_∞ 5.948

$P_{AVG.}$ 4.677

MAX. ΔP .664 AT P_{23}

MEAN ΔP .284

ΔP IS DIFFERENCE FROM $P_{AVG.}$

FIGURE 63 Base Pressure Distribution

CONFIG: $B_4FS_1D_2N_{1-5}PL_2$
M: 1.66

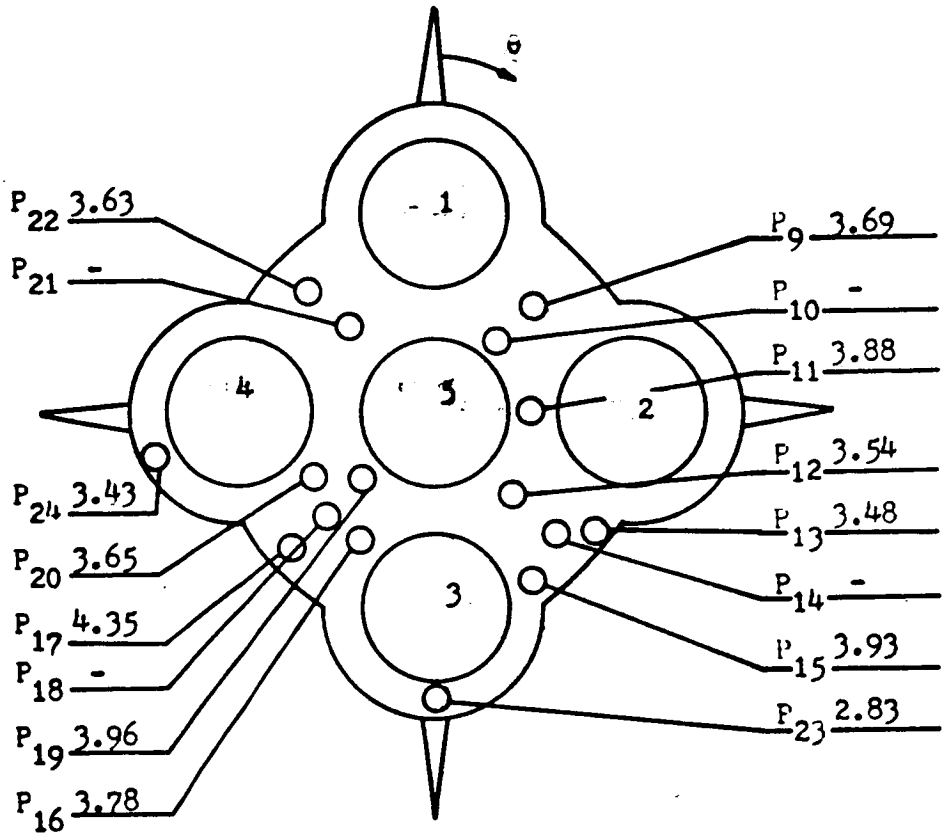

P	r/R	θ
9	.650	45°
10	.400	45
11	.451	90
12	.525	135
13	.900	125
14	.776	135
15	.864	158
16	.659	210
17	.900	225
18	.650	225
19	.400	225
20	.500	244
21	.525	315
22	.776	315
23	1.170	180
24	1.171	262

P_∞ 4.473

$P_{AVG.}$ 3.679

MAX. ΔP .846 AT P_{23}

MEAN ΔP .253

ΔP IS DIFFERENCE FROM $P_{AVG.}$

FIGURE 64 Base Pressure Distribution

CONFIG: $B_4FS_1D_1SC_2N_{1-5}PL_2$
M: 0.55

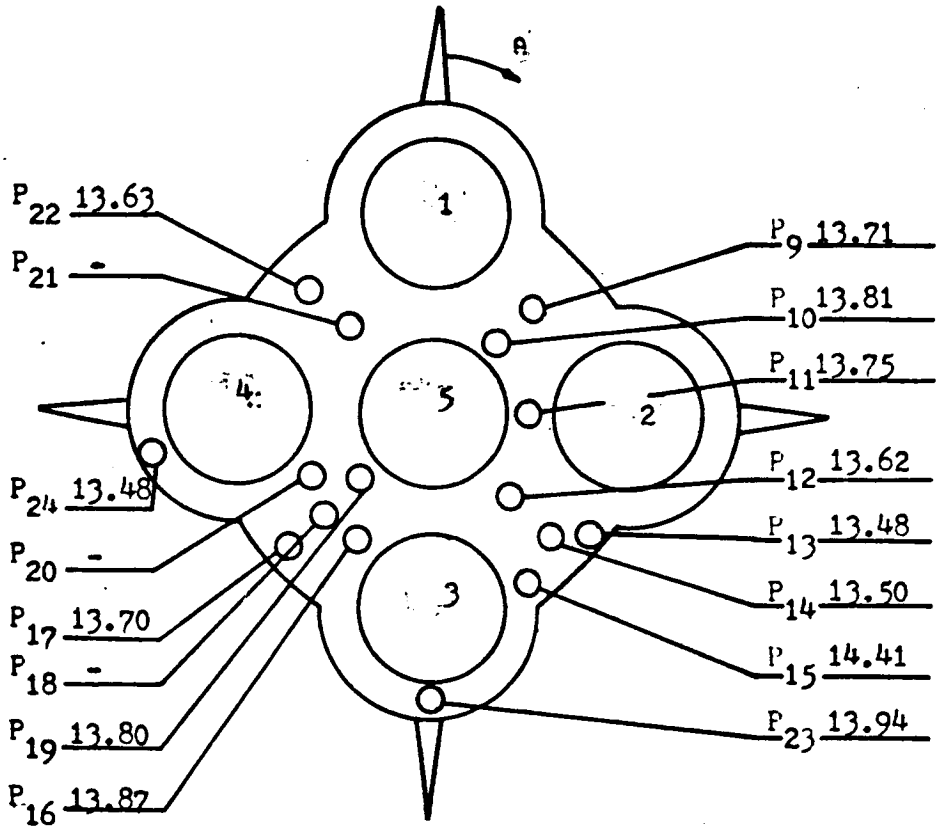

P	r/R	θ
9	.650	45°
10	.400	45
11	.451	90
12	.525	135
13	.900	125
14	.776	135
15	.864	158
16	.659	210
17	.900	225
18	.650	225
19	.400	225
20	.500	244
21	.525	315
22	.776	315
23	1.170	180
24	1.171	262

P_∞ 14.351

$P_{AVG.}$ 13.746

MAX. ΔP .666 AT P_{15}

MEAN ΔP .169

ΔP IS DIFFERENCE FROM $P_{AVG.}$

FIGURE 65 Base Pressure Distribution

CONFIG: $B_4FS_1D_1SC_2N_{1-5}PL_2$
M: 0.80

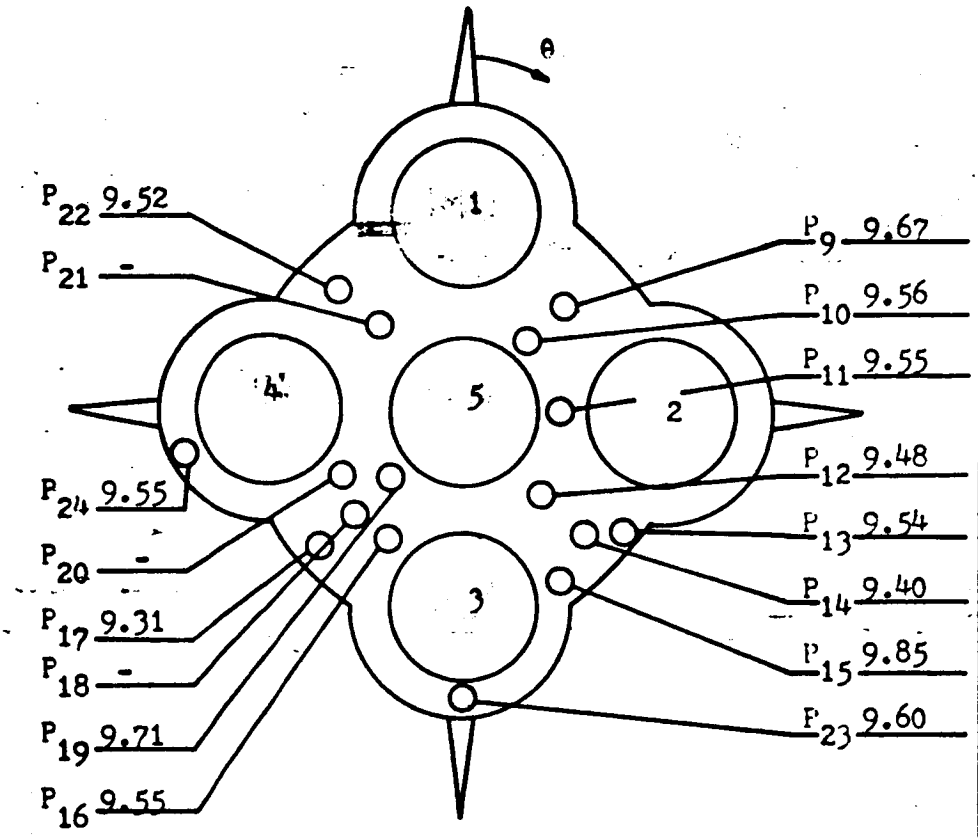

P	r/R	θ'
9	.650	45°
10	.400	45
11	.451	90
12	.525	135
13	.900	125
14	.776	135
15	.864	158
16	.659	210
17	.900	225
18	.650	225
19	.400	225
20	.500	244
21	.525	315
22	.776	315
23	1.170	180
24	1.171	262

P_∞ 11.052

$P_{AVG.}$ 9.561

MAX. ΔP .293 AT P_{15}

MEAN ΔP .090

ΔP IS DIFFERENCE FROM $P_{AVG.}$

FIGURE 66 Base Pressure Distribution

CONFIG: $B_4FS_1D_1SC_2N_{1-5}PL_2$

M: 1.00

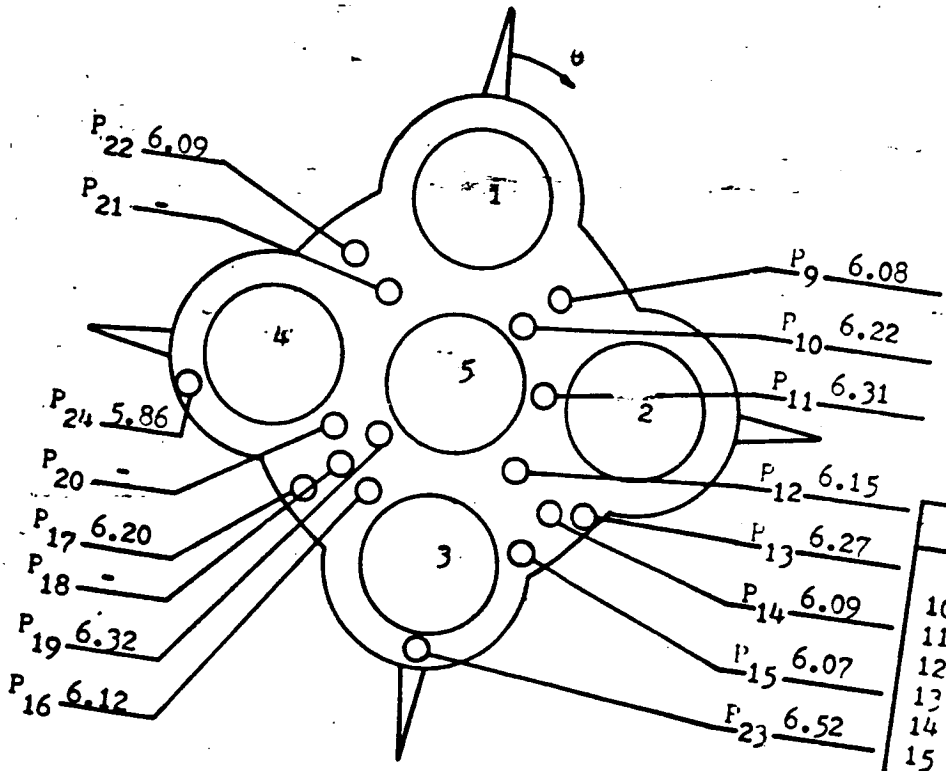

P	r/R	θ
9	.650	45°
10	.400	45
11	.451	90
12	.525	135
13	.900	125
14	.776	135
15	.864	158
16	.659	210
17	.900	225
18	.650	225
19	.400	225
20	.500	244
21	.525	315
22	.776	315
23	1.170	180
24	1.171	262

P_∞ 8.640

$P_{AVG.}$ 6.176

MAX. ΔP .347 AT P_{23}

MEAN ΔP .119

ΔP IS DIFFERENCE FROM $P_{AVG.}$

FIGURE 67 Base Pressure Distribution

CONFIG: $B_4FS_1D_1SC_2N_{1-5}PL_2$

M: 1.35

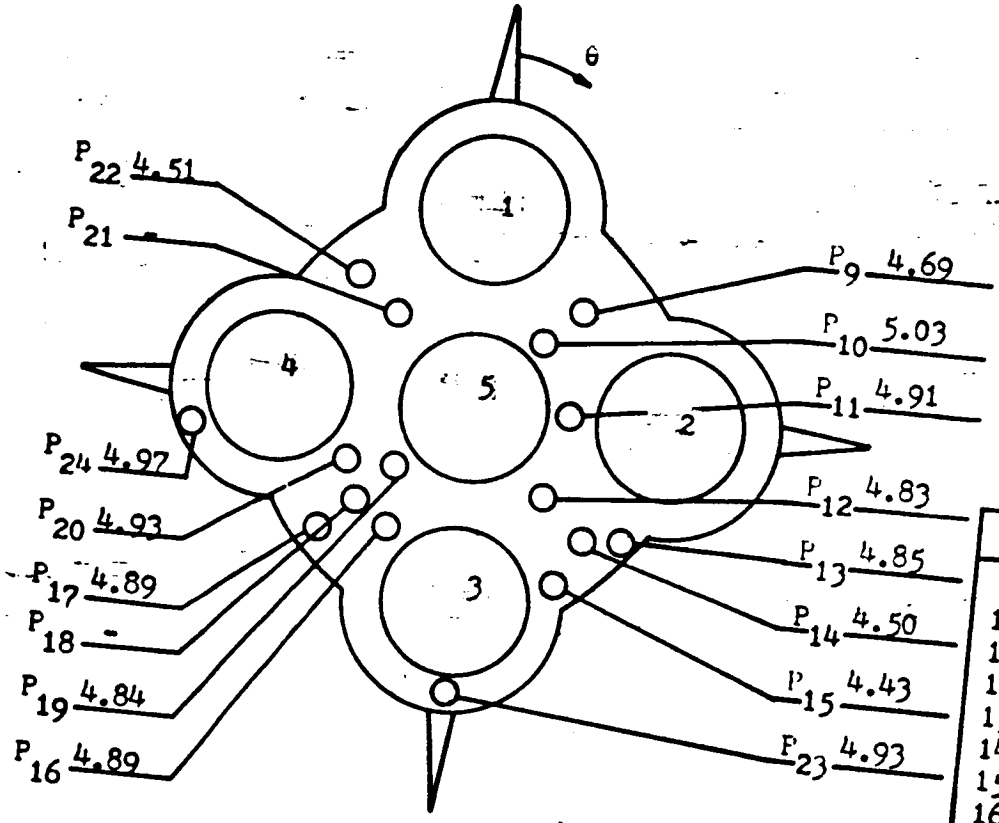

P	r/R	θ
9	.650	45°
10	.400	45
11	.451	90
12	.525	135
13	.900	125
14	.776	135
15	.864	158
16	.659	210
17	.900	225
18	.650	225
19	.400	225
20	.500	244
21	.525	315
22	.776	315
23	1.170	180
24	1.171	262

P_∞ 5.896

$P_{AVG.}$ 4.799

MAX. ΔP .365 AT P_{15}

MEAN ΔP .152

ΔP IS DIFFERENCE FROM $P_{AVG.}$

FIGURE 68 Base Pressure Distribution

CONFIG: $B_4FS_1D_1SC_2N_{1-5}PL_2$
M: 1.66

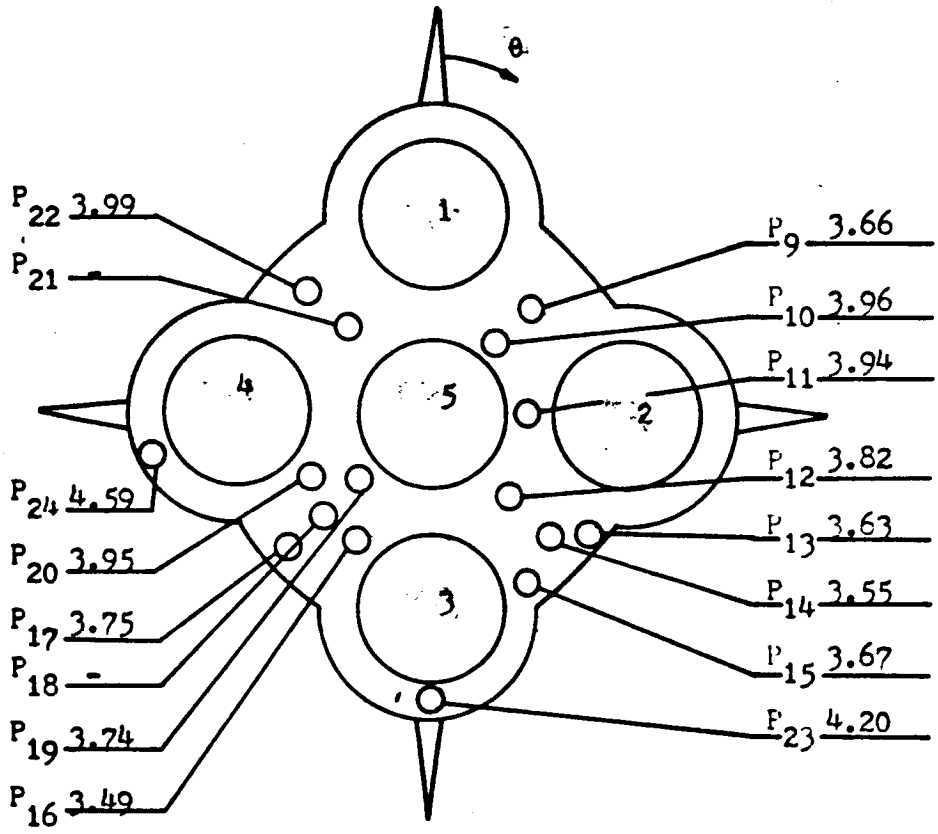

P	r/R	θ
9	.650	45°
10	.400	45
11	.451	90
12	.525	135
13	.900	125
14	.776	135
15	.864	158
16	.659	210
17	.900	225
18	.650	225
19	.400	225
20	.500	244
21	.525	315
22	.776	315
23	1.170	180
24	1.171	262

P_∞ 4.455

$P_{AVG.}$ 3.851

MAX. ΔP .734 AT P_{24}

MEAN ΔP .215

ΔP IS DIFFERENCE FROM $P_{AVG.}$

FIGURE 69 Base Pressure Distribution

CONFIG: $B_4FS_1D_1SC_2N_{1-5}PL_2$
M: 1.95

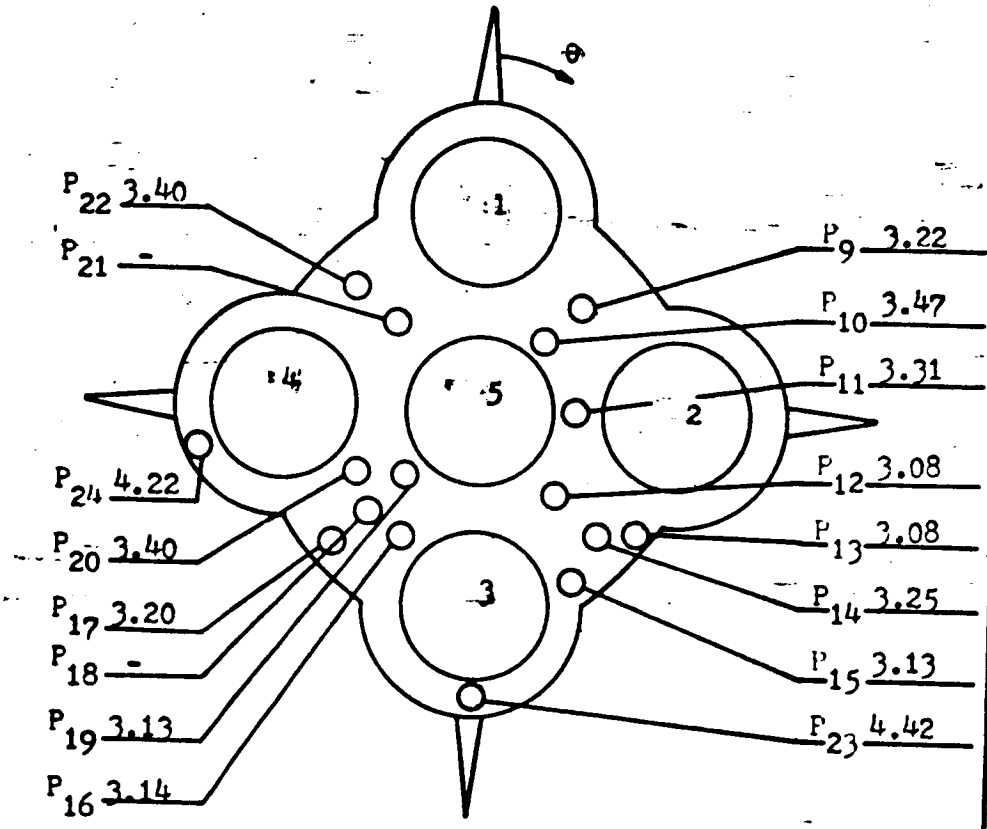

P	r/R	θ
9	.650	45°
10	.400	45
11	.451	90
12	.525	135
13	.900	125
14	.776	135
15	.864	158
16	.659	210
17	.900	225
18	.650	225
19	.400	225
20	.500	244
21	.525	315
22	.776	315
23	1.170	180
24	1.171	262

P_∞ 3.339

$P_{AVG.}$ 3.388

MAX. ΔP 1.027 AT P_{23}

MEAN ΔP .280

ΔP IS DIFFERENCE FROM $P_{AVG.}$

FIGURE 70 Base Pressure Distribution

CONFIG: $B_4FS_1D_2N_{G_7}N_{G_8}PL_2$

M: 0.80

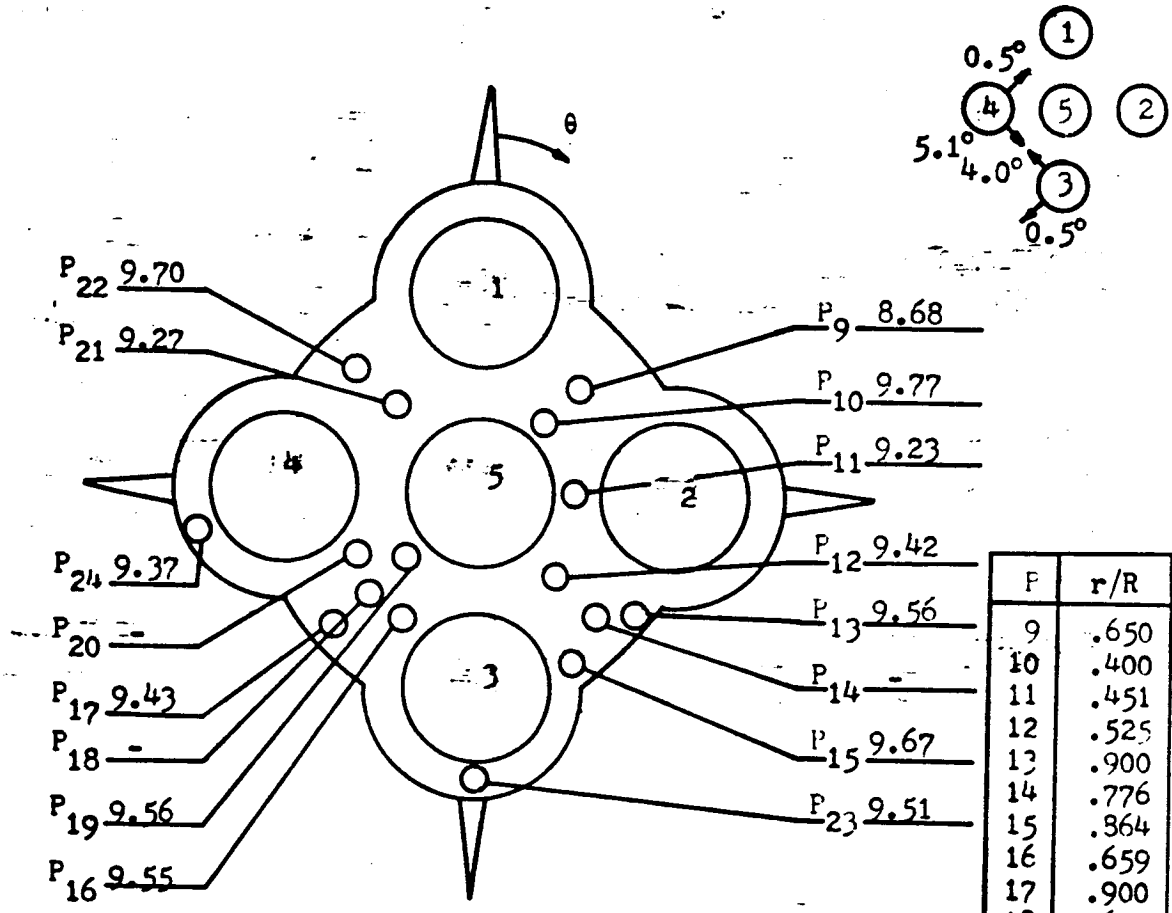

P	r/R	θ
9	.650	45°
10	.400	45
11	.451	90
12	.525	135
13	.900	125
14	.776	135
15	.864	158
16	.659	210
17	.900	225
18	.650	225
19	.400	225
20	.500	244
21	.525	315
22	.776	315
23	1.170	180
24	1.171	262

P_{∞} 11.028

$P_{AVG.}$ 9.438

MAX. ΔP .759 AT P_9

MEAN ΔP .191

ΔP IS DIFFERENCE FROM $P_{AVG.}$

FIGURE 71 Base Pressure Distribution

CONFIG: $B_4FS_1D_2N_{G_7}N_{G_8}PL_2$

M: 1.66

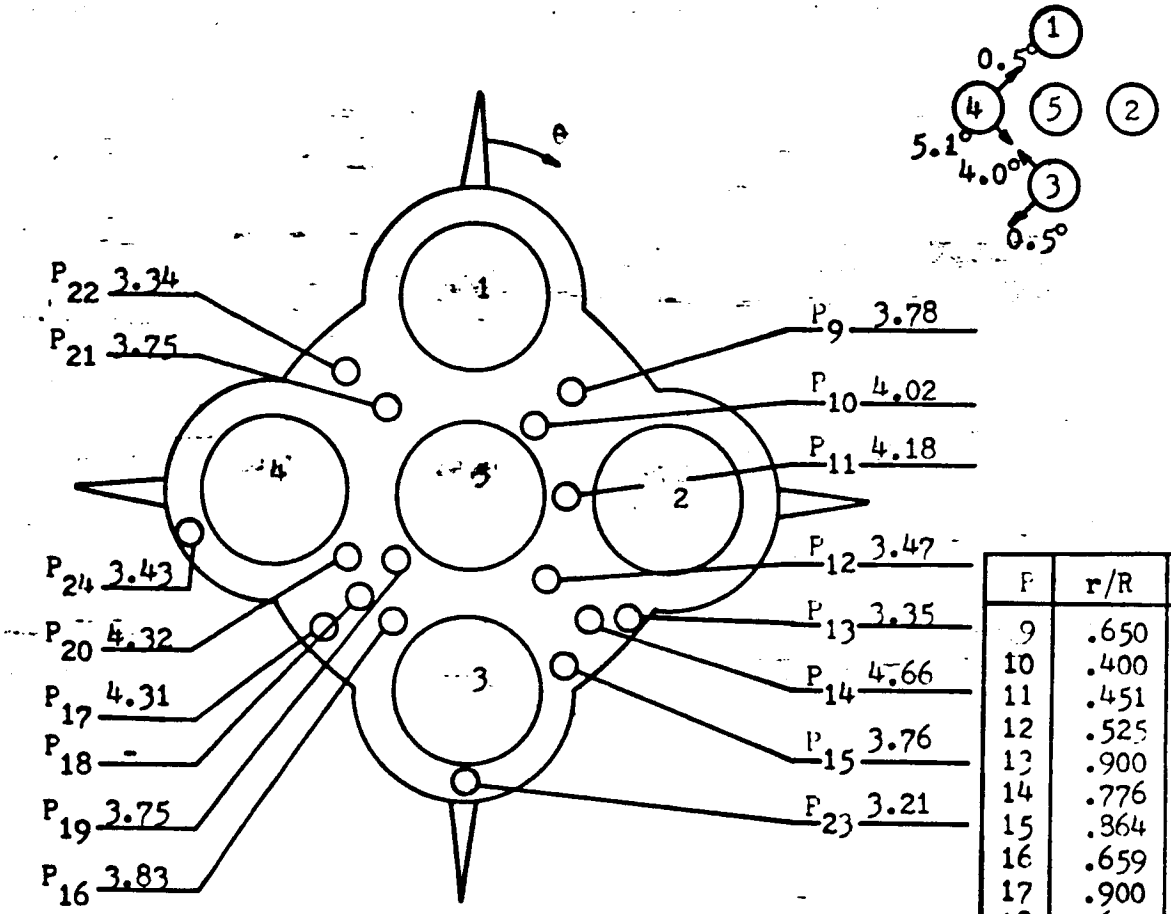

P	r/R	θ
9	.650	45°
10	.400	45
11	.451	90
12	.525	135
13	.900	125
14	.776	135
15	.864	158
16	.659	210
17	.900	225
18	.650	225
19	.400	225
20	.500	244
21	.525	315
22	.776	315
23	1.170	180
24	1.171	262

P_∞ 4.416

$P_{AVG.}$ 3.811

MAX. ΔP .848 AT P_{14}

MEAN ΔP .327

ΔP IS DIFFERENCE FROM $P_{AVG.}$

FIGURE 72 Base Pressure Distribution

CONFIG: $B_4FS_1D_2N_{10}N_{G_{11}}N_{G_{12}}N_{G_{13}}PL_2$

M: 0.80

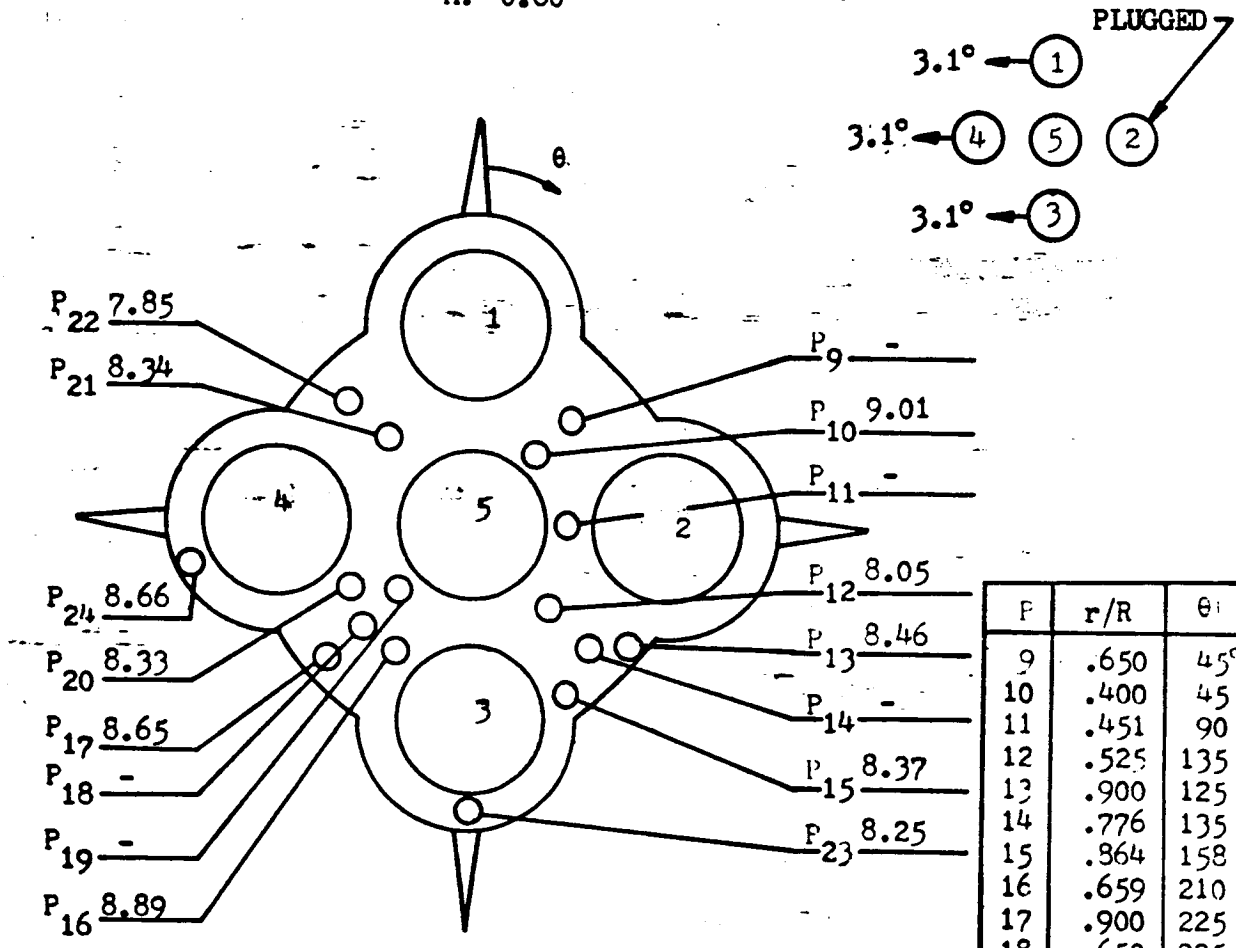

P	r/R	θ
9	.650	45°
10	.400	45
11	.451	90
12	.525	135
13	.900	125
14	.776	135
15	.864	158
16	.659	210
17	.900	225
18	.650	225
19	.400	225
20	.500	244
21	.525	315
22	.776	315
23	1.170	180
24	1.171	262

P_∞ 11.492

$P_{AVG.}$ 8.442

MAX. ΔP .588 AT P_{22}

MEAN ΔP .266

ΔP IS DIFFERENCE FROM $P_{AVG.}$

FIGURE 73 Base Pressure Distribution

CONFIG: $B_4FS_1D_2N_{10}N_{G_{11}}N_{G_{12}}N_{G_{13}}PL_2$

M: 1.66

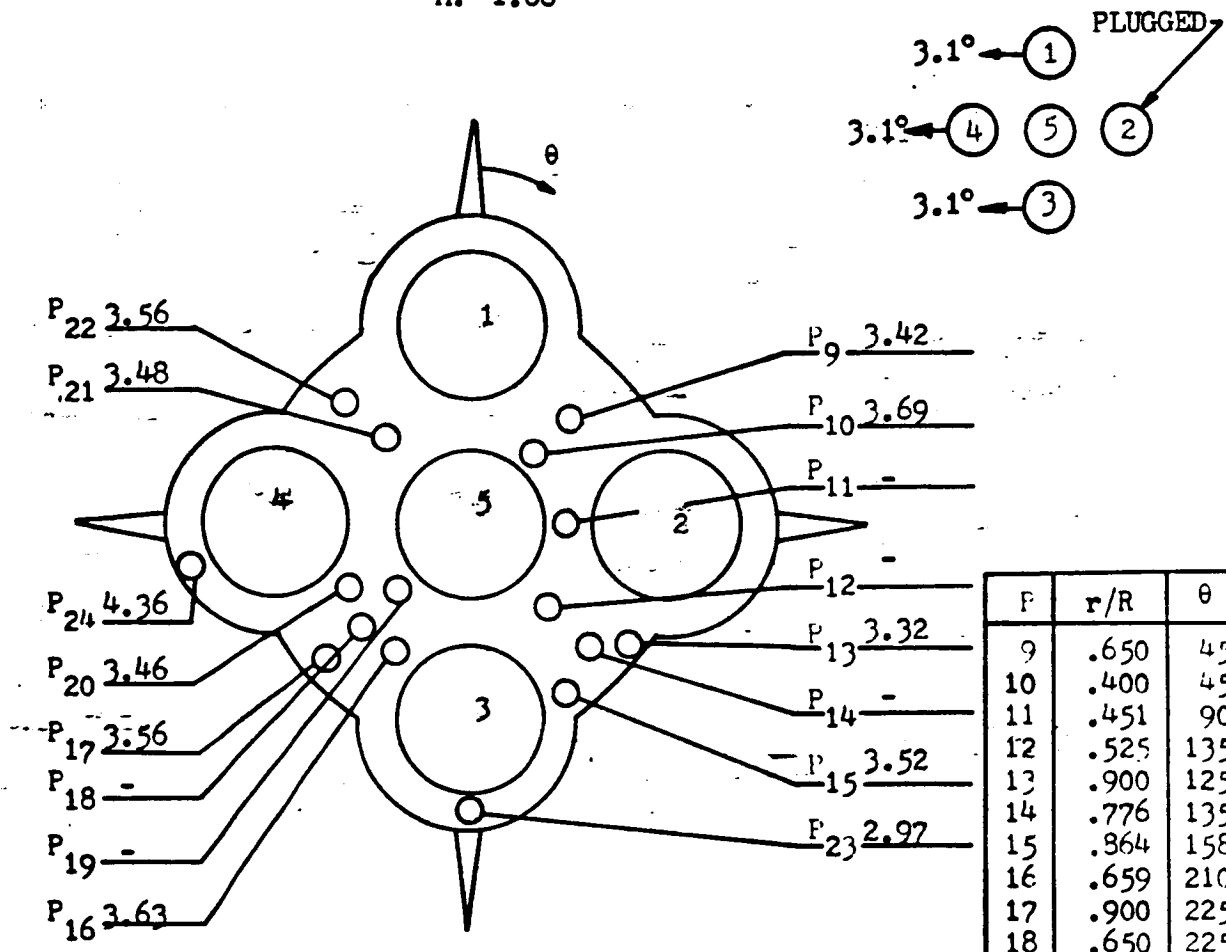

P	r/R	θ
9	.650	45°
10	.400	45
11	.451	90
12	.525	135
13	.900	125
14	.776	135
15	.864	158
16	.659	210
17	.900	225
18	.650	225
19	.400	225
20	.500	244
21	.525	315
22	.776	315
23	1.170	180
24	1.171	262

P_∞ 4.548

$P_{AVG.}$ 3.542

MAX. ΔP .818 AT P_{24}

MEAN ΔP .196

ΔP IS DIFFERENCE FROM $P_{AVG.}$

FIGURE 74 Base Pressure Distribution

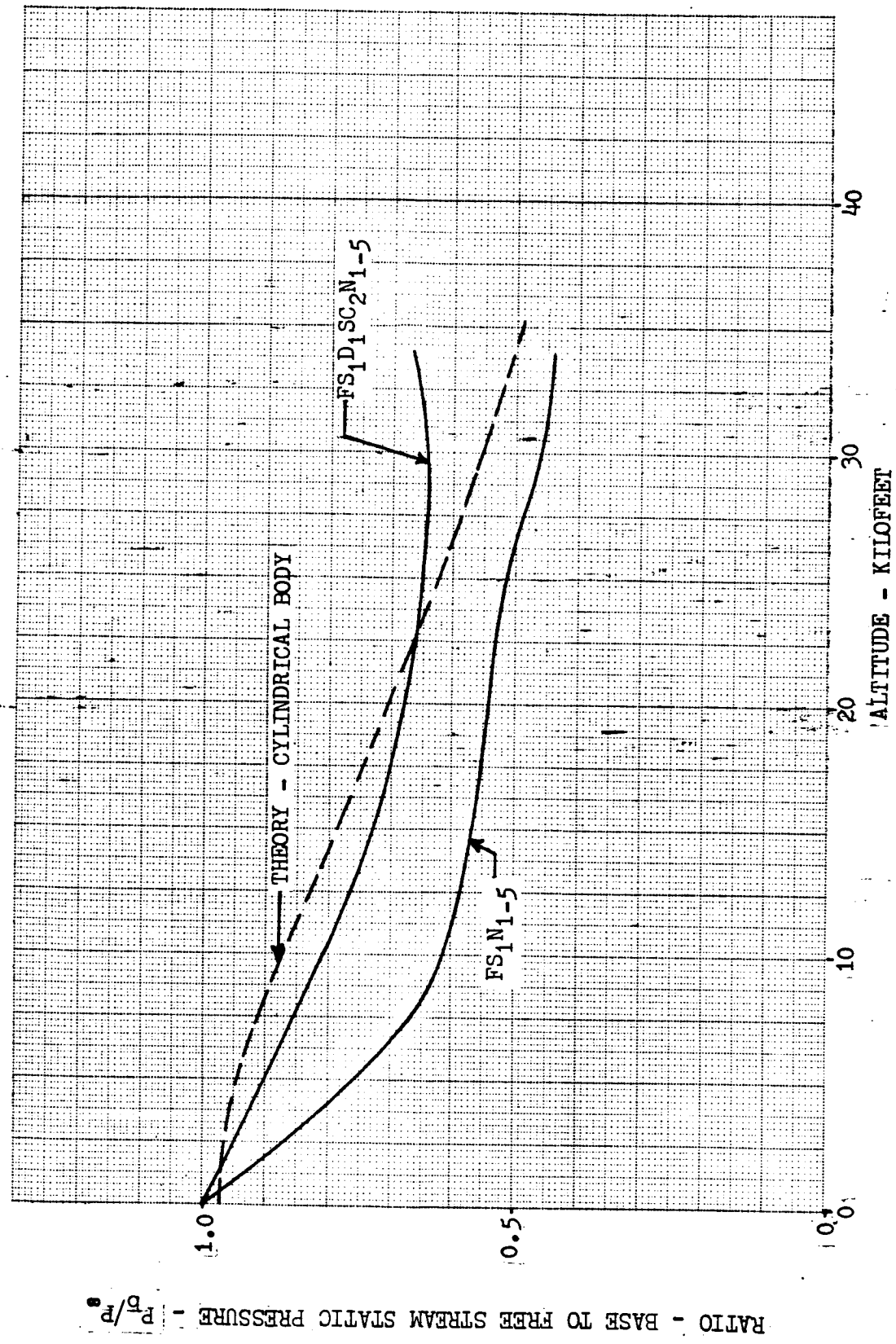

FIGURE 75 Engines Off Base Pressure Comparison - LRC 8 by 6 Tunnel

4.4.2 (Continued)

Figure 76 is a comparison of the corrected model base pressure with average Saturn I block II flight data and theoretical calculations of the scoop exit static pressure. The trends of the model and flight data are similar but agreement with absolute magnitudes are only good above a Mach number of 1.35. The theoretical scoop exit static pressure continually increases with increasing Mach number and is in fair agreement with the model and flight data above Mach 1.35.

Correction of tunnel data is accomplished using Figure 77 which is a compilation of several S-IC model tests both hot and cold flow. Fair agreement is obtained between the hot and cold models when the pressure data is plotted as a function of the ratio of nozzle exit static pressure to free stream ambient pressure. This graph suggests the correction to the hot pressure data which is used to account for the trajectory mismatch of the 8 by 6 tunnel. Since the exit pressure P_E is the same for model and prototype, a difference in the ratio P_b/P_∞ can be obtained by using the trajectory altitude and the tunnel altitude in the ratio P_E/P_∞. This difference is then added to the test data ratio (P_b/P_∞) to obtain the corrected data value.

4.5 DATA ACCURACY

Inaccuracies in the base plate test data are due to inaccuracy of the gages and the ability to accurately read the oscilloscope traces. There is further uncertainty in the data due to unsymetrical flow in the base. These two areas are described in detail below.

4.5.1 Repeatability

Repeatability of test data was determined by making six repeat runs with the different test configurations. Pressure repeatability data is shown in Figure 78. The average pressure difference for the seventeen repeat points shown is 0.134 psia with a maximum spread of less than 2 percent.

The convective heating rates show an average scatter between repeat points of 14 percent while the radiation scatter is 30 percent. It should be noted that the use of percentages alone can be deceptive. The heating rates are so low that a small error in magnitude is a large percentage of the value read. Sample heat transfer repeatability data at Mach 0.80 and 1.95 are shown in Figures 79 and 80.

4.5.2 Symmetry

Heat transfer and base pressure measurements were recorded in different quadrants of the base. Data comparisons between gages in identical positions, but adjacent quadrants, are a means of evaluating the degree of flow symmetry in the base. Measurements from gages located on each side of the center radial line of a given quadrant are used to evaluate the symmetry of flow within that quadrant. Heating data is compared in Figures 81 through 86; and pressure data is compared in Figure 87.

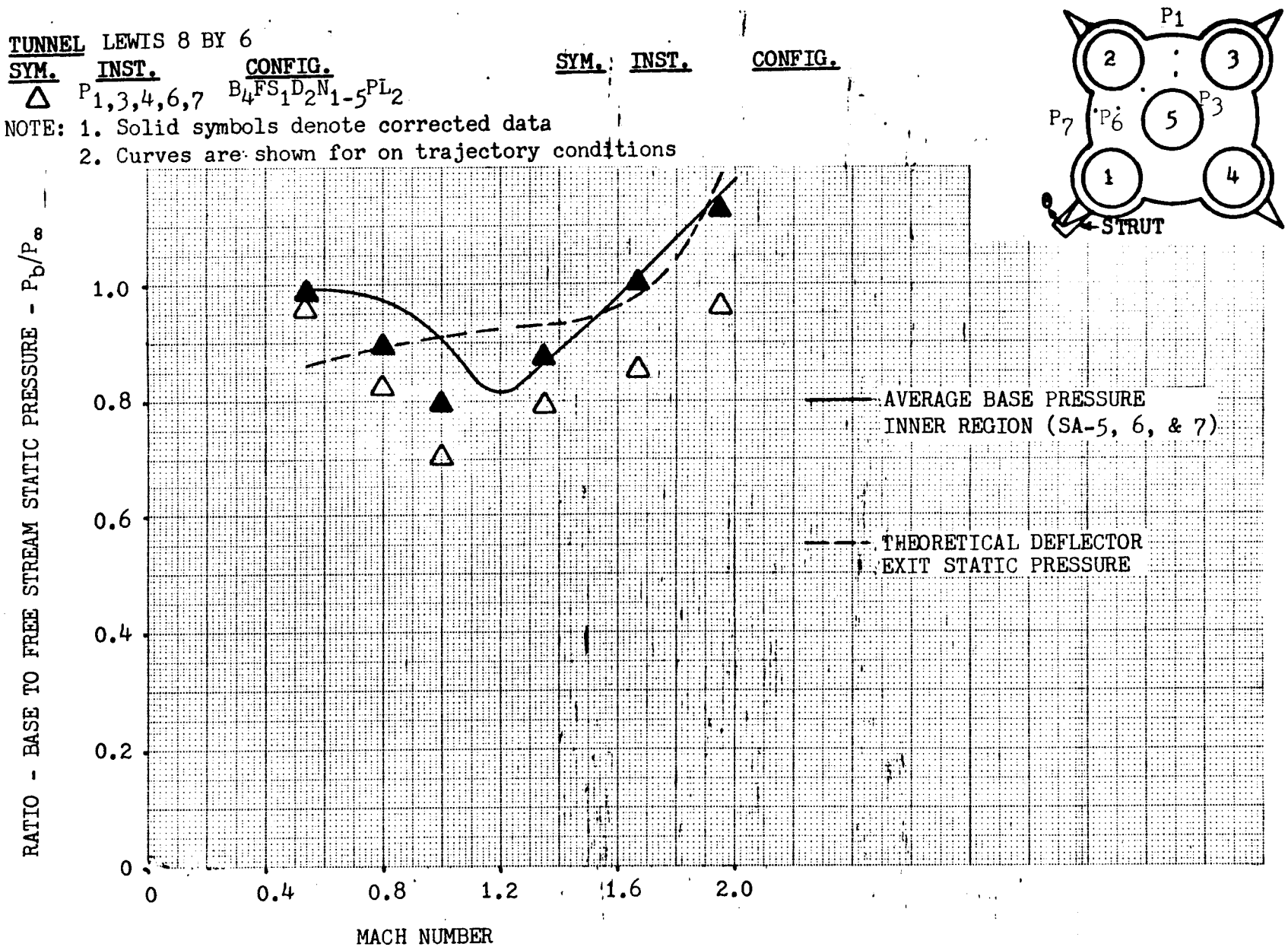

FIGURE 76 Base Pressure Versus Theory

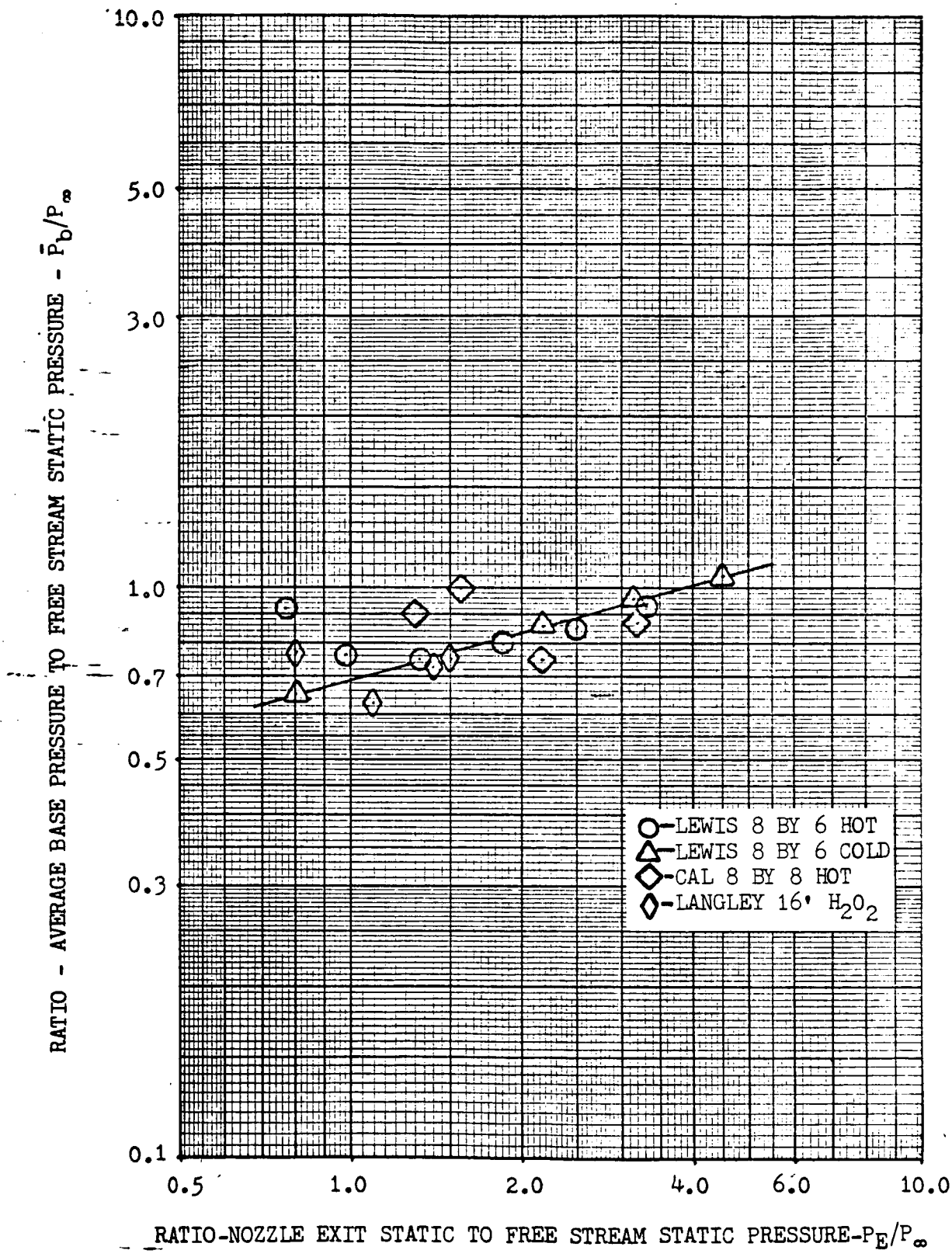

FIGURE 77 Comparison of S-IC Hot and Cold Models Base Pressure Data

TUNNEL LEWIS 8 BY 6

SYM.	INST.	CONFIG.
○	$P_{1,3,4,6}$	$B_4FS_1D_2N_{1-5}PL_1$
△	$P_{16,17,19}$	$B_4FS_1D_2N_{G_7}N_{G_8}PL_2$
◇	$P_{1,3}$	$B_4FS_1D_2N_{G_7}N_{G_8}PL_2$
◇	$P_{6,7}$	$B_4FS_1D_2N_{G_7}N_{G_8}PL_1$
□	$P_{16,17,19}$	$B_4FS_1D_2N_{G_7}N_{G_8}PL_1$
◿	$P_{16,17,19}$	$B_4FS_1D_1N_{G_7}N_{G_8}PL_1$

NOTE: 1. Solid symbol denotes repeatability run.
2. Data averaged.

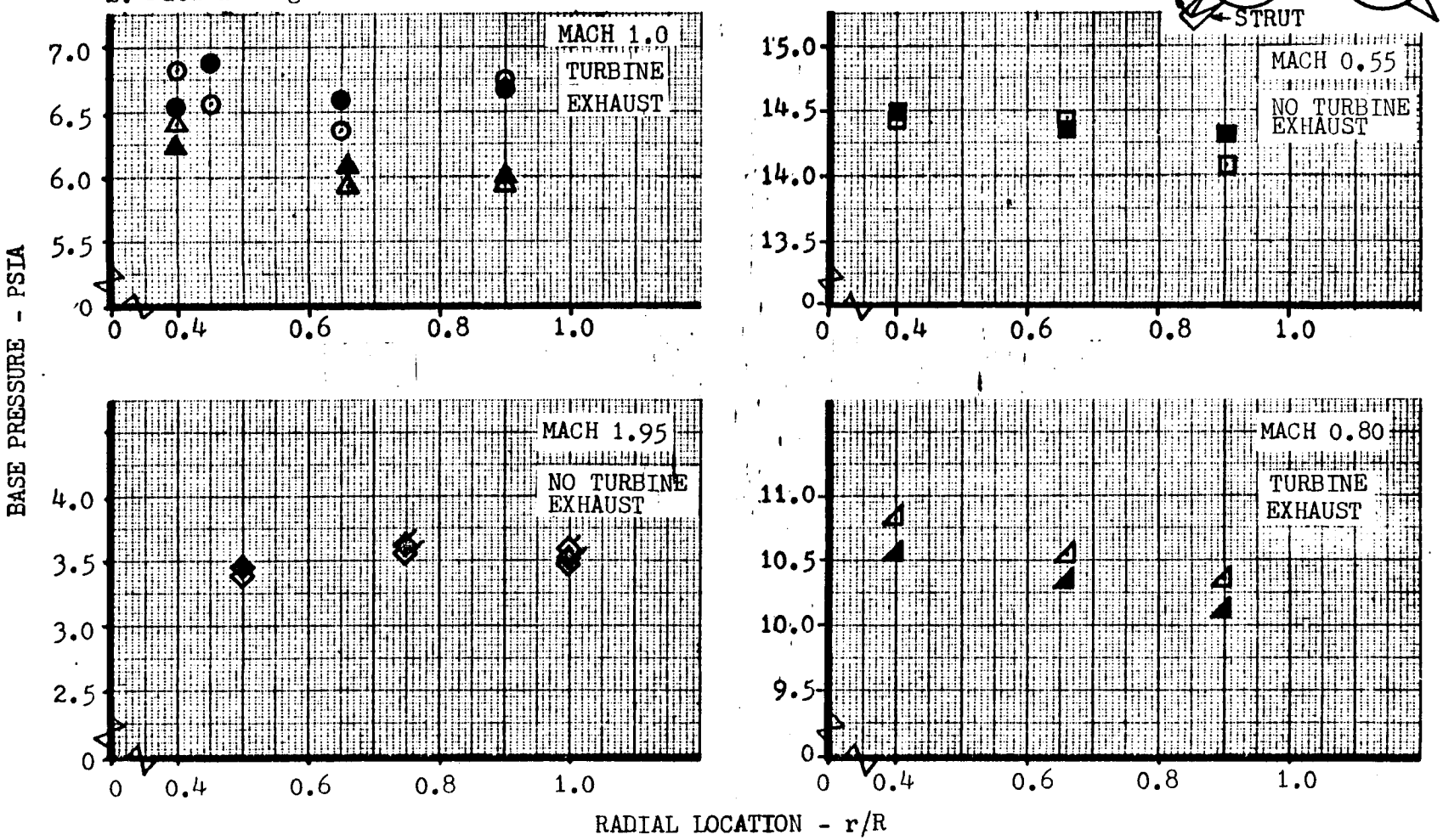

FIGURE 78 Base Pressure Repeatability

TUNNEL Lewis 8 by 6

SYM.	INST.	CONFIG.
○	$H_{1,13,15,17}$	$B_4FS_1D_2N_{G_7}N_{G_8}PL_1$
△	$H_{2,14,16,18}$	$B_4FS_1D_2N_{G_7}N_{G_8}PL_1$

NOTE: 1. Solid symbol denotes repeatability run.
2. Data averaged.

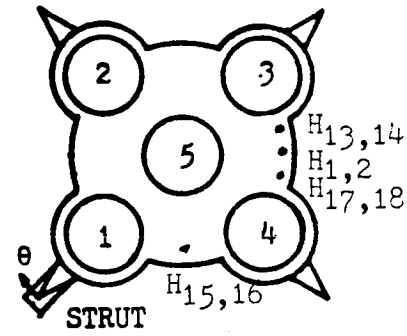

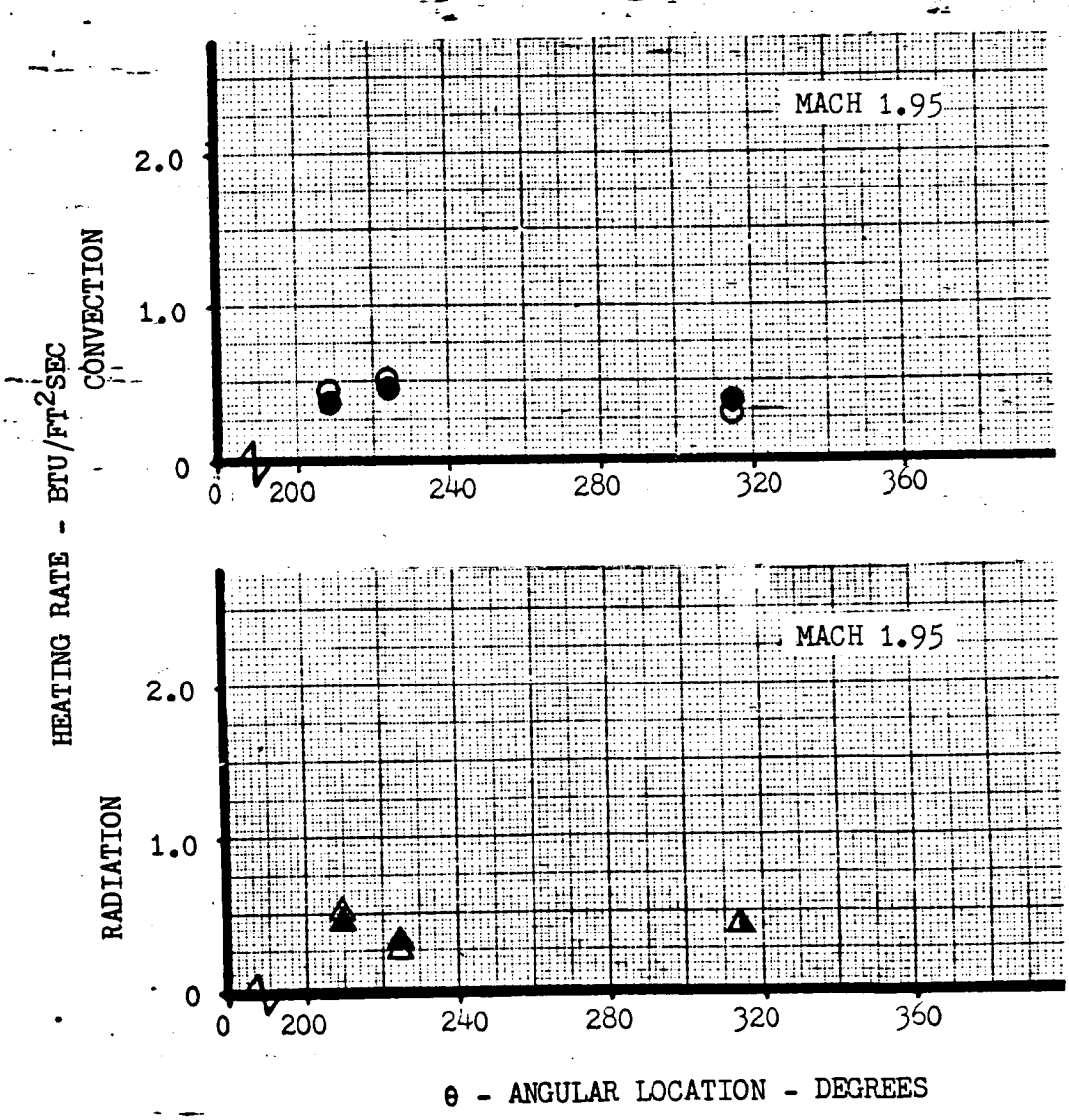

FIGURE 79 Base Heating - Repeatability

TUNNEL Lewis 8 by 6

SYM.	INST.	CONFIG.
○	$H_{1,13,15,17}$	$B_4FS_4N_{1-5}PL_1$
△	$H_{2,14,16,18}$	$B_4FS_4N_{1-5}PL_1$

NOTE: 1. Solid symbol denotes repeatability run.
2. Data averaged.
3. All data using H_2 turbine exhaust.

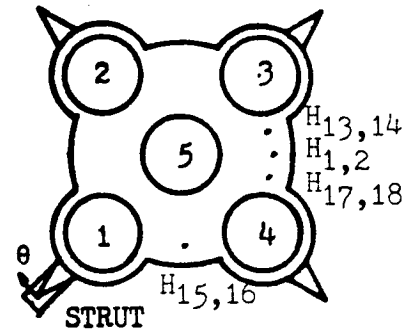

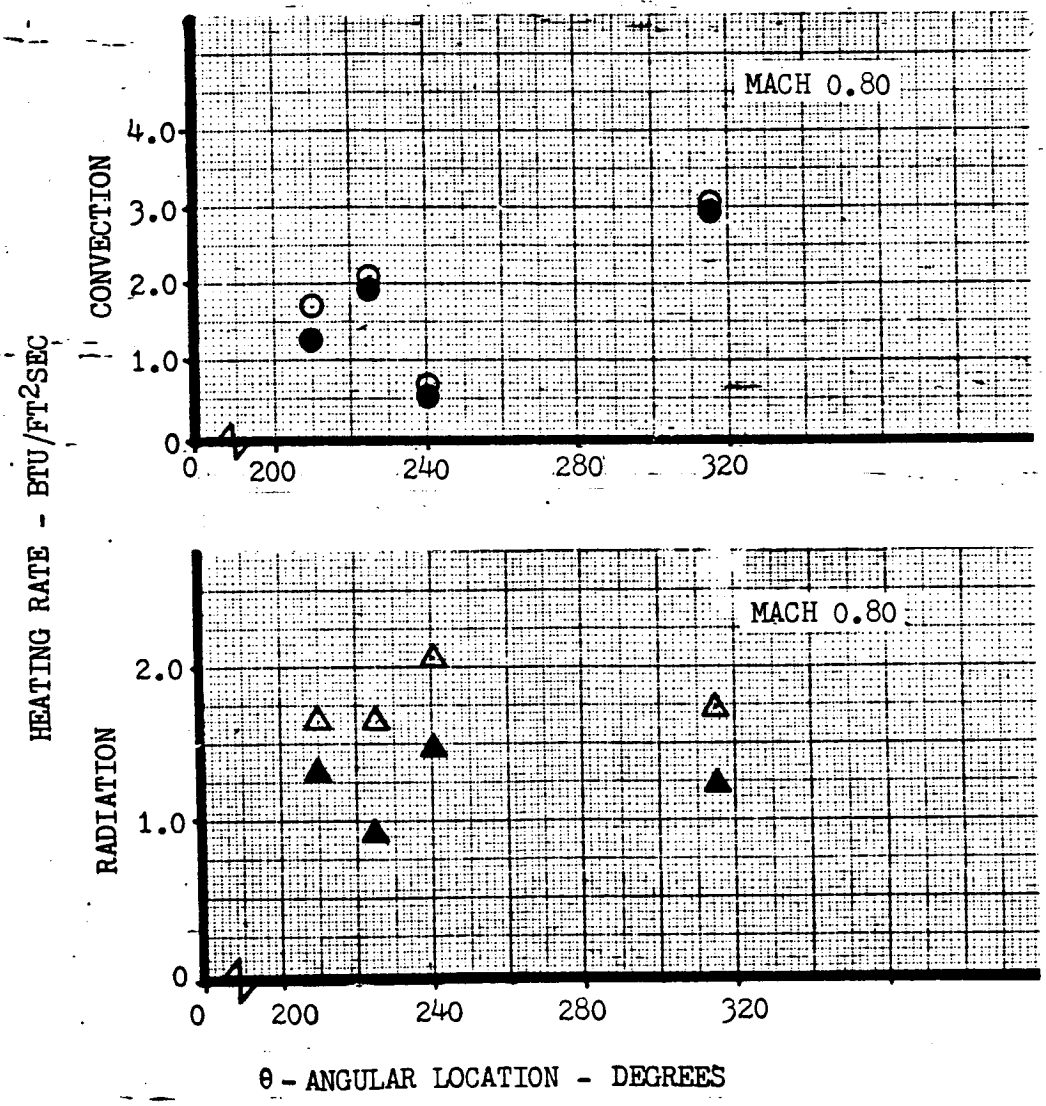

FIGURE 80 Base Heating - Repeatability

TUNNEL Lewis 8 by 6

SYM.	INST.	CONFIG.
○	$H_{1,15}$	$B_4FS_1N_{1-5}PL_1$
□	$H_{1,15}$	$B_4FS_1D_2N_{1-5}PL_1$
◇	$H_{1,15}$	$B_4FS_1D_1SC_2N_{1-5}PL_1$
△	$H_{1,15}$	$B_4FS_4D_2N_{1-5}PL_1$

NOTE: Solid symbol denotes H_1

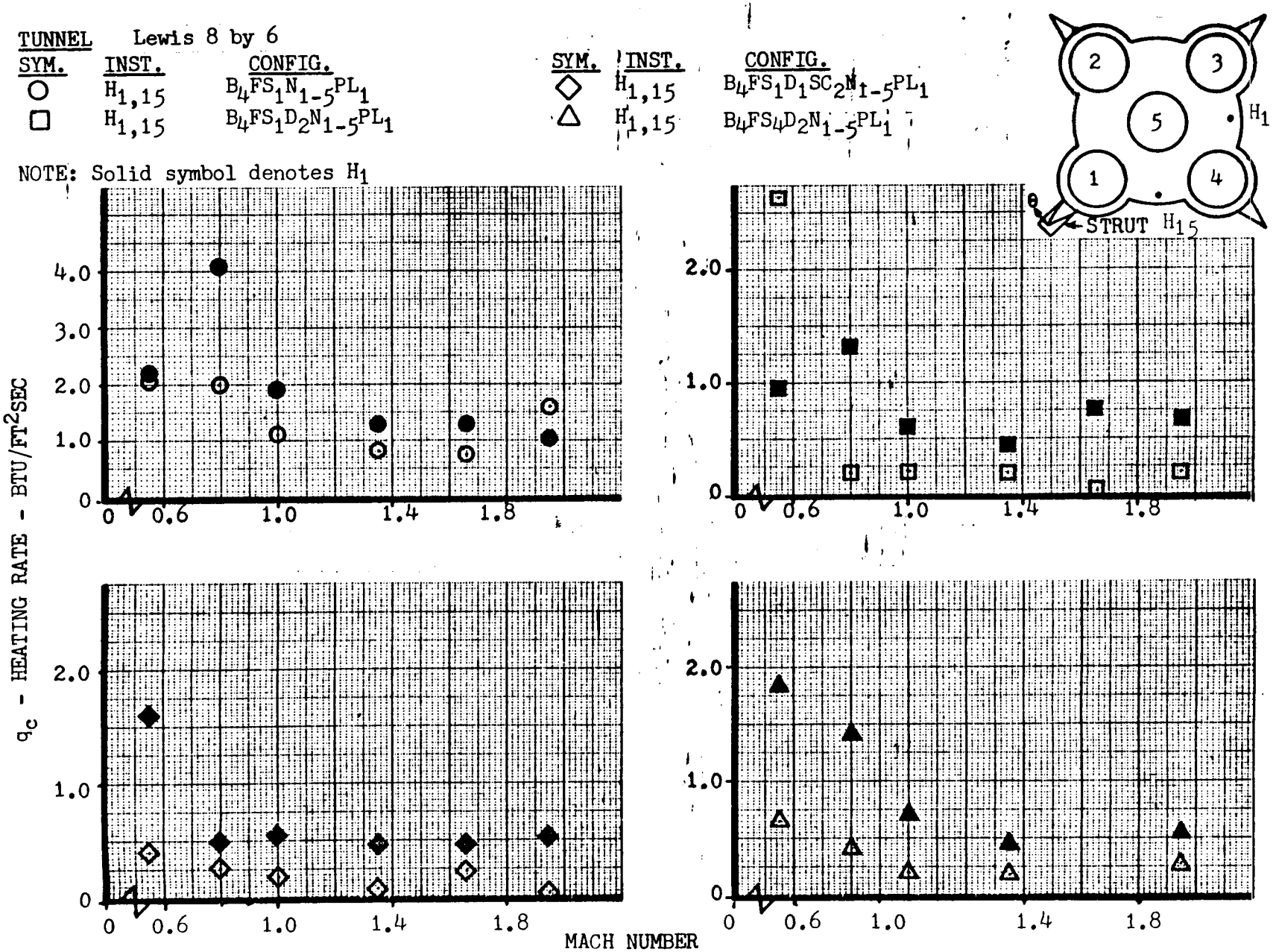

FIGURE 81 Base Heating - Convection (Symmetry)

TUNNEL LEWIS 8 BY 6

SYM.	INST.	CONFIG.
○	$H_{1,15}$	$B_4FS_1N_{1-5}PL_1$
□	$H_{1,15}$	$B_4FS_1D_2N_{1-5}PL_1$
◇	$H_{1,15}$	$B_4FS_1D_1SC_2N_{1-5}PL_1$
△	$H_{1,15}$	$B_4FS_4D_2N_{1-5}PL_1$

NOTE: 1. Solid symbol denotes H_1.
2. All data using turbine exhaust.

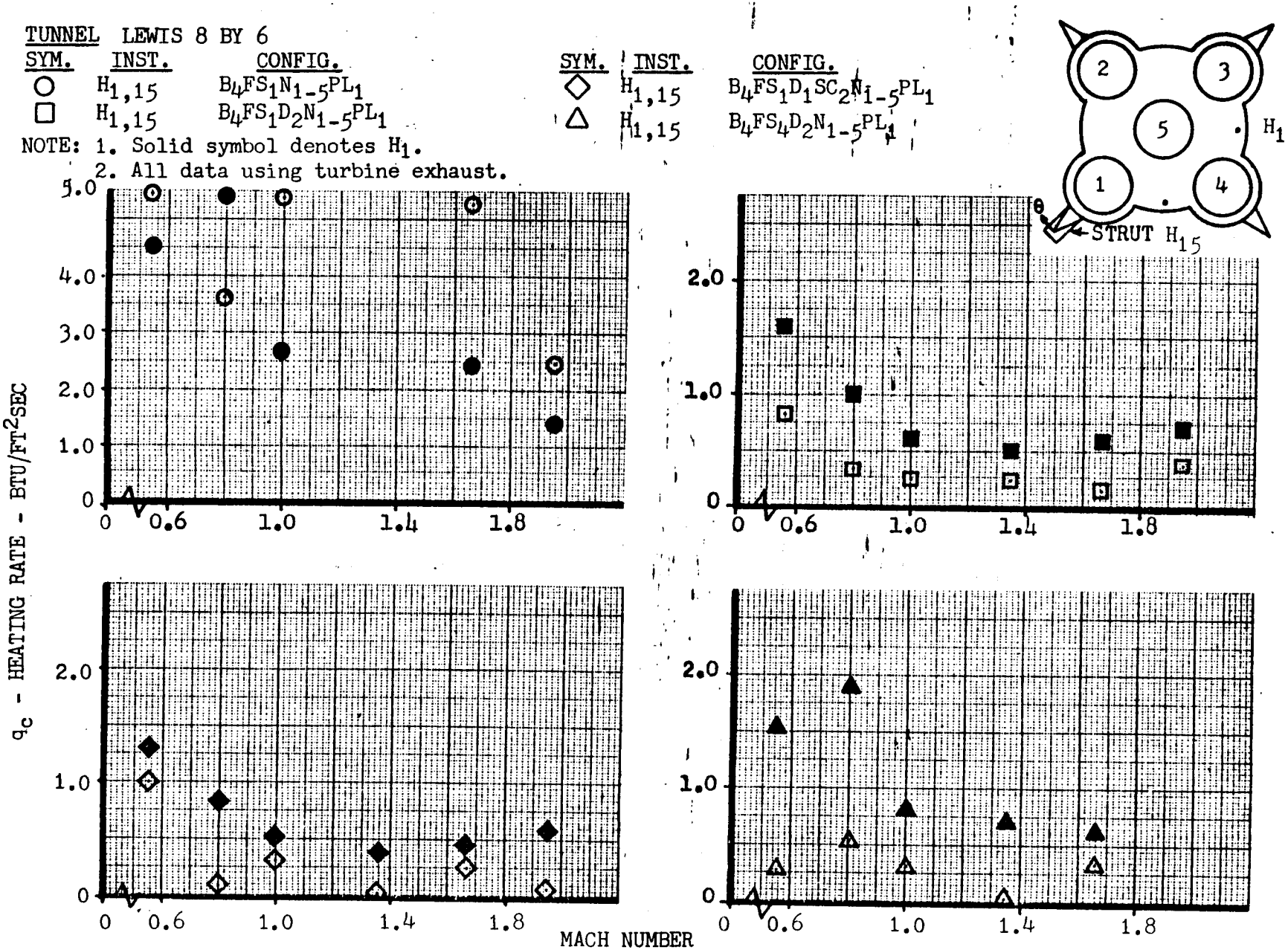

FIGURE 82 Base Heating - Convection (Symmetry)

TUNNEL Lewis 8 by 6

SYM.	INST.	CONFIG.
○	$H_{13,17}$	$B_4FS_1N_{1-5}PL_1$
□	$H_{13,17}$	$B_4FS_1D_2N_{1-5}PL_1$
◇	$H_{13,17}$	$B_4FS_1D_1SC_2N_{1-5}PL_1$
△	$H_{13,17}$	$B_4FS_4D_2N_{1-5}PL_1$

NOTE: Solid symbol denotes H_{17}

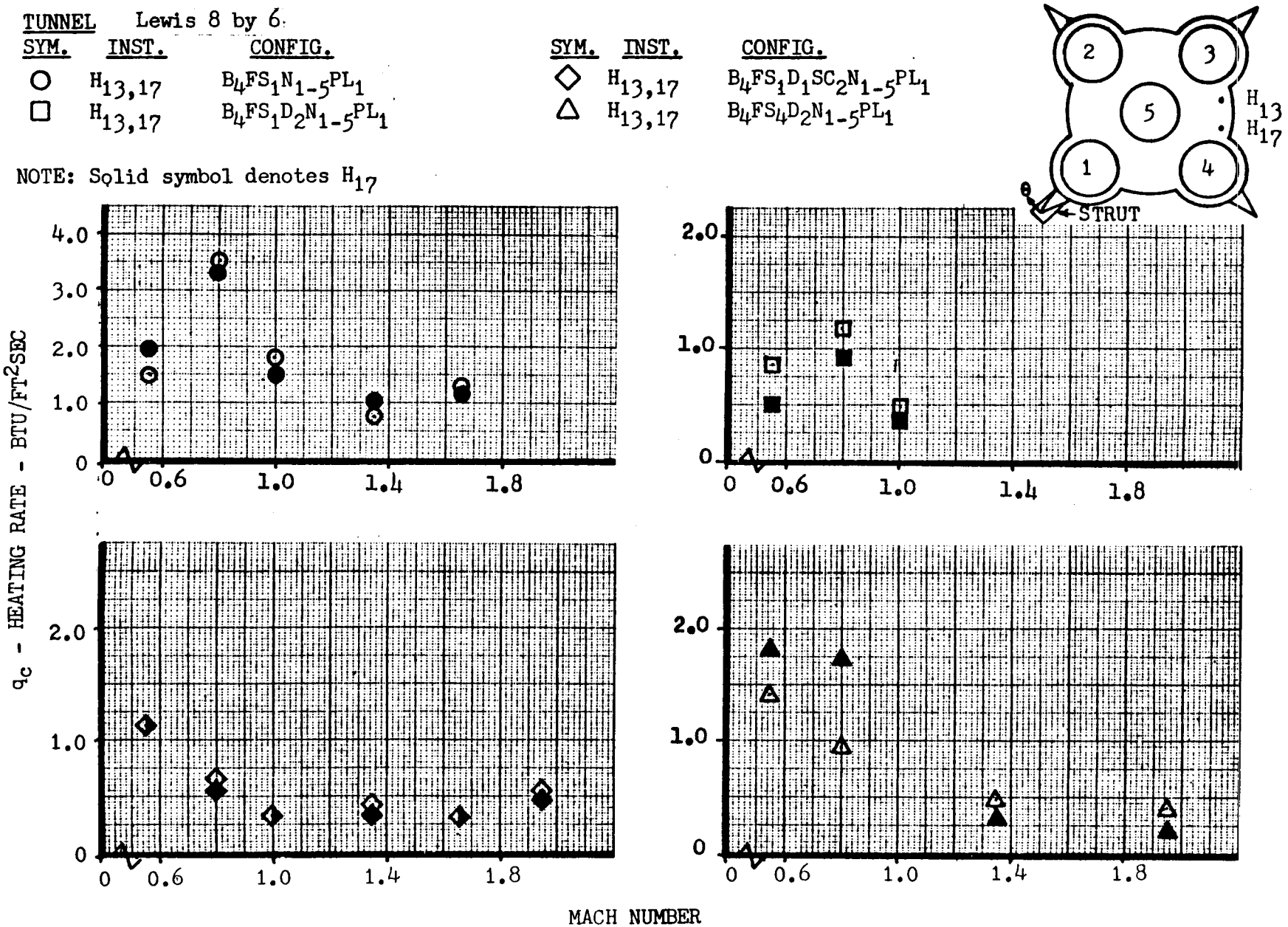

FIGURE 83 Base Heating - Convection (Symmetry)

TUNNEL Lewis 8 by 6

SYM.	INST.	CONFIG.
○	$H_{13,17}$	$B_4FS_1N_{1-5}PL_1$
□	$H_{13,17}$	$B_4FS_1D_2N_{1-5}PL_1$
◇	$H_{13,17}$	$B_4FS_1D_1SC_2N_{1-5}PL_1$
△	$H_{13,17}$	$B_4FS_4D_2N_{1-5}PL_1$

NOTE: 1. Solid symbol denotes H_{17}.
2. All data using turbine exhaust

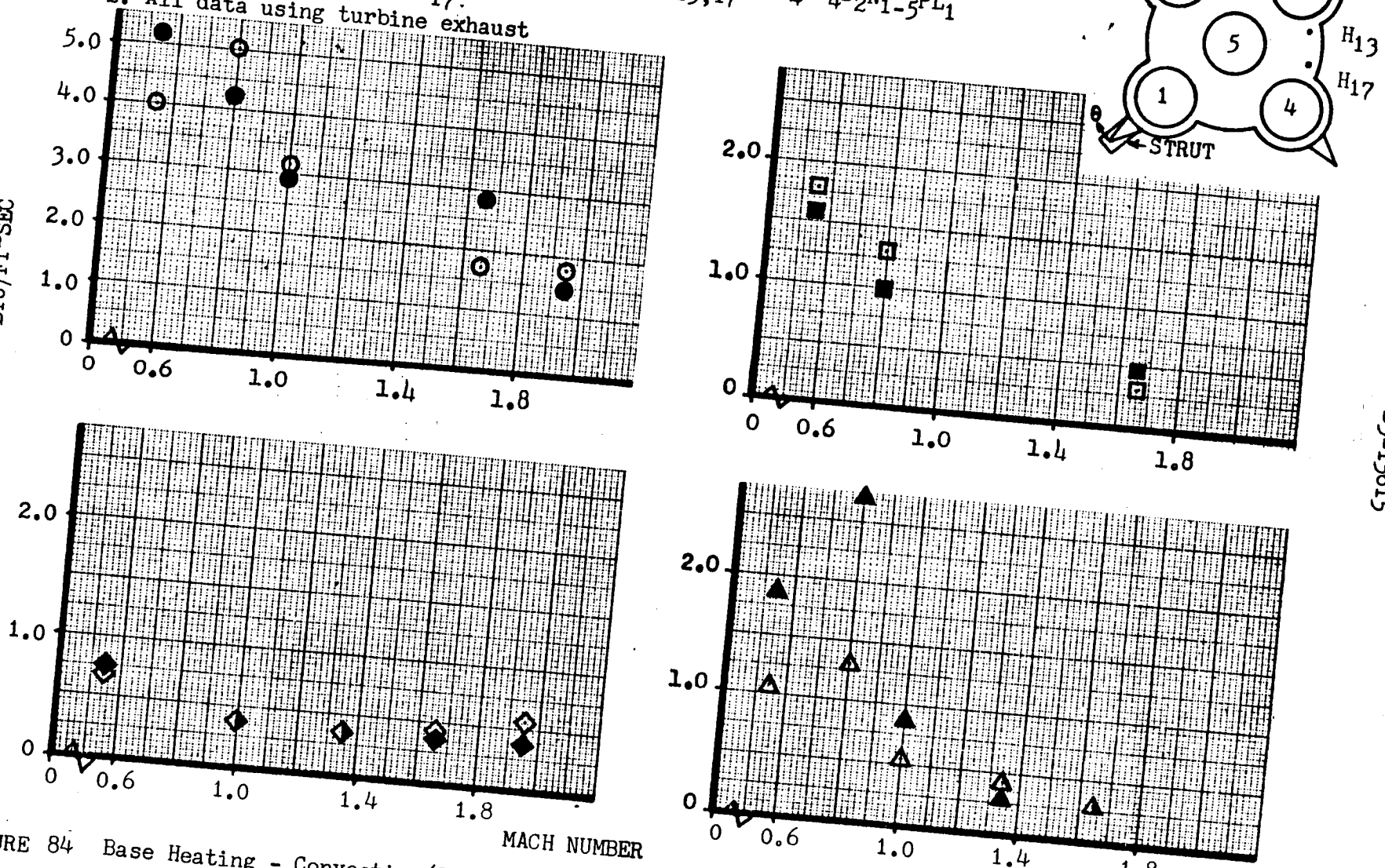

FIGURE 84 Base Heating - Convection (Symmetry)

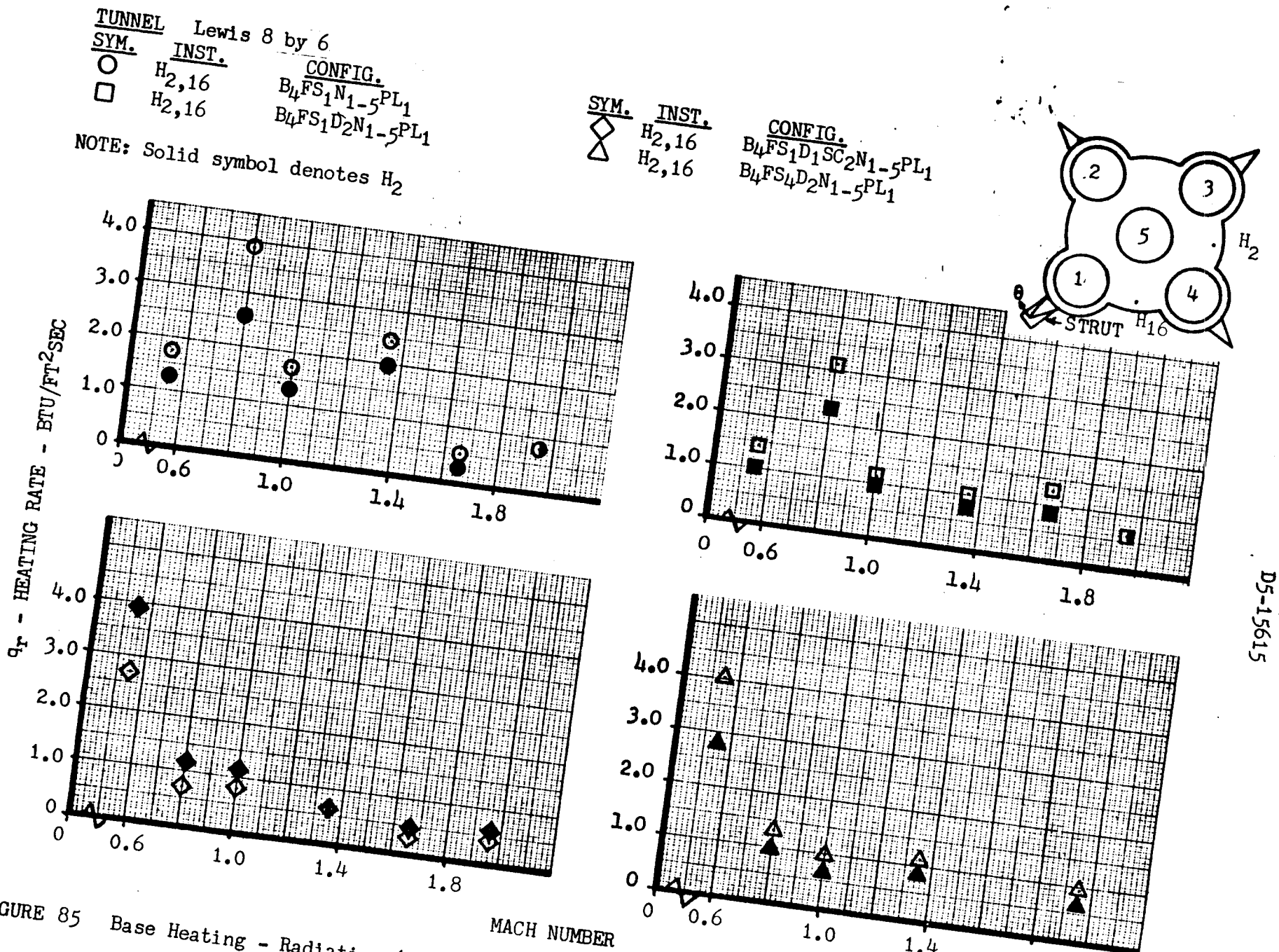

FIGURE 85 Base Heating - Radiation (Symmetry)

TUNNEL LEWIS 8 BY 6

SYM.	INST.	CONFIG.
○	$H_{14,18}$	$B_4FS_1N_{1-5}PL_1$
□	$H_{14,18}$	$B_4FS_1D_2N_{1-5}PL_1$
◇	$H_{14,18}$	$B_4FS_1D_1SC_2N_{1-5}PL_1$
△	$H_{14,18}$	$B_4FS_4D_2N_{1-5}PL_1$

NOTE: Solid symbol denotes H_{18}

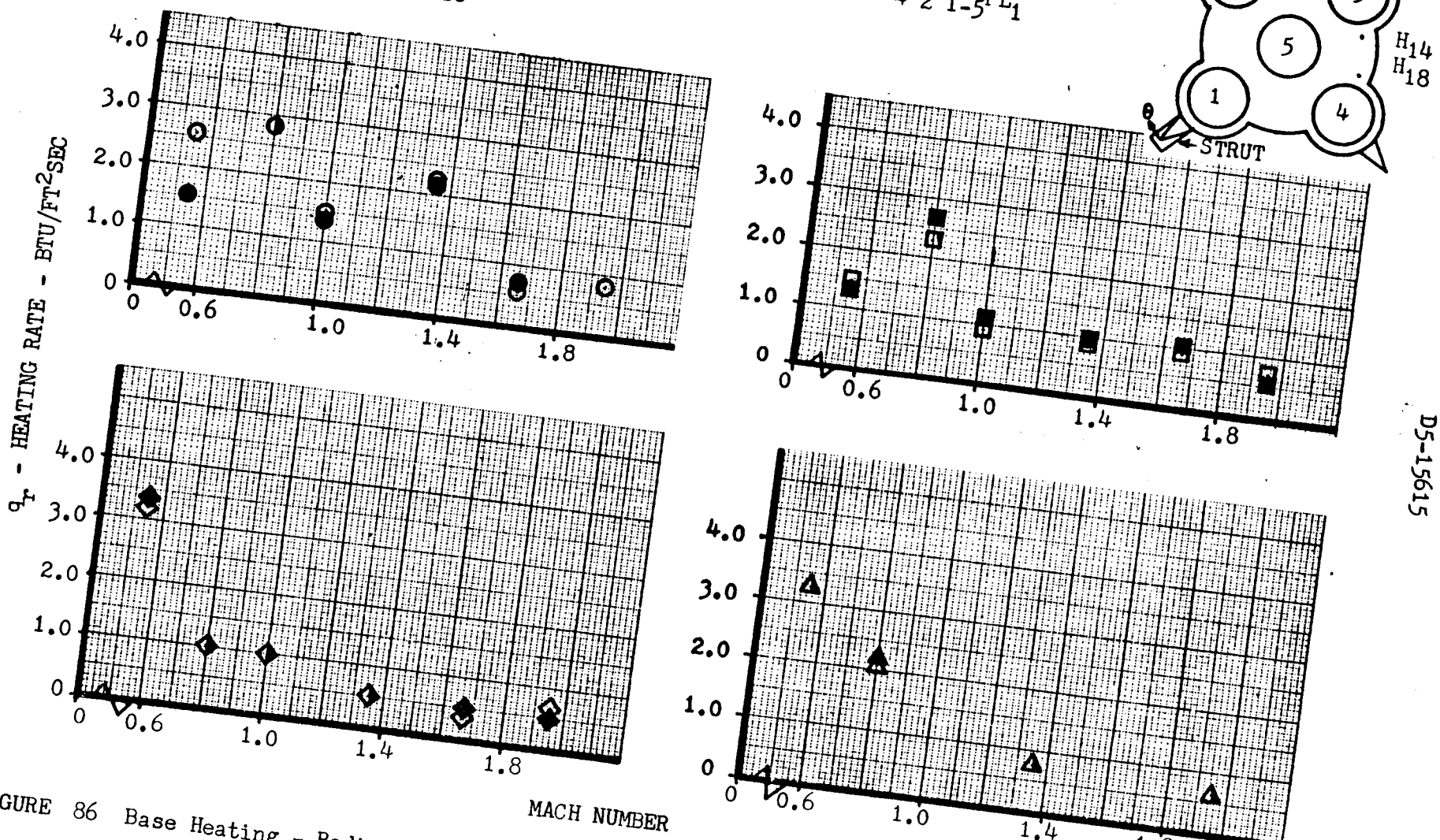

FIGURE 86 Base Heating - Radiation (Symmetry)

TUNNEL LEWIS 8 BY 6

SYM.	INST.	CONFIG.
○	P_{14}	$B_4FS_1D_1SC_2N_{1-5}PL_2$
△	P_{22}	$B_4FS_1D_1SC_2N_{1-5}PL_2$

NOTE: Solid symbol denotes turbine exhaust.

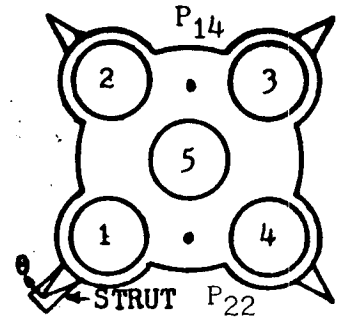

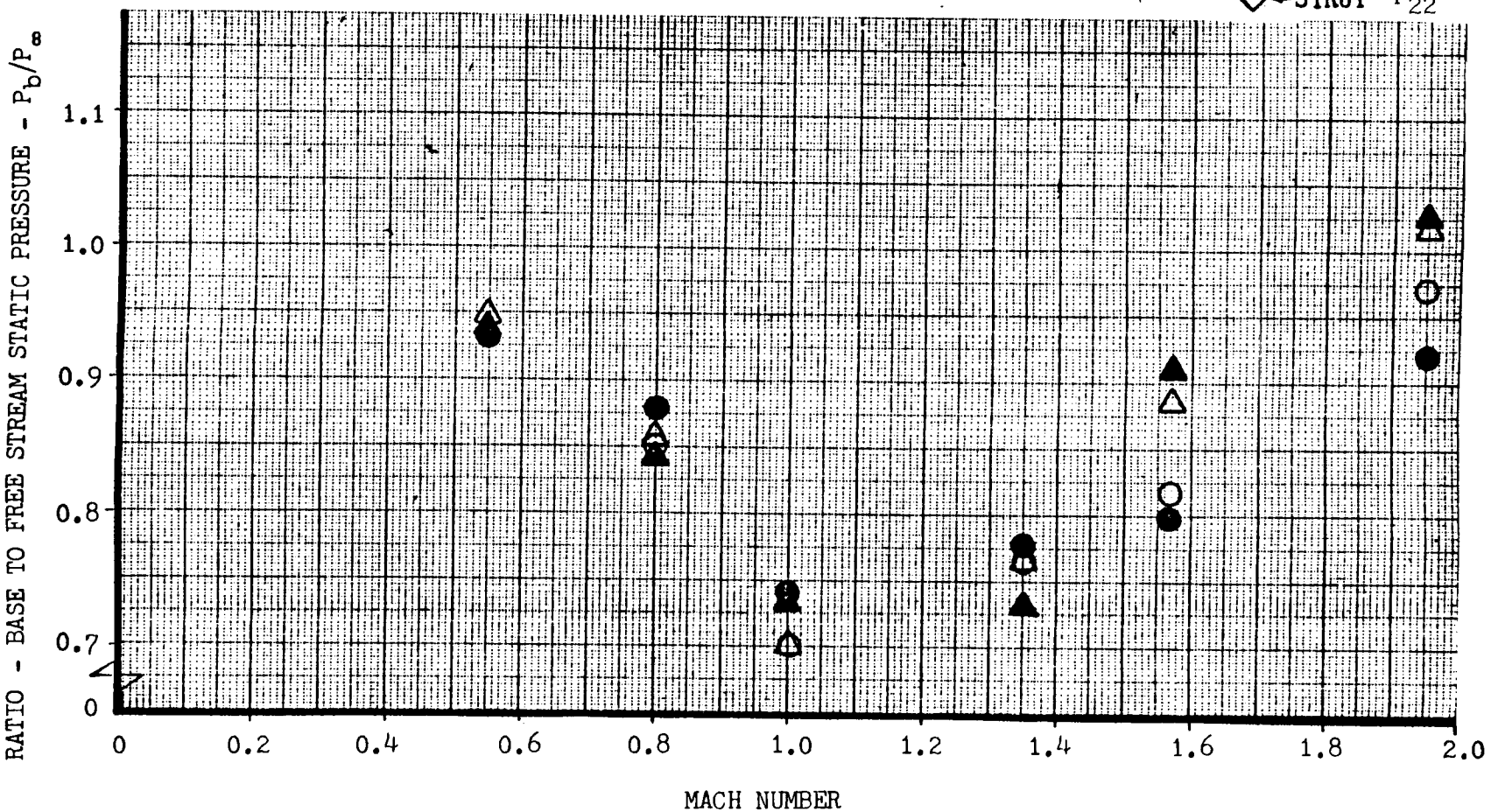

FIGURE 87 Base Pressure - Symmetry

4.5.2 (Continued)

The convective heating data show a non-symmetric condition both between quadrants and within one quadrant. The convective heating rates on gages H_1 and H_{15} are shown in Figures 81 and 82. These gages are in adjacent quadrants and indicate an average value of 1.114 BTU/FT^{2}SEC with an average difference between gages of 0.753 BTU/FT^{2}SEC. This is a 68 percent deviation from the average value for these two gages of which only 14 percent is non-repeatability.

A lack of symmetry also occurs with the convective rates within a quadrant. The convective heating rates from gages H_{13} and H_{17} are shown in Figures 83 and 84 for four different configurations and have indicated an average value of 1.196 BTU/FT^{2}SEC with an average difference between gages of 0.303 BTU/FT^{2}SEC (25 percent).

Radiation data is symmetrical both between quadrants and within a quadrant. The average difference between gages is less than the average repeatability of the data. Data from gages H_2 and H_{16} which are in different quadrants (Figure 85) show an average heating rate of 1.389 BTU/FT^{2}SEC with an average difference of 0.418 BTU/FT^{2}SEC (30 percent). Gages H_{14} and H_{18} which are in the same quadrant have an average heating rate of 1.344 BTU/FT^{2}SEC with an average difference of 0.146 BTU/FT^{2}SEC (10.9 percent) as shown in Figure 86. The repeatability of the radiation data is no better than 30 percent.

The pressure data in Figure 87 show excellent symmetry. The average difference in pressure between gages over the test range was only 0.192 psia, corresponding to 2.82 percent. The maximum spread obtained was only 0.381 psia.

4.6 CONCLUSIONS

Test data obtained from Lewis Research Center 8 by 6 foot transonic tunnel indicate that:

a. The boundary layer ahead of the model base is turbulent and approximately 2.0 inches thick.

b. Increasing Mach number and altitude cause a reduction in radiation heating.

c. Configuration changes and introduction of hydrogen turbine exhaust have a negligible effect on radiation heating.

d. The radiation level lies between hot gas theory and black body theory.

e. Scoops and deflectors effectively purge the base in the test altitude range.

f. All model convective data is considerably lower than design values.

4.6 (Continued)

g. The base pressure is increased slightly when flow deflectors are used.

h. Engine fairing scoops cause a notable pressure build up in the engine fairing area at Mach 1.66 and 1.95.

i. A lack of symmetry is evident with the convective data both between quadrants and within a particular quadrant. Radiation data appears symmetric.

j. The pressure data show excellent symmetry. The average spread between gages located at similar positions in different quadrants is within 3.0 percent.

k. Pressure, convection and hot base plate data correlate and indicate that free stream gases pass from outboard to inboard entraining some exhaust gases. No recirculation due to plume/plume impingement reaches the base in this test range.

l. The measured base gas temperature from the hot base plate was much higher than the free stream air temperature, indicating some exhaust gas is recirculated.

SECTION 5 - ANALYSIS OF LEWIS RESEARCH CENTER (LRC) 10 BY 10 FOOT SUPERSONIC TUNNEL TEST

5.0 INTRODUCTION

This section contains the data analysis of Phase II, Part II of the Saturn S-IC Model Base Heating Test Program. The test was conducted in the NASA-Lewis Research Center 10 by 10 foot Supersonic Wind Tunnel with a 2.22 percent scale model of the Saturn V, S-IC stage afterbody. Model installation in the tunnel is shown in Figure 88. Model tests were conducted at Mach numbers of 2.0, 2.5, 3.0 and 3.5 and at the simulated altitudes shown in Figure 89, during the period of October 2 through October 24, 1963. Trajectory altitude-Mach number relations are matched in this test facility. However, the tunnel total temperature is considerably less than the trajectory total temperature (Figure 89).

Flow conditions and boundary layer characteristics are determined on the body near the base by a total pressure rake. Model geometry changes consisting of engine fairing length, scoop size, engine gimbal patterns, engine out and turbine exhaust simulation are considered. The model and combustion parameters are discussed under paragraph 1.0, Volume 1.

Colored movies taken during this test series show a very light blue flame which indicates stoichemetric or oxygen rich combustion. Pressure measurements at the charge tubes indicate that the combustion should be fuel rich. A study conducted after this test series proved that the gaseous ethylene was liquifying in the propellant system during the test and therefore the actual oxygen fuel ratio (O/F) which occurred during the test is unknown.

Early in the test it was noted that radiation and convection heating rates were not significant with a standard configuration. For that reason, the test schedule was revised to do more testing without scoops and using more gimbal patterns and other configurations that would provide higher heating rates; therefore, some of the previously planned scoop and engine fairing configurations were deleted or shortened.

In comparing model test data with theory, the model test environment (external flow environment, combustion characteristics, plume shape, and model dimensions) is used in the theoretical calculations unless otherwise noted.

5.1 BOUNDARY LAYER

Total pressure measurements on the model body near the base, taken using a ten probe rake (illustrated in Figure 16, Section 1), are used to determine the boundary layer height. Actual total pressure in the boundary layer is determined by correcting the probe readings for the normal shock which stands in front of the rake. Figure 90 shows the ratio of the actual total pressure to tunnel total pressure, at the various probe heights and Mach numbers. The boundary layer edge is defined as the point at which

Reproduced from best available copy.

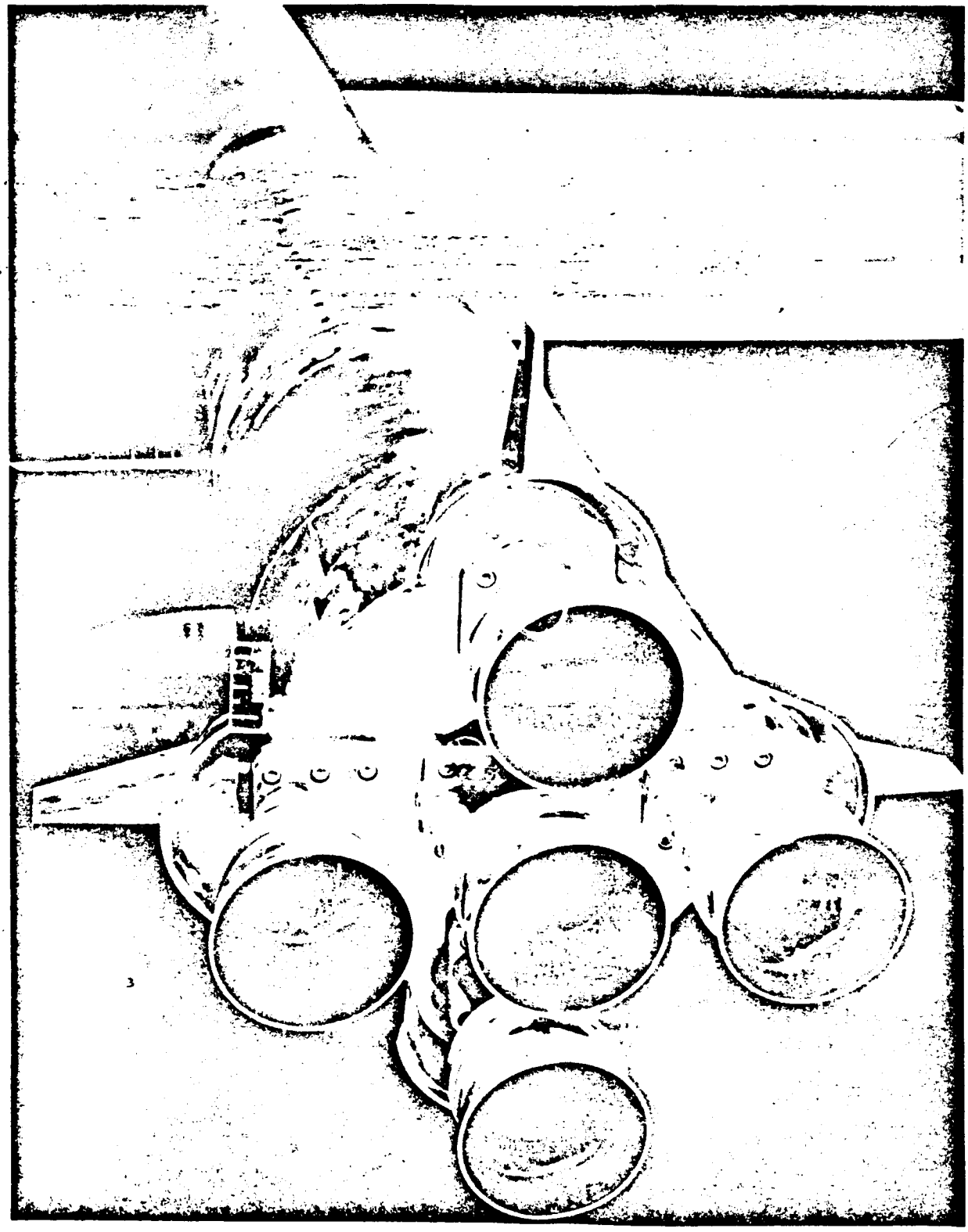

FIGURE 88 Model Installation - Lewis 10 by 10 Supersonic Wind Tunnel

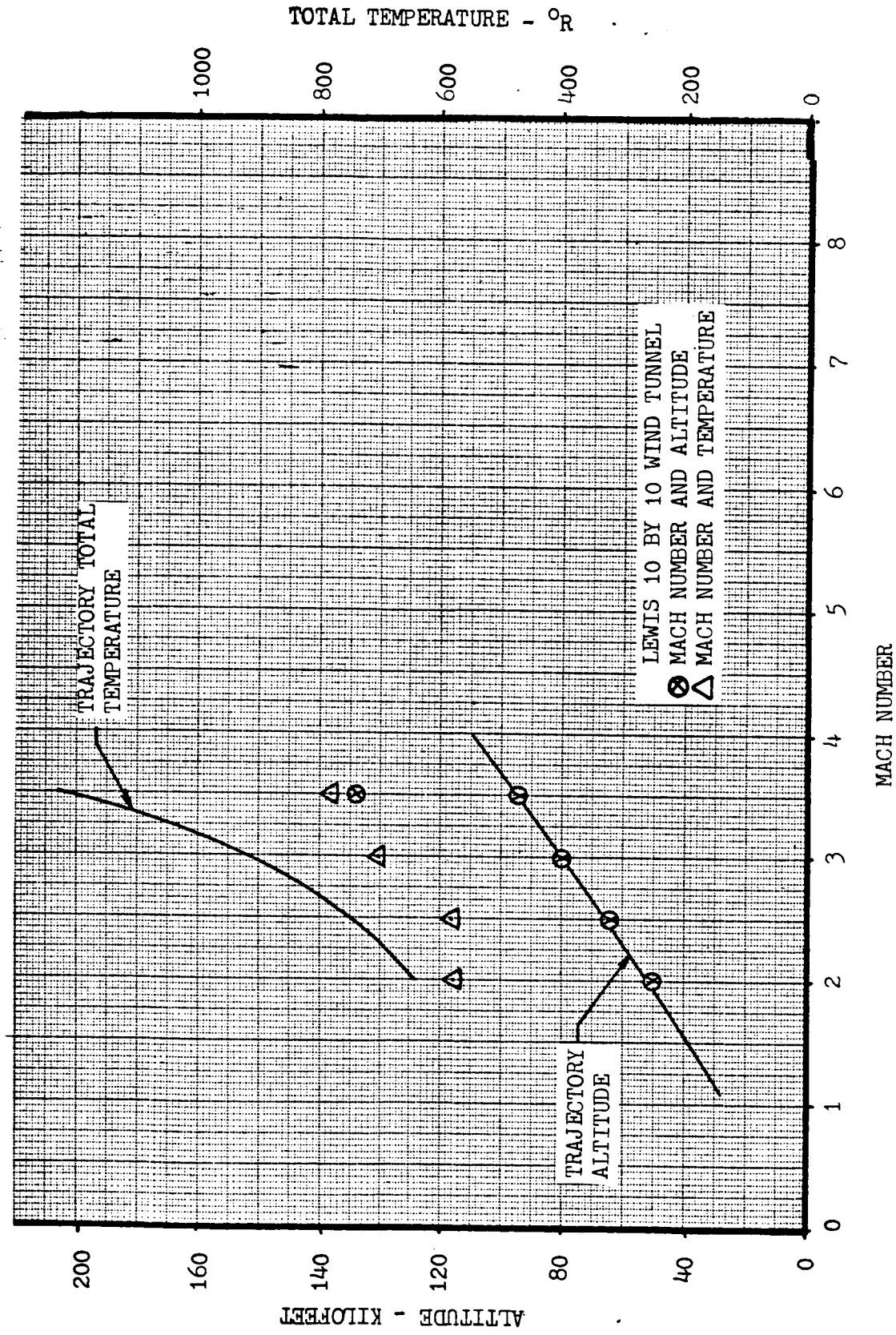

FIGURE 89 Test Conditions - Lewis 10 by 10 Tunnel

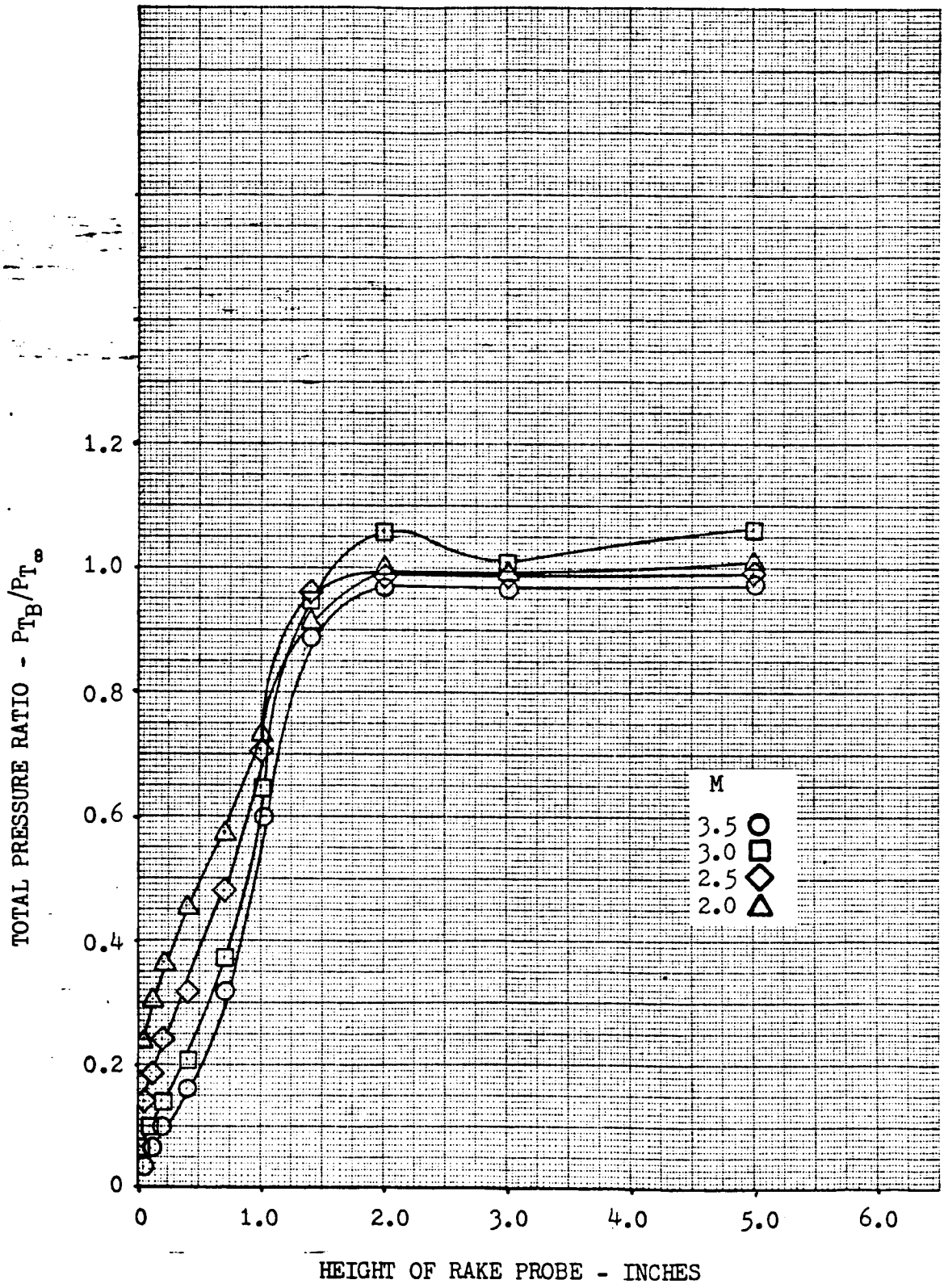

FIGURE 90 Boundary Layer Rake Data - Lewis 10 by 10 Tunnel

5.1 (Continued)

0.998 of the free stream velocity is reached. The measured boundary layer thickness (Figure 91) agrees very closely with the turbulent flow estimate described in paragraph 2.1 of volume 1.

5.2 RADIATION

In this altitude range flight test data from Saturn I indicates that radiation heating rates will be essentially constant with altitude. Theoretically this occurs because, although the form factor is increasing due to plume expansion, the temperature and emissivity are decreasing for the same reason. The two effects tend to cancel each other leaving the heating rate essentially constant.

Since the colored movies taken during the test indicate oxygen rich combustion, the emissivity will probably be very low and the magnitude of the radiation heating rates is not expected to be representative of actual flight conditions.

5.2.1 Radiation to Base

Variation in radiation to the base due to configuration changes is shown in Figure 92. Since the radiation level is so low (maximum of 0.26 BTU/FT^2SEC at Mach 2.0) only the maximum rates are shown. These may occur at any point on the base plate. As expected, no discernible effects can be attributed to the various configurations shown.

Figure 93 indicates that the radiation heating rate is constant along a radial line between engines 3 and 4 when using a configuration with both scoops and deflectors. Addition of turbine exhaust tends to reduce radiation, which indicates that the hydrogen turbine exhaust is not burning.

5.2.2 Radiation to Fin and Engine Fairing

Two radiation gages (H_{58}, H_{62}) are located on the engine facing the engine center line (See Figure 27, Volume 1). Gage H_{62} failed and data from gage H_{58} was obtained at Mach numbers of 2.0 and 2.5 only. In all cases the heating rate was between 0.118 and 0.094 BTU/FT^2SEC at Mach 2.5 and between 0.175 and 0.097 BTU/FT^2SEC at Mach 2.0.

Gage H_{20} located on the heat shield between the engine and the engine fairing produced data at Mach 2.0 and 2.5 in the same range as above. No data was obtained above Mach 2.5

Radiation heating to the base of the fin is obtained from gage H_{64} which is located close to the fin-fairing interface (See Figure 26, Volume 1). Gage H_{66}, farther out on the fin base, failed to produce data. All data shown in Figure 94 indicate radiation at less than 0.20 BTU/FT^2SEC.

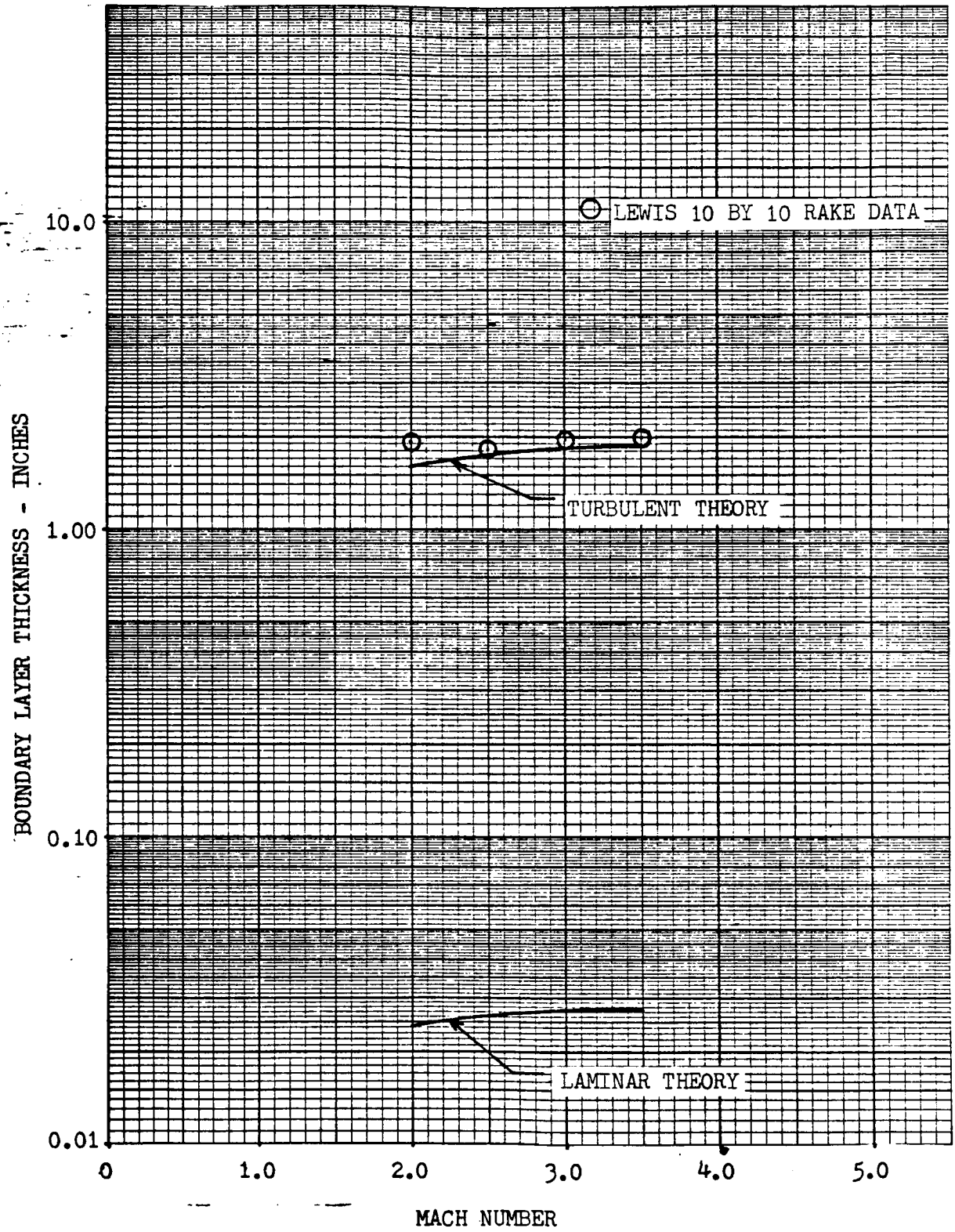

FIGURE 91 Model Boundary Layer Thickness versus Theory - LRC 10 by 10 Tunnel

TUNNEL Lewis 10 by 10

SYM.	INST.	CONFIG.
□		$B_3FS_1N_{1-5}PL_1$
○		$B_3FS_1SC_1D_1N_{1-5}PL_1$
△		$B_3FS_1SC_2D_3N_{1-5}PL_1$
◇		$B_3FS_4N_{1-5}PL_1$
◇		$B_3FS_1N_{G_3}N_{G_4}PL_1$
◺		$B_3FS_1N_{G_5}N_{G_6}PL_1$
⬠		$B_3FS_1N_7PL_1$

NOTE: Data shown are maximum recorded on base

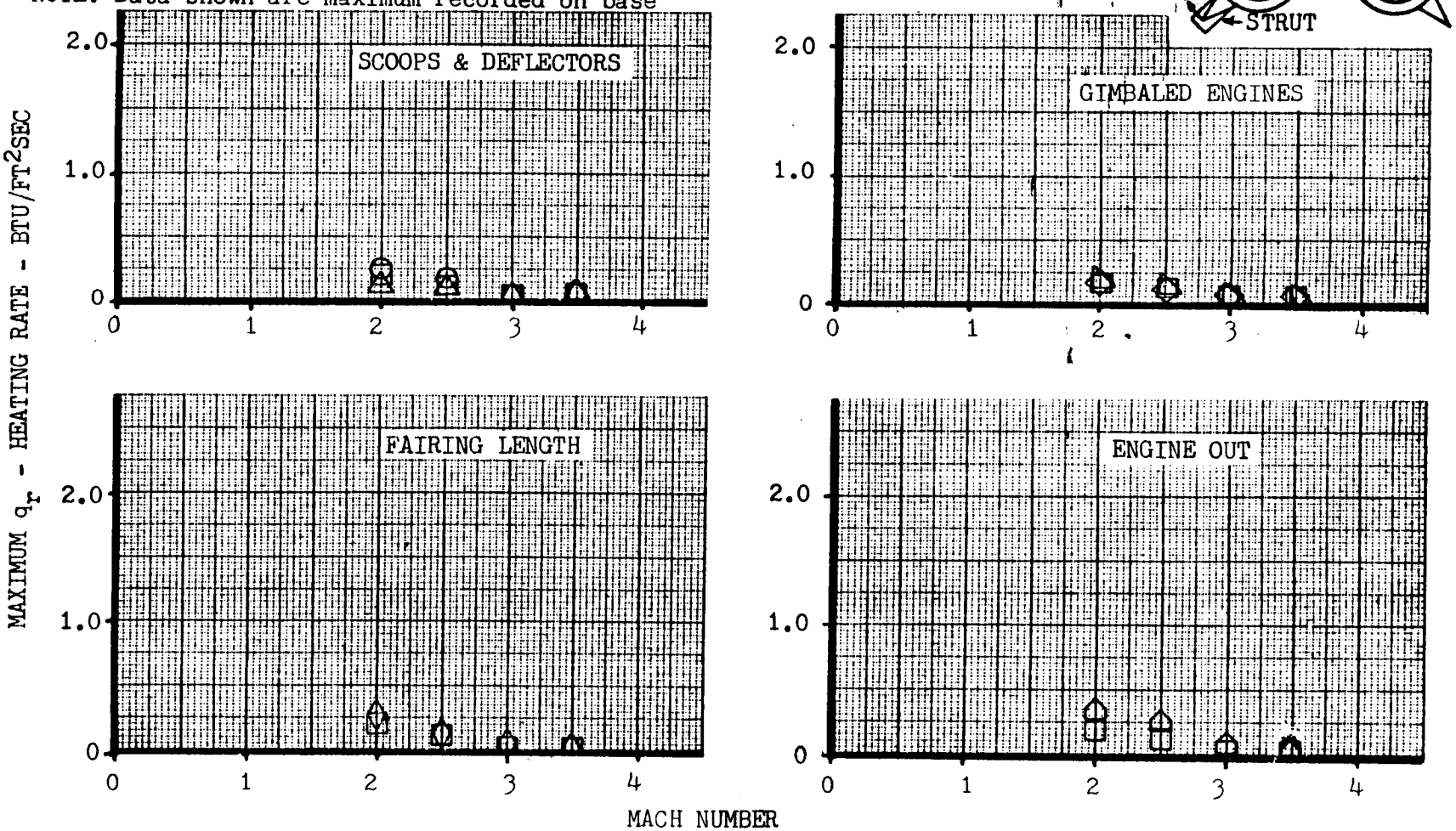

FIGURE 92 Base Heating - Radiation

TUNNEL Lewis 10 by 10

SYM.	INST.	CONFIG.
○	$H_{2,4,6,8,10}$	$B_3FS_1SC_1D_1N_{1-5}PL_1$

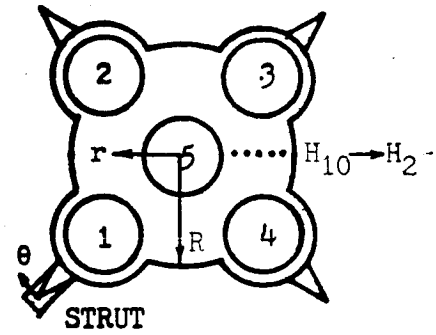

NOTE: 1. Solid symbol denotes turbine exhaust
2. Flag right denotes Mach 2.0 data
3. Flag left denotes Mach 3.5 data

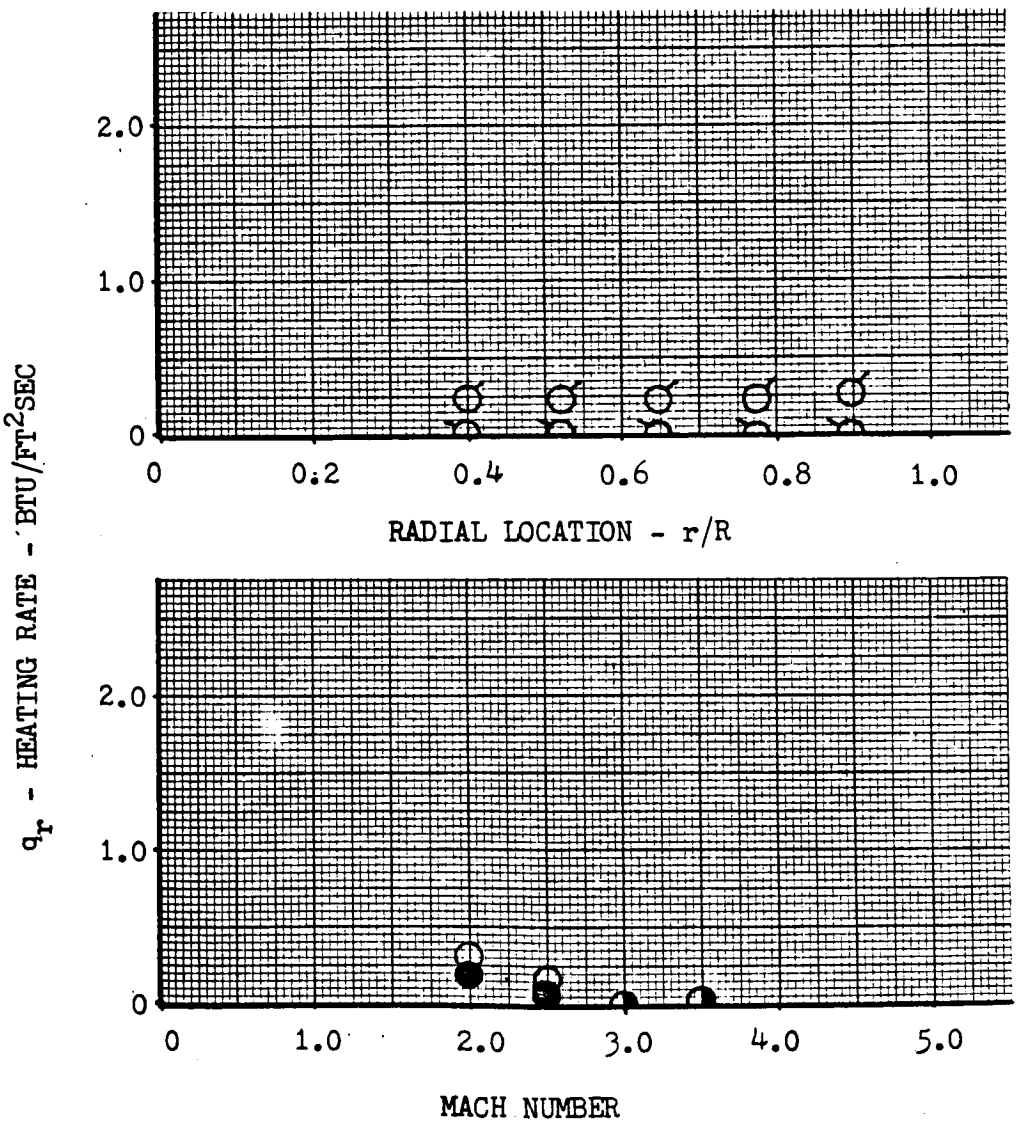

FIGURE 93 Base Heating - Radiation

TUNNEL Lewis 10 by 10

SYM.	**INST.**	**CONFIG.**
□	H_{64}	$B_3FS_1N_{1-5}PL_1$
○	H_{64}	$B_3FS_1SC_1D_1N_{1-5}PL_1$
△	H_{64}	$B_3FS_1SC_2D_3N_{1-5}PL_1$
◇	H_{64}	$B_3FS_4N_{1-5}PL_1$

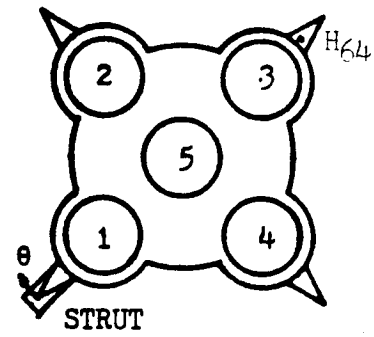

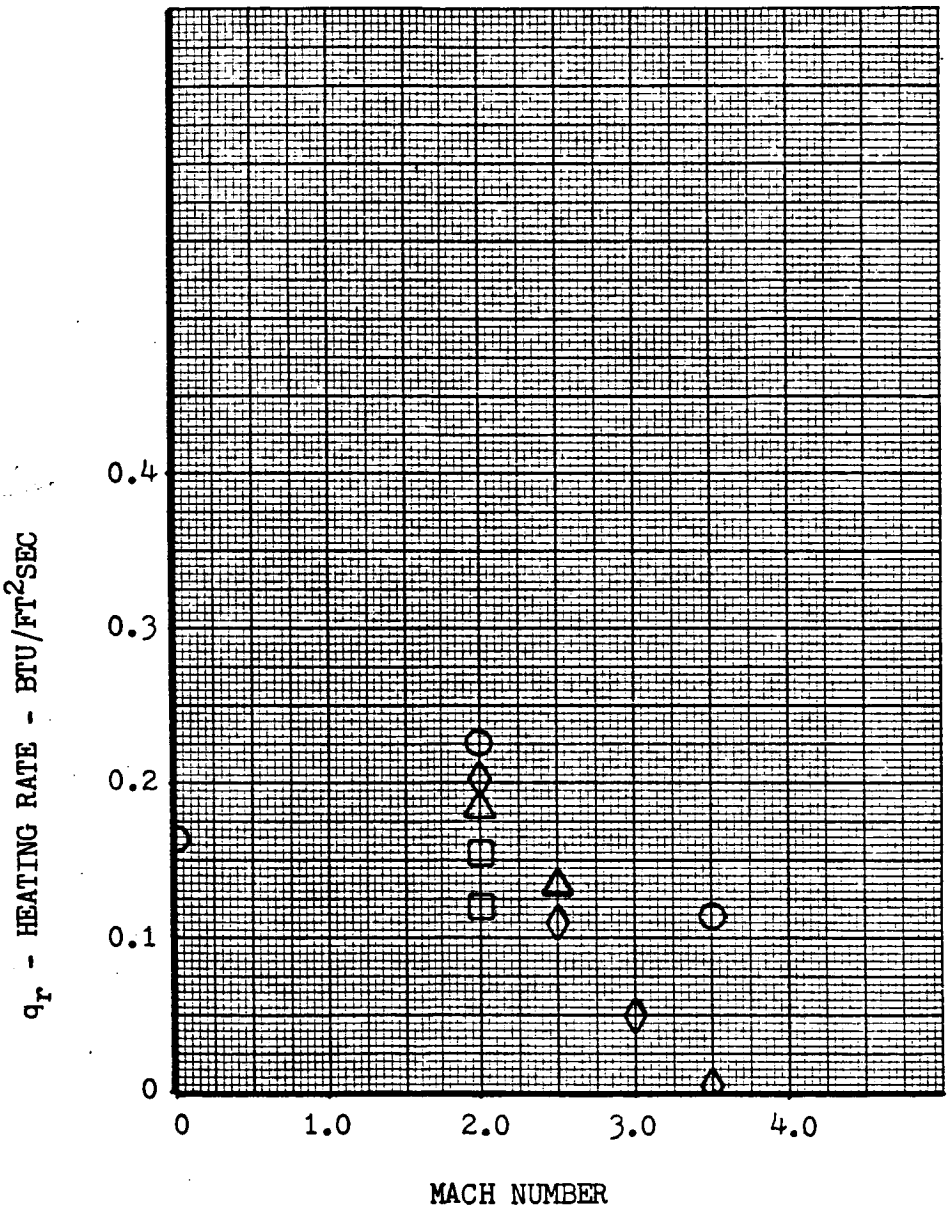

FIGURE 94 Fin Heating - Radiation

5.2.3 Radiation to Engines (External)

The center engine is instrumented on the outside as shown in Figure 22, Volume 1. The radiation heating rates to the gages were below a recordable level except H_{22} and H_{24}, which are located near the exit plane facing away from the center engine nozzle centerline. Data from these gages are sporatic, and insufficient to determine any trends. With all engines operating, the maximum heating rate recorded is 0.334 BTU/FT^{2}SEC and the average is less than 0.125 BTU/FT^{2}SEC.

5.2.4 Radiation to Engine (Engine-Out)

The center engine is plugged and instrumented as shown in Figure 24 of Volume 1. Test data for the lip, inside and outside of the engine, are shown in Figure 95. Data on the lip (gages H_{54} and H_{56}) show a rapid drop in radiation heating with increase in Mach number.

Gages H_{52} and H_{44} are located outside and inside the nozzle respectively, 180 degrees apart, near the exit plane. Gage H_{50} is located forward of and in line with H_{52}. Gage H_{48} is in line with H_{44} and near the throat.

5.2.5 Comparison with Theory

Using methods discussed in Appendix A of Volume 1, radiation on the base is estimated assuming both non-luminous hot gases and luminous particle radiation with an emissivity of 1.0. These estimates are shown on Figure 96 and compared with test data from a configuration with both scoops and deflectors. The test data compare favorably with the non-luminous gas estimate and tend to confirm the photographic evidence that combustion is occurring at a high O/F ratio.

5.3 CONVECTION

Expansion of the engine exhausts becomes significant in this test range. Impingement of the exhausts is expected to cause some recirculation of the hot gases which will create high convection heating rates, especially on the engine nozzle extension.

Convection heating rates are obtained by subtracting the measured radiation rate from the measured total heating rate.

5.3.1 Convection to Base

It became evident early in the test that heating rates would be very low for configurations with scoops and deflectors. Therefore, this phase of the planned test was de-emphasized in favor of configurations without scoops or deflectors. Results are shown in Figure 97 where heating rates represent the average for gages H_1, H_3, H_5, H_7, and H_9.

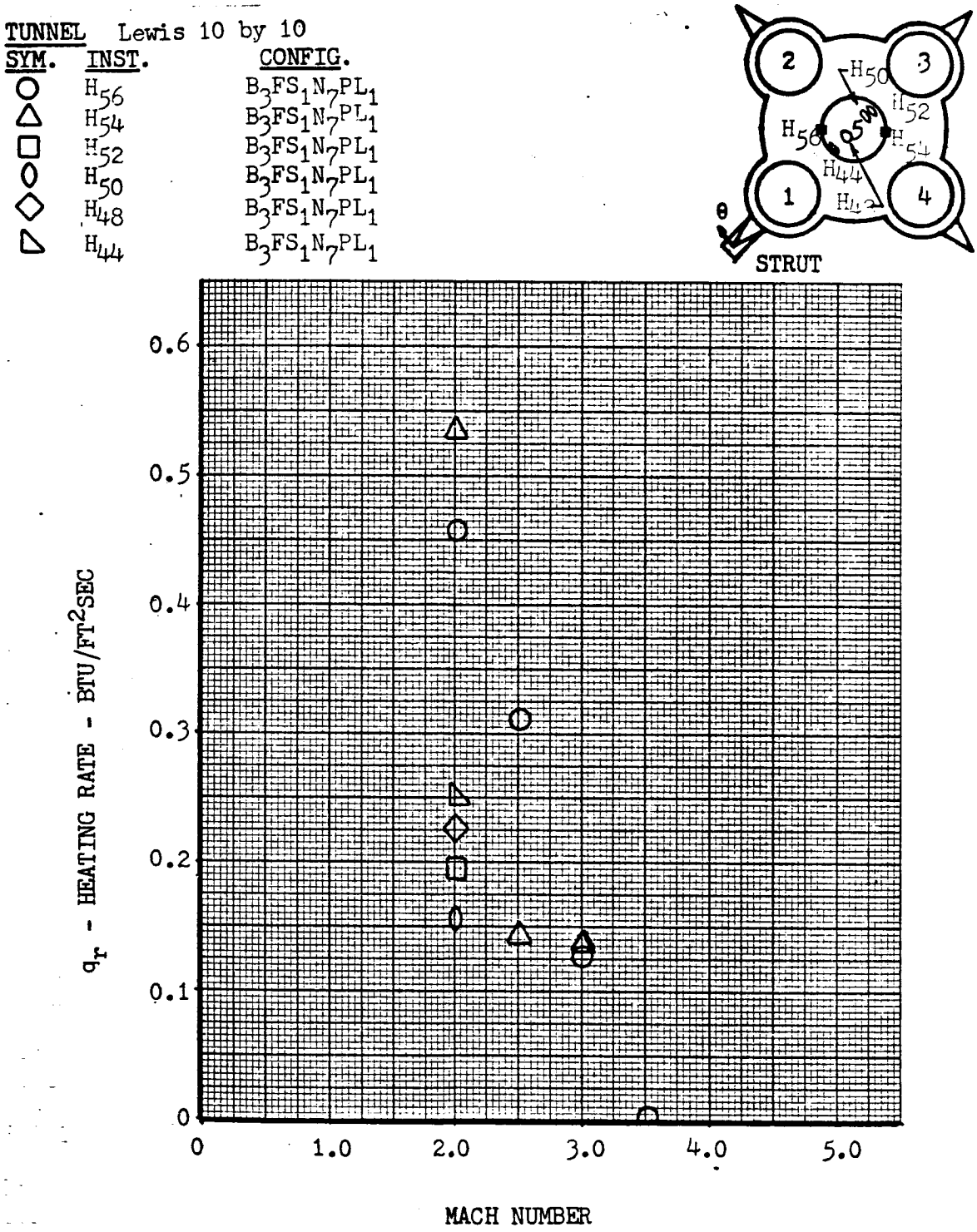

FIGURE 95 Engine Heating - Radiation (Internal)

TUNNEL Lewis 10 by 10

SYM.	INST.	CONFIG.	SYM.	INST.	CONFIG.
○	H_6	$B_3FS_1D_1SC_1N_{1-5}PL_1$			

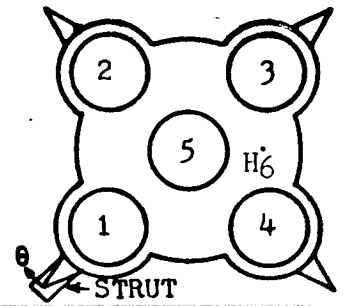

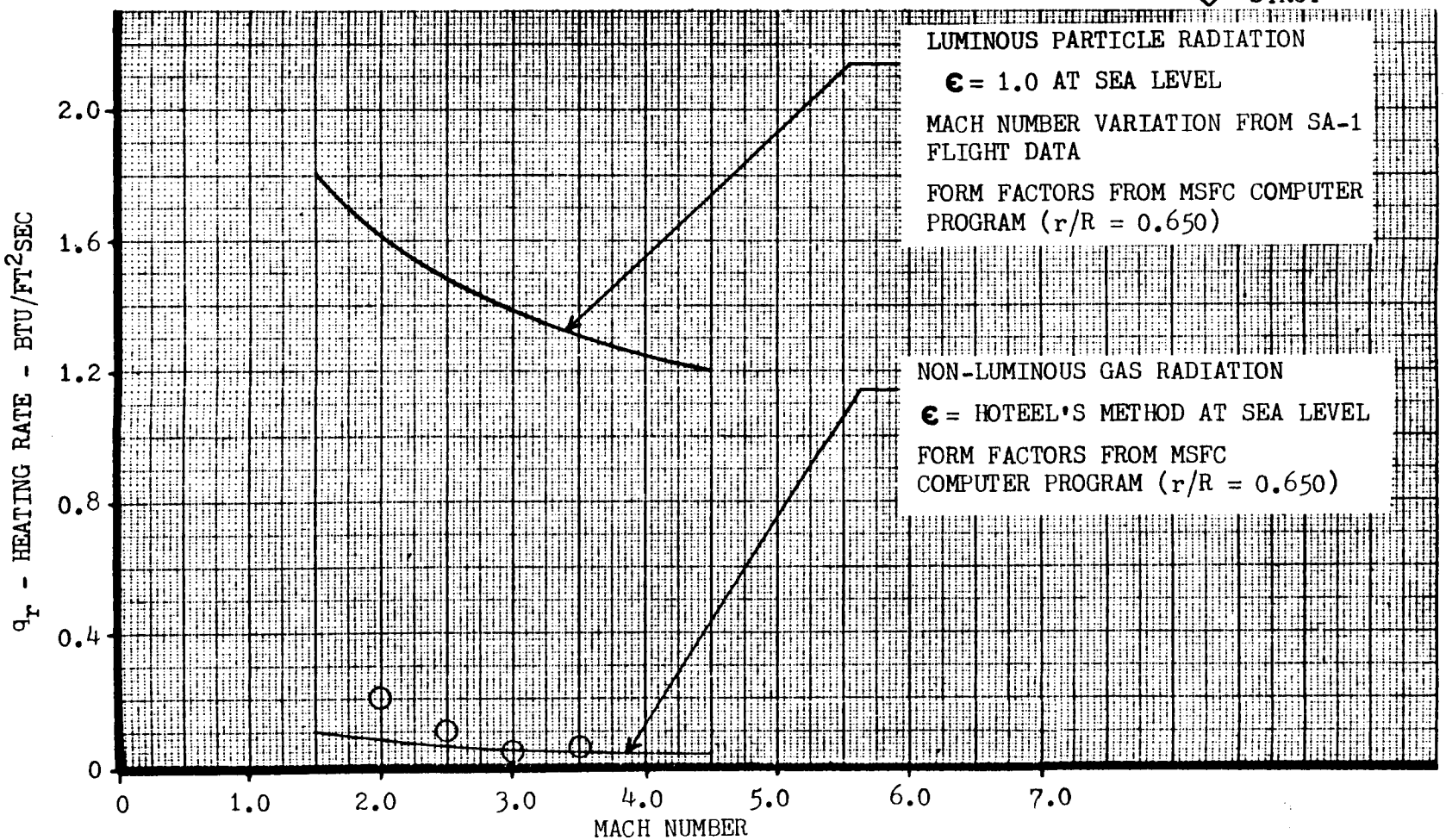

FIGURE 96 Base Heating - Radiation Versus Theory

TUNNEL Lewis 10 by 10

SYM.	INST.	CONFIG.
□	$H_{1,3,5,7,9}$	$B_3FS_1N_{1-5}PL_1$
○	$H_{1,3,5,7,9}$	$B_3FS_1SC_1D_1N_{1-5}PL_1$
△	$H_{1,3,5,7,9}$	$B_3FS_1SC_2D_3N_{1-5}PL_1$
◇	$H_{1,3,5,7,9}$	$B_3FS_4N_{1-5}PL_1$
◇	$H_{1,3,5,7,9}$	$B_3FS_1N_{G_3}N_{G_4}PL_1$
◺	$H_{1,3,5,7,9}$	$B_3FS_1N_{G_5}N_{G_6}PL_1$
⬠	$H_{1,3,5,7,9}$	$B_3FS_1N_7PL_1$

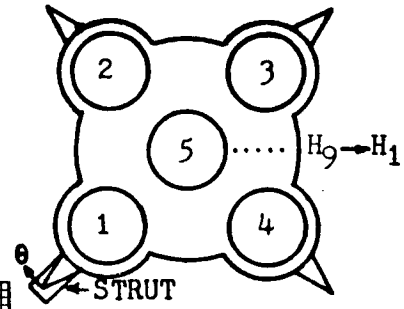

NOTE: Data averaged

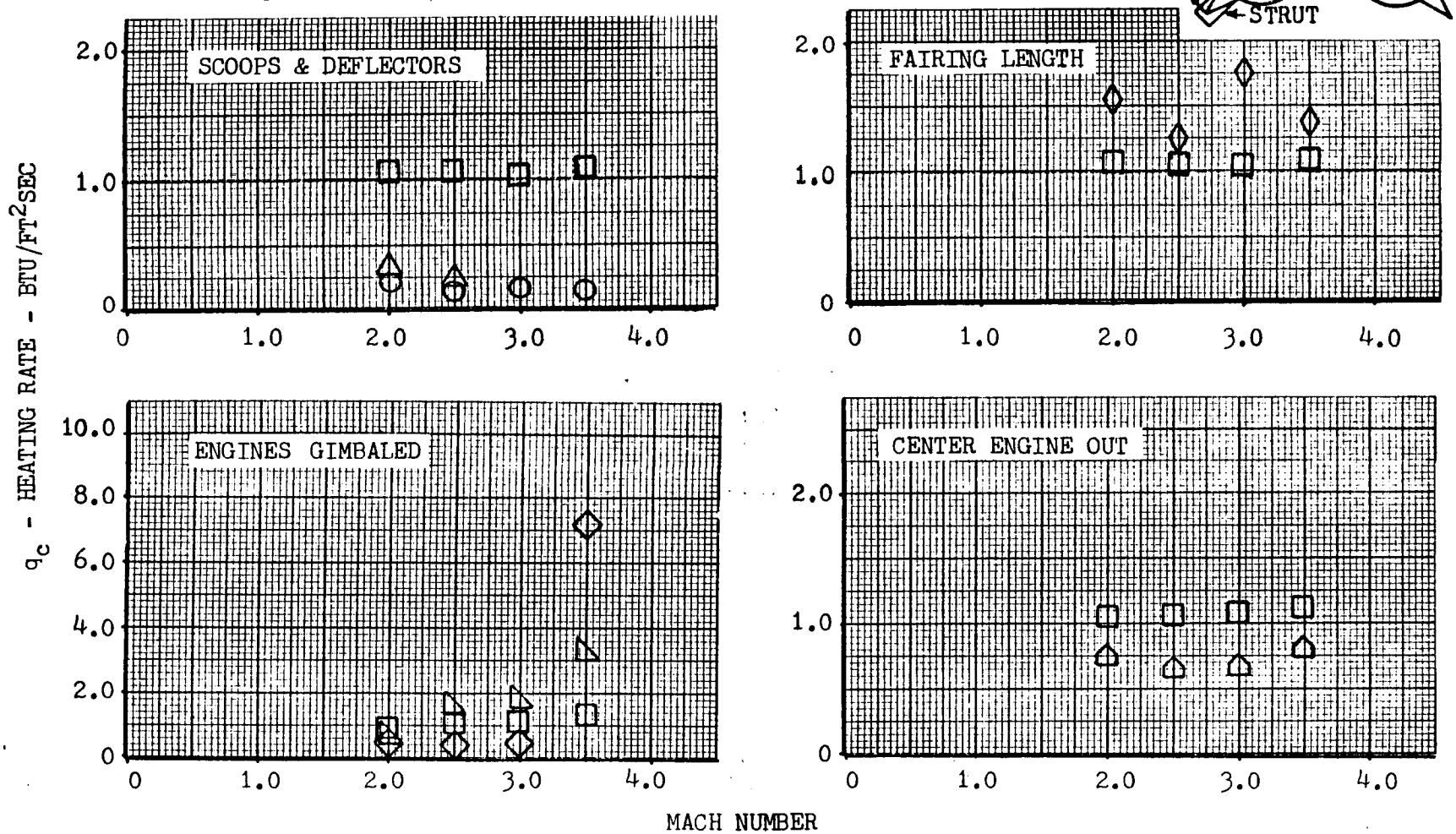

FIGURE 97 Base Heating - Convection

5.3.1 (Continued)

The base convective heating rate is substantially reduced by the addition of 10 percent scoops. Increasing the size of scoops from 10 percent to 20 percent did not significantly change the heating rates, indicating that the addition of the 10 percent scoops was sufficient. A radial distribution at Mach 3.5 is shown in Figure 98 for the same configurations. A reduction in engine fairing length from S_1 to S_3 affected an increase in the base convective heating rate as shown in Figures 97 and 98.

Two gimbal patterns on a configuration without scoops or deflectors were tested. The results, compared to the same configuration without gimballing, are shown in Figures 97 and 98. Gimbal pattern N_{G3} N_{G4} (Figure 3, Section 1), in which engines 3 and 4 are gimballed 6 degrees toward each other, has a constant average heating rate on the base of approximately 0.5 BTU/FT^{2}SEC, through Mach 3.0. At Mach number 3.5 there is a rise to 7.3 BTU/FT^{2}SEC. See Figure 97. The radial distribution at Mach 3.5 is shown in Figure 98. Data at Mach 3.5 (not shown) for the gimbal pattern on a configuration with scoops and deflectors indicate a heating rate of 0.64 BTU/FT^{2}SEC.

The effect of gimbal pattern N_{G5} N_{G6}, in which engines 3 and 4 are gimballed 8.5 degrees toward the center engine, is to increase average base heating throughout the Mach range. However the extreme is not as severe, reaching an average maximum of 2.6 BTU/FT^{2}SEC at Mach 3.5 (See Figure 97).

The results with the center engine plugged are shown in Figures 97 and 98. For all Mach numbers and radial positions the convective heating rate on the base was reduced, in some cases over 50 percent.

With the injection of turbine exhaust from all engines, the maximum convection heating rates were slightly lowered as can be noted in Figure 99 (no-scoop configuration). It is concluded that burning of the hydrogen exhaust in the base did not take place. The injection of the cooler hydrogen gas mixed with the exhaust gas lowers the overall temperature, producing a lower convective heating rate. With air being scooped into the base, the same result was evident.

5.3.2 Convection to Fin and Engine Fairing

Convective heating to the fin is shown in Figure 100. Gages H_{63} and H_{65} are located on the aft face of the fin as shown in Figure 26, Volume 1. The heating level is approximately 1 BTU/FT^{2}SEC. With the addition of turbine exhaust the rates decrease slightly.

Engine fairing heating rates for the basic fairing configuration with and without scoops and flow deflectors, and with and without turbine exhaust, are available from gage H_{57}. This gage is located on the inside of the fairing at an angle of 65 degrees from the fin centerline (See Figure 27, Volume 1). The instrument is facing the centerline of the engine. Data are shown in Figure 101.

TUNNEL Lewis 10 by 10

SYM.	INST.	CONFIG.
□	$H_{1,3,5,7,9}$	$B_3FS_1N_{1-5}PL_1$
○	$H_{1,3,5,7,9}$	$B_3FS_1SC_1D_1N_{1-5}PL_1$
△	$H_{1,3,5,7,9}$	$B_3FS_1SC_2D_3N_{1-5}PL_1$
◇	$H_{1,3,5,7,9}$	$B_3FS_4N_{1-5}PL_1$
◇	$H_{1,3,5,7,9}$	$B_3FS_1N_{G_3}N_{G_4}PL_1$
◺	$H_{1,3,5,7,9}$	$B_3FS_1N_{G_5}N_{G_6}PL_1$
⌂	$H_{1,3,5,7,9}$	$B_3FS_1N_7PL_1$

NOTE: Data are at Mach 3.5

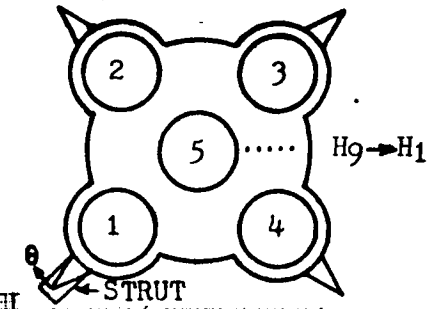

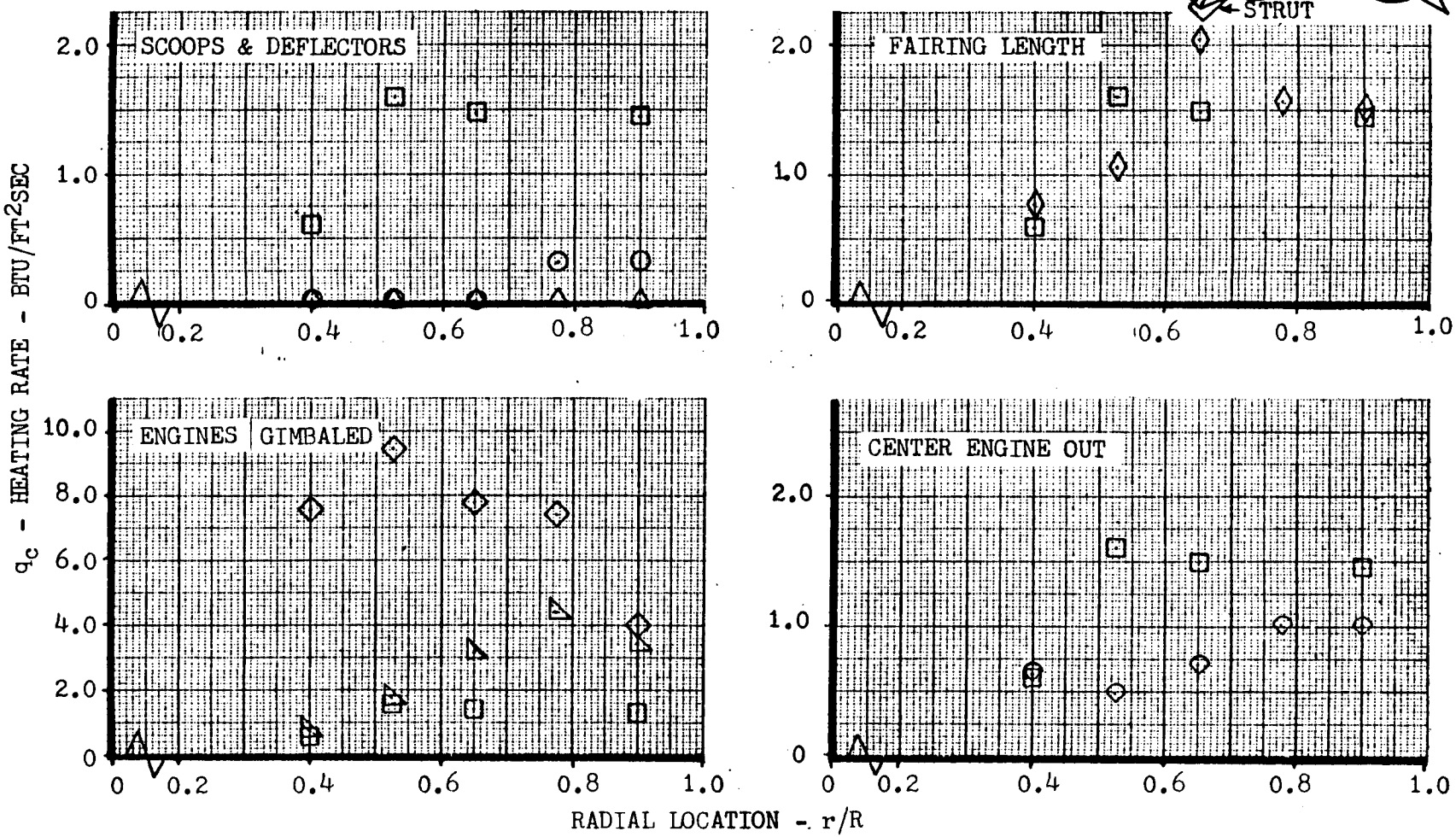

FIGURE 98 Base Heating - Convection

TUNNEL Lewis 10 by 10

SYM.	INST.	CONFIG.
□		$B_3FS_1N_{1-5}PL_1$
○		$B_3FS_1SC_1D_1N_{1-5}PL_1$

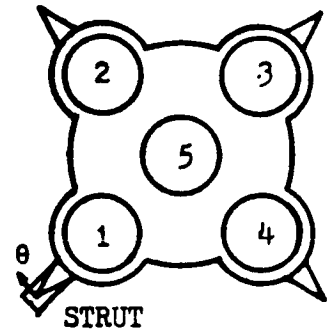

NOTE: 1. Data shown are maximums recorded on base.
2. Solid symbol denotes turbine exhaust

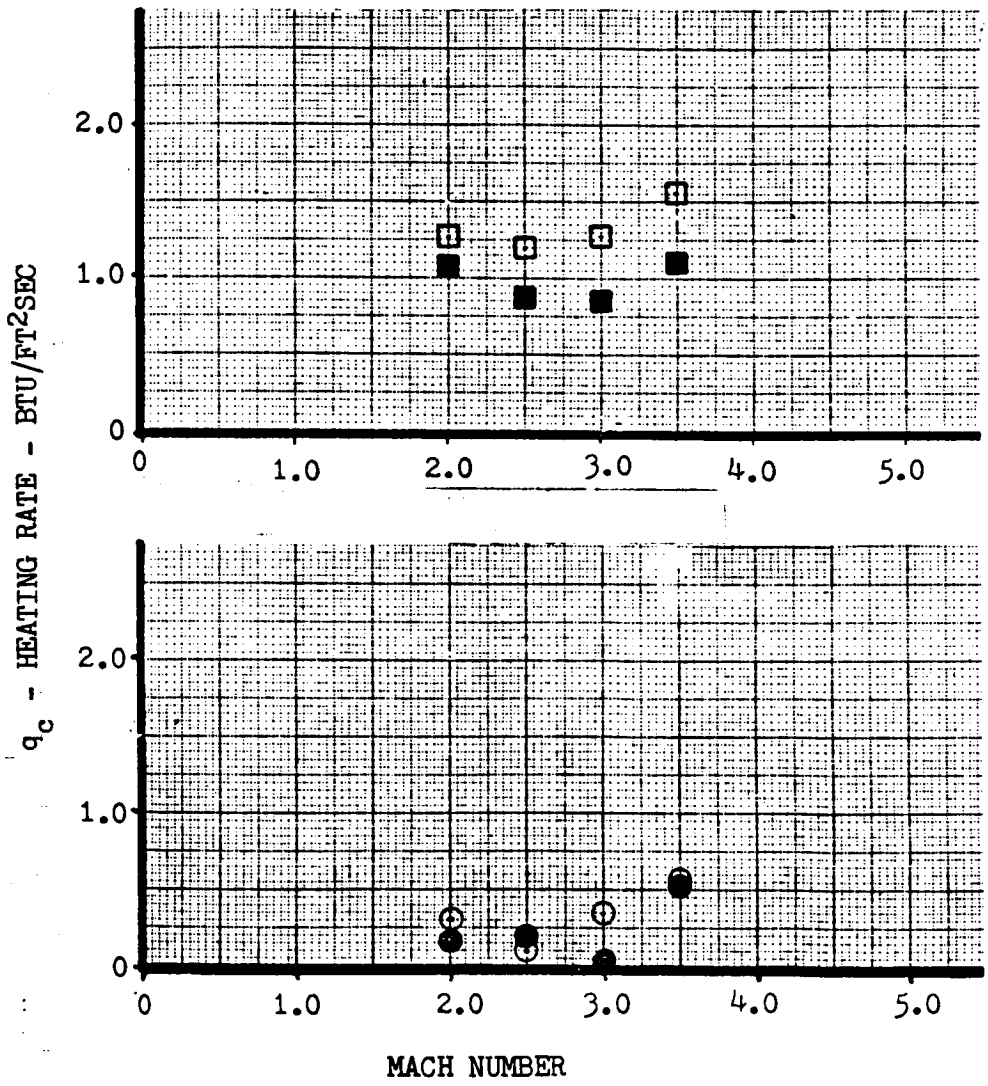

FIGURE 99 Base Heating - Convection

TUNNEL Lewis 10 by 10

SYM.	INST.	CONFIG.
◊	H_{63}	$B_3FS_4N_{1-5}PL_1$
◊	H_{65}	$B_3FS_4N_{1-5}PL_1$

NOTE: Solid symbol denotes turbine exhaust

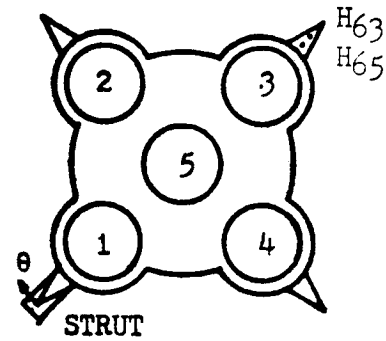

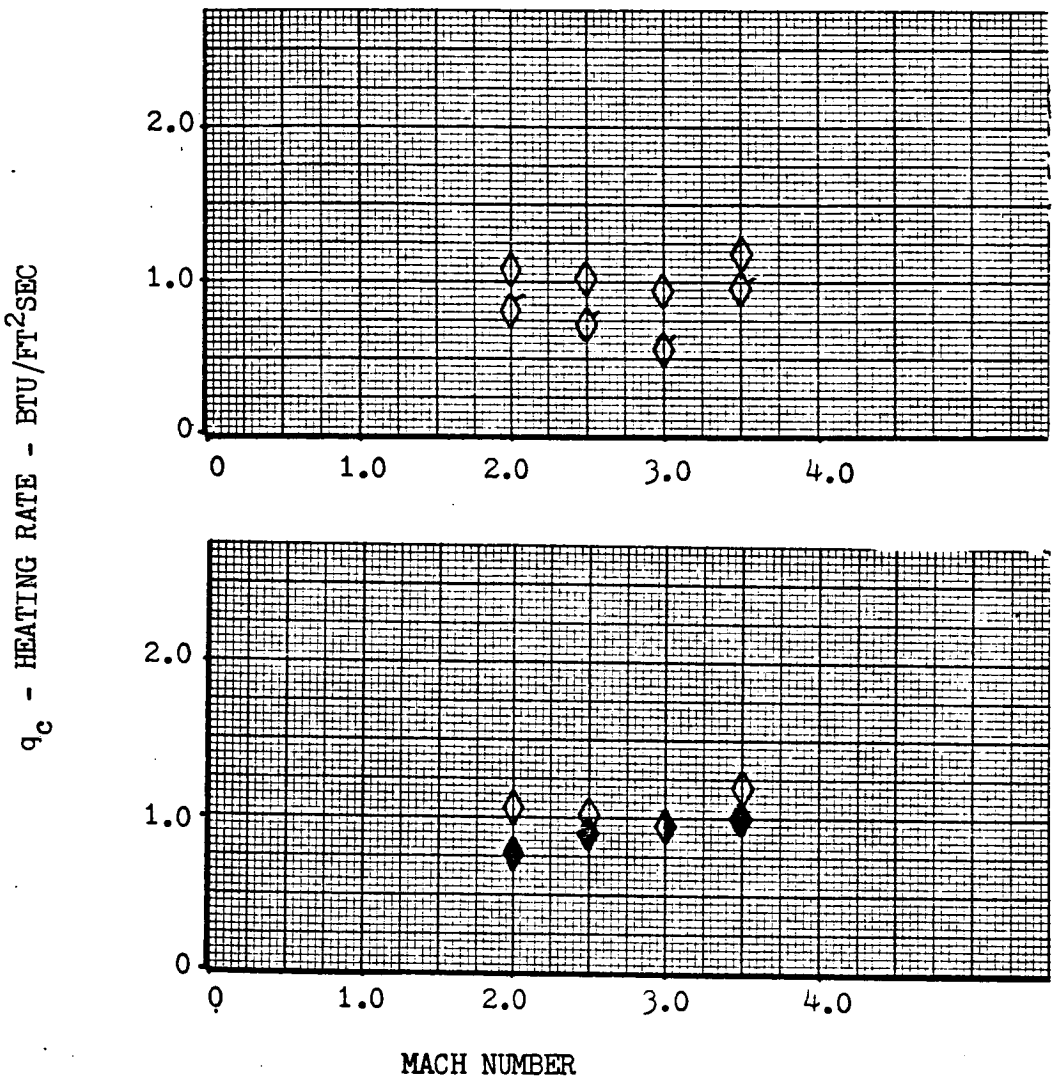

FIGURE 100 Fin Heating - Convection

TUNNEL Lewis 10 by 10

SYM.	INST.	CONFIG.
□	H_{57}	$B_3FS_1N_{1-5}PL_1$
□	H_{59}	$B_3FS_1N_{1-5}PL_1$
○	H_{57}	$B_3FS_1SC_1D_1N_{1-5}PL_1$
△	H_{59}	$B_3FS_1SC_2D_3N_{1-5}PL_1$
◇	H_{19}	$B_3FS_1N_{1-5}PL_1$
⬠	H_{19}	$B_3FS_1SC_1D_1N_{1-5}PL_1$

NOTE: Solid symbol denotes turbine exhaust.

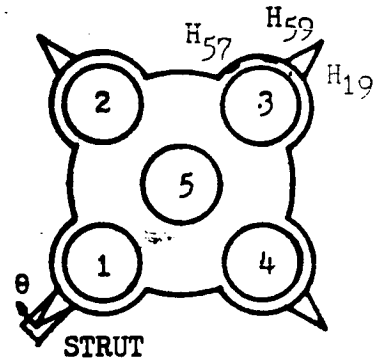

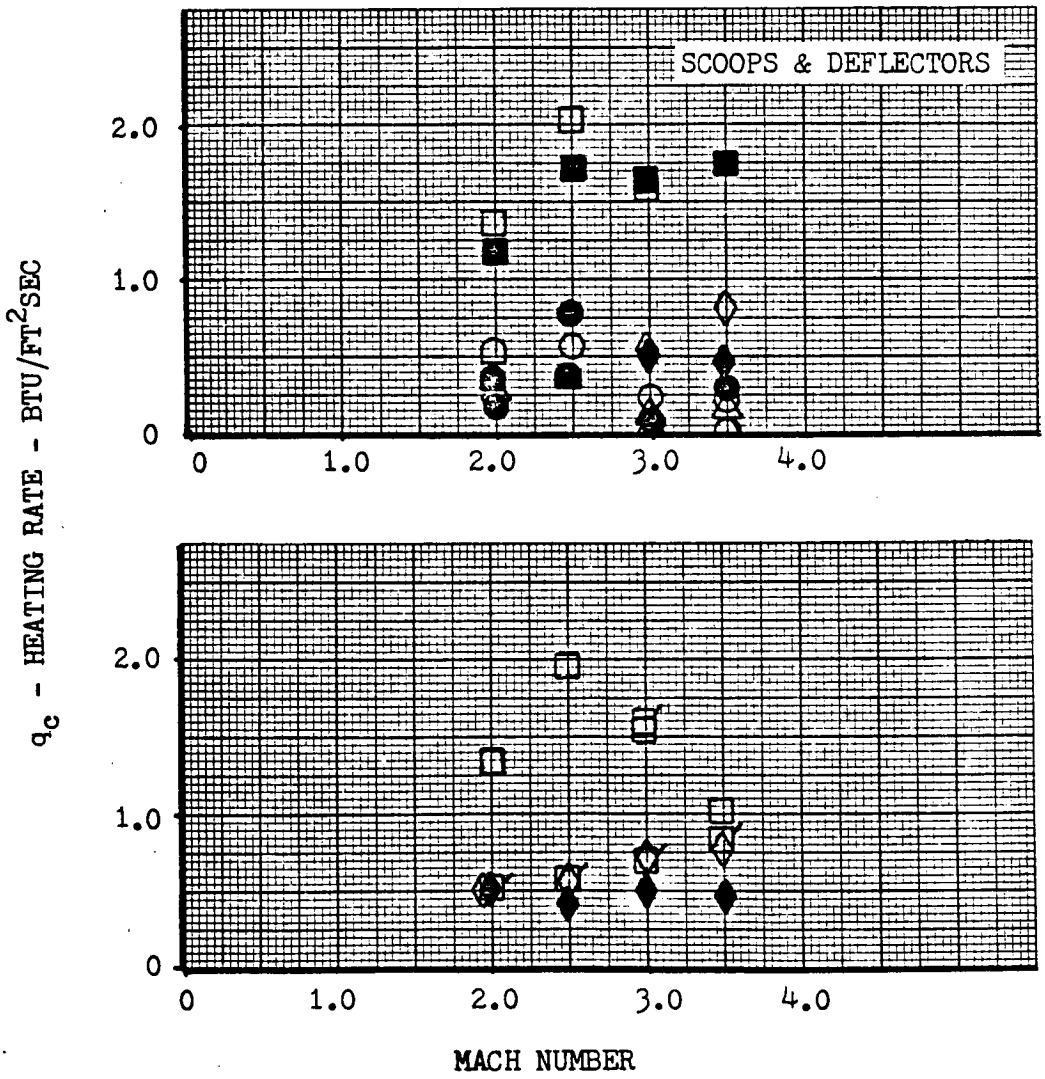

FIGURE 101 Engine Fairing Heating - Convection

5.3.2 (Continued)

The maximum fairing convective heating rate appears on the non-scooped configuration and is approximately 2.0 BTU/FT^{2}SEC at Mach 2.5. The addition of scoops substantially reduced the heating rate. Ten percent scoops and 20 percent scoops were equally effective in reducing the convecting heating level.

Gage H_{19}, which is located on the base plate between the fairing and engine, is compared with fairing and average base plate heating rates for the no scoop configuration in Figure 101.

5.3.3 Convection to Engine (External)

Convective heating rates are measured on the outside of the center engine using gages located as shown in Figures 22 and 23, Volume 1. Figures 102 and 103 show results for gages H_{21} and H_{23}, which are located near the exit plane. Gage H_{21} faces outboard between engines 3 and 4. Gage H_{23} faces engine 3.

Data from both H_{21} and H_{23} show that scoops and deflectors significantly reduce the heating rate to the outside of the center engine. The larger scoops and deflectors are more effective, especially at Mach 3.5.

Shortening the engine fairing has a negligible effect on engine heating. Gage H_{21} indicates a slight increase and gage H_{23} indicates a slight decrease in heating rate.

Effects of two gimbal patterns are shown. For configuration $B_3FS_1NG_3NG_4$ engines 3 and 4 are gimballed toward each other at angles of six degrees. (See Figure 3, Volume 1). Engines 3 and 4 are gimballed 8.5 degrees toward the center engine on configuration $B_3FS_1NG_5NG_6$. Both patterns increase heating to gage H_{21} from two to four times depending on Mach number. However, heating to gage H_{23} was not affected when the outside engines were gimballed toward each other. Both of these gimbal patterns are highly exaggerated and the effect of normal gimballing will probably be negligible.

On Figure 103 a comparison between heating rates to the inboard side of the engine skirts and gage H_{39} indicates a three fold decrease on the outboard side. Figure 104 shows that hydrogen turbine exhaust has an insignificant effect on the heating rate to the outside of the engine.

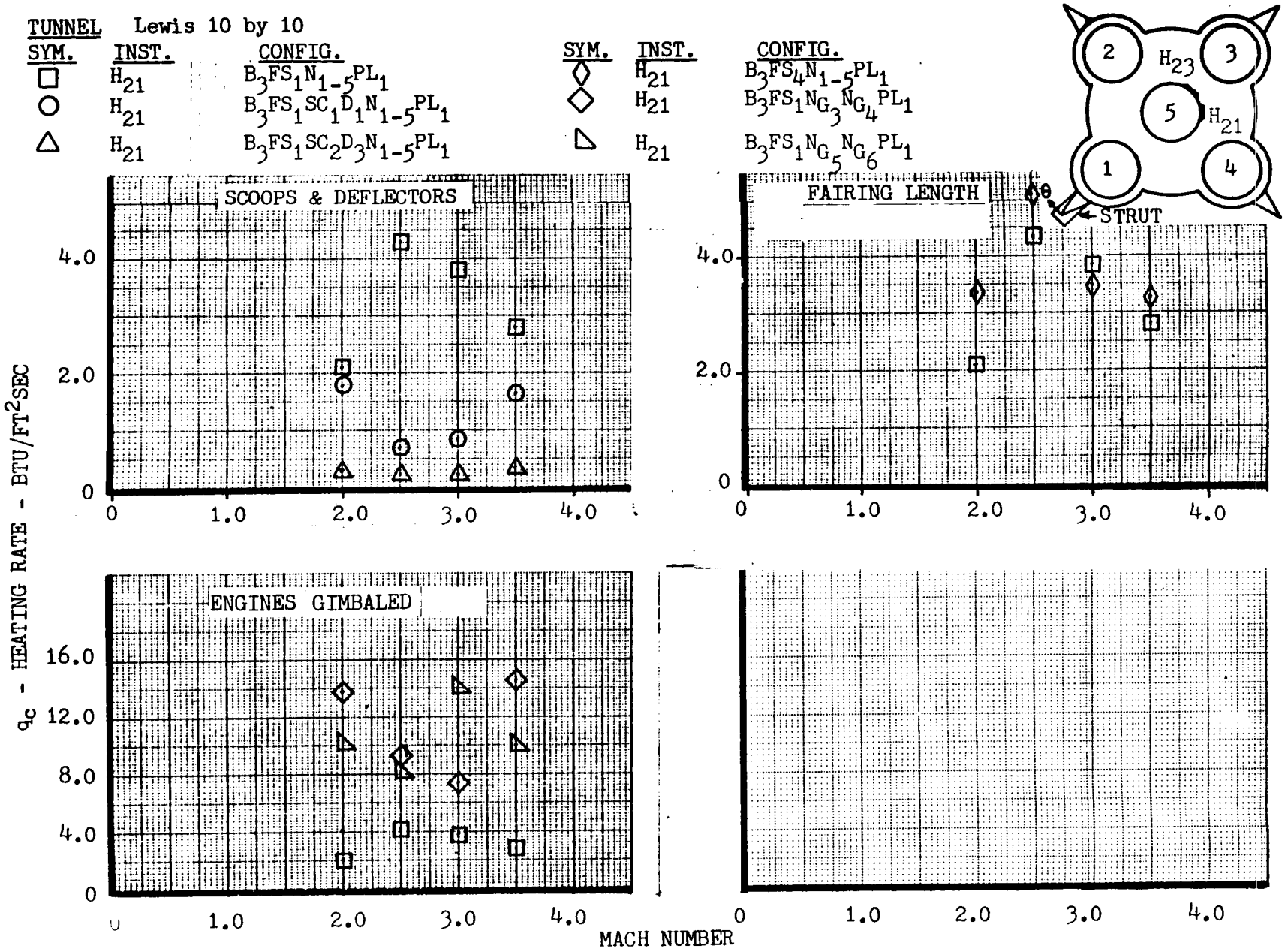

FIGURE 102 Engine Heating - Convection (External)

TUNNEL Lewis 10 by 10

SYM.	INST.	CONFIG.	SYM.	INST.	CONFIG.
□	H_{23}	$B_3FS_1N_{1-5}PL_1$	◇	H_{23}	$B_3FS_3N_{1-5}PL_1$
○	H_{23}	$B_3FS_1SC_1D_1N_{1-5}PL_1$	◇	H_{23}	$B_3FS_1N_{G_3}N_{G_4}PL_1$
△	H_{23}	$B_3FS_1SC_2D_3N_{1-5}PL_1$	◺	H_{23}	$B_3FS_1N_{G_5}N_{G_6}PL_1$
			⬠	H_{39}	$B_3FS_3N_{1-5}PL_1$

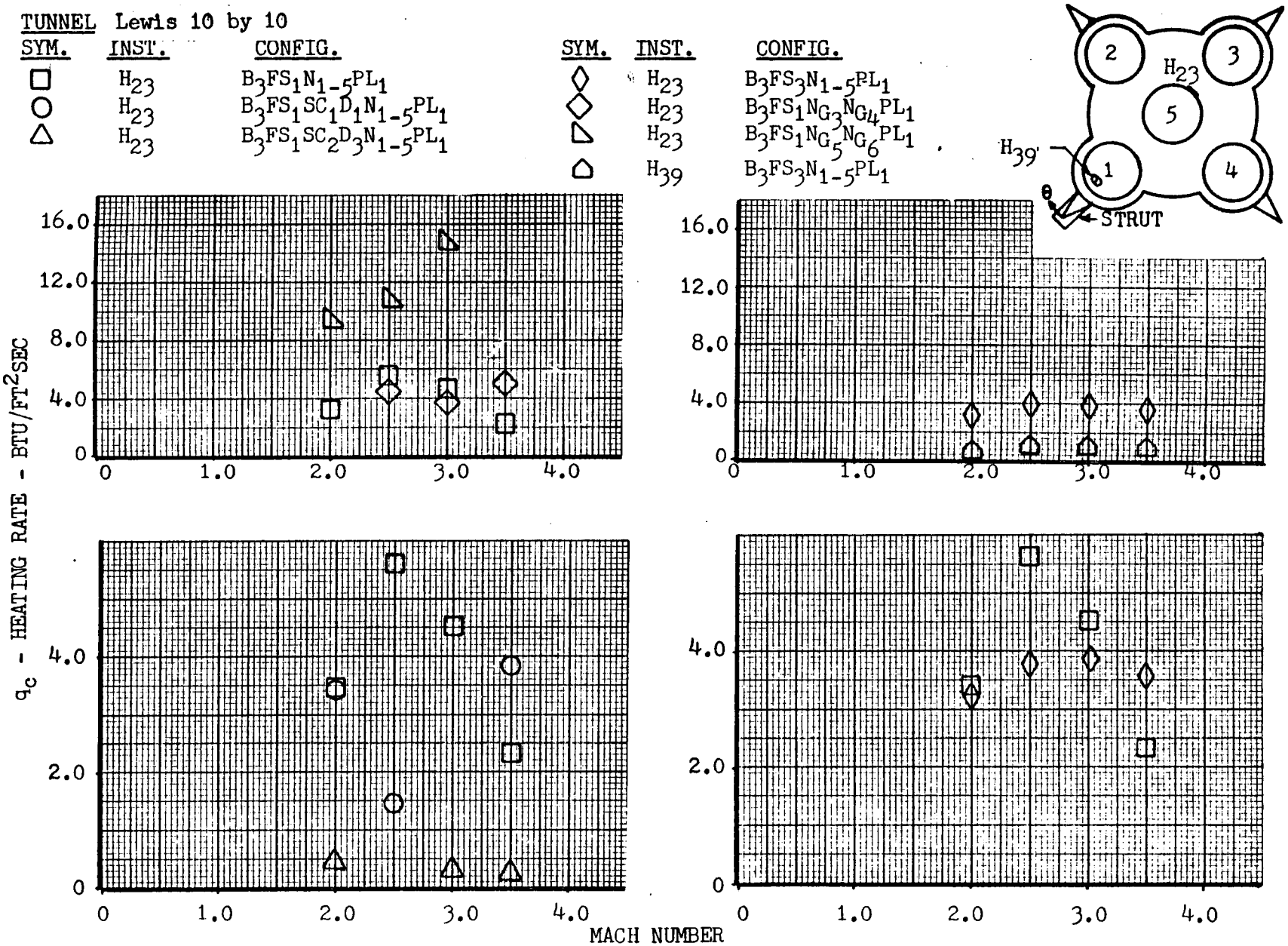

FIGURE 103 Engine Heating - Convection (External)

TUNNEL Lewis 10 by 10

SYM.	INST.	CONFIG.
□	H_{21}	$B_3FS_1N_{1-5}PL_1$
○	H_{21}	$B_3FS_1SC_1D_1N_{1-5}PL_1$

NOTE: Solid symbol denotes turbine exhaust

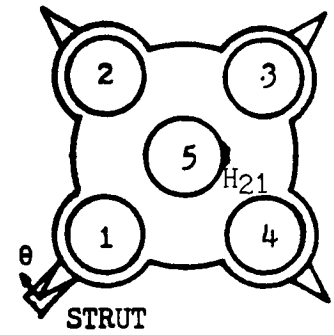

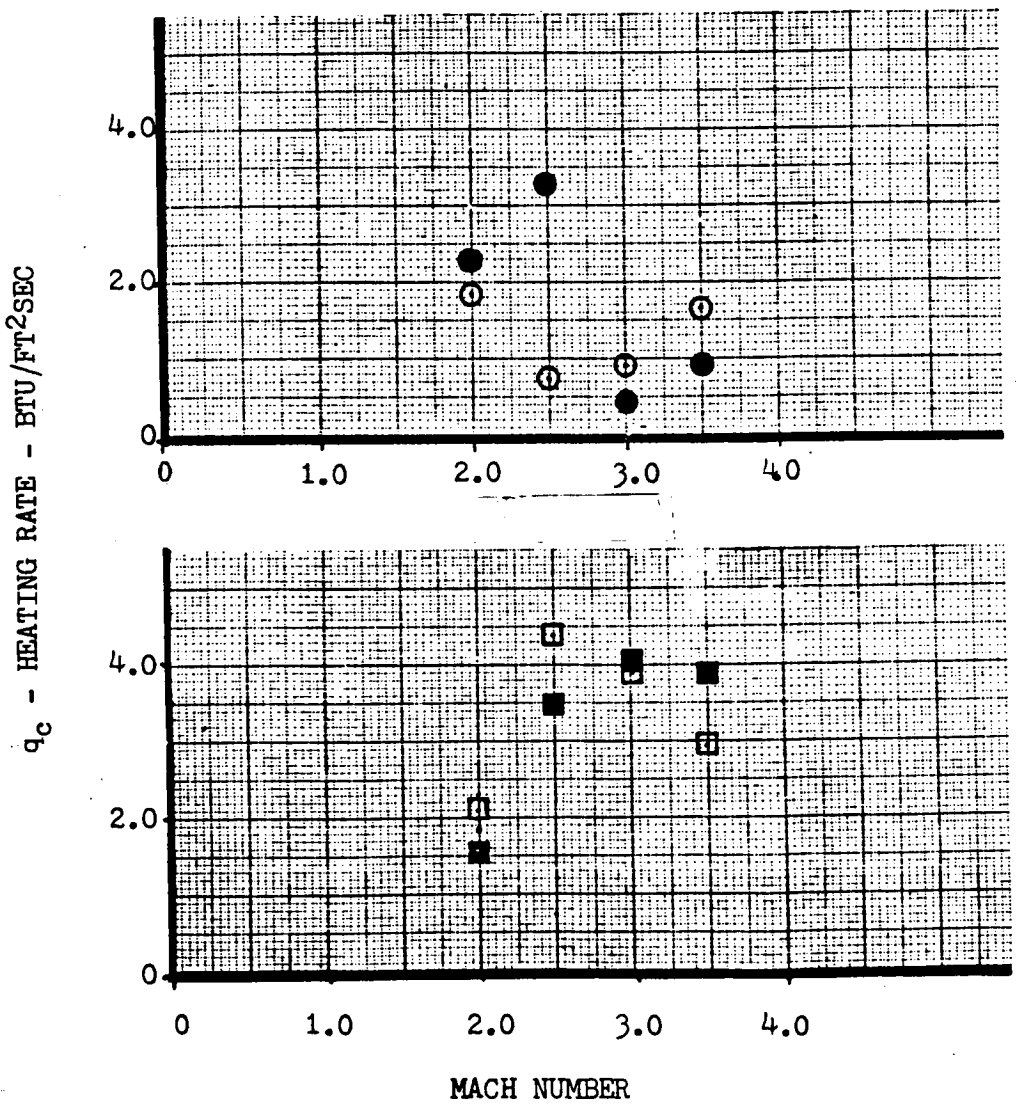

FIGURE 104 Engine Heating - Convection (External)

5.3.3 (Continued)

A combination of heating rates to various points on the center engine and base are shown in Figures 105 and 106 for the two gimbal configurations. The gages on the engine are located as shown on Figure 22 and 23, Volume 1. The gages on the base plate are located on a ray between engines 3 and 4. In Figure 105 it appears that when the engines are gimballed toward each other the engine exhaust gases flow down between the engines, causing a major effect on both engine and base heating at Mach 3.5. At Mach 2.5 it appears that the gases are only contributing to heating near the nozzle exit plane.

When the engines are gimballed toward the center engine (Figure 106) the flow of gases is apparently deflected away from the engine by the nozzle and affects only the base heating from r/R = 0.65 outward. The level of heating is less than half that for the other gimbal pattern.

5.3.4 Convection to Engine (Engine Out)

Convection heating data for the inside and outside surfaces of an instrumented and plugged center engine is shown in Figure 107. The gage locations are described in paragraph 4.2.4 and shown in Figure 24 and 25 of Volume 1. Gages H_{53} and H_{55} are located on the nozzle lip facing aft; H_{53} being between engines 2 and 3, and H_{55} being 180 degrees from H_{53}.

Convection inside the nozzle appears to increase slightly with Mach number. In general the data from similar locations are consistent with each other.

At Mach number 2.0 all data are somewhat higher than data shown in Figure 46 at Mach number 1.95 (Lewis 8 by 6). This data discrepancy is expected due to the altitude difference between the two tunnels.

Comparison between Figures 105 and 106 indicates that convective heating to the inside of an inoperative center engine nozzle will be considerably less than convective heating to the outside of the nozzle when all engines are firing in this Mach range. Data from gauges 53 and 55 indicate that plume-plume impingement is becoming more pronounced at the higher Mach numbers and some flow is being directed forward and outboard near the nozzle exit plane.

5.3.5 Comparison with Theory

Theoretical calculations have been made for comparison with the Lewis 10 by 10 convective heating data and are described in detail in appendix B, Volume 1. Figure 108 shows the data - theory comparison for configurations with and without scoops.

TUNNEL Lewis 10 by 10

SYM.	INST.	CONFIG.
◇	H_{21}	$B_3FS_1N_{G_3}N_{G_4}PL_1$
◆	H_{23}	$B_3FS_1N_{G_3}N_{G_4}PL_1$
◇	H_{27}	$B_3FS_1N_{G_3}N_{G_4}PL_1$

SYM.	INST.	CONFIG.
◆	H_{29}	$B_3FS_1N_{G_3}N_{G_4}PL_1$
◇	H_{31}	$B_3FS_1N_{G_3}N_{G_4}PL_1$
⊕	$H_{9,7,5,3,1}$	$B_3FS_1N_{G_3}N_{G_4}PL_1$

NOTE: 1. Base is located at X/L = 1.0
2. No flag denotes Mach 2.5
3. Flag right denotes Mach 3.5

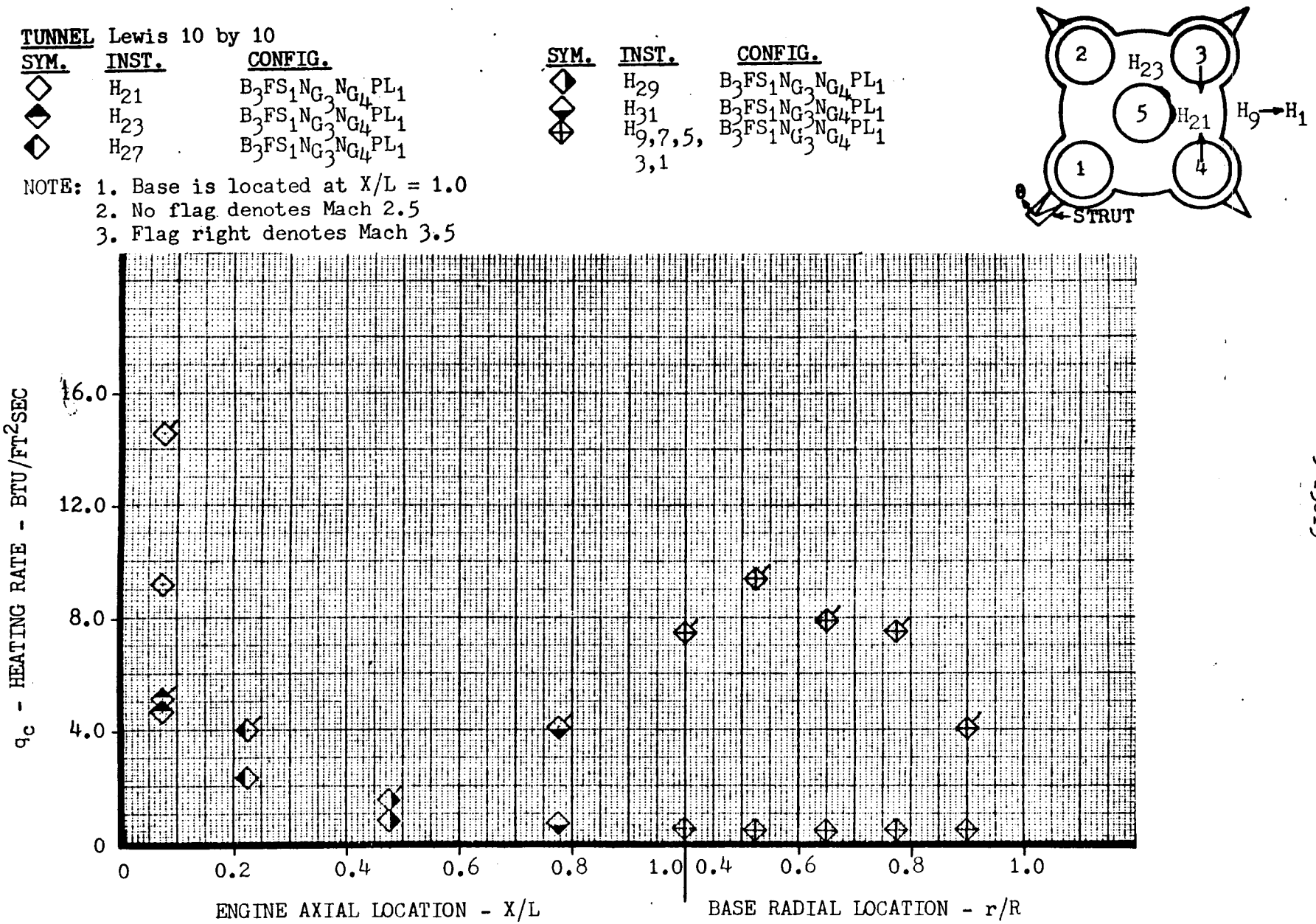

FIGURE 105 Engine and Base Heating - Convection

TUNNEL Lewis 10 by 10

SYM.	INST.	CONFIG.
◺	H_{21}	$B_3FS_1N_{G_5}N_{G_6}PL_1$
◭	H_{23}	$B_3FS_1N_{G_5}N_{G_6}PL_1$
◮	H_{27}	$B_3FS_1N_{G_5}N_{G_6}PL_1$
◮	H_{29}	$B_3FS_1N_{G_5}N_{G_6}PL_1$
◭	H_{31}	$B_3FS_1N_{G_5}N_{G_6}PL_1$
△	$H_{9,7,5,3,1}$	$B_3FS_1N_{G_5}N_{G_6}PL_1$

NOTE: 1. Base is located at X/L = 1.0
2. No flag denotes Mach 2.5
3. Flag right denotes Mach 3.5

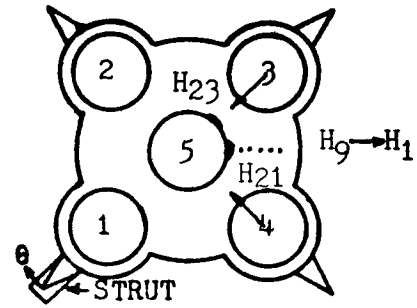

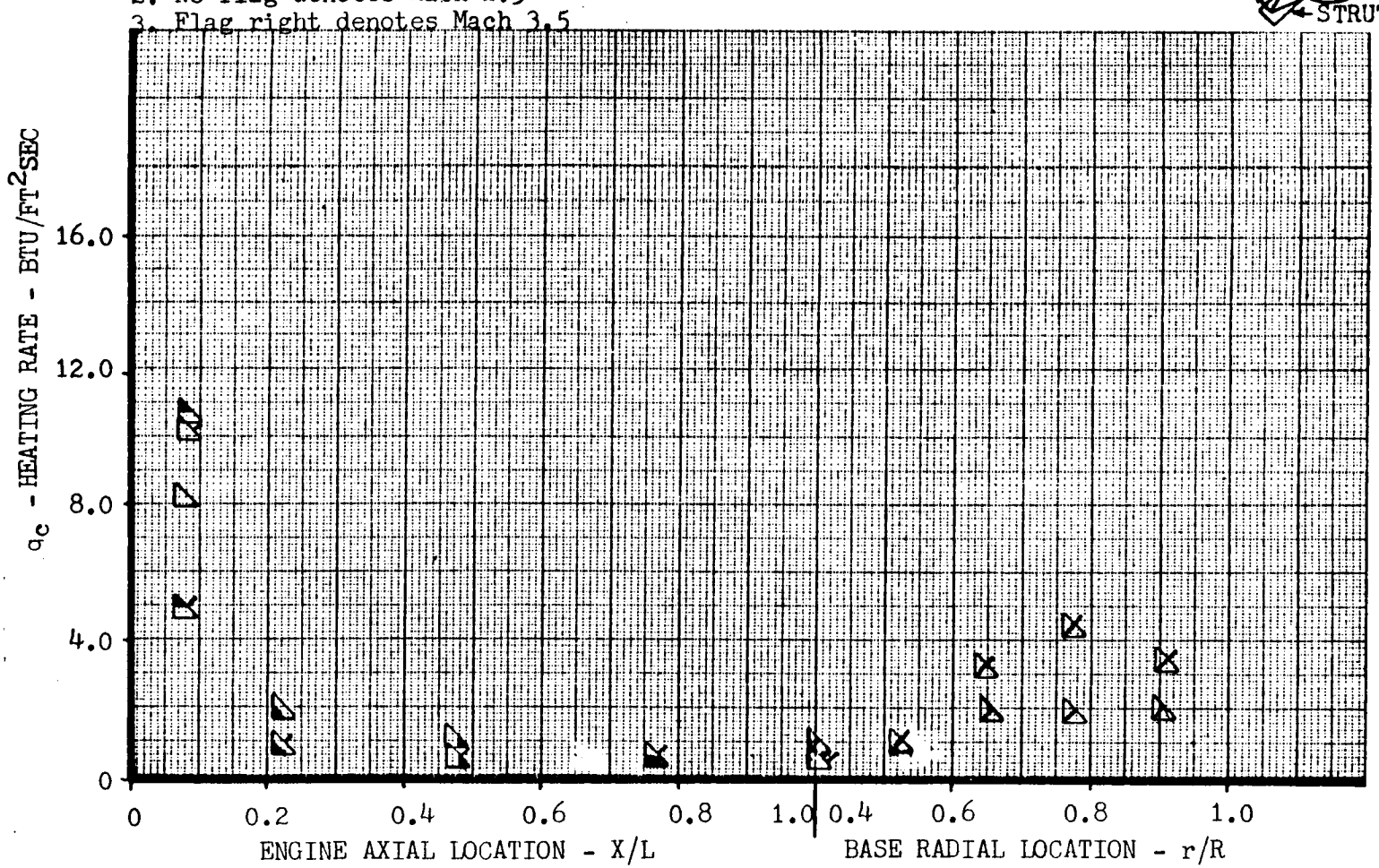

FIGURE 106 Engine and Base Heating - Convection

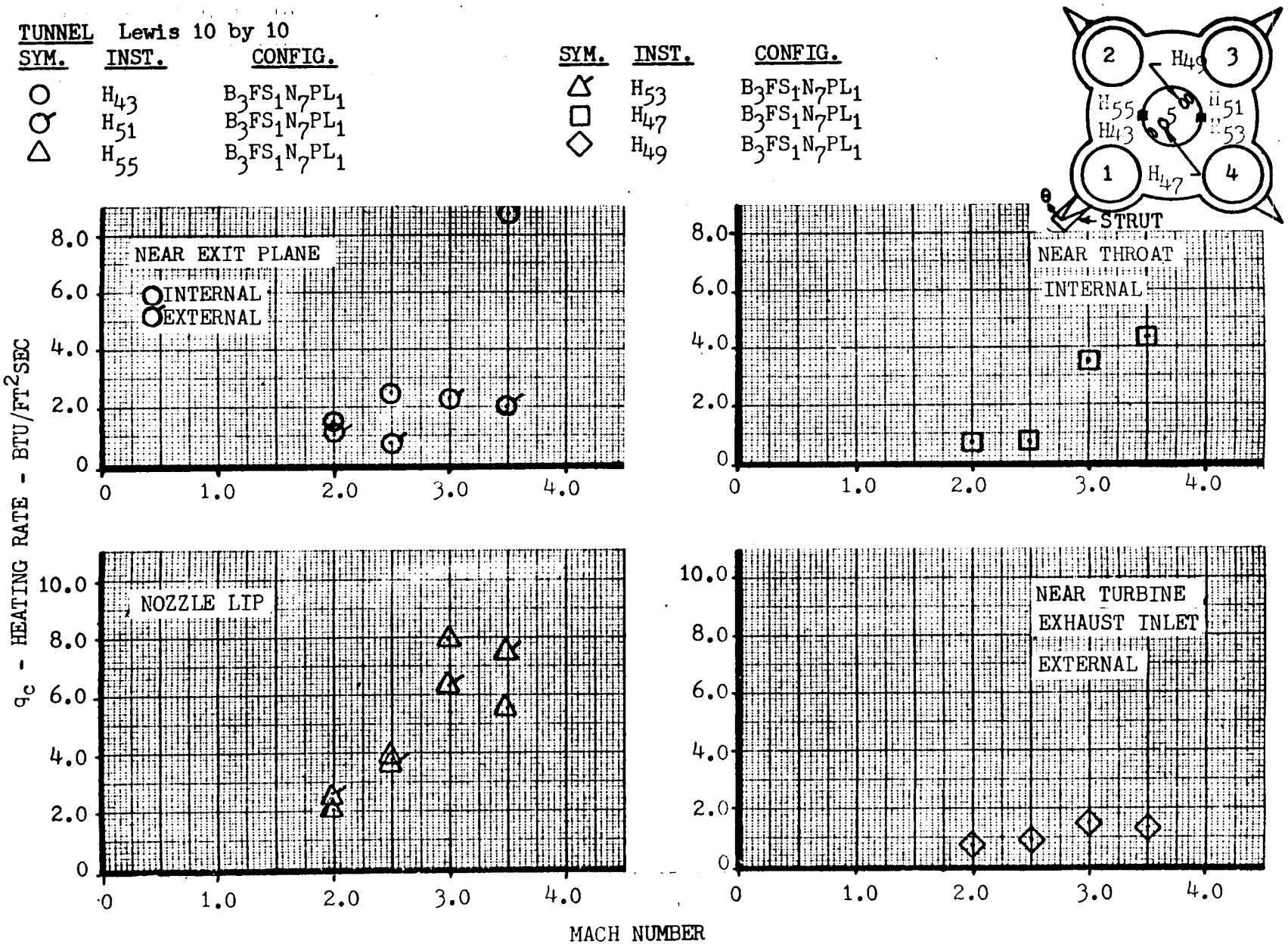

FIGURE 107 Engine Heating - Convection (Internal)

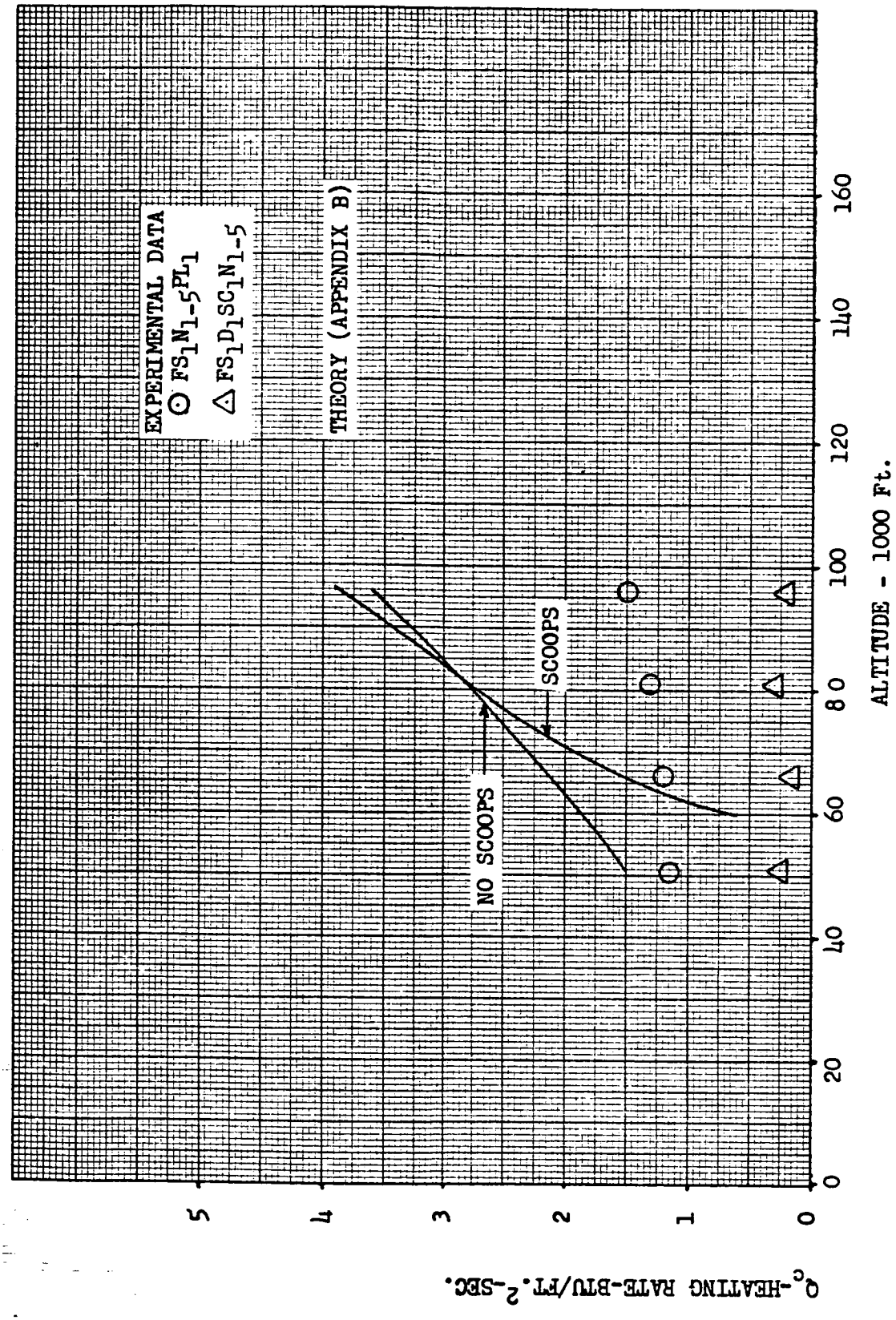

FIGURE 108 Convective Heating - Comparison with Theory - Lewis 10 by 10 Tunnel

5.3.5 (Continued)

The theoretical curves indicate a rapid rise in convective heating as a function of altitude. Model data is essentially constant in this test range. The magnitude of the theoretical prediction of the effects of scoops is similar to that measured experimentally at the low altitudes.

5.4 BASE PRESSURE

Pressure data are available on the base plate only. The pressure ports are located as shown in Figure 19, Volume 1. Base pressures are not recorded in the quadrant where gimballing occurs, and therefore comparison between heating and pressure for gimballed configurations is not possible.

For all configurations tested, base pressures are recorded before the engines fired. A seven reading average is calculated and referred to as the average "engine off" base pressure (Figure 109). The test pressure is obtained by measuring a change in pressure during the test period, which is then added to the engine off base pressure.

5.4.1 Configuration Effects on Base Pressure

Base pressure distribution along a radial line on the base is shown in Figure 110 for the basic and short engine fairing configurations, and for the 10 percent and 20 percent scoop configurations. The minimum base pressure occurs at the radial position corresponding to the minimum vent area for these configurations. This same trend was noted in the Lewis 8 by 6 tunnel tests for Mach numbers 1.35 and greater and is believed to reflect a velocity increase as gases pass from outboard to inboard through the orifice created by the engines. The high pressure inboard occurs as velocity head is changed to static pressure. Since the same trend is noted with and without deflectors it is evident that considerable gas flow into the engine compartment occurs due to the free stream expansion around the base of the vehicle. Addition of deflectors raises the level of base pressure. Comparison of the "engine off" data (Figures 109 & 111) for the configurations without scoops indicates that the effect of the free stream on base pressure is nearly constant with Mach number increase in this Mach range. The data with deflectors and scoops show that the rate of base pressure increase is decreasing with Mach number but the deflectors are still effective.

Average base pressure as a function of test Mach number is shown in Figure 109 for the same configurations. An increase in base pressure is generally associated with an increase in scoop size, as expected. Base pressure for the short engine fairing (S_4) configuration is consistently less than that measured with other configurations, and the pressure of the basic engine fairing (S_1) configuration decreases when the center engine is inoperative.

TUNNEL LEWIS 10 BY 10

SYM.	**INST.**	**CONFIG.**
□	$P_{1,2,3,4,5,6,7}$	$B_3FS_1N_{1-5}PL_1$
◇	$P_{1,2,3,4,5,6,7}$	$B_3FS_4N_{1-5}PL_1$
○	$P_{1,2,3,4,5,6,7}$	$B_3FS_1D_1SC_1N_{1-5}PL_1$
◺	$P_{1,2,3,4,5,6,7}$	$B_3FS_2D_1SC_1N_{1-5}PL_1$
△	$P_{1,2,3,4,5,6,7}$	$B_3FS_1D_3SC_2N_{1-5}PL_1$

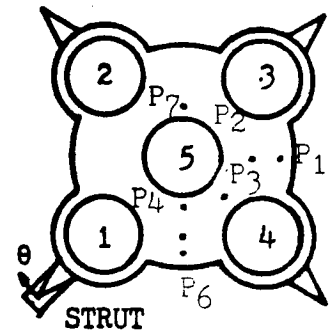

NOTE: Data averaged

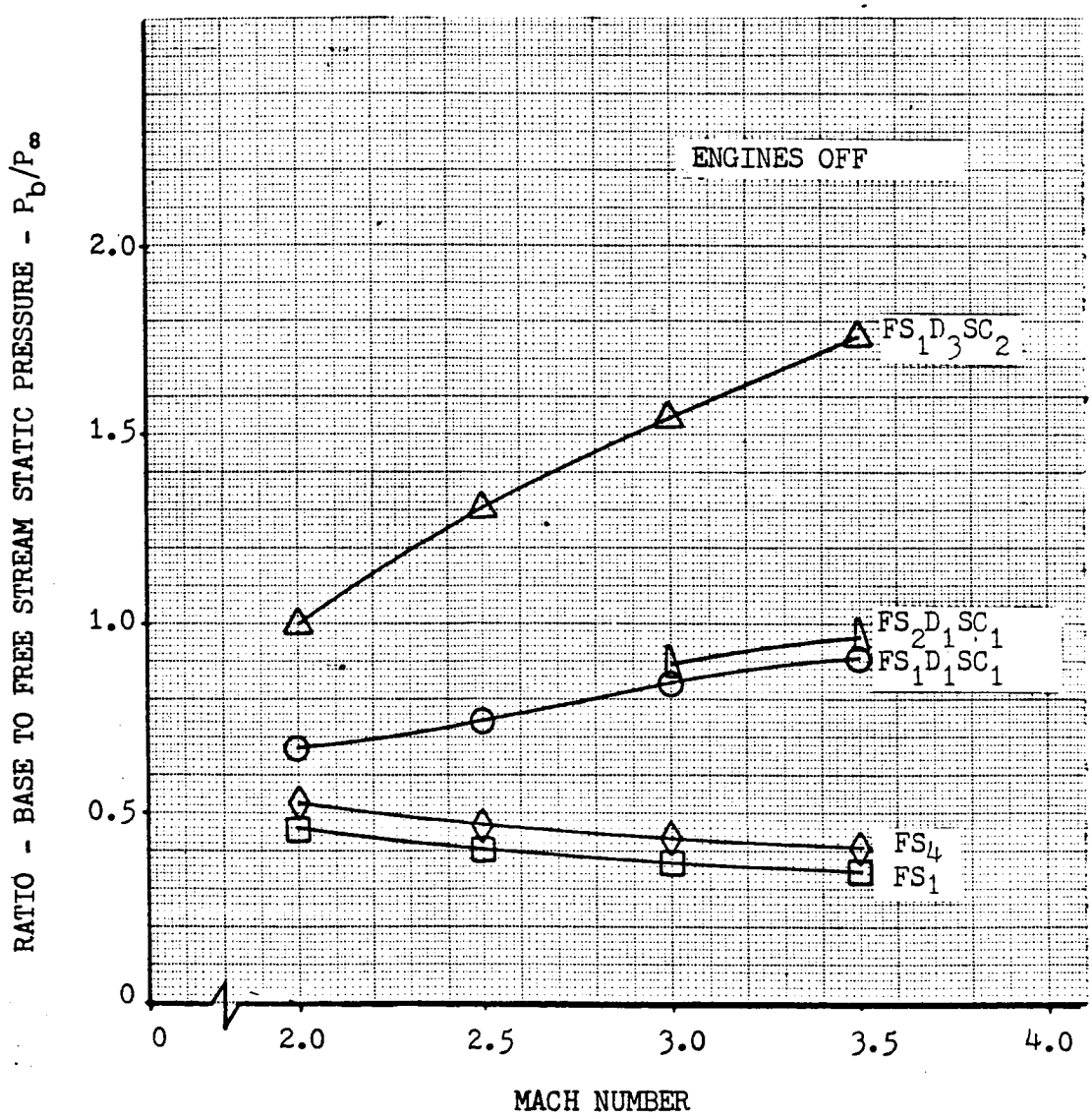

FIGURE 109 Base Pressure

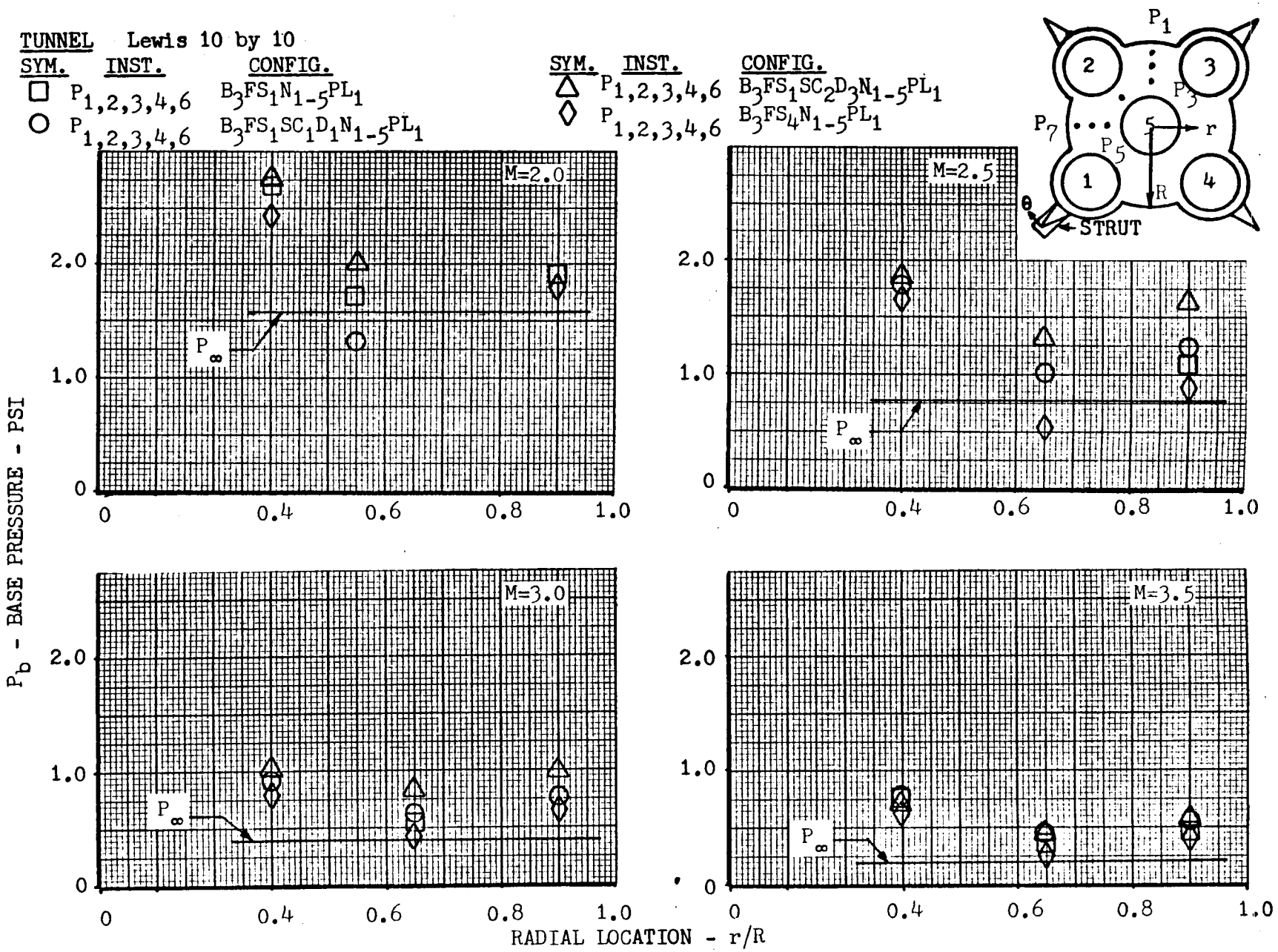

FIGURE 110 Base Pressure

TUNNEL LEWIS 10 BY 10 TUNNEL

SYM.	INST.	CONFIG.
□	$P_{1,2,3,4,6,7}$	$B_3FS_1N_{1-5}PL_1$
△	$P_{1,2,3,4,6,7}$	$B_3FS_1D_3SC_2N_{1-5}PL_1$
◇	$P_{1,2,3,4,6,7}$	$B_3FS_1N_{1-5}PL_1$
○	$P_{1,2,3,4,6,7}$	$B_3FS_1D_1SC_1N_{1-5}PL_1$

NOTE: Data averaged

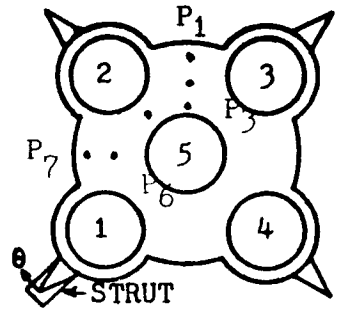

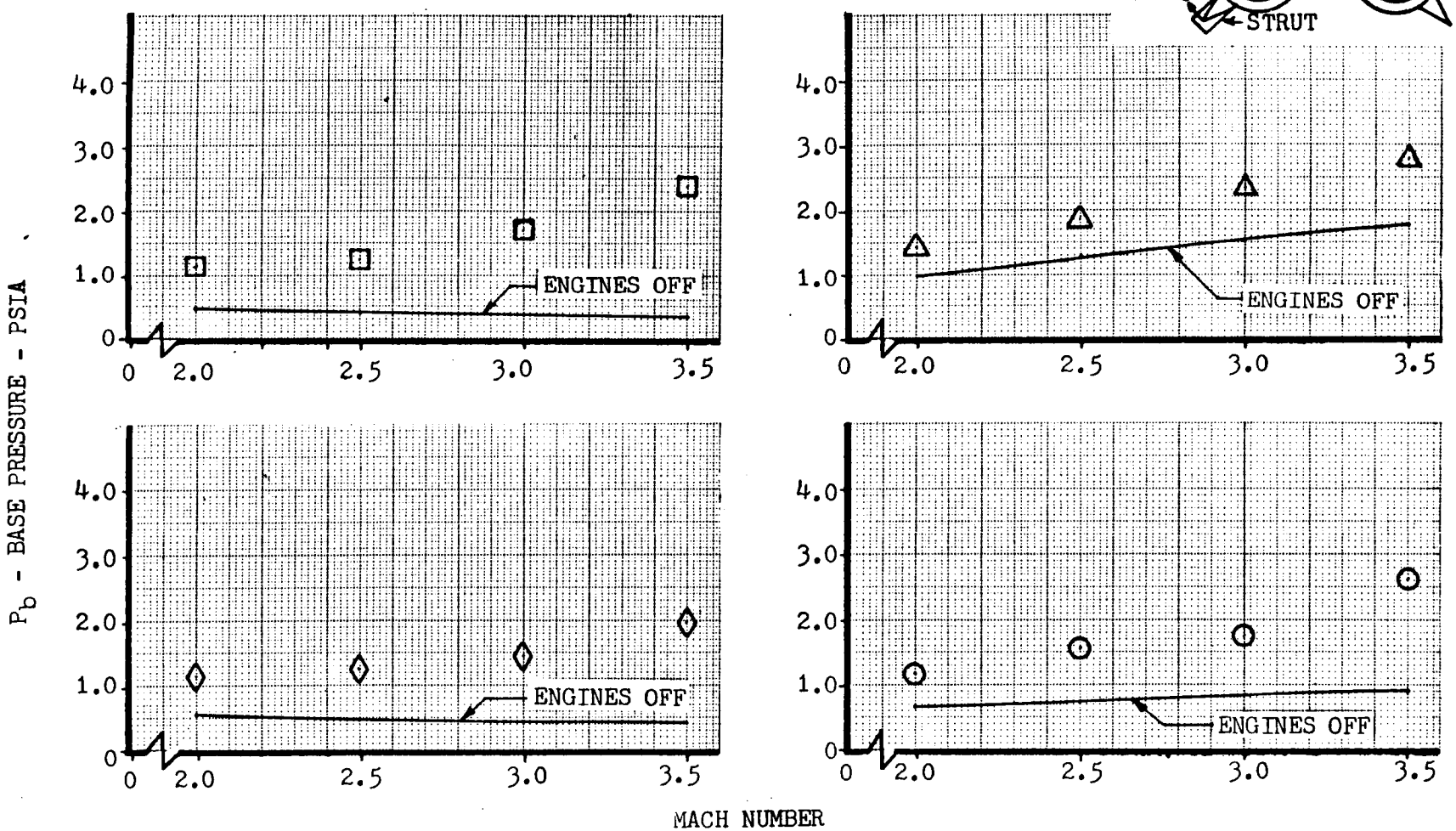

FIGURE 111 Base Pressure

5.4.1 (Continued)

Figure 112 shows base pressures for gimbal Pattern N_{G3} N_{G4} and Gimbal Pattern N_{G5} N_{G6} in a quadrant 90° from the quadrant in which the engines are gimballed.

Base pressure was not significantly changed by the addition of hydrogen turbine exhaust (see Figure 113) and is higher than the average "engine off" base pressure at all Mach numbers regardless of configuration.

5.4.2 Correlation with Theory

Experimental base pressure data and theoretical calculations are compared in Figures 114 and 115. Figure 114 is a comparison of the "engines-off" theoretical base pressure (Appendix C) and the "engines-off" experimental data with and without scoops. The theory is for a blunt-base cylinder and compares favorably with the no scoop configuration data.

Figure 115 shows the theoretical scoop exit pressure compared with "engines-on" experimental base pressure data with and without scoops. Theory in all cases is above the experimental data. However, the experimental data is above the ambient pressure and indicates a build up in the base pressure.

5.5 DATA ACCURACY

Inaccuracies in the test data are due to inaccuracy of the gage and the ability of the person reducing the data to read the oscilloscope traces. There is further uncertainity in the data due to unsymmetrical flow in the base. These two areas are discussed in detail below.

5.5.1 Repeatability

Repeatability of test data is available since repeat runs were made throughout the test. Radiation heating rate repeatability is impossible to determine due to the near zero heating levels measured. Convective heating rate repeatability is shown in Figure 116 to be within 20 percent. The radial distribution trends are preserved with repeated data. Base pressure data are repeatable within 20 percent (Figure 117). Most of this error could be attributed to acoustical noise and vibration.

5.5.2 Symmetry

Heat transfer and base pressure measurements are available for two quadrants of the base. Data comparisons between measurements in identical positions, but separate quadrants, are a means of evaluating symmetric flow in the base. Measurements identically located on each side of the center radial line of a quadrant are used to evaluate the symmetry of flow

TUNNEL Lewis 10 by 10

SYM.	INST.	CONFIG.
□	P_1	$B_3FS_1N_{1-5}PL_1$
○	P_1	$B_3FS_1SC_1D_1N_{1-5}PL_1$
△	P_1	$B_3FS_1SC_2D_3N_{1-5}PL_1$
◇	P_1	$B_3FS_4N_{1-5}PL_1$
◇	P_7	$B_3FS_1N_{G_3}N_{G_4}PL_1$
◺	P_7	$B_3FS_1N_{G_5}N_{G_6}PL_1$
⬠	P_7	$B_3FS_1N_7PL_1$

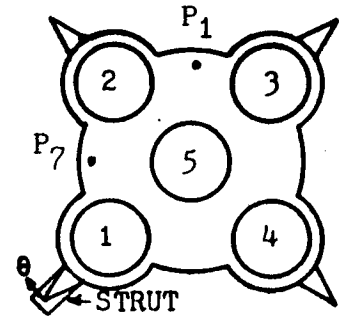

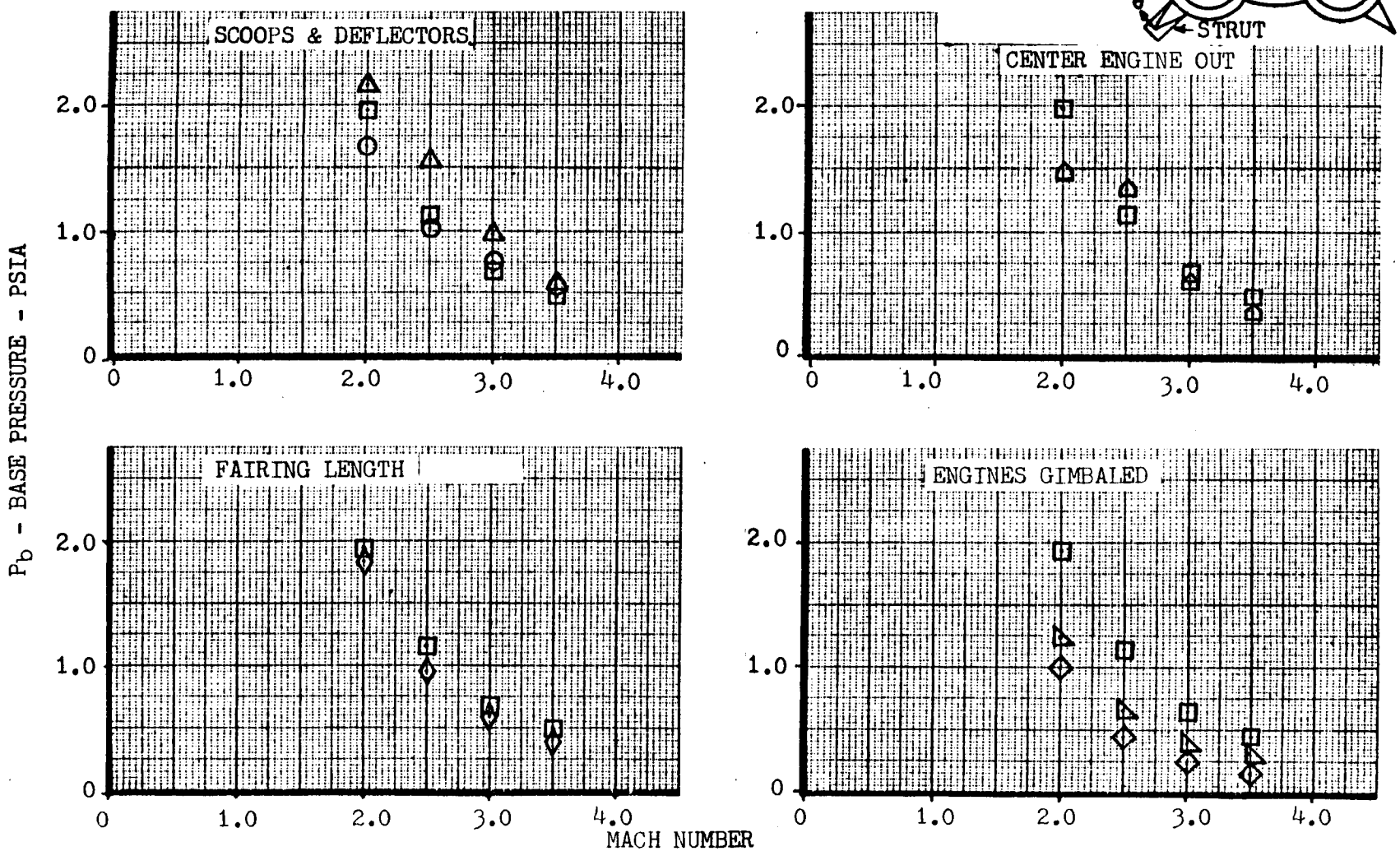

FIGURE 112 Base Pressure

TUNNEL Lewis 10 by 10

SYM.	INST.	CONFIG.
□	P_2	$B_3FS_1N_{1-5}PL_1$
○	P_2	$B_3FS_1SC_1D_1N_{1-5}PL_1$

NOTE: 1. Solid symbol denotes turbine exhaust
2. Flagged symbol denotes average engine off base pressure

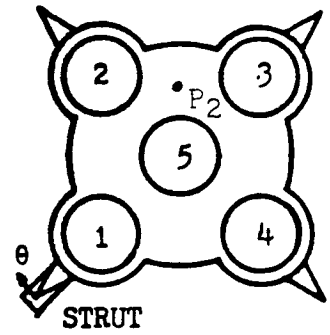

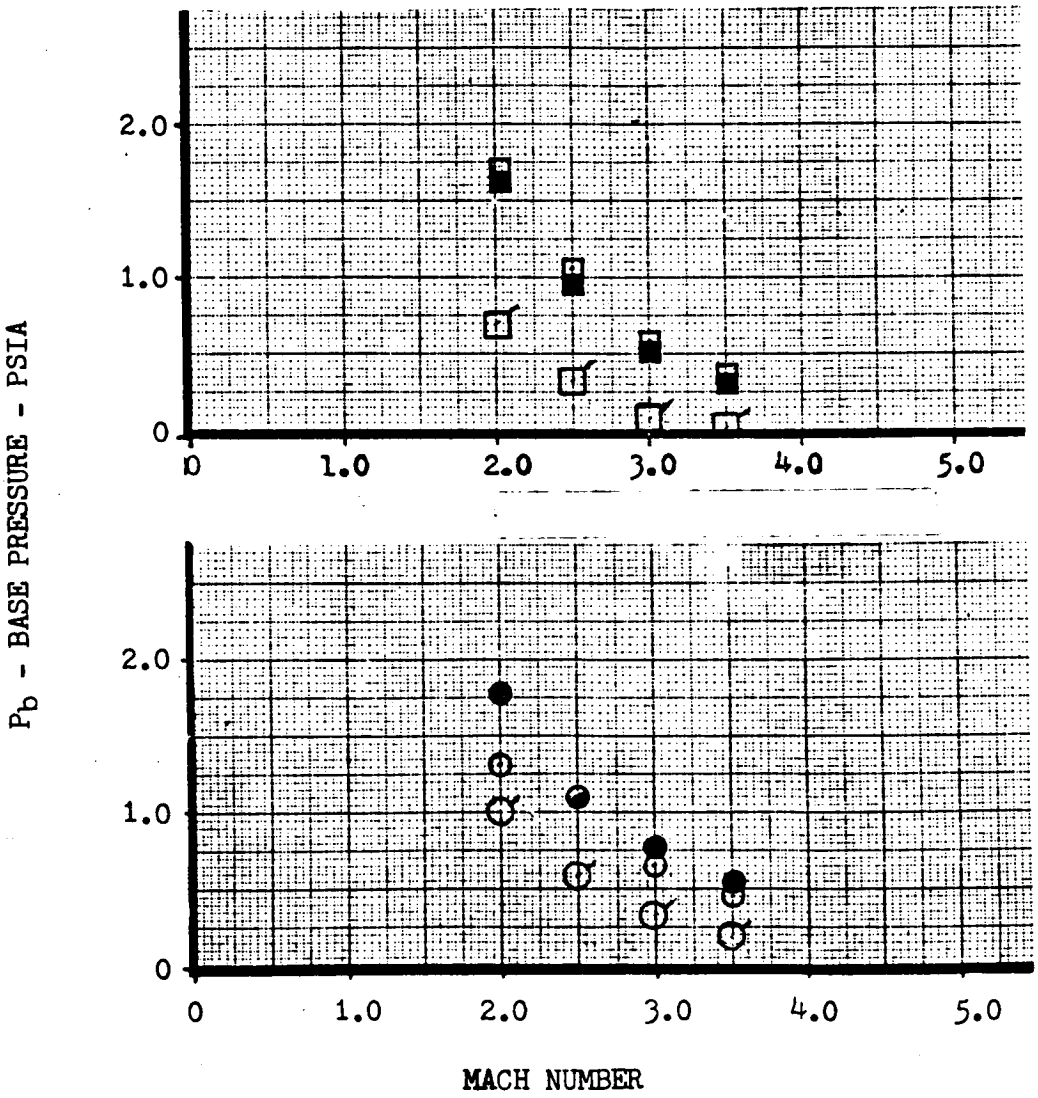

FIGURE 113 Base Pressure - Turbine Exhaust Effect

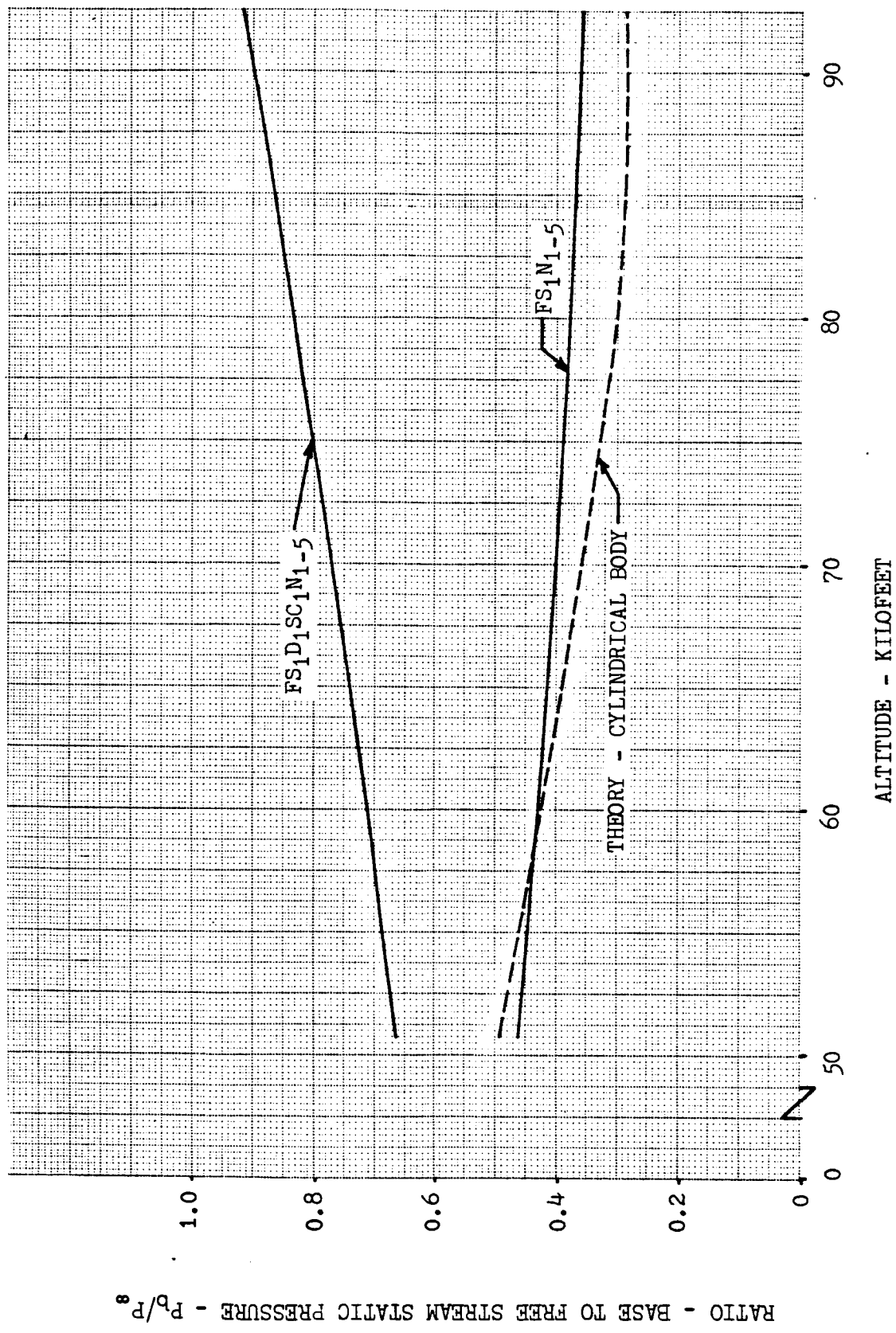

FIGURE 114 Engines Off Base Pressure Comparison - Lewis 10 by 10 Tunnel

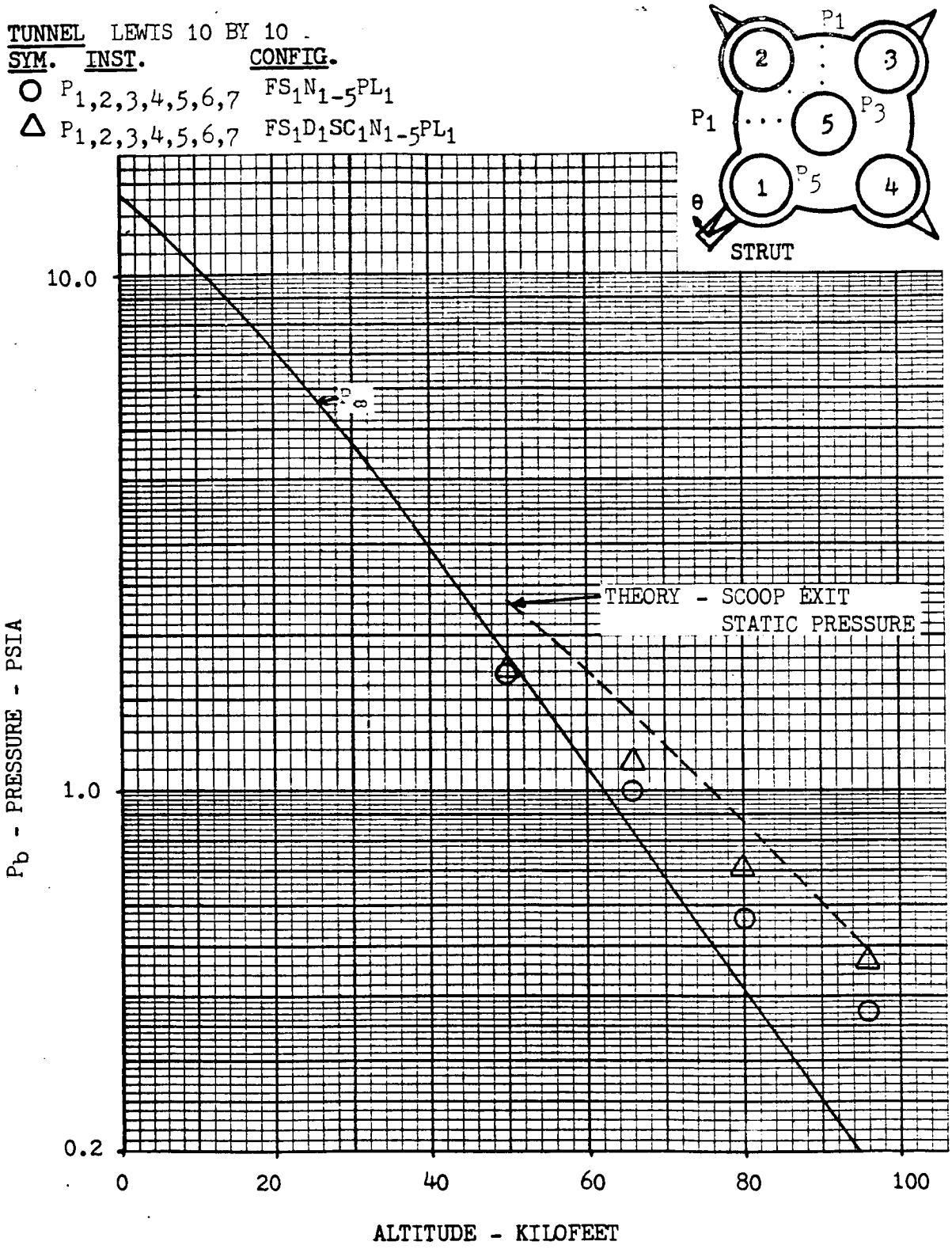

FIGURE 115 Base Pressure Comparison with Theory - Lewis 10 by 10 Tunnel

TUNNEL Lewis 10 by 10

SYM.	INST.	CONFIG.	SYM.	INST.	CONFIG.
□	$H_{1,3,5,7,9}$	$B_3FS_1N_{1-5}PL_1$			

NOTE: Flagged symbol is repeat run

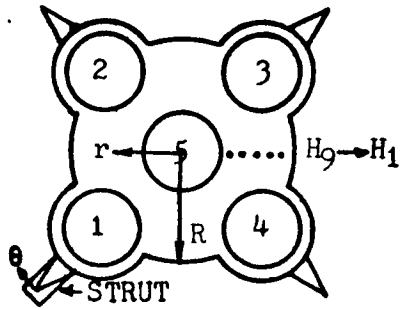

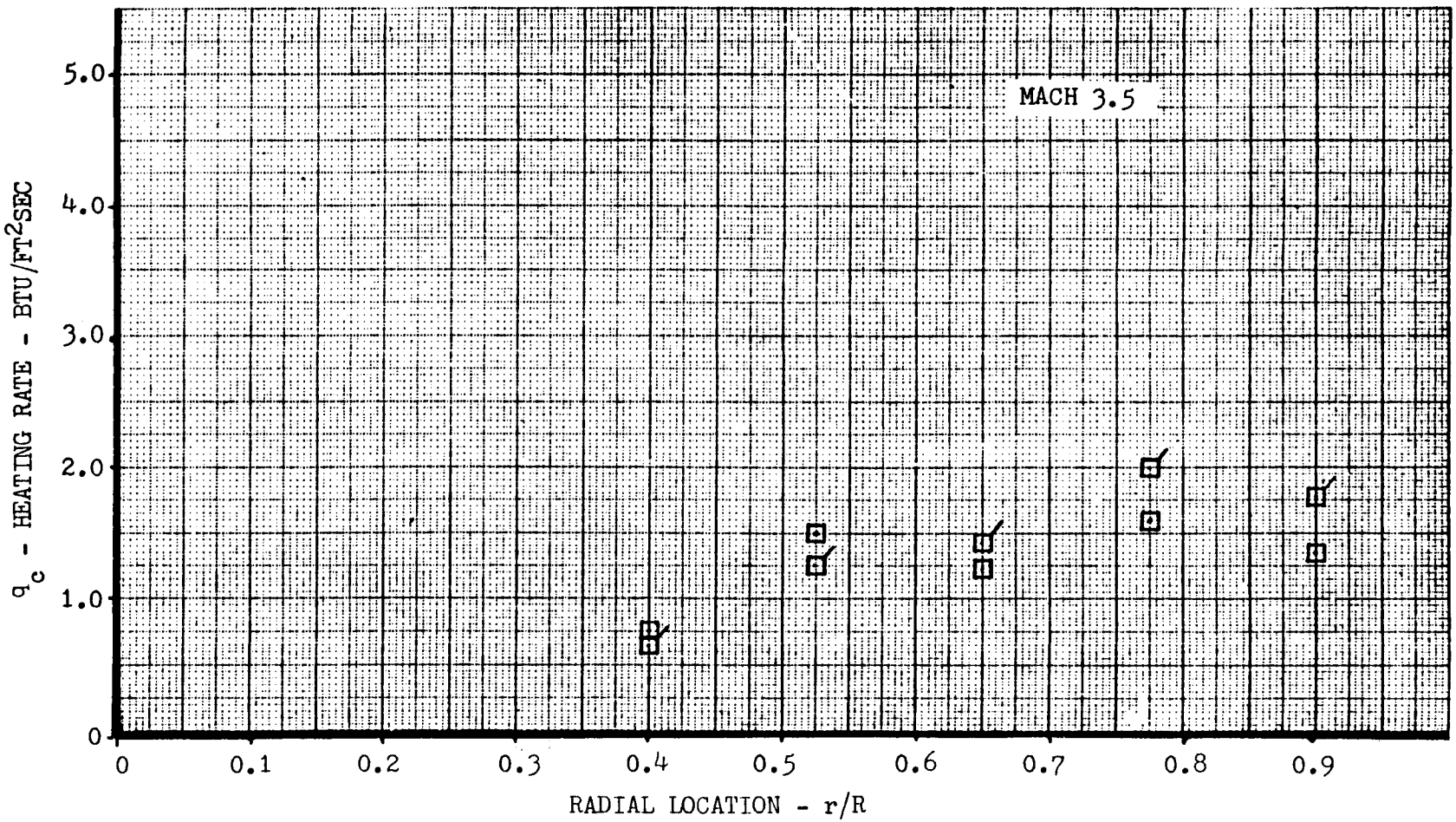

FIGURE 116 Base Heating - Convection (Repeatability)

TUNNEL Lewis 10 by 10

SYM.	INST.	CONFIG.
□	$P_{1,2,3}$	$B_3FS_1N_{1-5}PL_1$
○	$P_{1,2,3}$	$B_3FS_1SC_1D_1N_{1-5}PL_1$

NOTE: 1. Flagged symbol is repeat run
2. Solid symbol denotes turbine exhaust

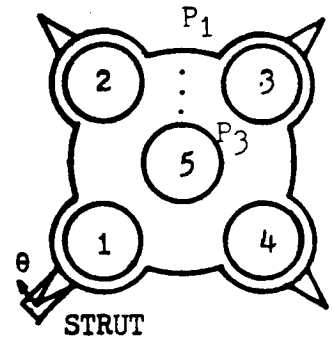

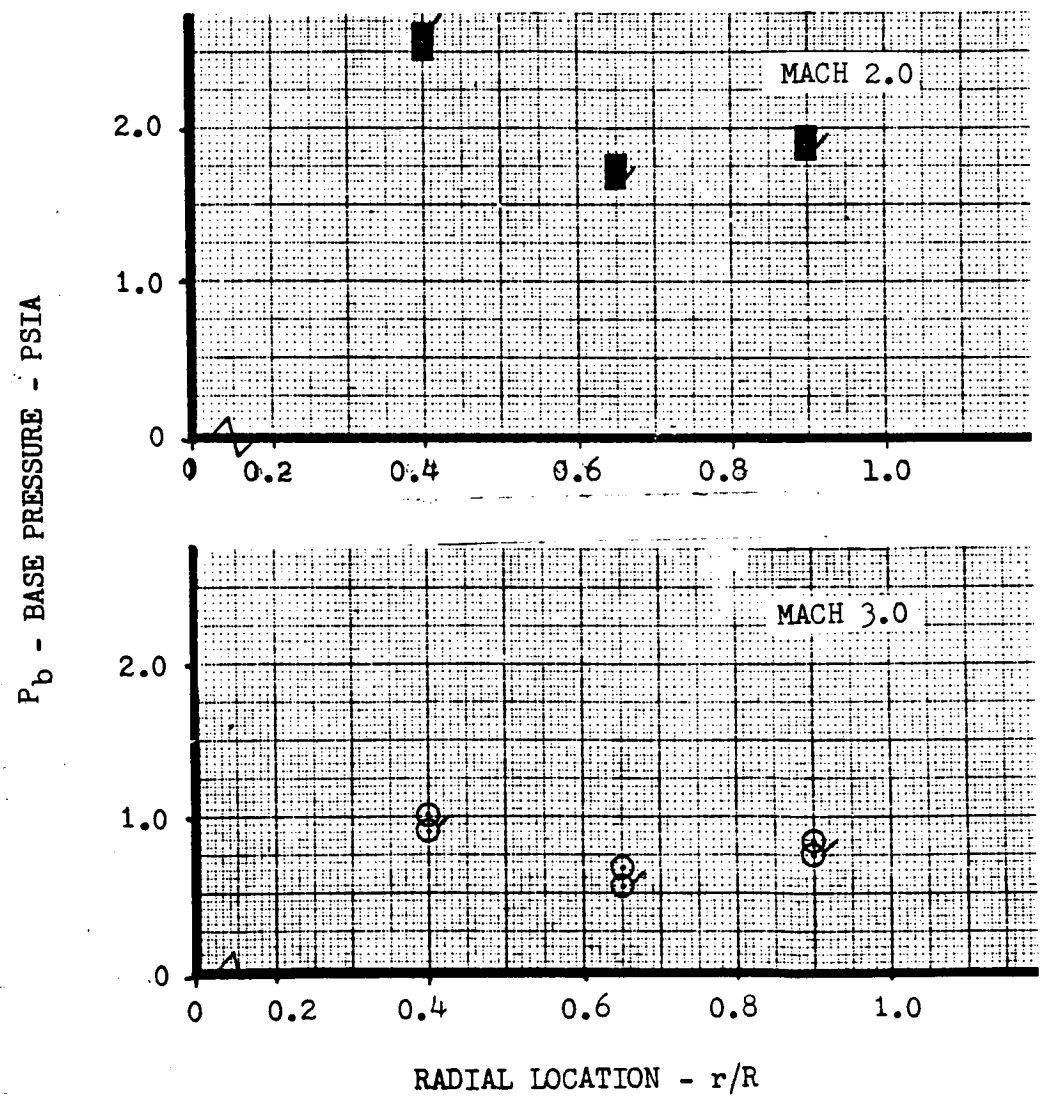

FIGURE 117 Base Pressure Repeatability

5.5.2 (Continued)

within that quadrant. Convective heating symmetry is shown in Figures 118 and 119, and symmetry of pressure data by Figure 120.

The level of convective heating rates in quadrants 3 and 4 on the basic configuration with scoops are extremely low, and no conclusions about symmetric flow are possible (see Figure 118). Convective heating rates vary by 30 percent between quadrants 3 and 4 on the basic configuration without scoops. Similar variations with the short engine fairing configuration indicate that the flow fields are not greatly disturbed by the model strut assembly. Gimballing the engines will change the flow patterns on the base as shown in Figure 118. Non-symmetric flow and heat gage variations within a quadrant causes variations in heating rates of 25 percent as shown in Figure 119.

Base pressure measurements varied 15 percent between quadrants at the same radial location as seen on Figure 120.

5.6 CONCLUSIONS

Test data obtained from the LRC 10 by 10 foot supersonic tunnel indicate that:

a. The boundary layer ahead of this model base is turbulent and is 1.6 to 1.8 inches thick.

b. Radiation data approached non-luminous gas theory in this test and geometrical changes had no appreciable effect on the radiation base.

c. Heating rates to the base and outside of the engine are reduced in this test range when flow deflectors are present. Size of deflectors above 10 percent did not materially change the convection data.

d. Gimballing two of the outboard engines increases the base and engine heating rates significantly above Mach 3.0.

e. Center engine out at all Mach numbers caused a small reduction in the convective heating to the base.

f. In general, minimum base pressure occurs at the minimum vent area between outboard engines.

g. Loss of a center engine reduces the base pressure.

h. Engine gimballing may effect convection heating, especially to engines above Mach 3.0.

TUNNEL Lewis 10 by 10

SYM.	INST.	CONFIG.	SYM.	INST.	CONFIG.
□	$H_{1,15}$	$B_3FS_1N_{1-5}PL_1$	◊	$H_{1,15}$	$B_3FS_4N_{1-5}PL_1$
○	$H_{1,15}$	$B_3FS_1SC_1D_1N_{1-5}PL_1$	◇	$H_{1,15}$	$B_3FS_1N_{G3}N_{G4}PL_1$

NOTE: 1. Flagged symbol denotes H_{15}
2. Solid symbol denotes turbine exhaust

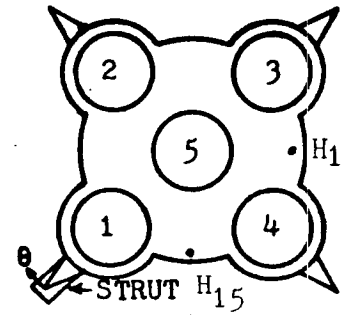

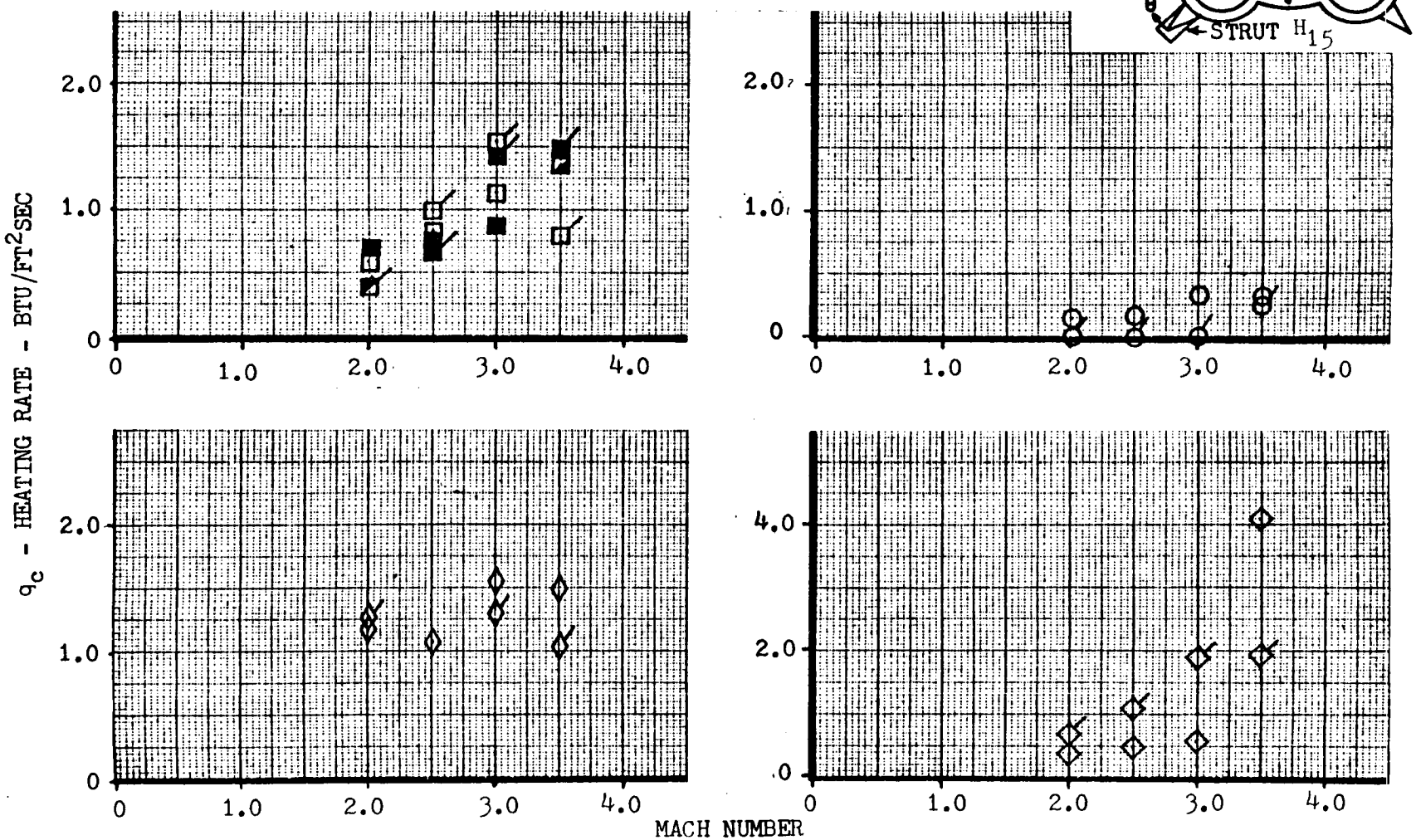

FIGURE 118 Base Heating - Convection (Symmetry)

TUNNEL Lewis 10 by 10

SYM.	INST.	CONFIG.	SYM.	INST.	CONFIG.
□	H_{13}	$B_3FS_1N_{1-5}PL_1$	◇	H_{13}	$B_3FS_4N_{1-5}PL_1$
⌂				H_{13}	$B_3FS_1N_7PL_1$

NOTE: 1. Solid symbol denotes turbine exhaust
2. Flagged symbol denotes H_{17}

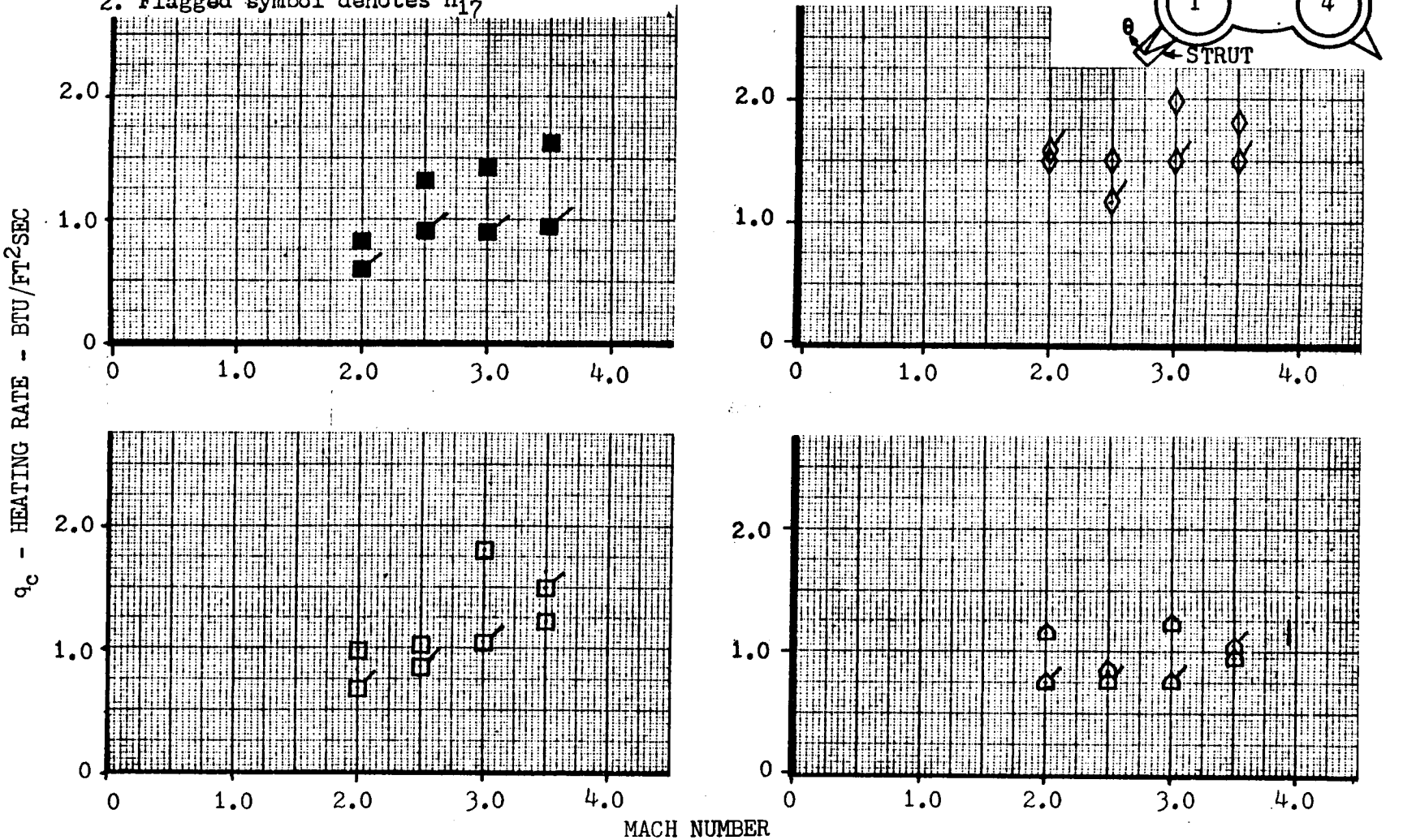

FIGURE 119 Base Heating - Convection (Symmetry)

TUNNEL Lewis 10 by 10

SYM.	INST.	CONFIG.	SYM.	INST.	CONFIG.
⊙	$P_{2,6}$	$B_3FS_1SC_1D_1N_{1-5}PL_1$			

NOTE: Flagged symbol denotes P_6

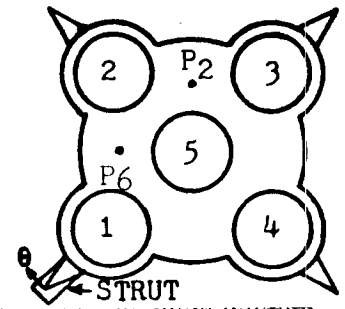

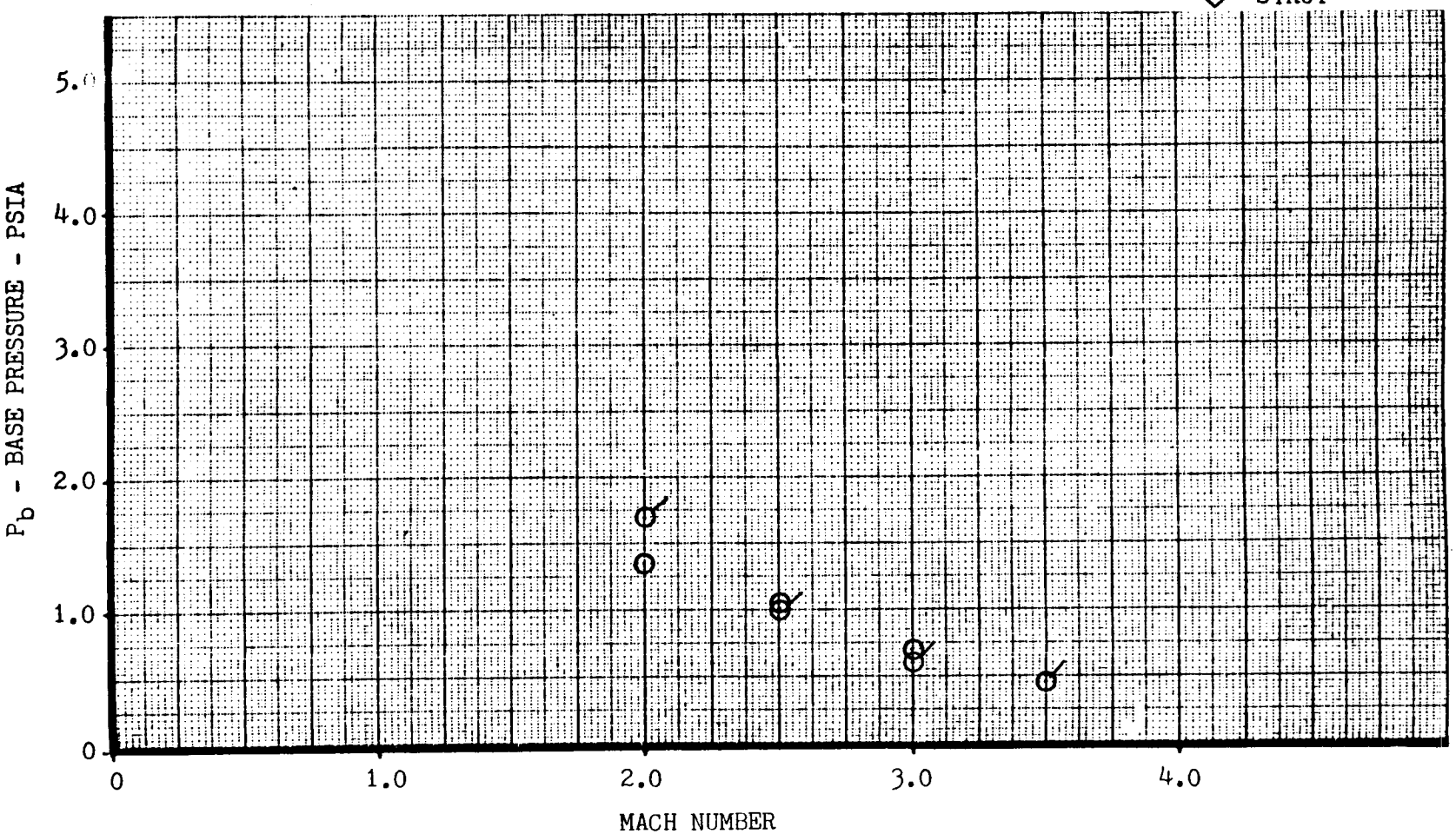

FIGURE 120 Base Pressure-Symmetry

5.6 (Continued)

i. Theoretically, convective heating increases much more rapidly with increase in Mach number than does the experimental data.

j. The theoretical calculation of the base pressure without engine flow agrees with the experimental data from the no scoop configuration. The theoretical scoop exit pressure is higher than the measured base pressures.

SECTION 6 - ANALYSIS OF CORNELL AERONAUTICAL LABORATORY (CAL) ALTITUDE CHAMBER TEST

6.0 INTRODUCTION

This section contains the data analysis of Phase I of Saturn S-IC Model Base Heating Test Program. The test was conducted in the Cornell Aeronautical Laboratory (CAL) high altitude chamber with a 2.22 percent scale model of the Saturn V, S-IC stage afterbody. Figure 121 shows the model installation in the tunnel. Model tests were conducted at simulated altitudes of 125,000 to 205,000 feet without external flow during the period of June 7 - July 1, 1963.

Since the test is conducted in an altitude chamber without a free stream the effects of scoops and flow deflectors on radiation, convection and base pressure should be negligible and therefore scoop variations are not tested. Configurations are tested to evaluate effects of engine fairing length, engine out, and gimbal patterns with and without turbine exhaust simulation. A hot base plate is also used in an attempt to determine the base gas temperature. The model and combustion parameters are discussed under paragraph 1.0 of Volume 1.

Prior to this test, the engine combustion chamber was lengthened in an attempt to improve combustion defects noted in the 8 by 8 foot test at CAL. Pictures taken during these tests indicated some improvement in combustion but disclosed apparent unsymmetrical flow from the nozzles. Pictorial evidence also indicates a variation in O/F ratio between runs.

Data from the hot base runs have been corrected to exclude the radiation. The non-heated base plate (cold) temperature for convective heating rates was 80°F. Data presented in this report are not necessarily consistent with the preliminary data release (Reference 5, Volume I). This material is based on revised data released by CAL on August 8, 1963.

6.1 RADIATION

The lack of a free stream has the effect of allowing greater expansion of the engine exhaust than would occur with a free stream. However, the effect on radiation at the test altitudes is believed negligible.

6.1.1 Radiation to Base

Radiation data for two non-gimballed configurations are shown in Figure 122. The data represent the maximum heating rate at any point on the base and may vary from point to point for different test conditions. The locations of the heat transfer gages are shown in Figure 19, Volume 1. Data are shown for all test runs. It appears that radiation is essentially constant for these configurations at all altitudes. Addition of turbine exhaust has no consistent affect on radiation heating rate.

Reproduced from best available copy.

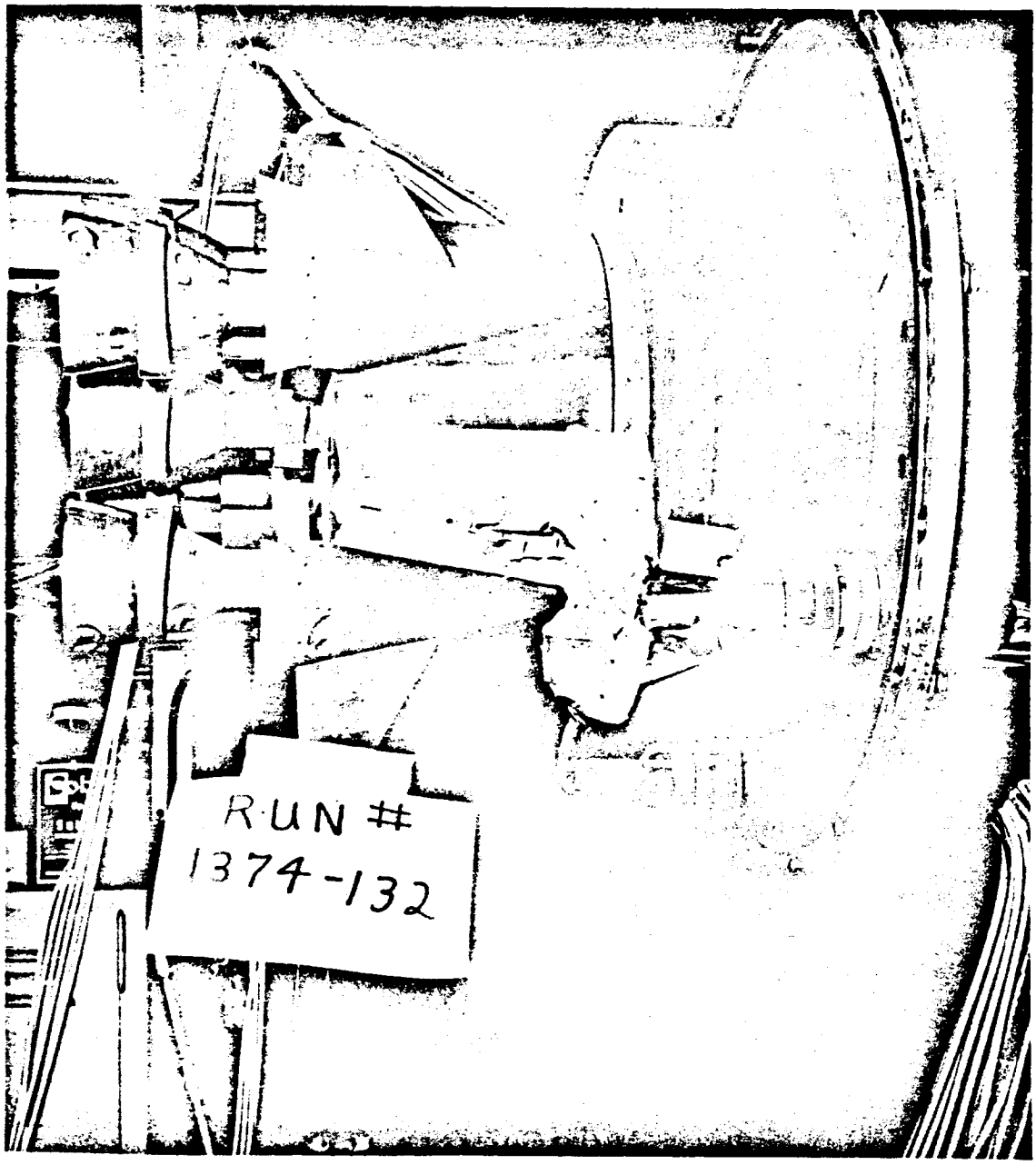

FIGURE 121 Model Installation - Cornell High Altitude Chamber

TUNNEL Cornell Altitude Chamber

SYM.	INST.	CONFIG.	SYM.	INST.	CONFIG.
□		$B_1FS_1N_{1-5}PL_1$			
○		$B_1FS_4SC_1N_{1-5}PL_1$			

NOTE: 1. Solid symbol denotes turbine exhaust.
2. Data shown are maximum on base

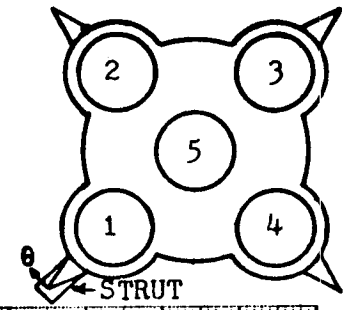

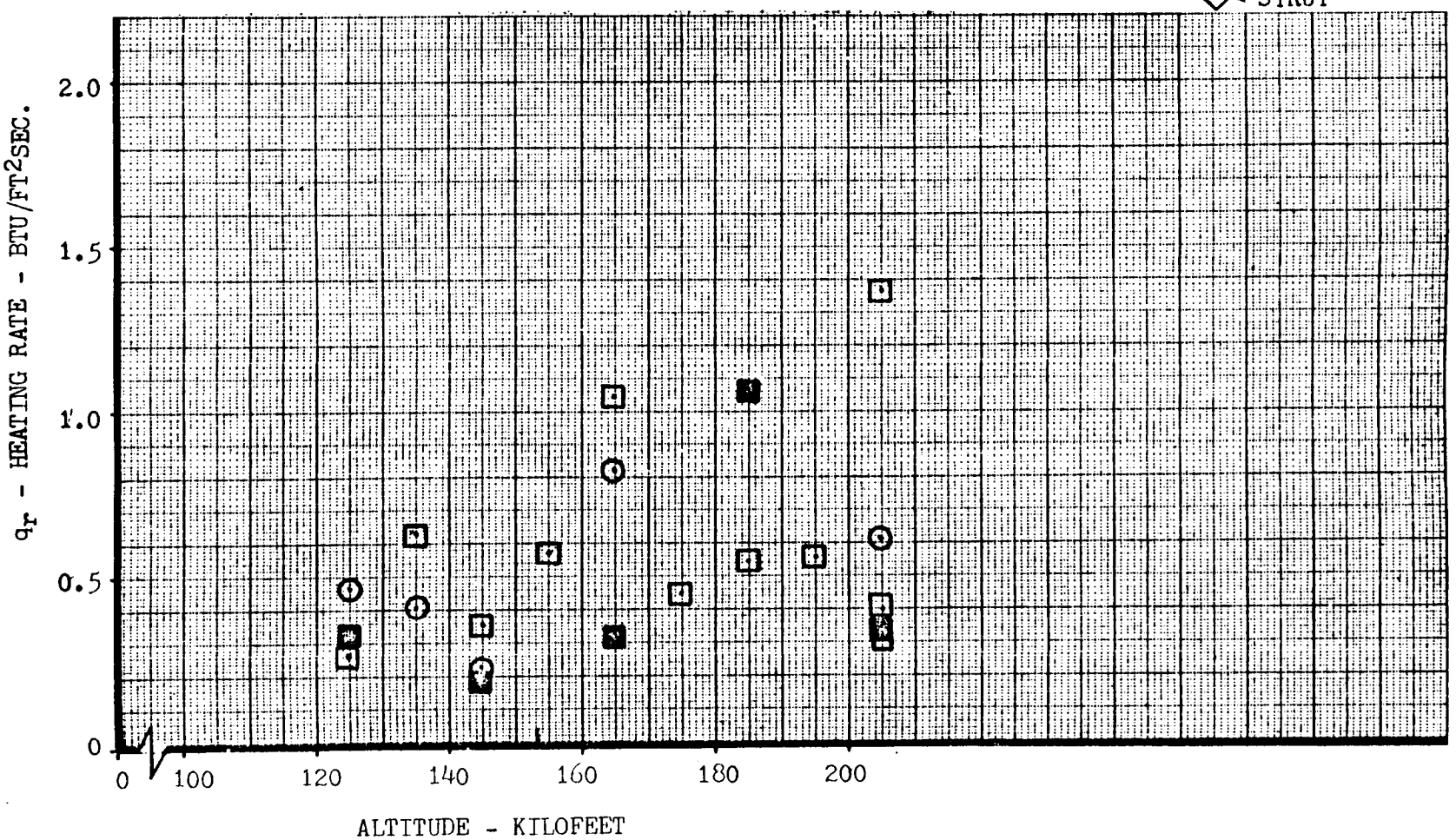

FIGURE 122 Base Heating - Radiation

6.1.1 (Continued)

The effect of gimballing the engines and operating with the center engine inoperative is shown in Figures 123 and 124. Data points reflect altitudes of 125,000, 165,000, and 205,000 feet at base positions along a ray located midway between engines 3 and 4. Radiation heating shows little variation along the ray. In general gimballing increases the heating rate; however, the effect decreases with an increase in altitude. With an inoperative engine, radiation to the base is equal to or less than radiation measured on other configurations at all altitudes.

6.1.2 Radiation to Fin and Engine Fairing

Radiation data for the fin and engine fairing are shown in Figure 125. Data are obtained from gages H_{64} and H_{66} located on the aft face of the fin; gages H_{58} and H_{60} located on the inside surface of the engine fairing facing the centerline of the engine. These data are eratic and therefore only the maximums are shown. Heating rate for the bulk of the fin data is approximately the same level as the heating rate to the base. Data for the fairing are less, as expected, since the fairing gage view factor for the near engine is very small.

6.1.3 Radiation to Engine (External)

Figure 126 shows data from a radiation calorimeter attached to the outside of the nozzle near the exit plane of the center engine. The calorimeter (H_{22}) is facing outward between engines 3 and 4 approximately perpendicular to the nozzle axis. Heating rates to the outside of the engine are less than to the base. Since the instrument view of the outboard plumes is very small, changes due to gimballing is not expected. Direct radiation to H_{22} from the center engine is zero.

6.1.4 Radiation to Engine (Engine Out)

On the center engine out configuration, radiation heating rates were measured inside the center engine and are shown in Figure 126. Gages H_{44} and H_{48} are located on the inside surface facing the nozzle centerline near the exit plane and near the throat respectively. Gage H_{54} is located on the nozzle lip facing aft. Heating is generally higher near the throat than at the exit plane and compares favorably with radiation to the base. Heating to the nozzle lip is approximately twice the highest rates inside the nozzle.

6.1.5 Comparison with Theory

Theoretical calculations were made for comparison with the model test data and are shown in Figure 127. The details of the theoretical calculations can be found in Appendix A, Volume 1.

TUNNEL Cornell Altitude Chamber

SYM.	INST.	CONFIG.
□	$H_{2,4,6,8,10}$	$B_1FS_1N_{1-5}PL_1$
△	$H_{2,4,6,8,10}$	$B_1FS_1N_{G_3}N_{G_4}PL_1$
◺	$H_{2,4,6,8,10}$	$B_1FS_1N_{G_5}N_{G_6}PL_1$
◇	$H_{2,4,6,8,10}$	$B_1FS_1N_7PL_1$

NOTE: 1. Unflagged symbol - 205,000 feet altitude
2. Flagged right - 165,000 feet altitude
3. Flagged left - 125,000 feet altitude

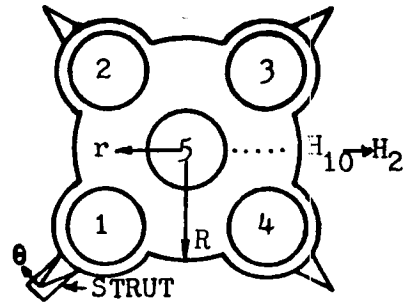

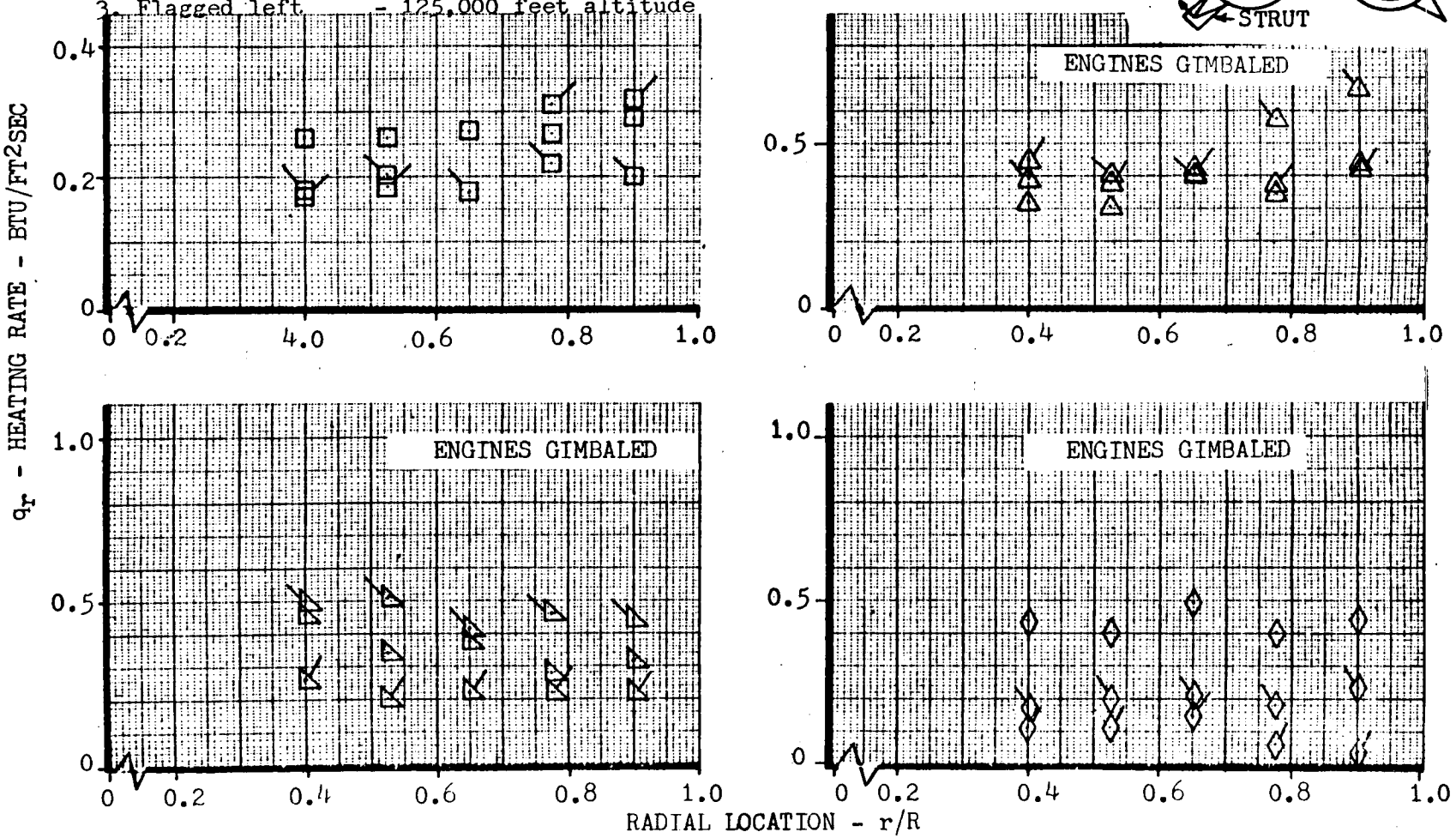

FIGURE 123 Base Heating - Radiation

TUNNEL Cornell Altitude Chamber

SYM.	INST.	CONFIG.
□	$H_{2,4,6,8,10}$	$B_1FS_1N_{1-5}PL_1$
△	$H_{2,4,6,8,10}$	$B_1FS_1N_{G_3}N_{G_4}PL_1$
◺	$H_{2,4,6,8,10}$	$B_1FS_1N_{G_5}N_{G_6}PL_1$
◇	$H_{2,4,6,8,10}$	$B_1FS_1N_7PL_1$

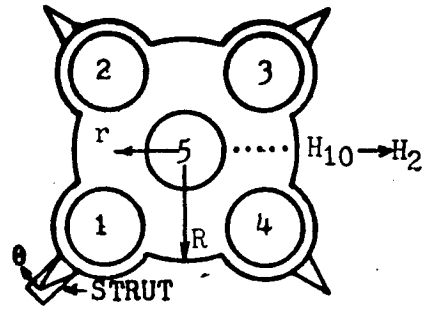

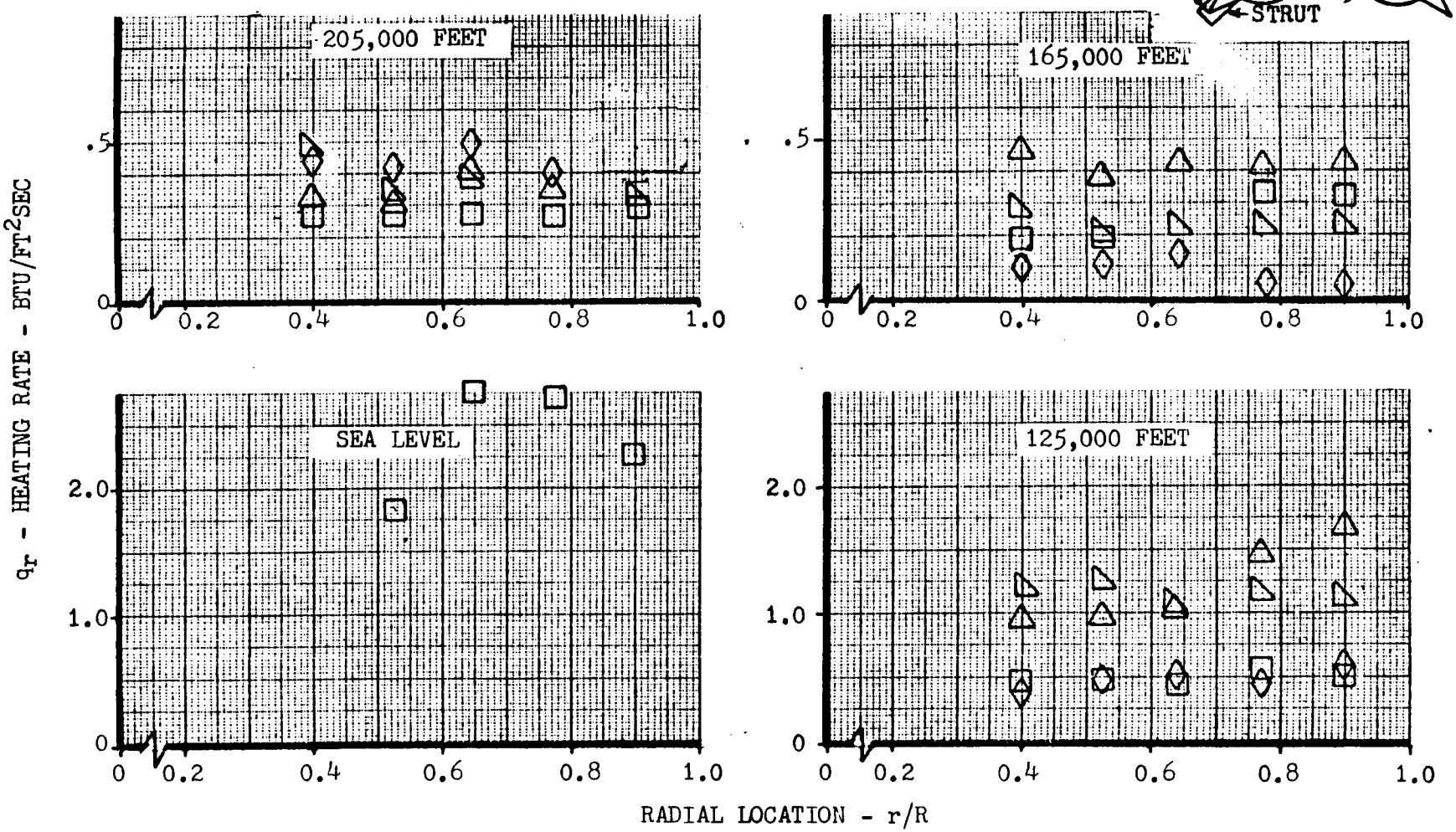

FIGURE 124 Base Heating - Radiation

TUNNEL Cornell Altitude Chamber

SYM.	INST.	CONFIG.
O	$H_{64,66}$	All
σ	$H_{58,60}$	$B_1FS_1N_{1-5}PL_1$

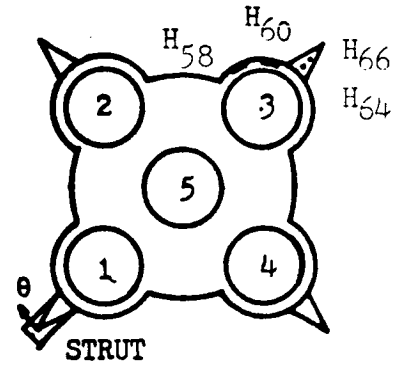

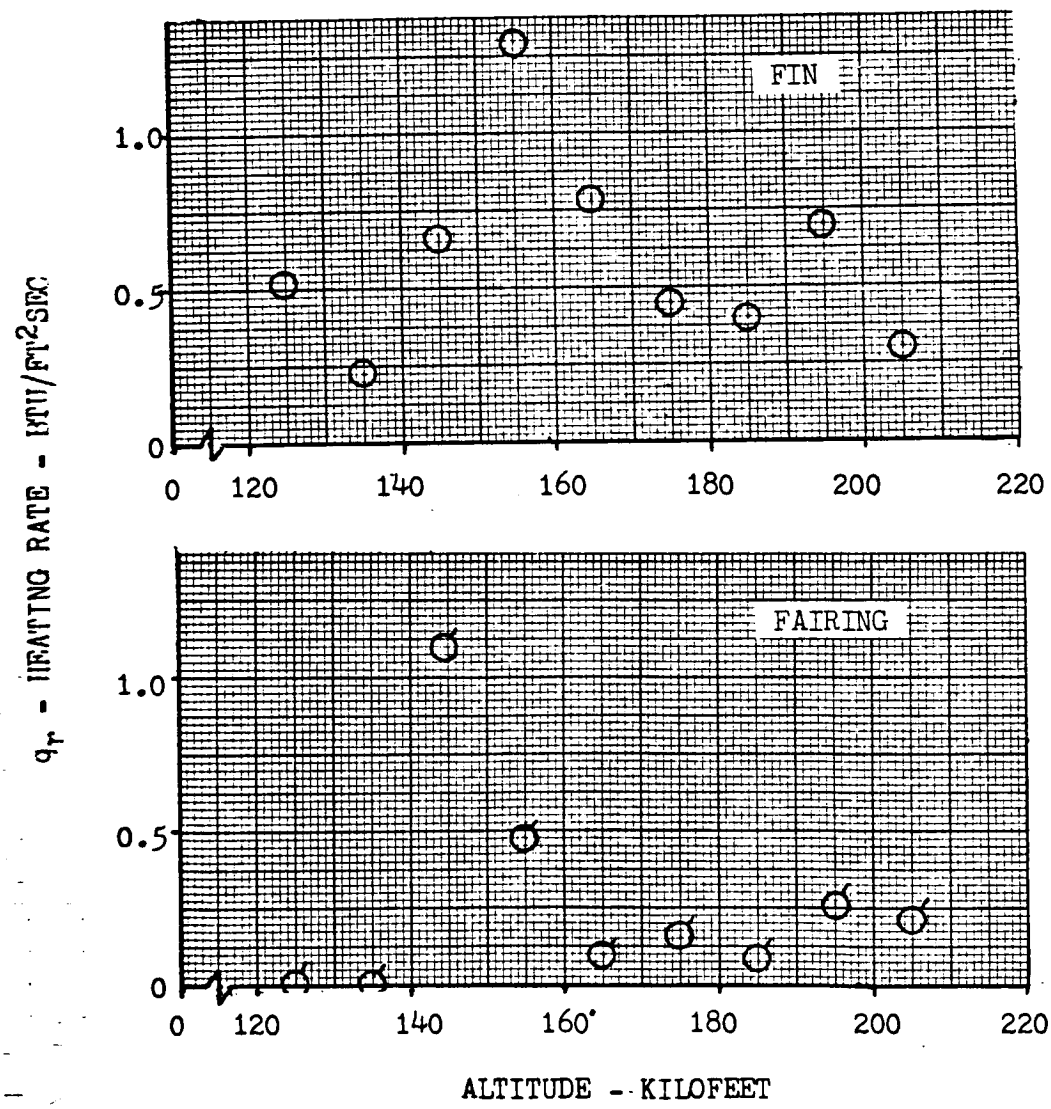

FIGURE 125 Fin and Engine Fairing Heating - Radiation

TUNNEL Cornell Altitude Chamber

SYM.	INST.	CONFIG.
□	H_{22}	$B_1FS_1N_{1-5}PL_1$
◇	H_{44}	$B_1FS_1N_7PL_1$
◇	H_{48}	$B_1FS_1N_7PL_1$
○	H_{54}	$B_1FS_1N_7PL_1$

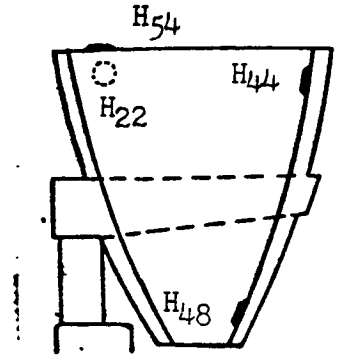

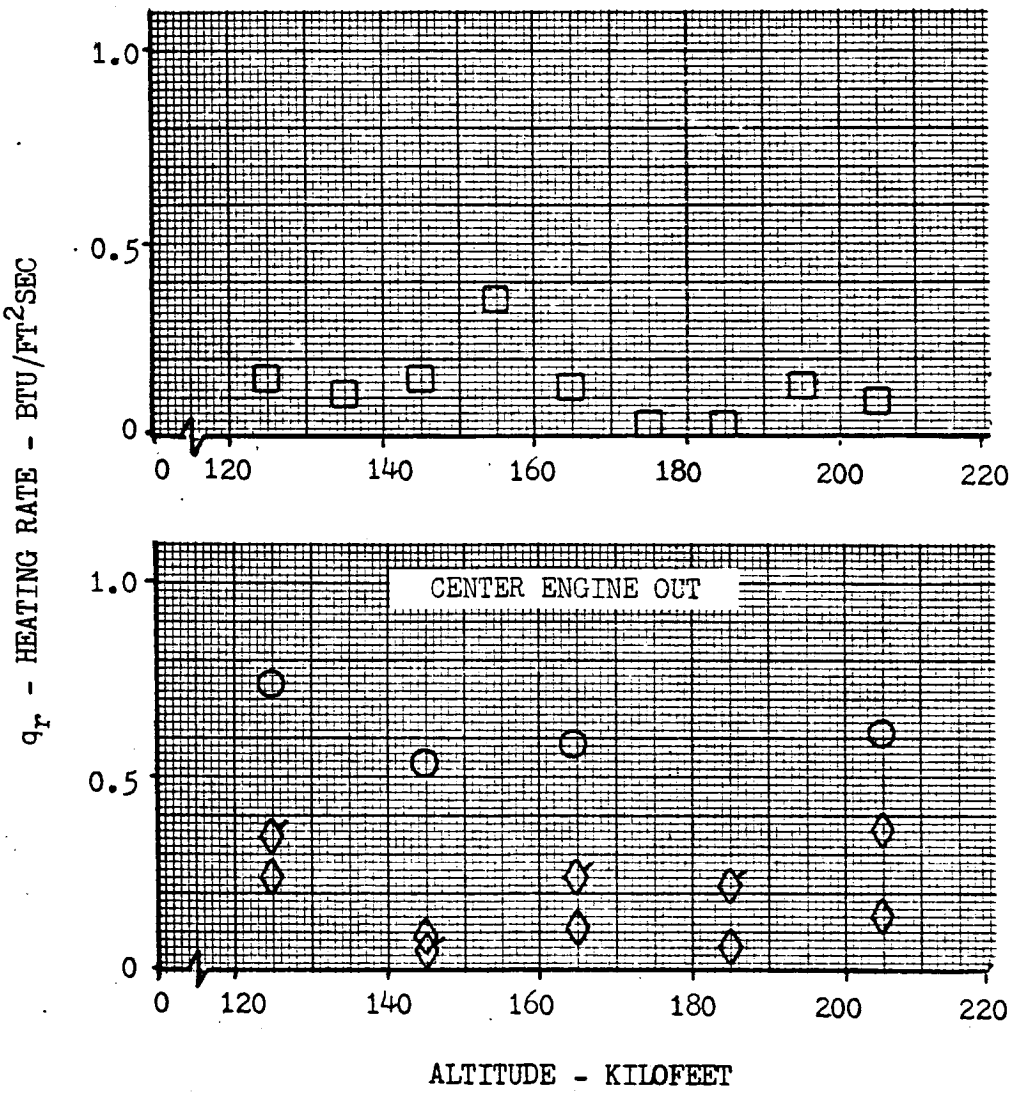

FIGURE 126 Engine Heating - Radiation

6.1.5 (Continued)

Figure 127 shows the comparison of sea level radiation data and theoretical calculations as a function of base radial distribution. The lower theoretical curve is based on a non-luminous hot gas analysis and is considerably below the model test data. The upper theoretical curve was calculated using the same shape factor and plume temperature as the non-luminous hot gas analysis assuming an emissivity equal to 1.0. Calculations assuming an emissivity of 0.5 fit the data quite well. The scatter in the data indicates that the concentration of carbon particles or plume temperature may vary significantly from run to run.

Figure 127 also shows the radiation data obtained at altitude compared with the two theoretical approaches already discussed. The data lie between the two theoretical curves.

6.2 CONVECTION

Since these data are obtained in an altitude chamber without a free stream, the effect of scoops and deflectors is negligible and recirculation of exhaust gases due to plume impingement is unimpeded. Data are shown comparing a standard configuration against those with a short engine fairing, engines gimballed, and the inoperative center engine.

6.2.1 Convection to Base

Figure 128 illustrates the data obtained using the basic configuration $B_1FS_1N_{1-5}$. Convective heating rates vary from 1.0 to 10.0 BTU/FT^{2}SEC depending on radial location and altitude. These data represent the maximum recorded values along a ray between engines 3 and 4. The heating rate is highest outboard of the location of the minimum vent area (r/R = 0.65). Variation with altitude is relatively small and appears to be largely data scatter. Figure 129 shows data with hydrogen turbine exhaust. Comparison between Figures 128 and 129 indicate that heating is reduced by injection of hydrogen.

Data for the short fairing, two gimbal patterns and inoperative engine are shown in Figure 130 for the altitudes 125,000, 165,000 and 205,000 feet. Shortening the fairing has little effect on base heating compared to the basic configuration shown in Figure 128. Convection heating is reduced to approximately one-half that of the basic configuration when the center engine is inoperative.

When engines 3 and 4 are gimballed toward the center engine (N_{G_5} N_{G_6}) the heating rate is relatively unaffected. However, when the engines are gimballed toward each other (N_{G_3} N_{G_4}) the heating rate is approximately doubled outboard of the point r/R = 0.525.

TUNNEL Cornell Altitude Chamber

SYM.	INST.	CONFIG.
□	$H_{2,4,6,8,10}$	$B_1FS_1N_{1-5}PL_1$
□	H_2	$B_1FS_1N_{1-5}PL_1$

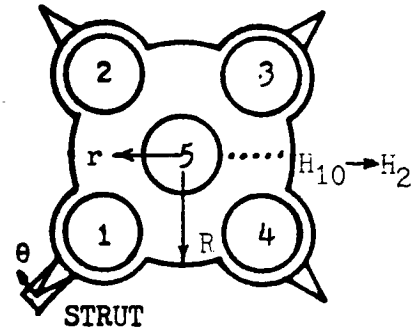

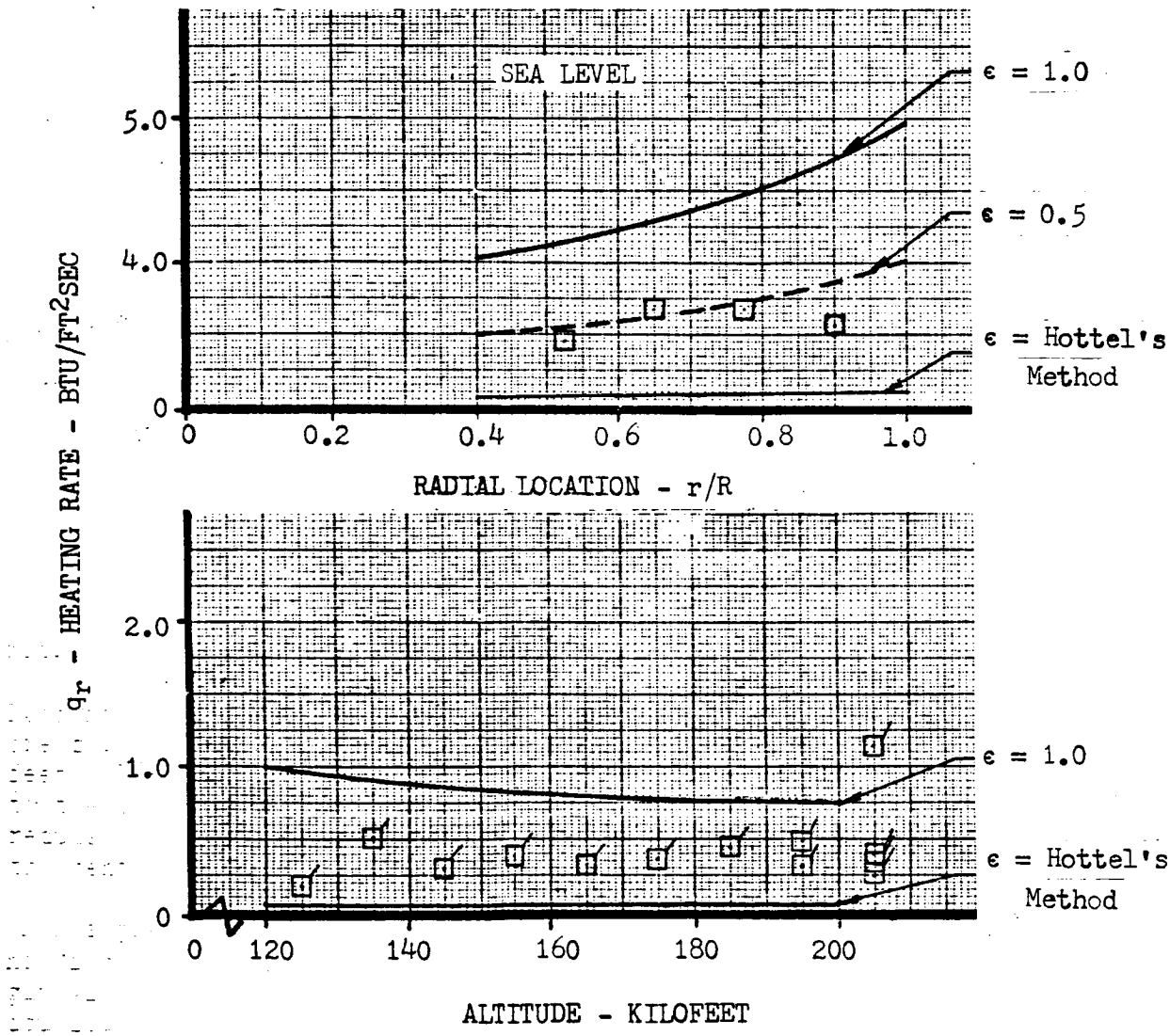

FIGURE 127 Base Heating - Radiation Versus Theory

TUNNEL Cornell Altitude Chamber

SYM.	INST.	CONFIG.
□	$H_{1,3,5,7,9}$	$B_1FS_1N_{1-5}PL_1$
◇	H_1	$B_1FS_1N_{1-5}PL_1$
◇	H_5	$B_1FS_1N_{1-5}PL_1$
⬠	H_7	$B_1FS_1N_{1-5}PL_1$

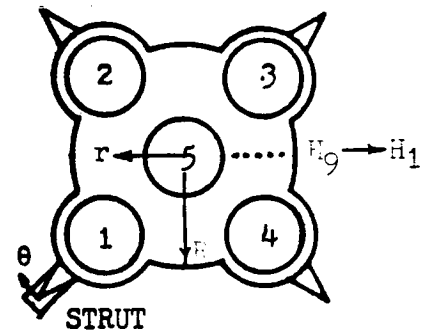

NOTE: □ 205 Kilofeet
□ 165 Kilofeet
□ 125 Kilofeet

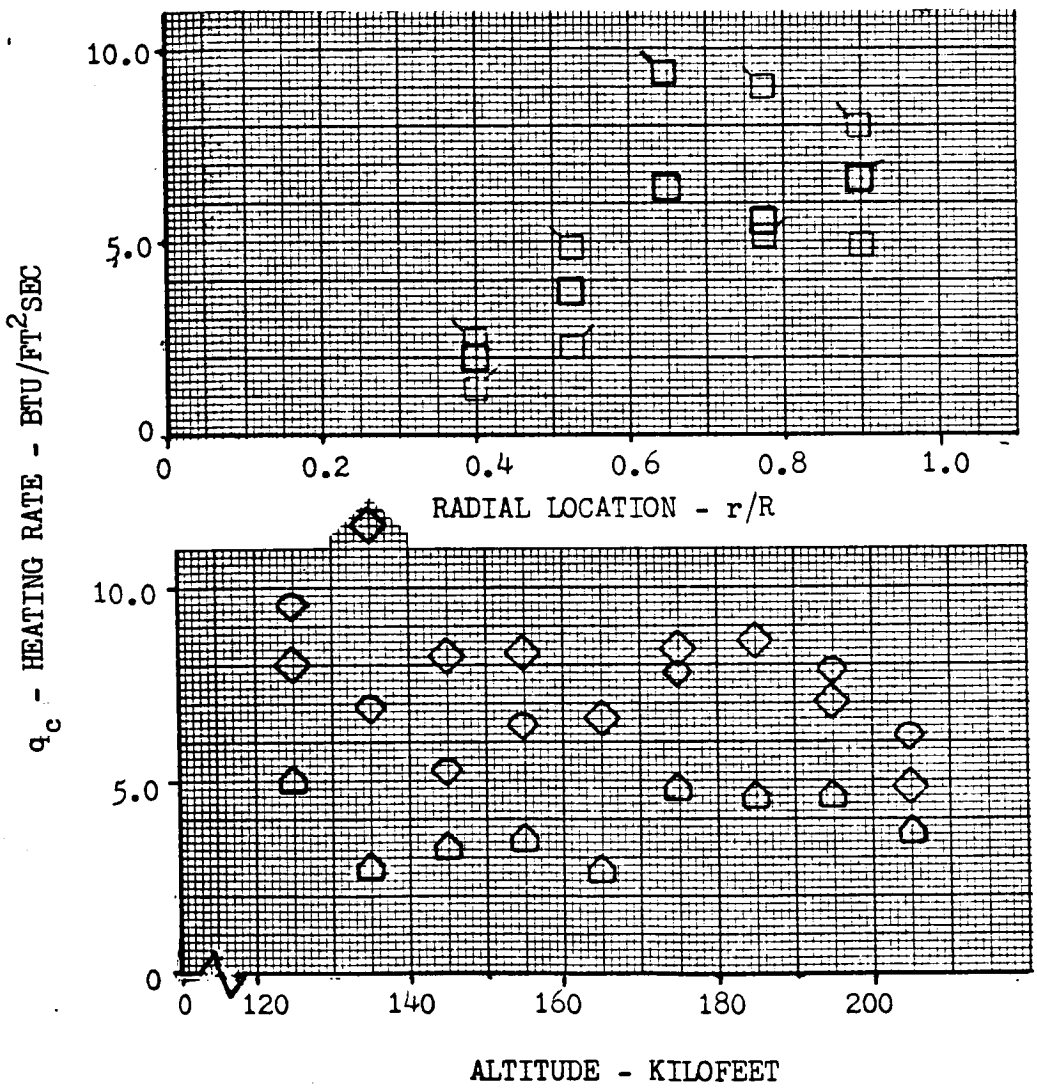

FIGURE 128 Base Heating - Convection

TUNNEL Cornell Altitude Chamber

SYM.	INST.	CONFIG.	SYM.	INST.	CONFIG.
□	$H_{1,3,5,7,9}$	$B_1FS_1N_{1-5}PL_1$			

NOTE: 1. □ 205 kilofeet
2. □ 165 kilofeet
3. □ 125 kilofeet
4. Solid symbol denotes turbine exhaust

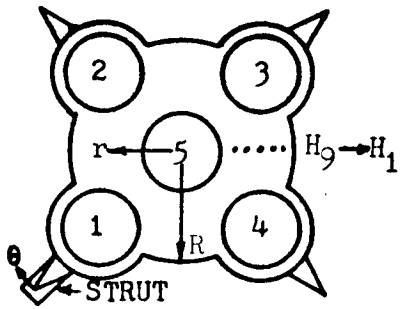

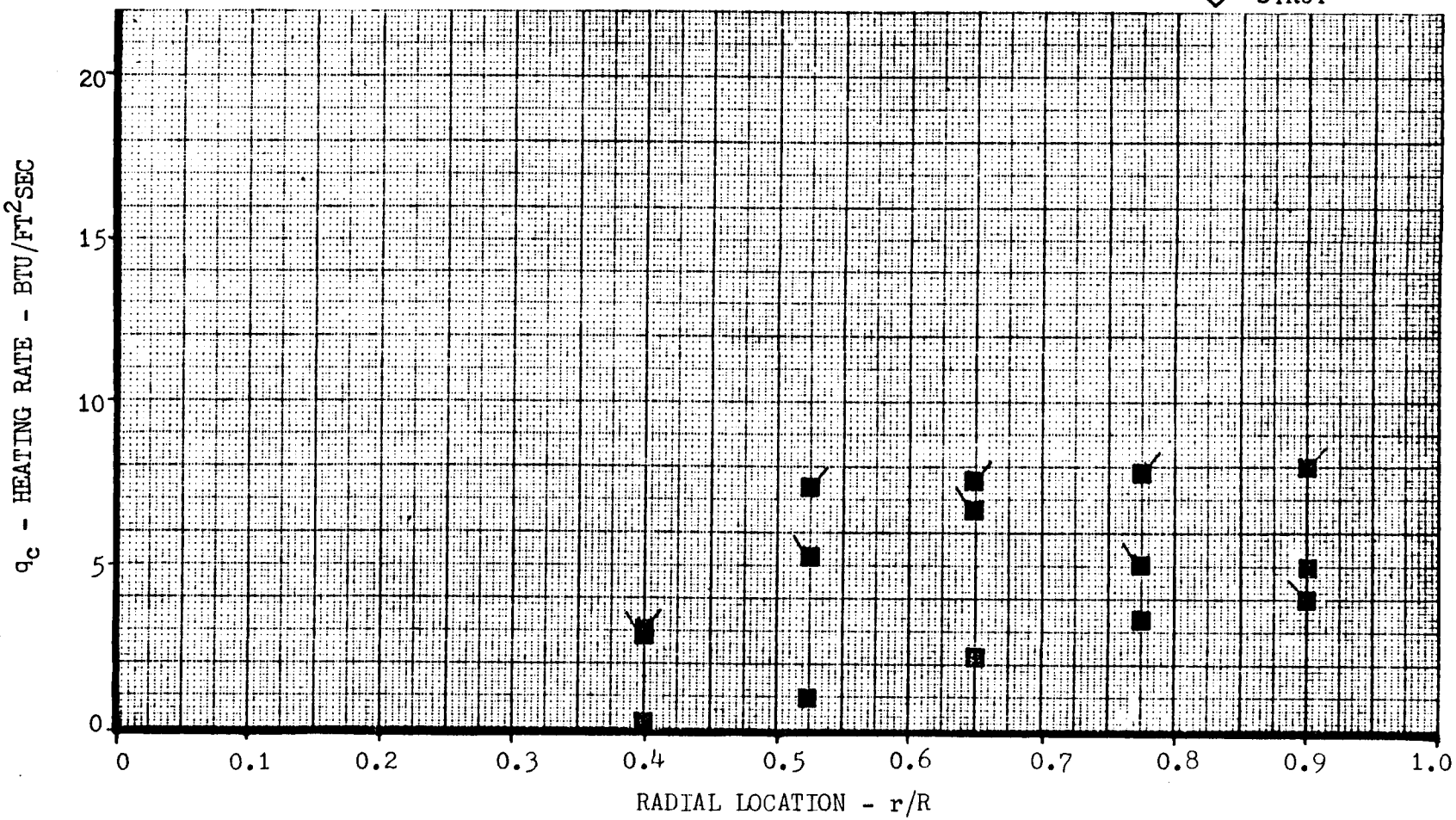

FIGURE 129 Base Heating - Convection

TUNNEL Cornell Altitude Chamber

SYM.	INST.	CONFIG.
○	$H_{1,3,5,7,9}$	$B_1FS_4SC_1N_{1-5}PL_1$
△	$H_{1,3,5,7,9}$	$B_1FS_1N_{G_3}N_{G_4}PL_1$
◺	$H_{1,3,5,7,9}$	$B_1FS_1N_{G_5}N_{G_6}PL_1$
◇	$H_{1,3,5,7,9}$	$B_1FS_1N_7PL_1$

NOTE: 1. Unflagged symbol - 205,000 kilofeet
2. Flagged right - 165,000 kilofeet
3. Flagged left - 125,000 kilofeet

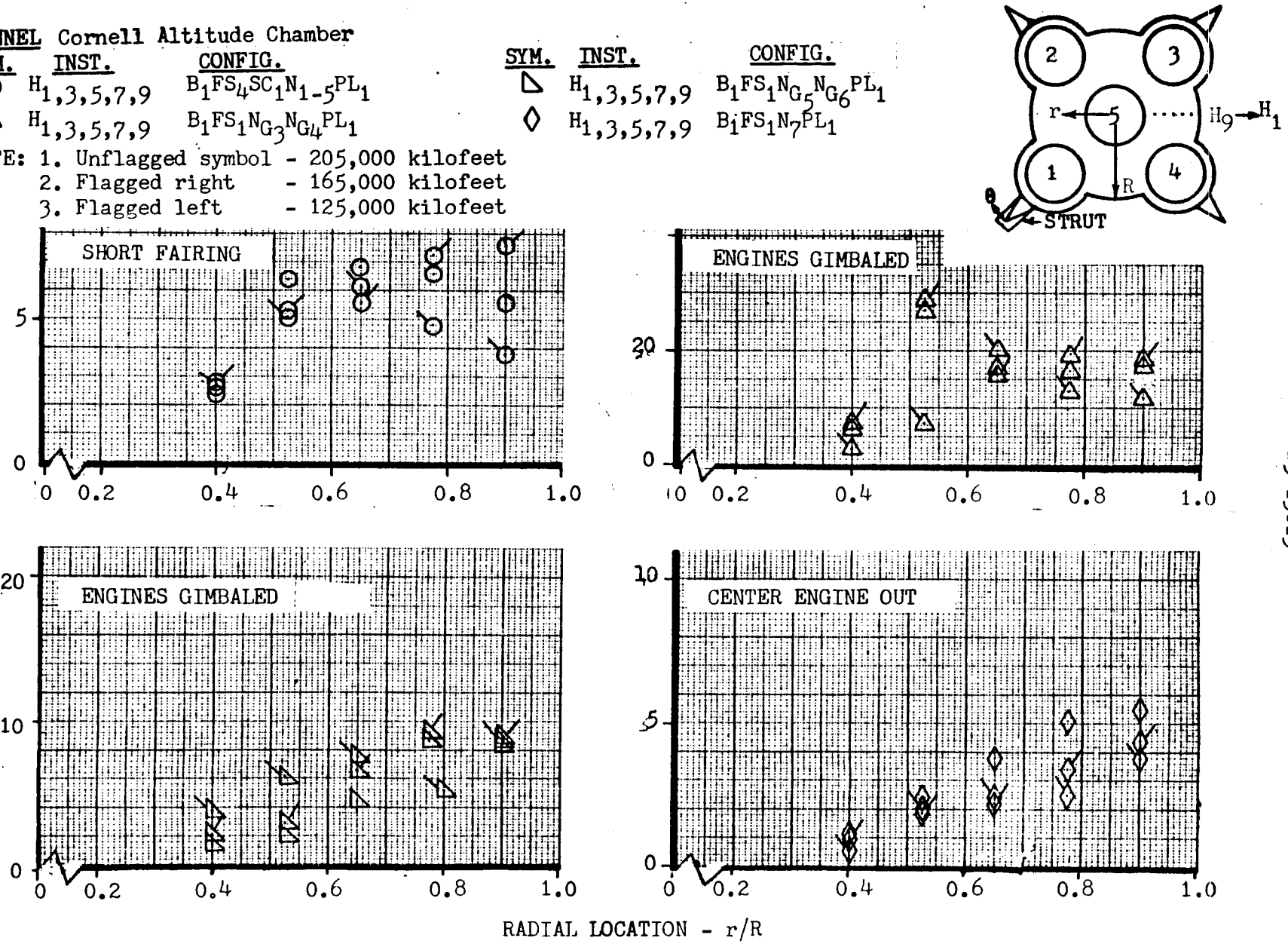

FIGURE 130 Base Heating - Convection

6.2.1 (Continued)

The maximum convective heating point is expected to move inboard with increase in altitude until complete plume impingement has occurred. The data shown in Figures 131 through 135 indicate that peak heating does not move inboard above 145,000 feet. This conclusion could be in error due to insufficient instrumentation to measure the peak of the heating.

6.2.2 Convection to Fin and Engine Fairing

The aft face of the fin is instrumented at two locations as shown in Figure 26, Volume 1. Gage H_{63} is located near the fin-fairing interface and H_{65} is approximately midway along the fin. Fairing instrumentation is located on the inside surface of the fairing near the aft edge and is placed parallel to the fairing surface. Data for the fin and fairing are shown in Figure 136.

Heating to the fairing is essentially constant throughout the altitude range at a value of approximately 2 BTU/FT^2SEC. Data on the fin indicate a slight increase in heating rate with distance outboard on the fins. The short fairing has no apparent effect on heating rate to the fin. Heating rates are considerably less on the fin and fairing than on the base plate.

6.2.3 Convection Heating to Engine (External)

Heating measurements were made on the outside of the center engine with instruments positioned as shown in Figure 22 and 23, Section 1. Figure 137 shows that convection heating rates near the nozzle exit plane and directly opposite an outboard engine (H_{23}) are relatively small compared to the heating rates for surfaces located near the nozzle exit plane between outboard engines (H_{21}). It is also seen that neither gimbal pattern has a significant effect on heating directly opposite an outboard engine. Figure 137 indicates that the heating rates are considerably increased between outboard engines for both gimbal patterns and are much higher than similar heating on the basic configuration.

Data obtained with a short engine fairing are shown in Figure 138. Results are inconclusive. Additional basic configuration data (not shown) from repeat runs are approximately 5 BTU/FT^2SEC higher and indicate that removing the fairing will considerably reduce heating to the center engine.

A combination of heating rates to various points on the center engine and base are shown in Figures 139, 140 and 141 for the two gimbal patterns at altitudes of 125,000, 165,000 and 205,000 feet respectively.

TUNNEL Cornell Altitude Chamber

SYM.	INST.	CONFIG.
□	$H_{1,3,5,7,9}$	$B_1FS_1N_{1-5}PL_1$
○	$H_{1,3,5,7,9}$	$B_1FS_4SC_1N_{1-5}PL_1$
△	$H_{1,3,5,7,9}$	$B_1FS_1N_{G_3}N_{G_4}PL_1$
◺	$H_{1,3,5,7,9}$	$B_1FS_1N_{G_5}N_{G_6}PL_1$
◇	$H_{1,3,5,7,9}$	$B_1FS_1N_7PL_1$

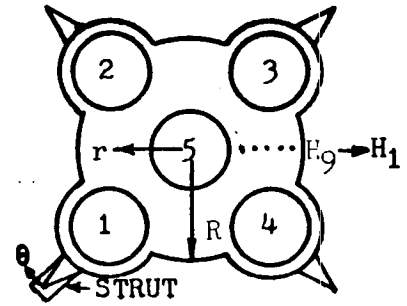

NOTE: Solid symbol denotes turbine exhaust.

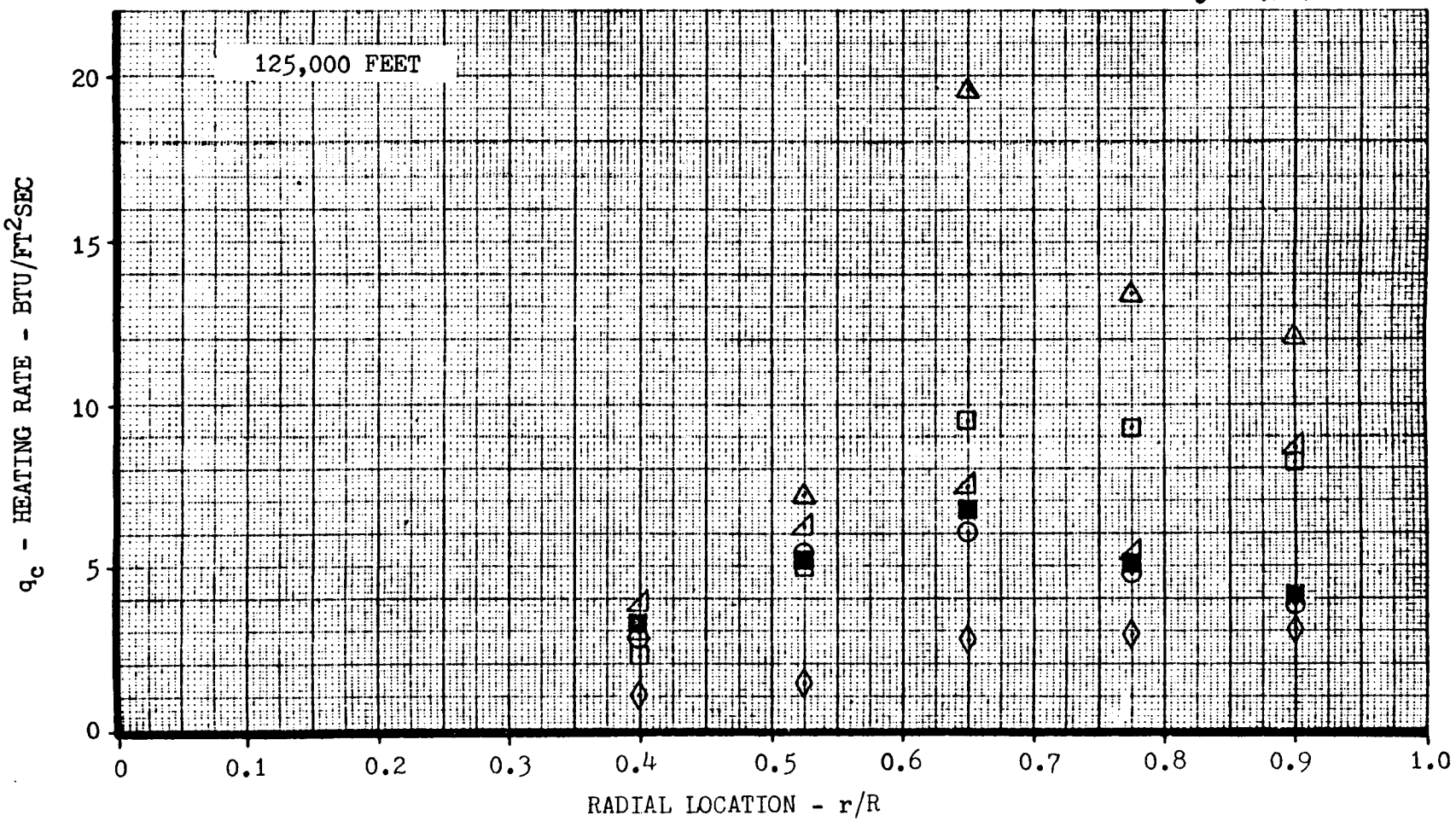

FIGURE 131 Base Heating - Convection

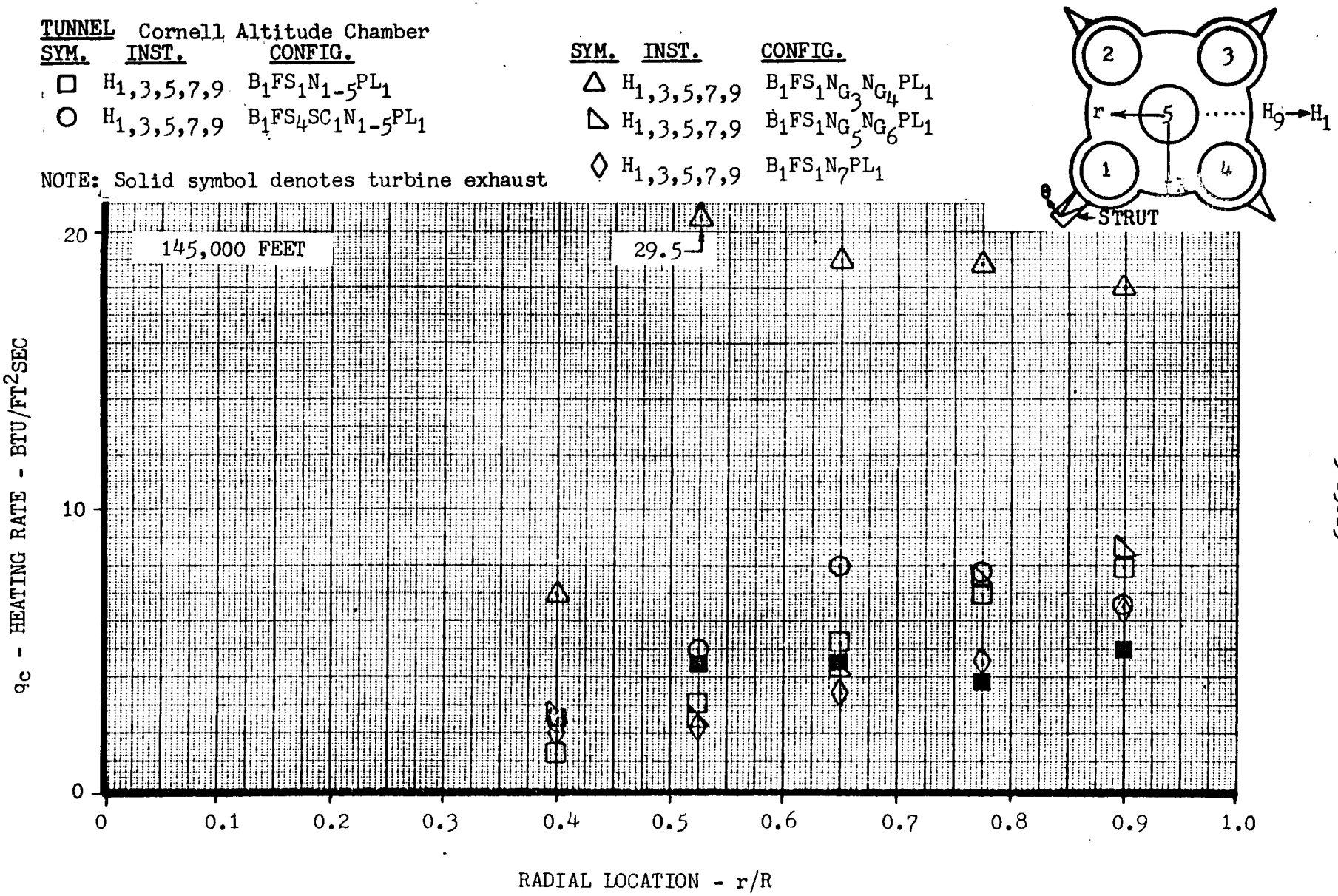

FIGURE 132 Base Heating - Convection

TUNNEL SYM.	Cornell Altitude Chamber INST.	CONFIG.
□	$H_{1,3,5,7,9}$	$B_1FS_1N_{1-5}PL_1$
○	$H_{1,3,5,7,9}$	$B_1FS_4SC_1N_{1-5}PL_1$

SYM.	INST.	CONFIG.
△	$H_{1,3,5,7,9}$	$B_1FS_1N_{G_3}N_{G_4}PL_1$
◺	$H_{1,3,5,7,9}$	$B_1FS_1N_{G_5}N_{G_6}PL_1$
◇	$H_{1,3,5,7,9}$	$B_1FS_1N_7PL_1$

NOTE: Solid symbol denotes turbine exhaust

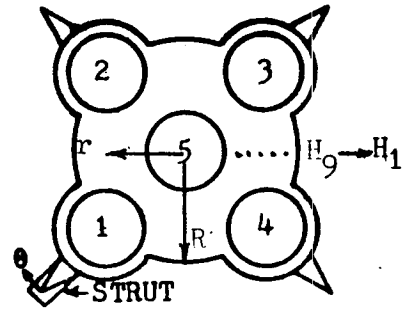

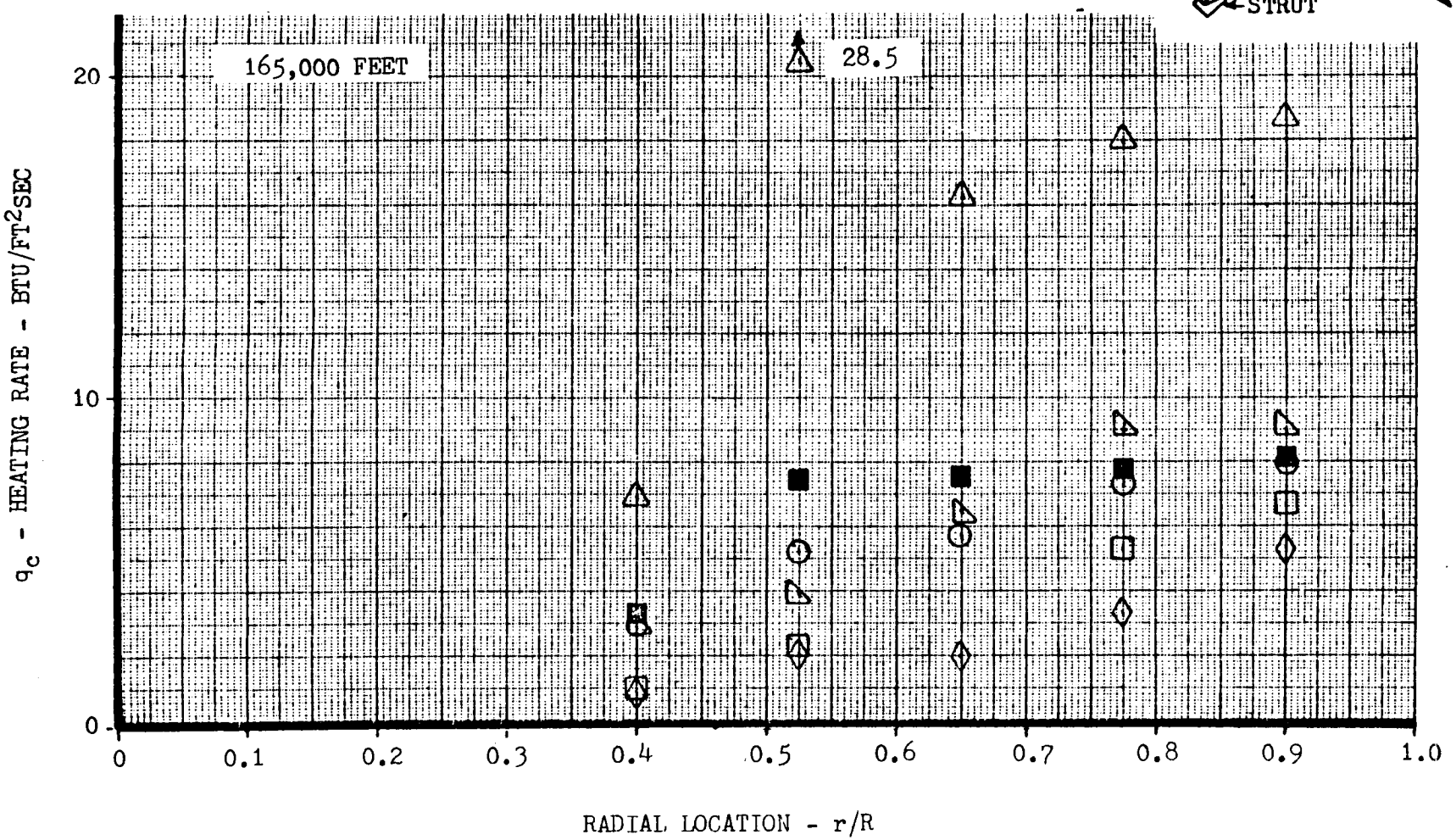

FIGURE 133 Base Heating - Convection

TUNNEL Cornell Altitude Chamber

SYM.	INST.	CONFIG.
□	$H_{1,3,5,7,9}$	$B_1FS_1N_{1-5}PL_1$
△	$H_{1,3,5,7,9}$	$B_1FS_1N_{G_3}N_{G_4}PL_1$
◺	$H_{1,3,5,7,9}$	$B_1FS_1N_{G_5}N_{G_6}PL_1$
◇	$H_{1,3,5,7,9}$	$B_1FS_1N_7PL_1$

NOTE: Solid symbol denotes turbine exhaust

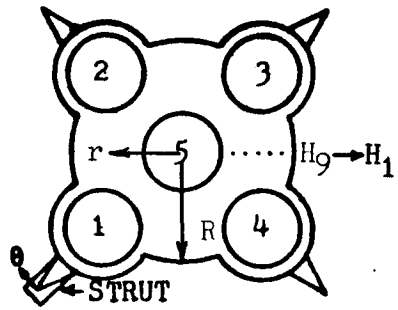

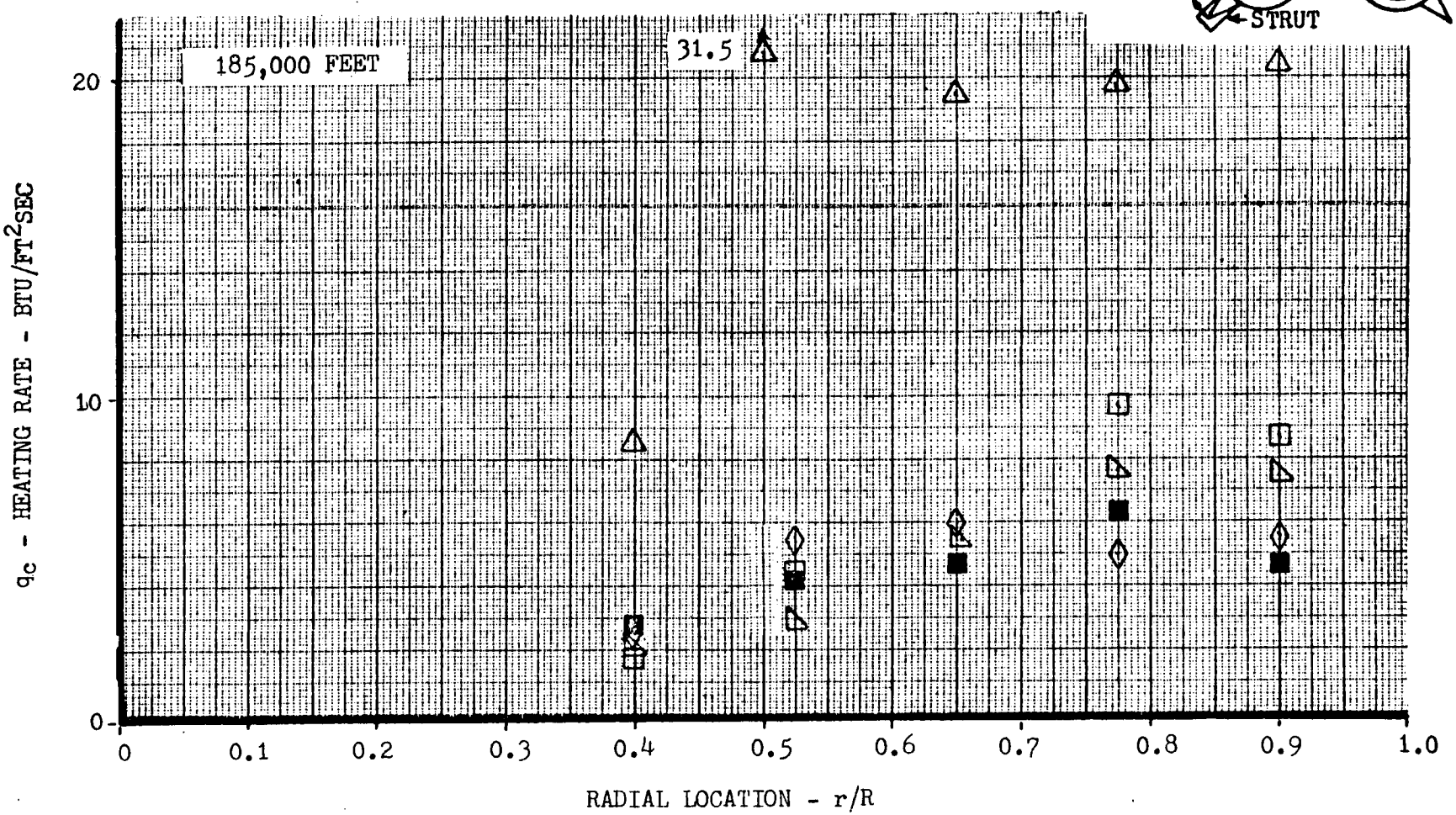

FIGURE 134 Base Heating Convection

TUNNEL Cornell Altitude Chamber

SYM.	INST.	CONFIG.
□	$H_{1,3,5,7,9}$	$B_1FS_1N_{1-5}PL_1$
○	$H_{1,3,5,7,9}$	$B_1FS_4SC_1N_{1-5}PL_1$
△	$H_{1,3,5,7,9}$	$B_1FS_1N_{G_3}N_{G_4}PL_1$
◺	$H_{1,3,5,7,9}$	$B_1FS_1N_{G_5}N_{G_6}PL_1$
◇	$H_{1,3,5,7,9}$	$B_1FS_1N_7PL_1$

NOTE: Solid symbol denotes turbine exhaust.

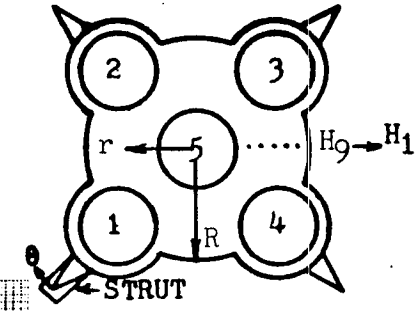

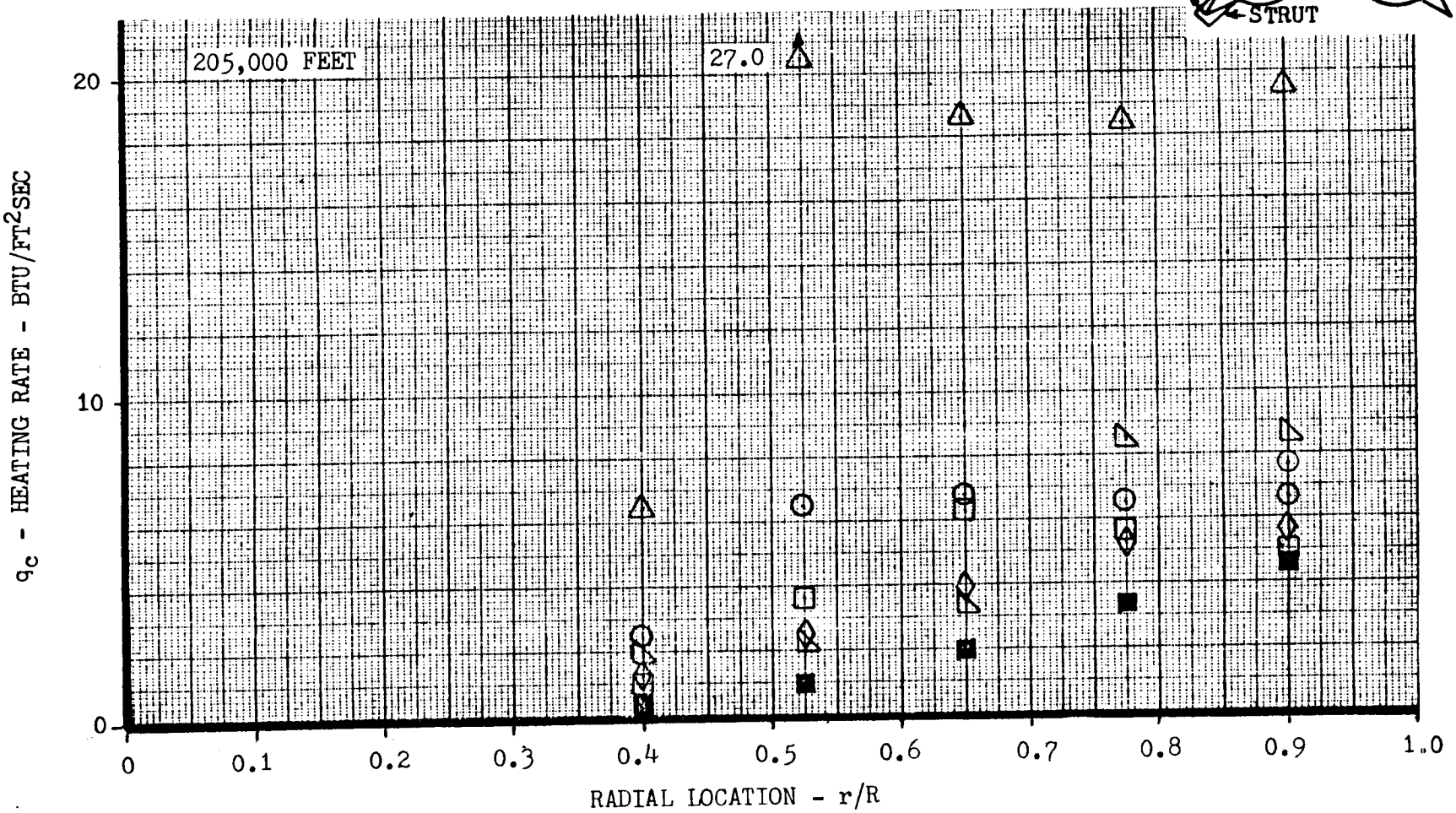

FIGURE 135 Base Heating Convection

TUNNEL Cornell Altitude Chamber

SYM.	INST.	CONFIG.
□	H_{57}	$B_1FS_1N_{1-5}PL_1$
◪	H_{59}	$B_1FS_1N_{1-5}PL_1$
■	H_{65}	$B_1FS_1N_{1-5}PL_1$
◪	H_{63}	$B_1FS_4SC_1N_{1-5}PL_1$
●	H_{65}	$B_1FS_4SC_1N_{1-5}PL_1$

NOTE: Solid symbol denotes turbine exhaust

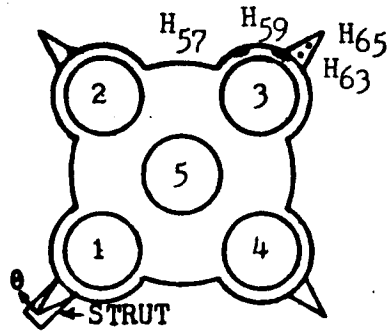

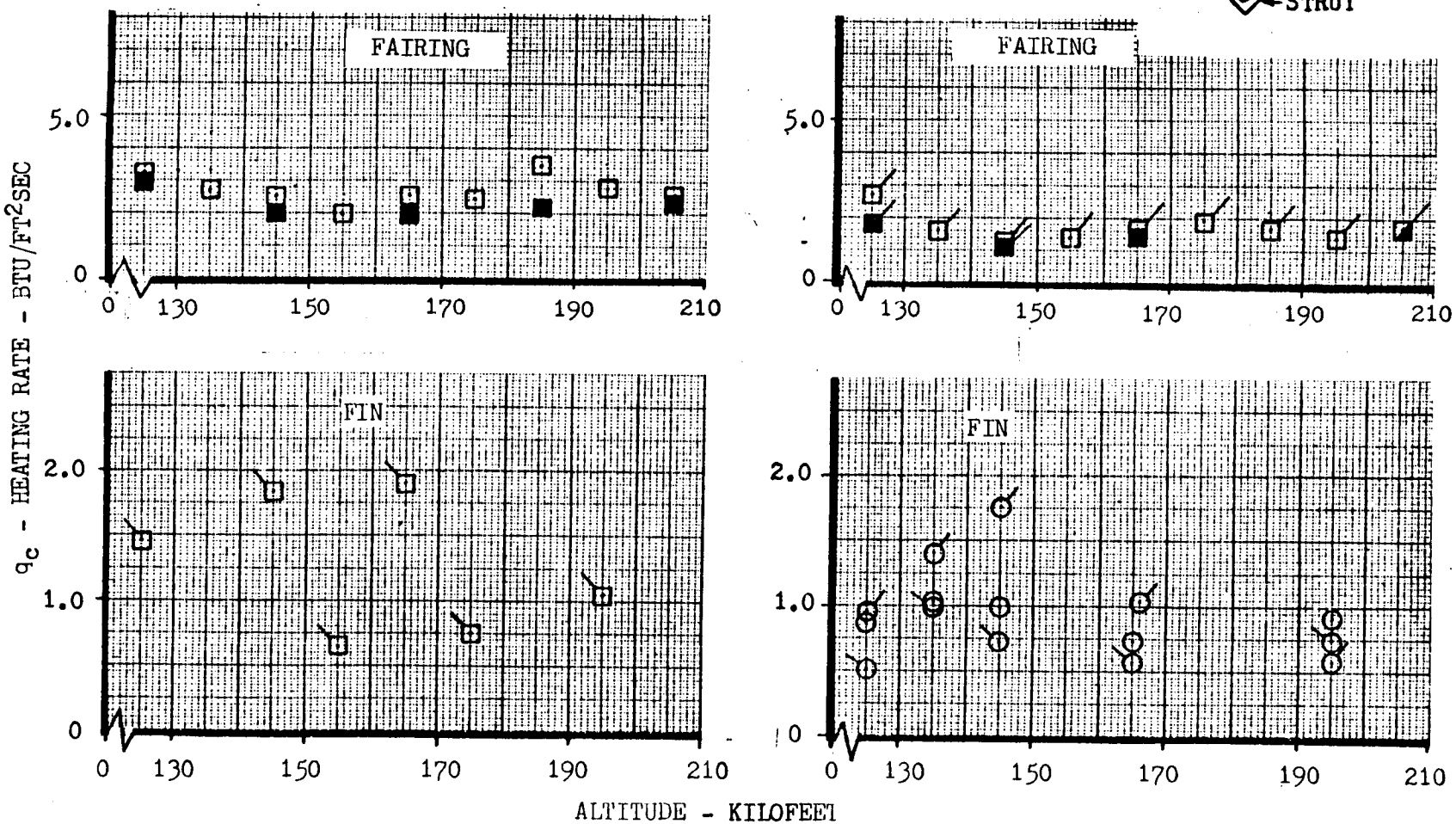

FIGURE 136 Fin and Engine Heating - Convection

TUNNEL Cornell Altitude Chamber

SYM.	INST.	CONFIG.
□	H_{23}	$B_1FS_1N_{1-5}PL_1$
○	H_{23}	$B_1FS_4SC_1N_{1-5}PL_1$
△	H_{23}	$B_1FS_1N_{G_3}N_{G_4}PL_1$
◺	H_{23}	$B_1FS_1N_{G_5}N_{G_6}PL_1$
◸	H_{21}	$B_1FS_1N_{1-5}PL_1$

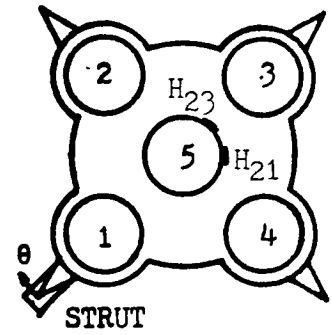

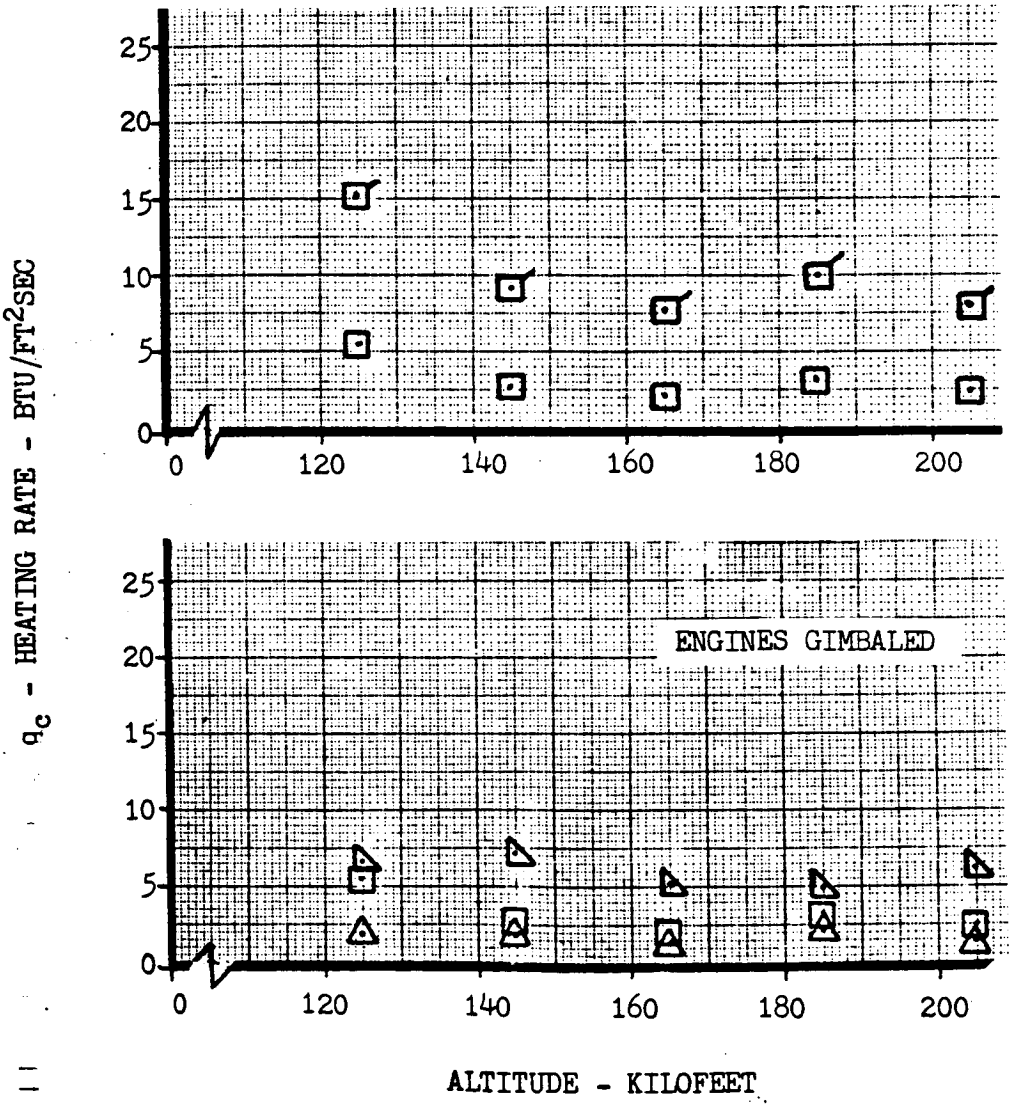

FIGURE 137 Engine Heating - Convection (External)

TUNNEL Cornell Altitude Chamber

SYM.	INST.	CONFIG.
□	H_{21}	$B_1FS_1N_{1-5}PL_1$
○	H_{21}	$B_1FS_4SC_1N_{1-5}PL_1$
△	H_{21}	$B_1FS_1N_{G_3}N_{G_4}PL_1$
◺	H_{21}	$B_1FS_1N_{G_5}N_{G_6}PL_1$

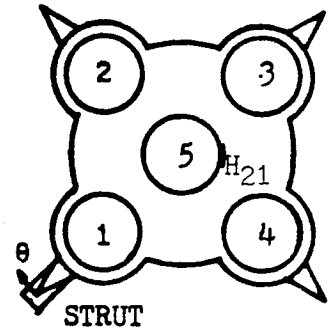

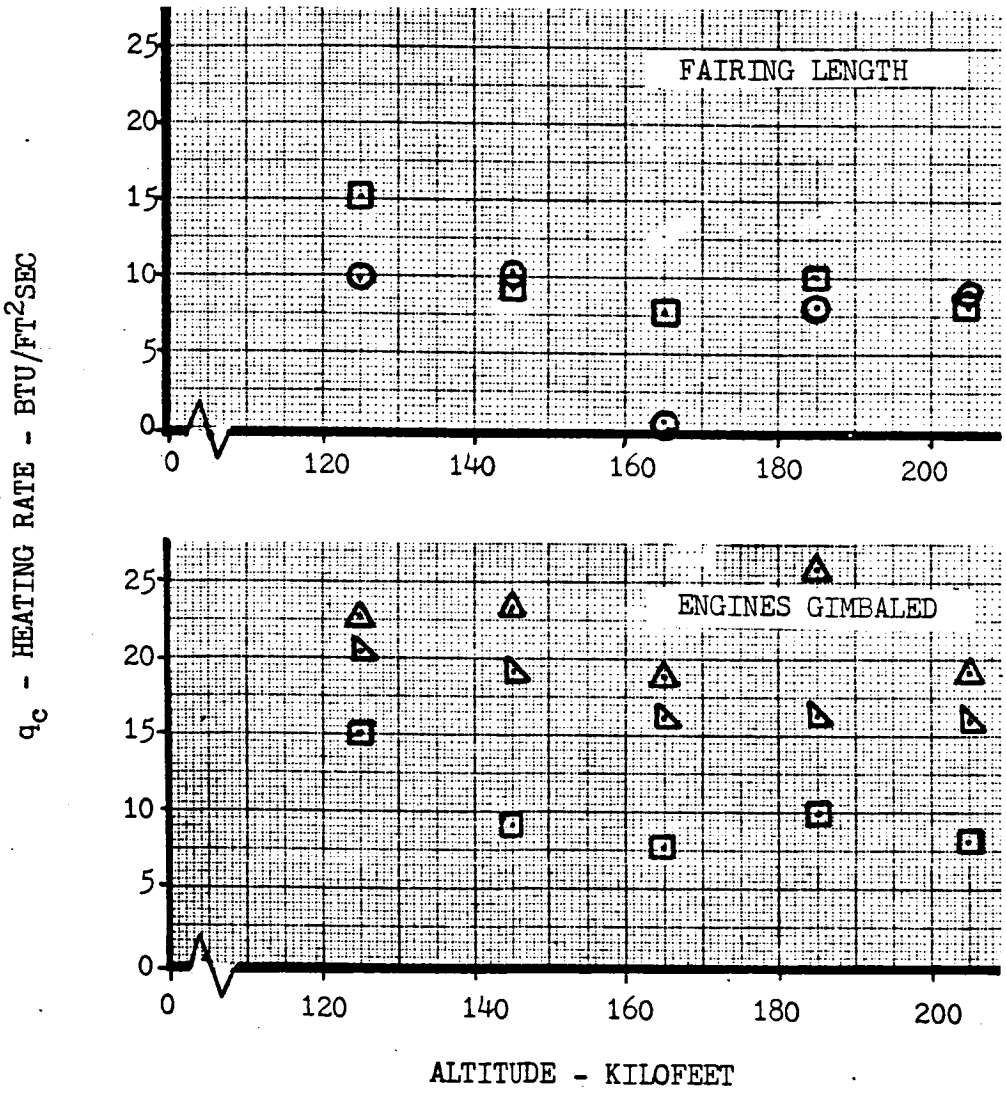

FIGURE 138 Engine Heating - Convection (External)

TUNNEL Cornell Altitude Chamber

SYM.	INST.	CONFIG.	SYM.	INST.	CONFIG.
△	H_{21}	$B_1FS_1N_{G_3}N_{G_4}PL_1$	◭	H_{29}	$B_1FS_1N_{G_3}N_{G_4}PL_1$
◭	H_{23}	$B_1FS_1N_{G_3}N_{G_4}PL_1$	◭	H_{31}	$B_1FS_1N_{G_3}N_{G_4}PL_1$
◭	H_{27}	$B_1FS_1N_{G_3}N_{G_4}PL_1$	◭	$H_{9,7,5,3,1}$	$B_1FS_1N_{G_3}N_{G_4}PL_1$

NOTE: Symbol ◺ denotes configuration $B_1FS_1N_{G_5}N_{G_6}$

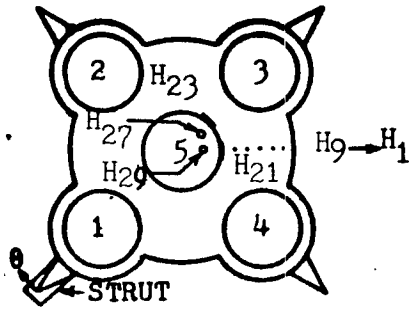

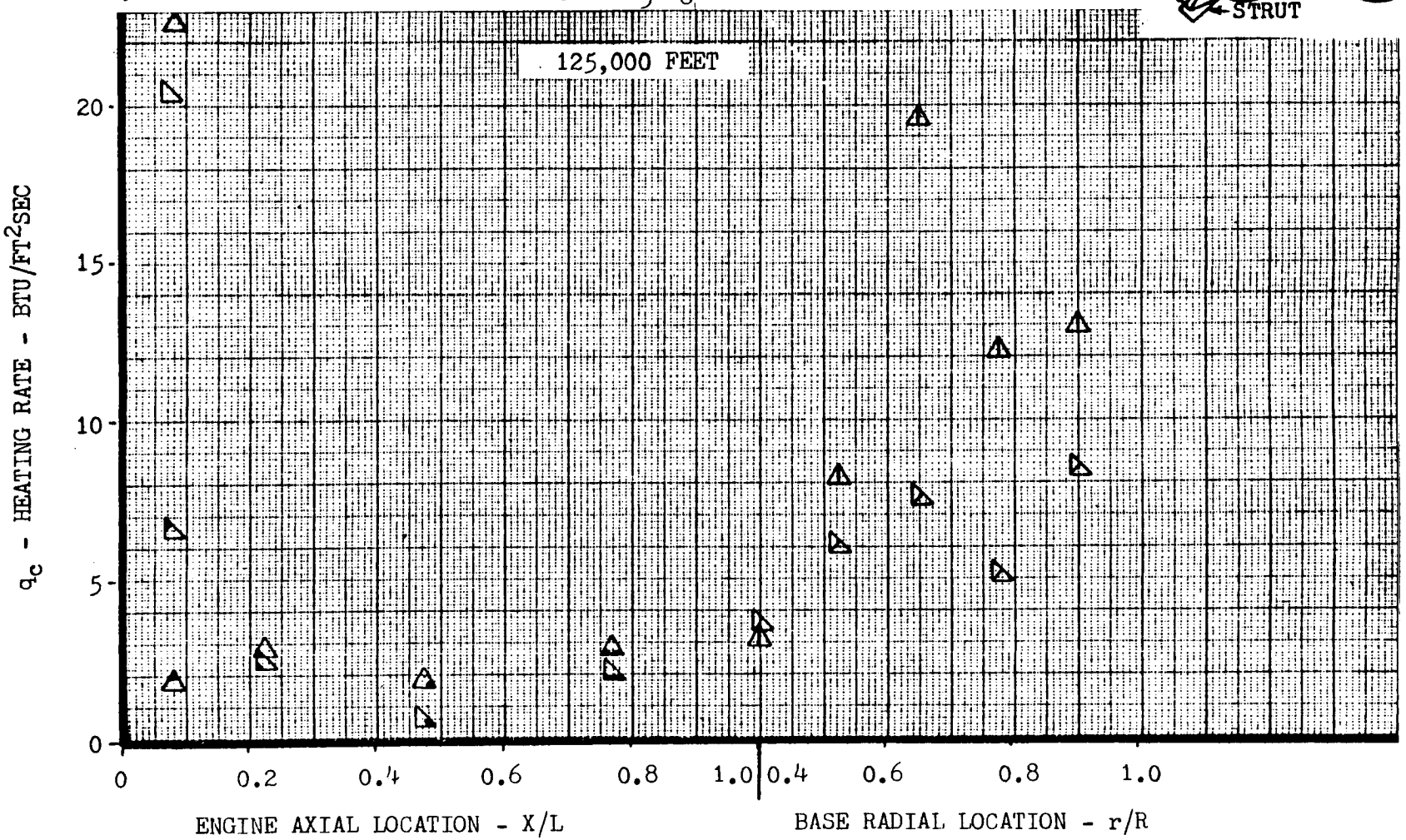

FIGURE 139 Engine and Base Heating - Convection (External)

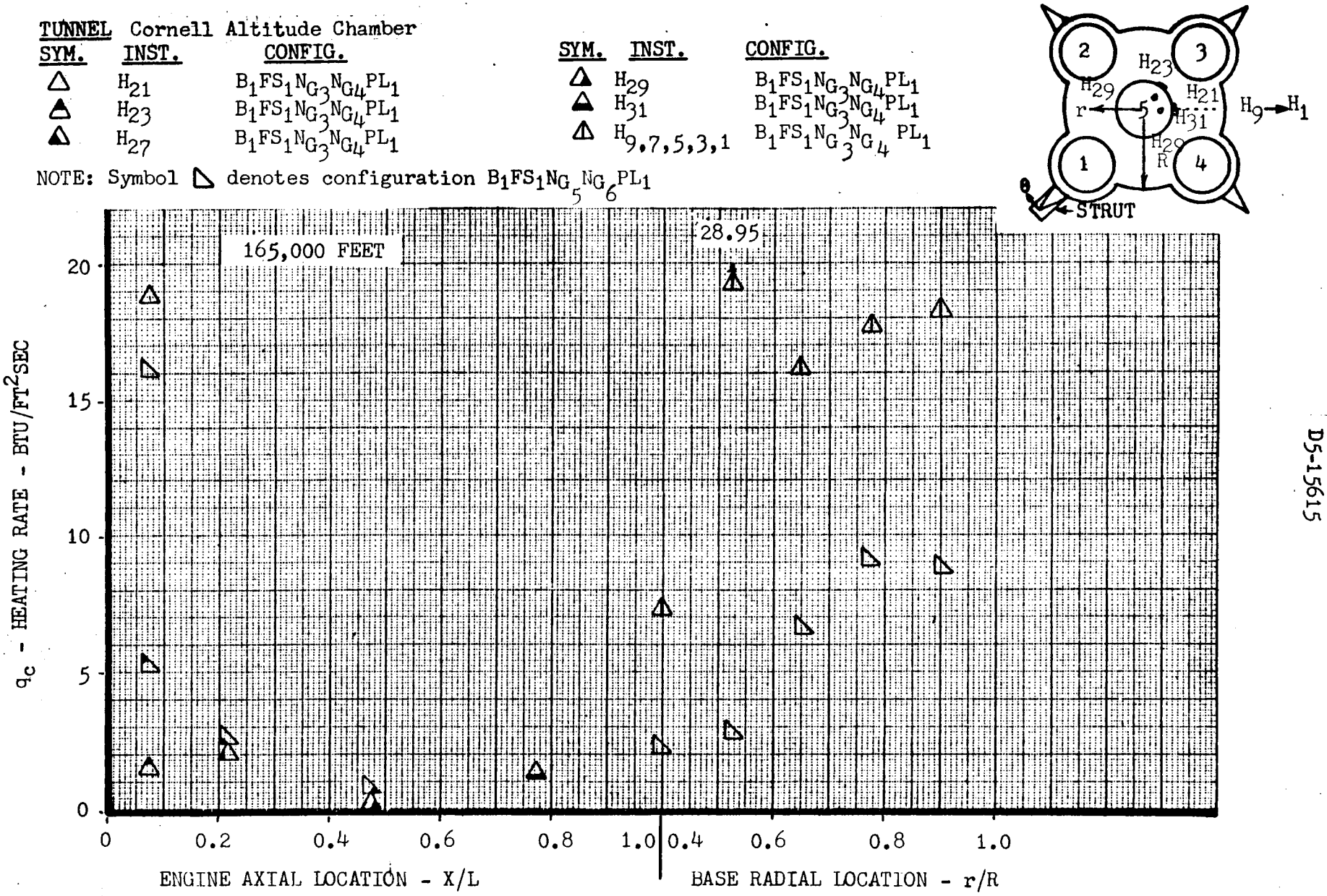

FIGURE 140 | Engine and Base Heating - Convection (External)

TUNNEL Cornell Altitude Chamber

SYM.	INST.	CONFIG.
△	H_{21}	$B_1FS_1N_{G_3}N_{G_4}PL_1$
▲	H_{23}	$B_1FS_1N_{G_3}N_{G_4}PL_1$
◭	H_{27}	$B_1FS_1N_{G_3}N_{G_4}PL_1$
◭	H_{29}	$B_1FS_1N_{G_3}N_{G_4}PL_1$
▲	H_{31}	$B_1FS_1N_{G_3}N_{G_4}PL_1$
◭	$H_{9,7,5,3,1}$	$B_1FS_1N_{G_3}N_{G_4}PL_1$

NOTE: Symbol ◺ denotes configuration $B_1FS_1N_{G_5}N_{G_6}PL_1$

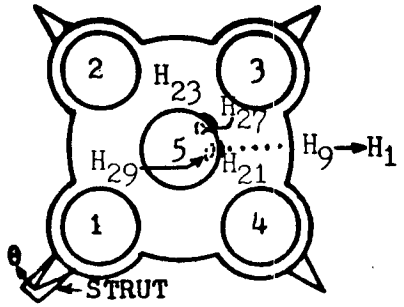

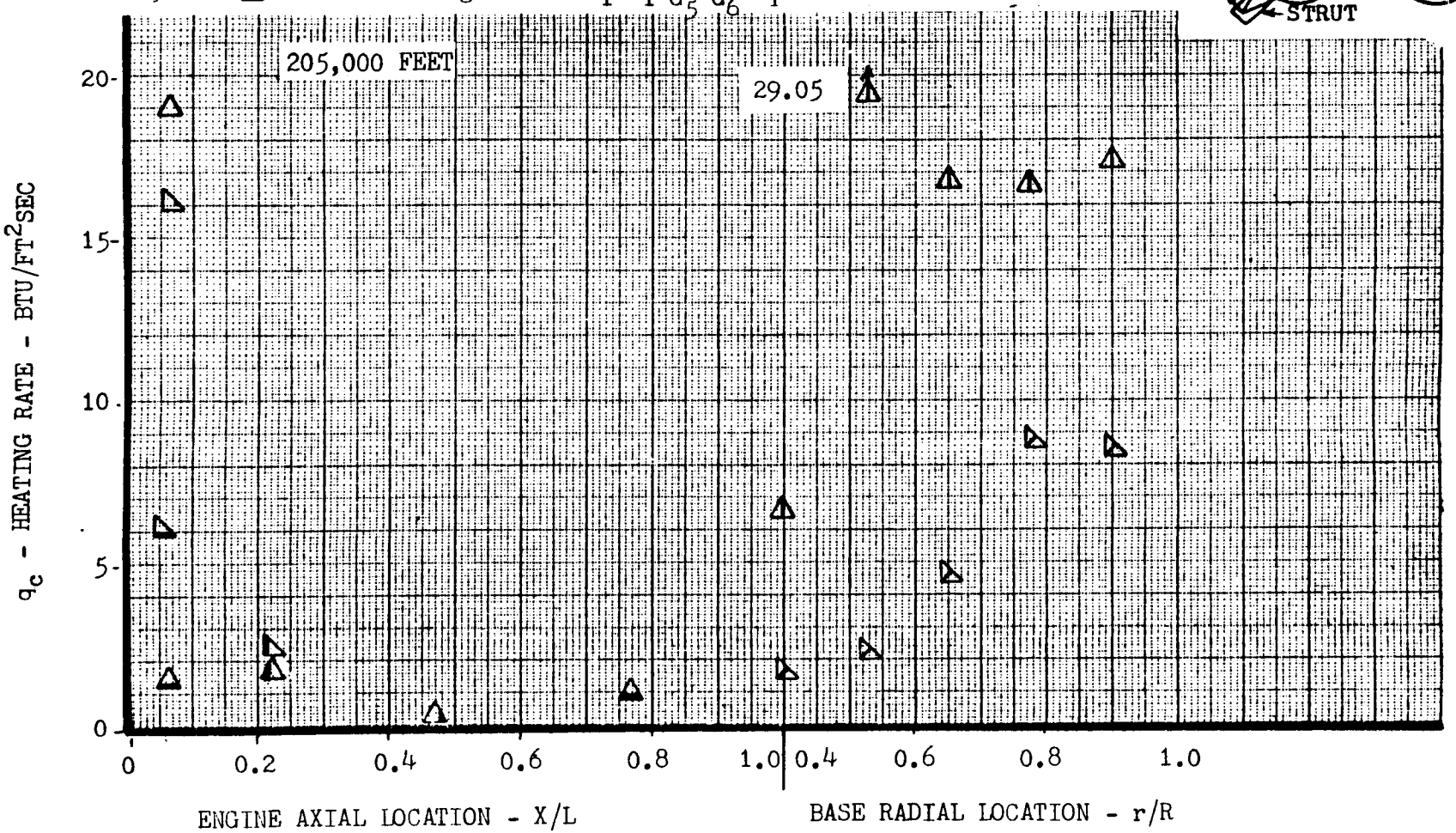

FIGURE 141 Engine and Base Heating - Convection (External)

6.2.3 (Continued)

Results show that the gas flow patterns for each configuration are essentially the same at all altitudes. Heating rates to all points on the engine except near the nozzle exit plane are affected similarly regardless of gimbal pattern. However, gimballing engines 3 and 4 toward each other creates much higher base heating rates than when the engines are gimballed toward the center engine (N_{G_5} N_{G_6}).

6.2.4 Convection to Engine (Engine Out)

Convection heating data for the inside surface of an instrumented and plugged center engine is shown in Figure 142. The gage locations are described in paragraph 4.2.4 and are shown in Figures 24 and 25 of Volume 1.

Gages H_{53} and H_{55} are located on the nozzle lip facing aft, H_{53} being between engine 2 and 3 and H_{55} being 180 degrees from H_{53}.

Data on the nozzle lip are in good agreement with each other. These data are two to three times greater than convection to the base for the same configuration (see Figure 130). The convective heating to H_{43} is much higher than the lip heating, which is unexpected. Heating to the outside of the nozzle is very small and indicates that the engine is trapping all the recirculating gas and very little is flowing between engines toward the base.

6.2.5 Comparison with Theory

Theoretical convective heating calculations have been made for comparison with the model test data. The theoretical heating was calculated by combining the heat transfer coefficient with the base gas temperature and base plate temperature through the equation

$$q_c = h(T_G - T_W)$$

Base plate temperature for the model was approximately 80°F, which is used for all theoretical calculations. The details of the heat transfer coefficient and base gas temperature calculations are given in Appendix B, Volume 1. Because no external flow existed, the base gas temperature was equal to the recirculated gas temperature. The base gas temperature was measured using the hot base plate configuration at 165,000 feet simulated altitude.

The base gas temperature measurements are compared with the theoretical base gas temperature (Appendix B) in Figure 143. It is evident that the measured data is below the theoretical calculations.

TUNNEL Cornell Altitude Chamber

SYM.	INST.	CONFIG.
◇	H_{53}	$B_1FS_1N_7PL_1$
◇	H_{55}	$B_1FS_1N_7PL_1$
◇	H_{43}	$B_1FS_1N_7PL_1$
◇	H_{51}	$B_1FS_1N_7PL_1$
◇	H_{47}	$B_1FS_1N_7PL_1$

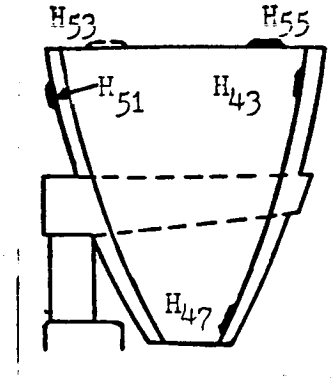

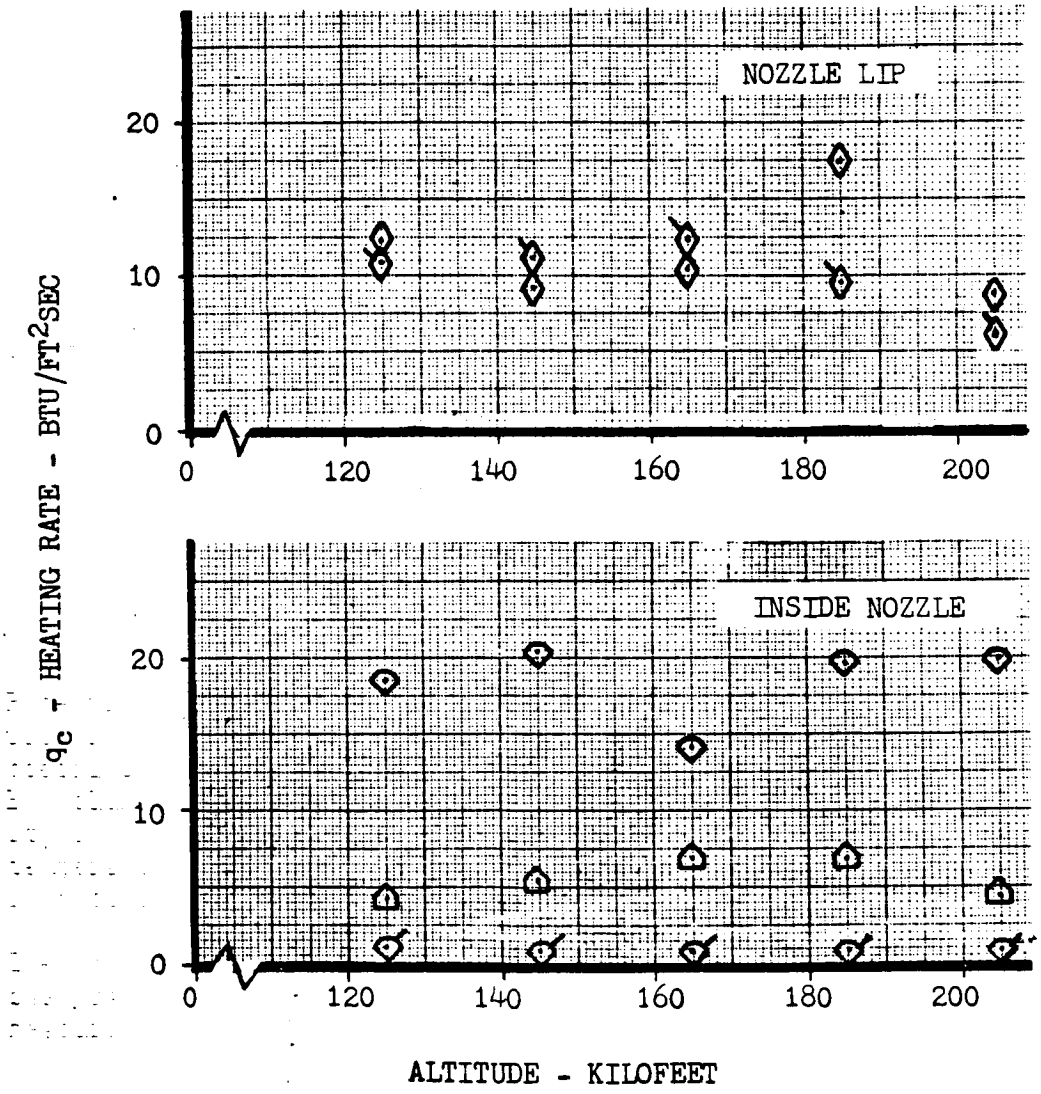

FIGURE 142 Engine Heating - Convection

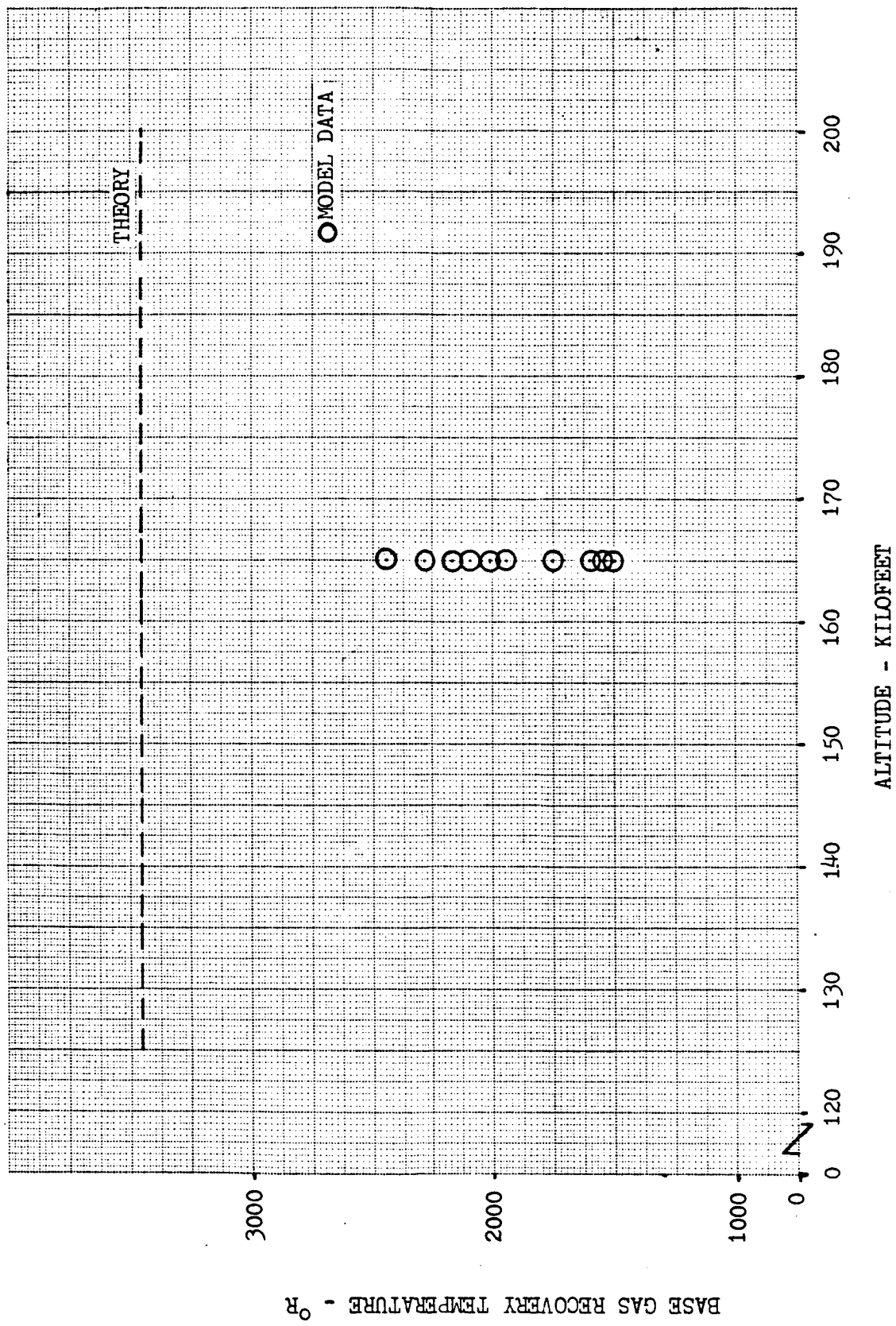

FIGURE 143 Base Gas Temperature - Comparison with Theory - CAL High Altitude Chamber

6.2.5 (Continued)

The theoretical convective heating rates from Appendix B are compared with the experimental convective heating data in Figure 144. Theoretical calculations were made for base pressures of 0.07 psia and 0.04 psia. The experimental data are above the theoretical calculations but are of the same order of magnitude. The two flagged symbols indicate the convective heating measured in the Lewis 10 by 10 tunnel at Mach 3.5 and 150,000 feet. The free stream flow affects tend to reduce the heating with or without scoops.

6.3 BASE PRESSURE

Base pressure has been shown to be a function of altitude and vehicle configuration by Goethert (Reference 22, Volume 1). At some altitude which depends on vehicle configuration, the base pressure will become greater than ambient, and combustion products will recirculate and escape between the outboard engines. The flow passage between the engines resembles a converging -diverging nozzle. Flow velocity is expected to become sonic if the critical pressure ratio is reached and further reduction of the ambient pressure due to increasing altitude will not effect the recirculated mass which can escape. Additional mass can escape only if the pressure is increased. Therefore, at some altitude the base pressure may cease to follow ambient pressure and either remain constant or increase.

Base pressure is not monitored in the quadrants in which heating rates are measured. Therefore, no pressure and heating correlation is possible for gimballed configurations.

6.3.1 Configuration Effect on Base Pressure

Figures 145 and 146 depict the base pressure data for two non-gimballed configurations. The data are not consistent but in general indicate that the pressure gradient inside of the minimum area ratio between nozzles ($r/R = 0.65$) tend to flatten out with an increase in altitude. The pressure outside ($r/R = 0.90$) are for the most part higher.

Base pressure data tends to follow the tunnel static pressure to an altitude of 155,000 feet. Above this altitude the data diverge from the tunnel static and appear to remain constant or increase even though the ambient is decreasing. Clearly, flow between the outside engines is choked for altitudes above 155,000 feet.

Data for the two configurations compare favorably and indicate that removal of the engine fairing has negligible effect on base pressure. With the center engine out the base pressure decreases with an increase in altitude throughout the range of the data indicating that flow through the minimum area between nozzles is still subsonic. The base pressures

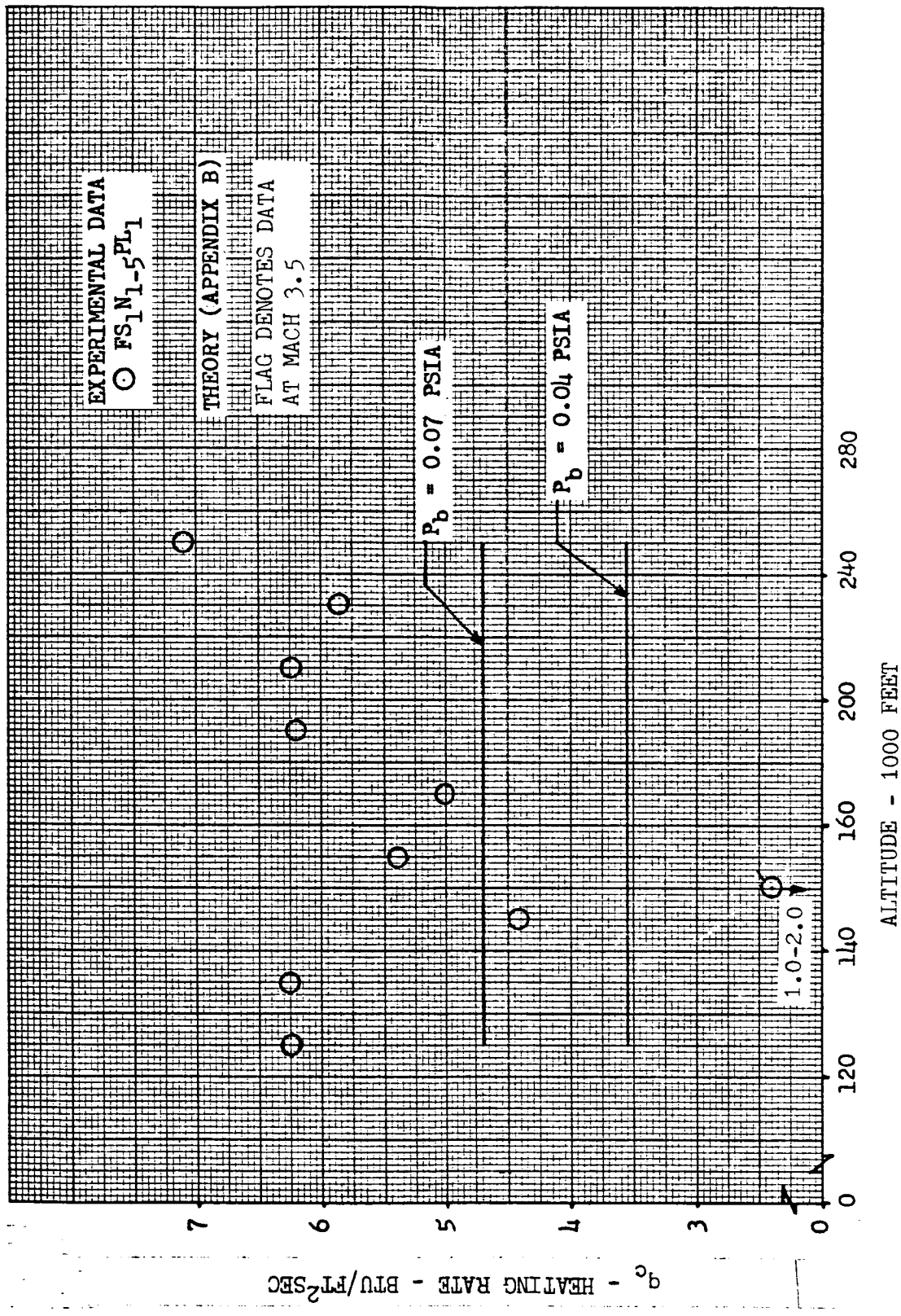

FIGURE 144 Convective Heating - Comparison with Theory - CAL High Altitude Chamber

TUNNEL Cornell Altitude Chamber

SYM.	INST.	CONFIG.
□	$P_{5,6,7}$	$B_1FS_1N_{1-5}PL_1$
◇	P_5	$B_1FS_1N_{1-5}PL_1$
⬠	P_6	$B_1FS_1N_{1-5}PL_1$
◇	P_7	$B_1FS_1N_{1-5}PL_1$

NOTE: 1. □ 205 kilofeet
2. □ 175 kilofeet
3. □ 125 kilofeet

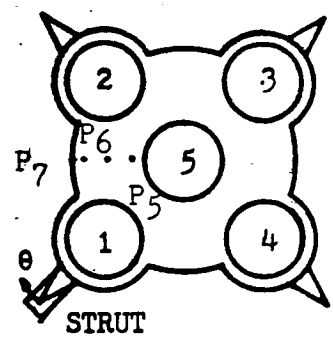

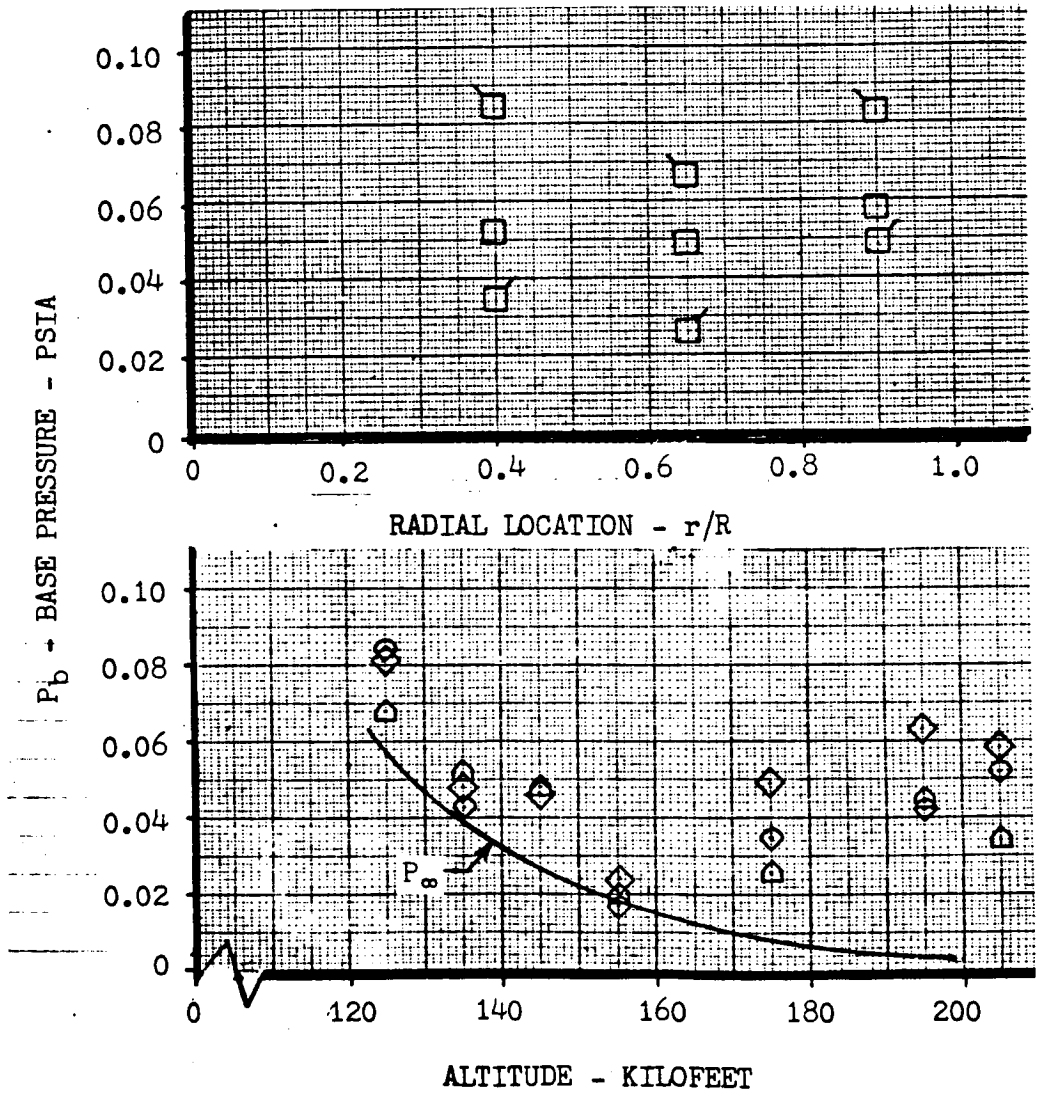

FIGURE 145 Base Pressure

TUNNEL Cornell Altitude Chamber

SYM.	INST.	CONFIG.
○	$P_{1,2,3,5,6,7}$	$B_1FS_4SC_1N_{1-5}PL_1$
◇	P_5	$B_1FS_4SC_1N_{1-5}PL_1$
⬠	P_6	$B_1FS_4SC_1N_{1-5}PL_1$
◇	P_7	$B_1FS_4SC_1N_{1-5}PL_1$

NOTE: 1. Solid symbol is $P_{1,2,3}$
2. ○ 205 kilofeet
○ 165 kilofeet
○ 145 kilofeet

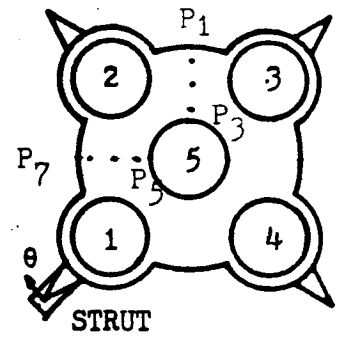

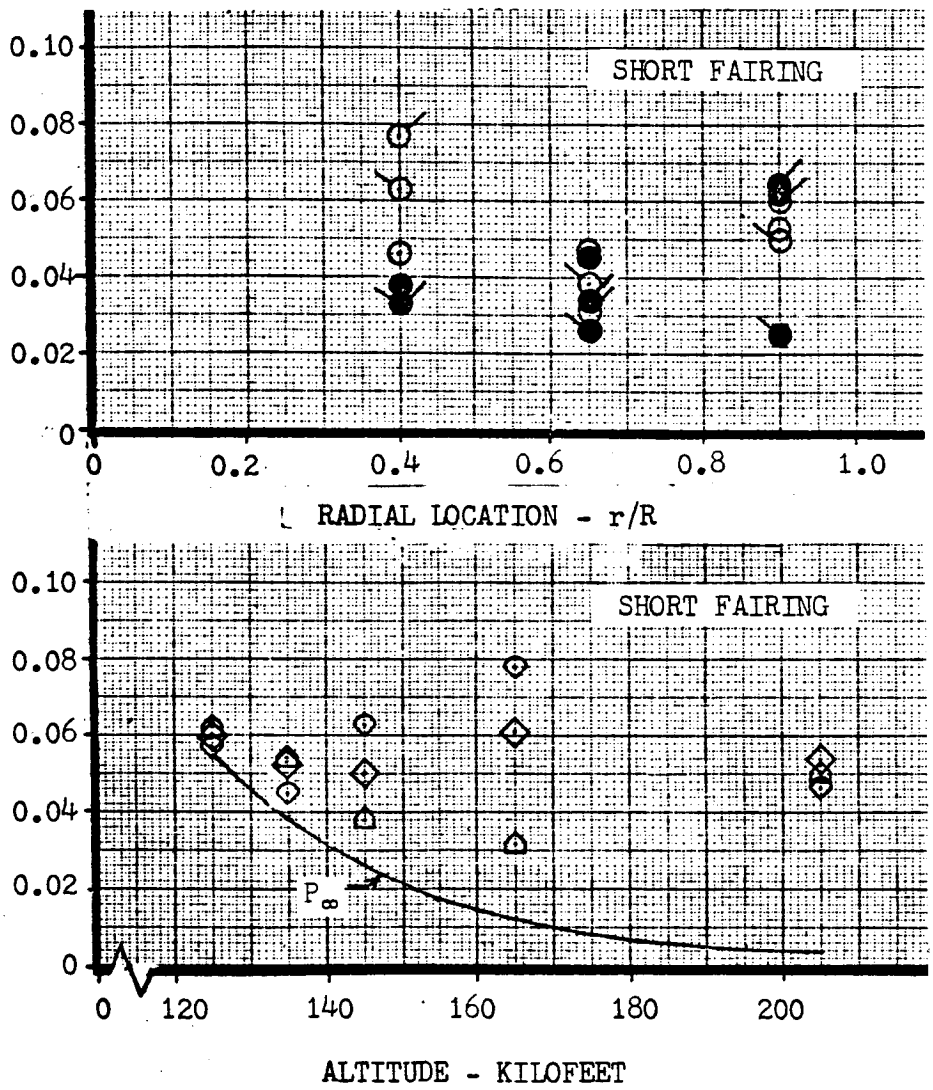

FIGURE 146 Base Pressure

6.3.1 (Continued)

with the inoperative center engine are lower than those with 5 engines firing due to the decrease in recirculated mass (Figure 147).

Base pressures were not measured in the quadrants between the gimballed engines. The pressures for the gimbal configuration are presented for two other quadrants (Figure 148); therefore, comparison between heating and base pressures cannot be made.

6.3.2 Comparison with Theory

Theoretical base pressure calculations were made using the mixing layer theory developed by Korst. The details of this calculation are described in Appendix C, Volume 1. Figure 149 shows a comparison of the theoretical calculations and the model base pressure data. The theoretical calculations are total pressures as compared to the model data which can be a pressure between a static and total pressure, depending on flow field and model instrumentation orientation.

6.4 DATA ACCURACY

Inaccuracies in the test data are due to inaccuracy of the gages and the ability to accurately read the oscilloscope traces. There is further uncertainty in the data due to unsymetrical flow in the base. These two errors are discussed below.

6.4.1 Repeatability

Repeat runs were made on every configuration throughout the test program to determine data repeatability. Radiation heating rates are shown in Figure 150. The maximum data variation in Figure 150 is 90 percent above and below an average value. The average variation is 50 percent. The radiation heating rates were usually less than 1.0 BTU/FT^{2}SEC and, therefore, a small delta error appears as a large percentage error. Convective heating rates are shown in Figure 151. The maximum data variation in Figure 151 is 60 percent above and below an average value. Base pressure data is shown in Figure 152.

The data presented is representative of that obtained throughout the test. When configuration changes were made, it was noted that the pressure transducers had moved and were no longer spring supported. Therefore, a realistic repeatability of base pressure as a function of instrumentation was not obtained. At no time before testing or during testing was an attempt made to determine the external effects on the instrumentation.

TUNNEL Cornell Altitude Chamber

SYM.	INST.	CONFIG.	SYM.	INST.	CONFIG.
◇	P_5	$B_1FS_1N_7PL_1$			
◇	P_6	$B_1FS_1N_7PL_1$			
◇	P_7	$B_1FS_1N_7PL_1$			

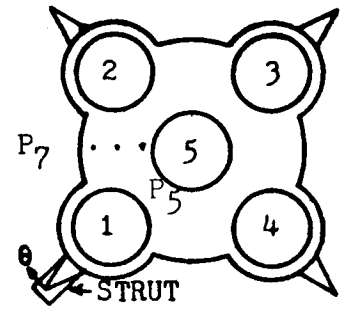

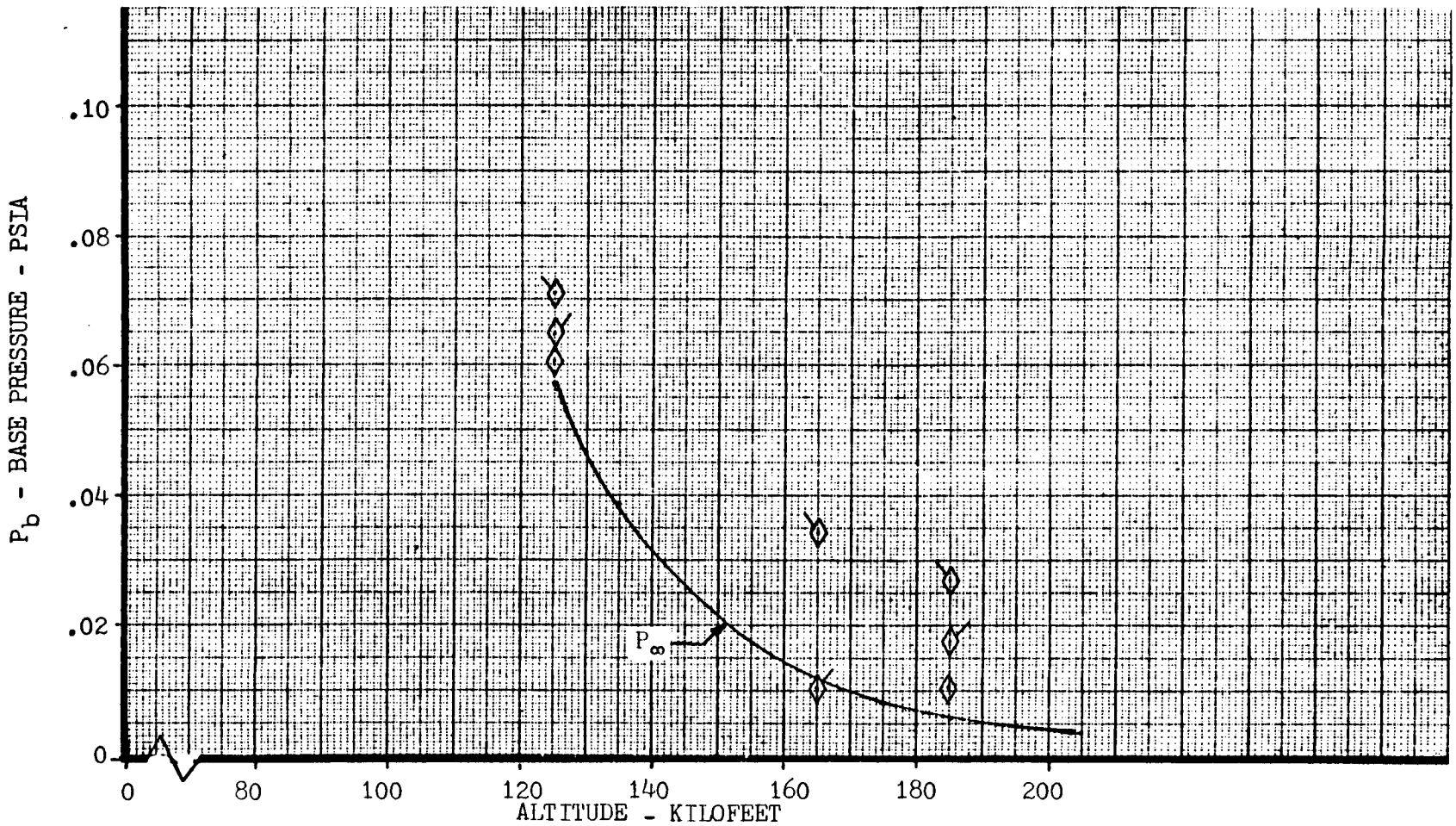

FIGURE 147 Base Pressure

TUNNEL Cornell Altitude Chamber

SYM.	INST.	CONFIG.
△	P_1	$B_1FS_1N_{G_3}N_{G_4}PL_1$
◺	P_3	$B_1FS_1N_{G_3}N_{G_4}PL_1$
◸	P_5	$B_1FS_1N_{G_3}N_{G_4}PL_1$
▷	P_1	$B_1FS_1N_{G_5}N_{G_6}PL_1$
◹	P_3	$B_1FS_1N_{G_5}N_{G_6}PL_1$
◷	P_5	$B_1FS_1N_{G_5}N_{G_6}PL_1$
◇	P_7	$B_1FS_1N_{G_5}N_{G_6}PL_1$

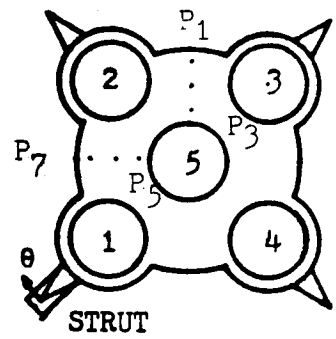

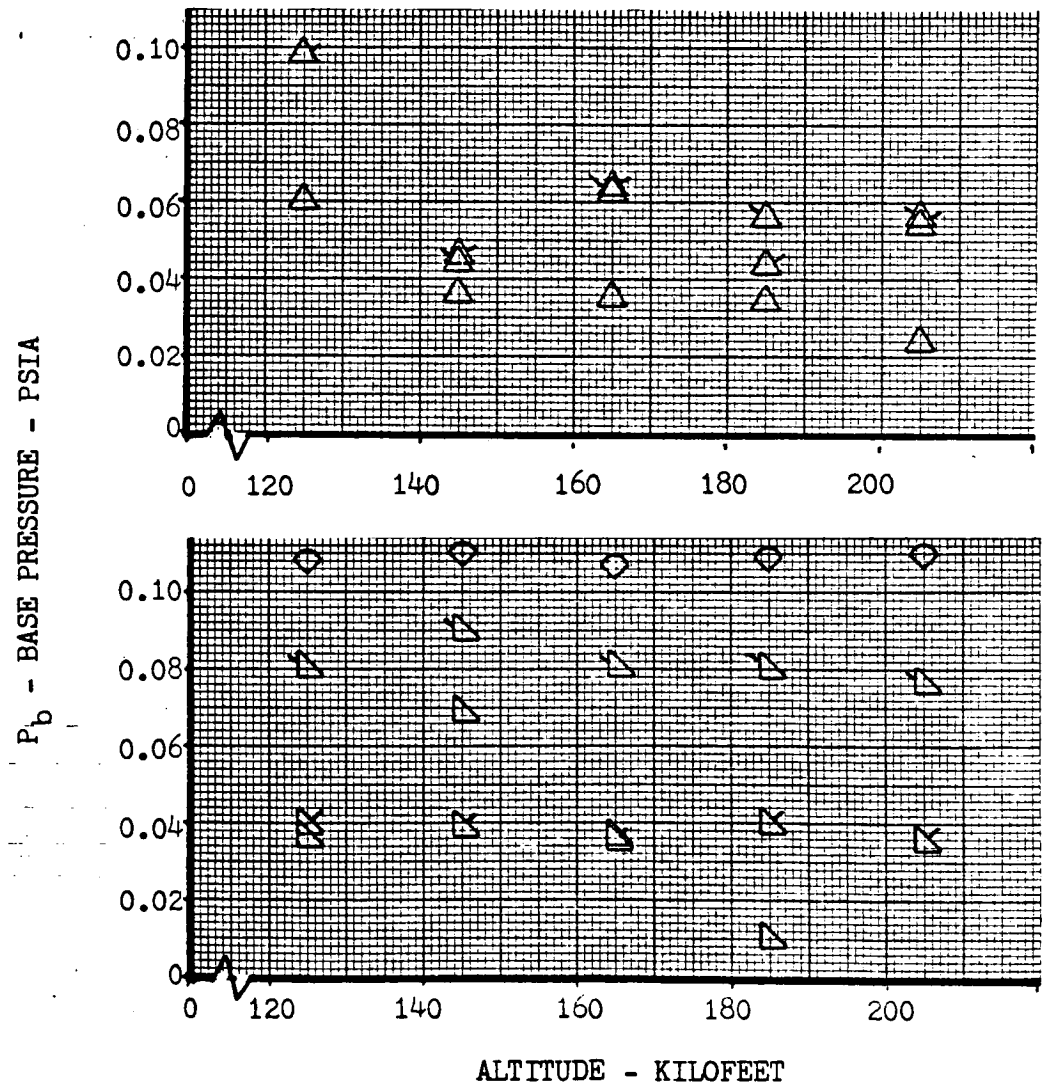

FIGURE 148 Base Pressure

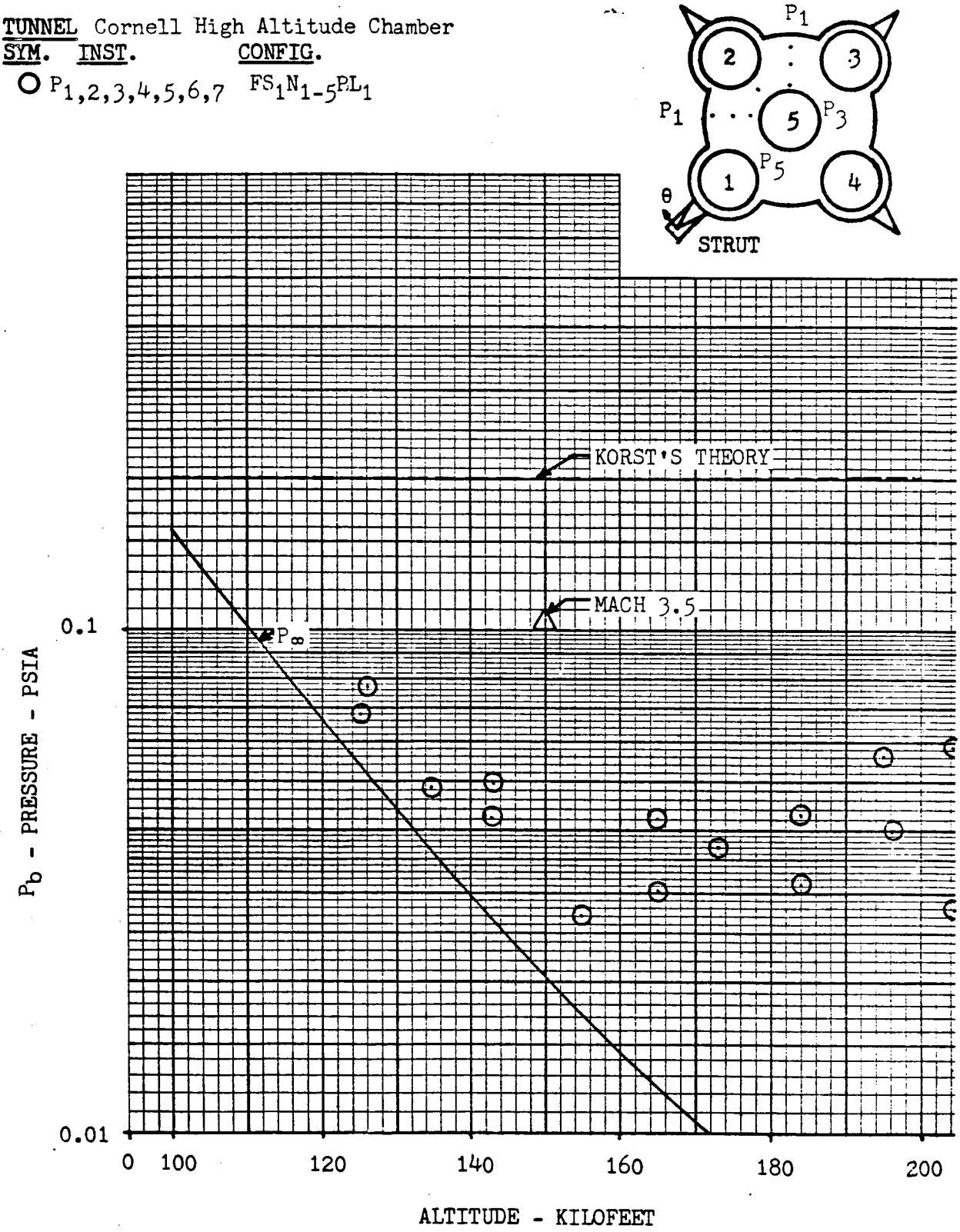

FIGURE 149 Base Pressure Comparison with Theory - CAL High Altitude Chamber

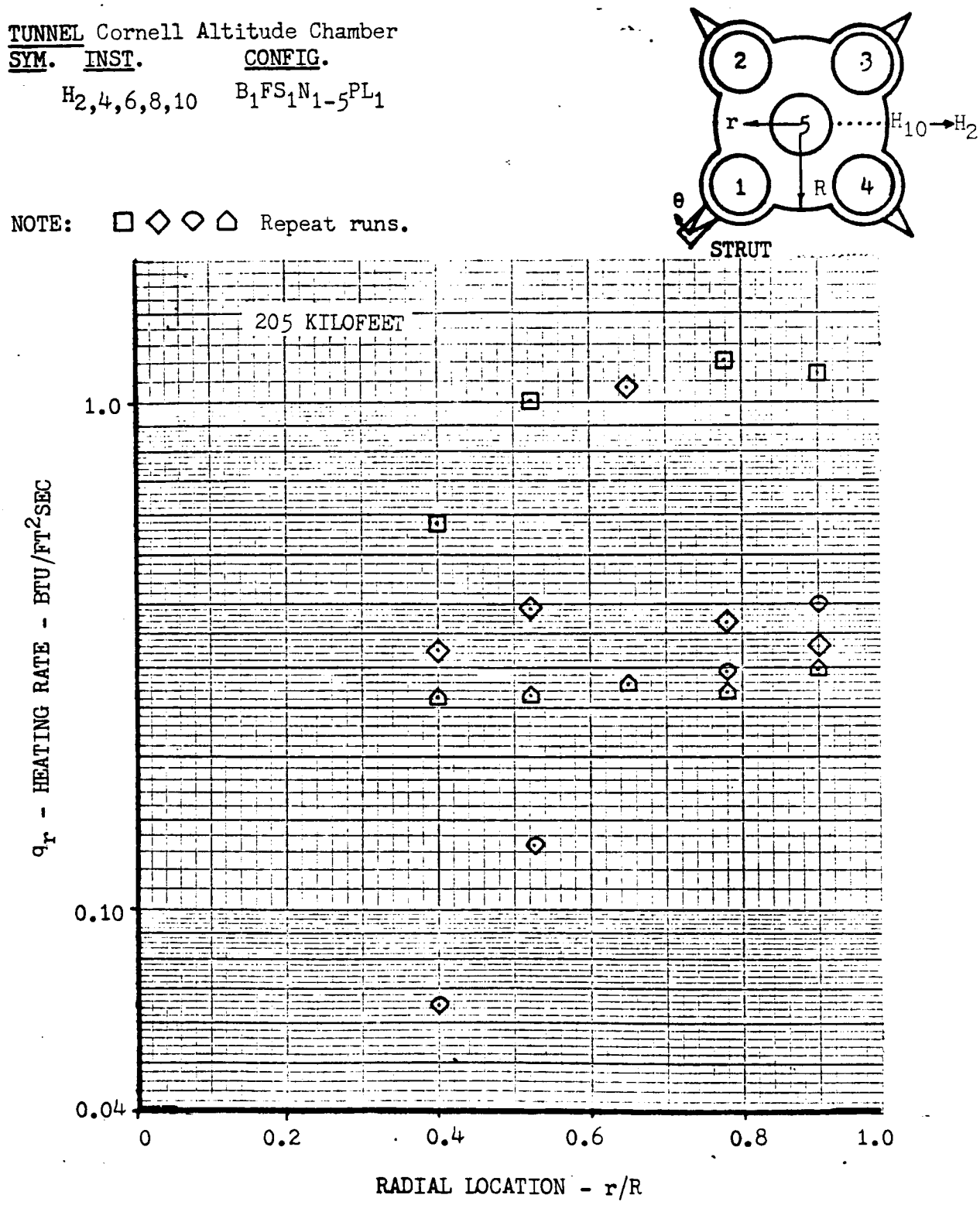

FIGURE 150 Base Heating - Radiation (Repeatability)

TUNNEL Cornell Altitude Chamber

SYM.	INST.	CONFIG.
□	$H_{1,3,5,7,9}$	$B_1FS_1N_{1-5}PL_1$
△	$H_{1,3,5,7,9}$	$B_1FS_1N_{G_3}N_{G_4}PL_1$
◿	$H_{1,3,5,7,9}$	$B_1FS_1N_{G_5}N_{G_6}PL_1$
◇	$H_{1,3,5,7,9}$	$B_1FS_1N_7PL_1$

NOTE: Flagged symbols are repeat runs.

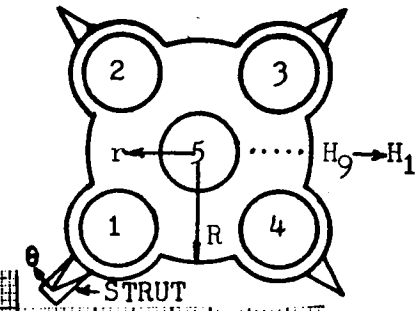

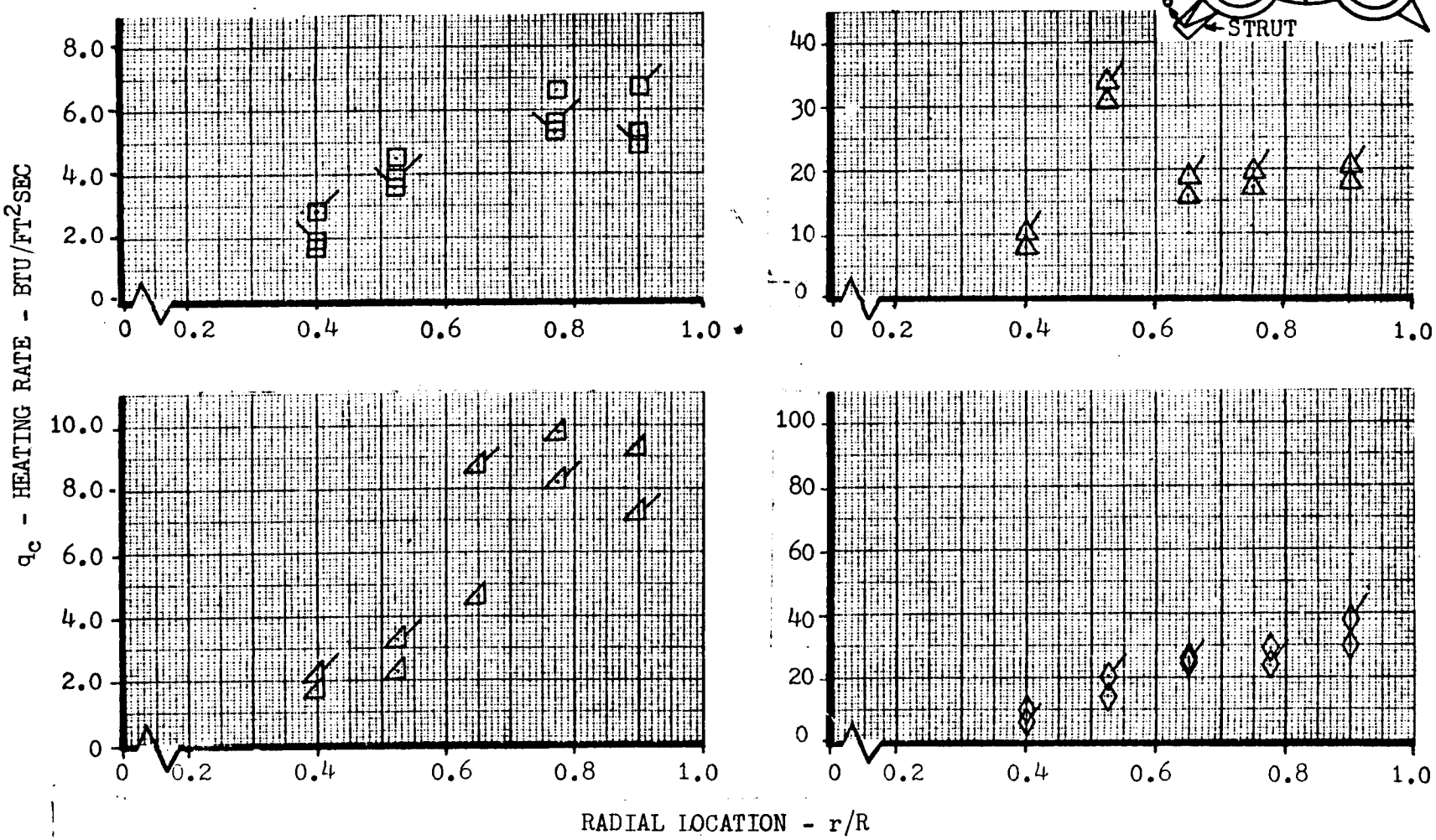

FIGURE 151 Base Heating - Convection (Repeatability)

TUNNEL Cornell Altitude Chamber

SYM.	INST.	CONFIG.
□	$P_{5,6,7}$	$B_1FS_1N_{1-5}PL_1$
△	$P_{6,7}$	$B_1FS_1N_{G_3}N_{G_4}PL_1$
◿	$P_{5,3}$	$B_1FS_1N_{G_5}N_{G_6}PL_1$
◇	$P_{5,7}$	$B_1FS_1N_{G_5}N_{G_6}PL_1$

NOTE: Flagged symbol denotes repeat run

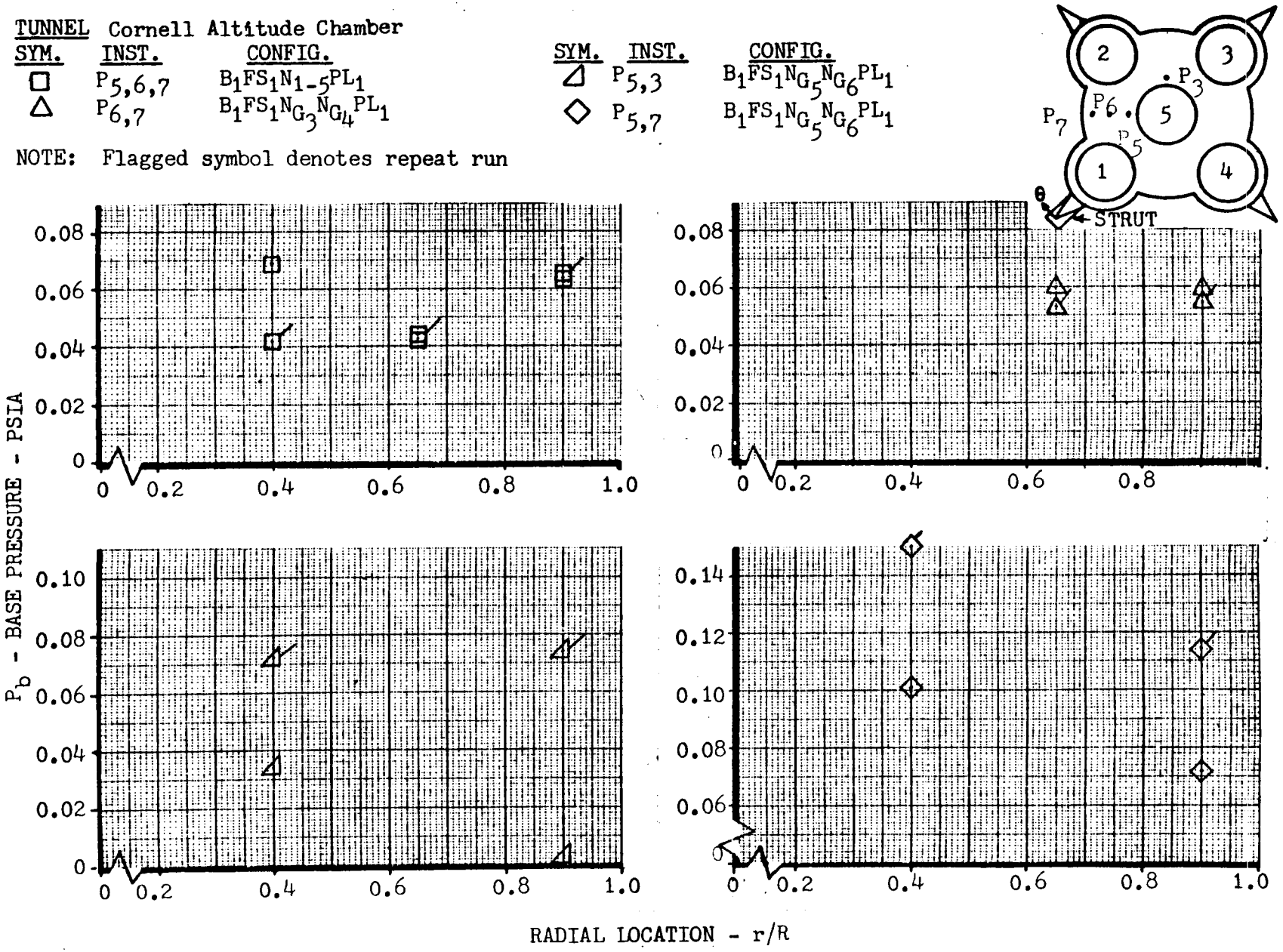

FIGURE 152 Base Pressure - Repeatability

6.4.2 Symmetry

Before this test series started, CAL conducted a flow symmetry test. This test was to include an engine exit pressure and heating survey. Attempts to complete the engine exit heating survey were never successful since instrumentation to withstand the heating rates was unavailable. The pressure survey was completed, with the results being shown in Figure 153. Total pressure calculated using frozen and equilibrium conditions are also shown in Figure 153.

Pressure and heat transfer measurements were also recorded in two quadrants on the base to show the degree of flow symmetry. Figure 154 shows the convective base heating symmetry and Figure 155 shows base pressure symmetry. The convective heating data indicate unsymmetrical flow. Since heating is related to velocity from the 1/2 to 1/5 power, a large difference in flow in the various quadrants is evident. Flow symmetry from base pressure data looks reasonable except for a few scattered points. The pressure data are subject to question because of the very low pressures being measured.

6.5 HEATED BASE PLATE

A heated base plate was used during the test to determine base gas temperature and a heat transfer coefficient. Convective heating rates were measured at wall temperatures of 80°F, 400°F, 700°F, and 900°F. The measured q was plotted versus wall temperature and the data extrapolated until the convective heating was zero (Figure 156). The wall temperature corresponding to $q_c = 0.0$ is the recovery gas temperature and the slope of the line is the heat transfer coefficient. The following assumptions were made using this method.

1. The heat transfer coefficient does not vary with either wall temperature or gas temperature, and,

2. The gas recovery temperature is independent of the wall temperature.

The average recovery gas temperature obtained on the test was 1500°F. Problems were encountered which make hot base data interpretation difficult. The total heating rates with the hot base at ambient conditions do not compare well with those obtained using the non-heated (cold) base. Radiation heating rates are considerably higher on the hot base plate. It was expected that the radiation heating would be lower. For these reasons, the recovery gas temperature obtained is questionable.

TUNNEL Cornell Altitude Chamber

SYM.	INST.	RUN	O/F	P_c	TURB.EX.	CONFIG.
□	-	87	2.27	986	No	$B_1FS_1N_{1-5}PL_1$
◇	-	89	1.72	943	No	$B_1FS_1N_{1-5}PL_1$
◇	-	90	2.215	944	No	$B_1FS_1N_{1-5}PL_1$
⬠	-	91	2.23	972	No	$B_1FS_1N_{1-5}PL_1$

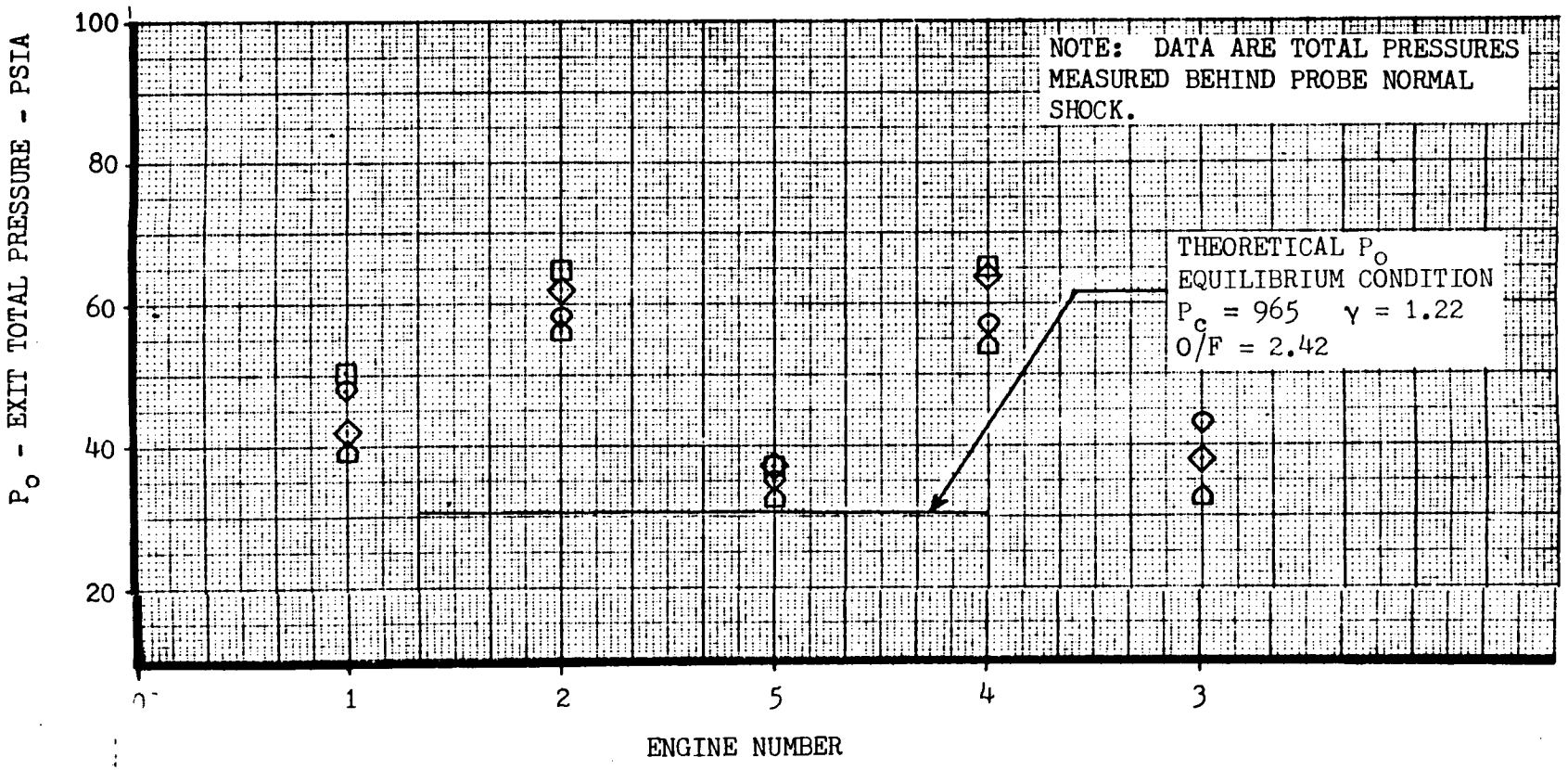

FIGURE 153 Nozzle Exit Pressure Survey

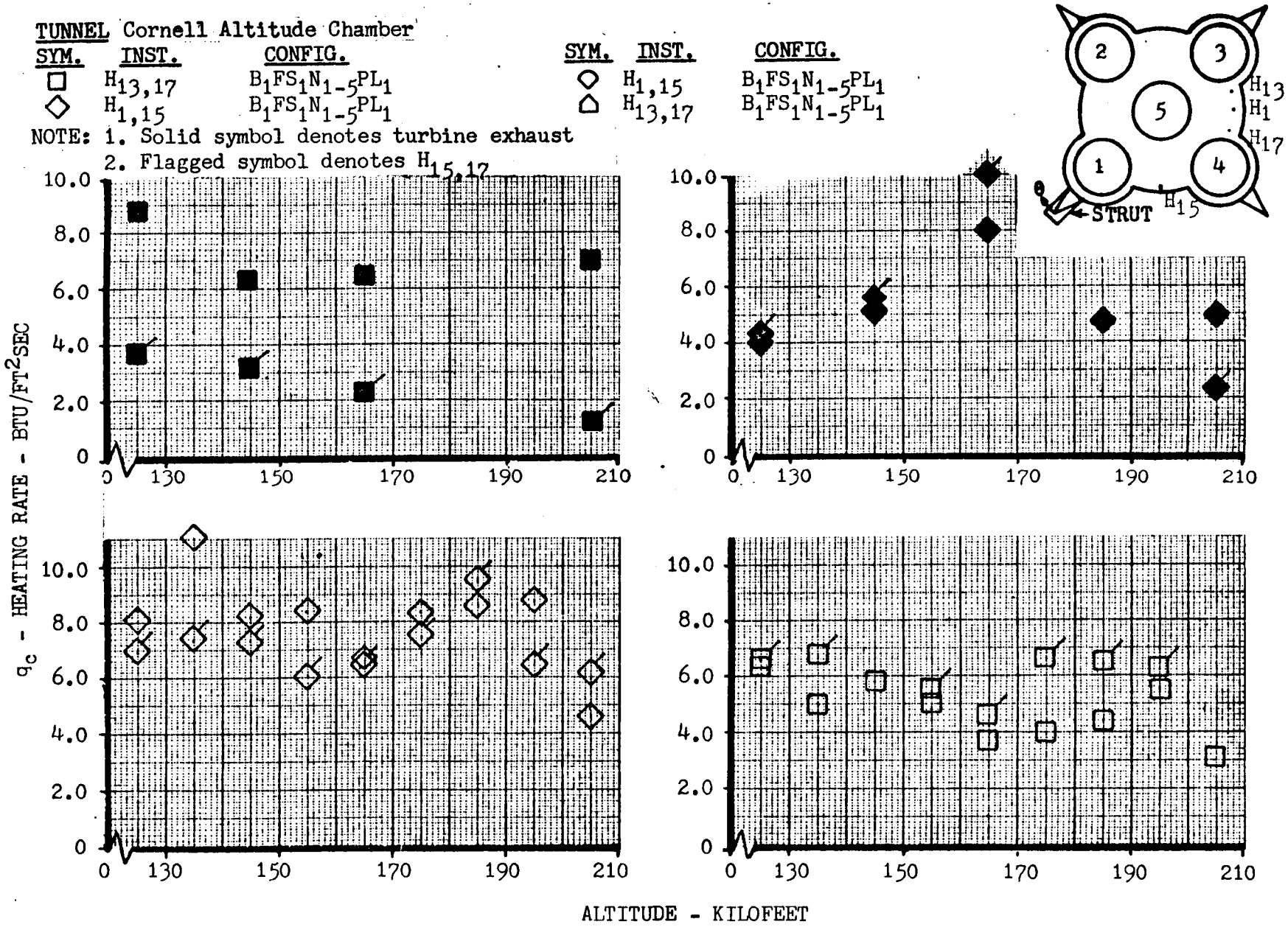

FIGURE 154 Base Heating - Convection (Symmetry)